

**Adaptive Mesh Refinement Cosmological Simulations of  
Cosmic Rays in Galaxy Clusters**

by

**Samuel William Skillman**

B.S., Harvey Mudd College, 2007

M.S., University of Colorado at Boulder, 2010

A thesis submitted to the  
Faculty of the Graduate School of the  
University of Colorado in partial fulfillment  
of the requirements for the degree of  
Doctor of Philosophy  
Department of Astrophysical and Planetary Sciences

2013

This thesis entitled:  
Adaptive Mesh Refinement Cosmological Simulations of Cosmic Rays in Galaxy Clusters  
written by Samuel William Skillman  
has been approved for the Department of Astrophysical and Planetary Sciences

---

Jack O. Burns

---

Brian W. O'Shea

---

Nils Halverson

---

Jason Glenn

---

Elizabeth Jessup

Date \_\_\_\_\_

The final copy of this thesis has been examined by the signatories, and we find that both the content and the form meet acceptable presentation standards of scholarly work in the above mentioned discipline.

Skillman, Samuel William (Ph.D., Astrophysical and Planetary Sciences)

Adaptive Mesh Refinement Cosmological Simulations of Cosmic Rays in Galaxy Clusters

Thesis directed by Prof. Jack O. Burns

Galaxy clusters are unique astrophysical laboratories that contain many thermal and non-thermal phenomena. In particular, they are hosts to cosmic shocks, which propagate through the intracluster medium as a by-product of structure formation. It is believed that at these shock fronts, magnetic field inhomogeneities in a compressing flow may lead to the acceleration of cosmic ray electrons and ions. These relativistic particles decay and radiate through a variety of mechanisms, and have observational signatures in radio, hard X-ray, and Gamma-ray wavelengths.

We begin this dissertation by developing a method to find shocks in cosmological adaptive mesh refinement simulations of structure formation. After describing the evolution of shock properties through cosmic time, we make estimates for the amount of kinetic energy processed and the total number of cosmic ray protons that could be accelerated at these shocks.

We then use this method of shock finding and a model for the acceleration of and radio synchrotron emission from cosmic ray electrons to estimate the radio emission properties in large scale structures. By examining the time-evolution of the radio emission with respect to the X-ray emission during a galaxy cluster merger, we find that the relative timing of the enhancements in each are important consequences of the shock dynamics. By calculating the radio emission expected from a given mass galaxy cluster, we make estimates for future large-area radio surveys.

Next, we use a state-of-the-art magnetohydrodynamic simulation to follow the electron acceleration in a massive merging galaxy cluster. We use the magnetic field information to calculate not only the total radio emission, but also create radio polarization maps that are compared to recent observations. We find that we can naturally reproduce Mpc-scale radio emission that resemble many of the known double radio relic systems.

Finally, motivated by our previous studies, we develop and introduce a numerical library,

CRT, for following cosmic ray transport. Using this new tool, we are able to follow the acceleration and aging of cosmic rays as they flow throughout the intracluster medium. Using synthetic observations, we outline how this new capability will revolutionize our study of galaxy cluster non-thermal populations by allowing comparisons with current and upcoming telescopes.



## Dedication

To my parents William and Darlene.

## Acknowledgements

First of all I'd like to thank my Ph.D. advisor, Jack Burns, for his guidance and conviction to always place simulations in the context of observations. I would like to thank the entire Enzo and yt community for their support, friendship, and effort. I look forward to the day when each of you are rewarded for your selflessness, and await our next workshop. In particular I thank Brian O'Shea, Matthew Turk, Britton Smith, Jeffrey Oishi, and Cameron Hummels. I would like to thank the following people for wonderful conversations and correspondence – Marcus Brüggem, Greg Bryan, Stirling Colgate, Megan Donahue, Sunil Golwala, Eric Hallman, Matthias Hoefft, Hui Li, Tom Jones, Daisuke Nagai, Christoph Pfrommer, Dongsu Ryu, Jack Sayers, and Mark Voit. I also thank my committee members Nils Halverson, Jason Glenn, and Elizabeth Jessup. I would like to thank the DOE Computational Science Graduate Fellowship for the opportunity to explore the work in this dissertation, for the wonderful conversations at the annual conferences, and for funding under grant number DE-FG02-97ER25308. Computations described in this work were performed using the Enzo code (<http://enzo-project.org>), which is the product of a collaborative effort of scientists at many universities and national laboratories. Collaborators have been funded by the following NSF, DOE, and NASA grants and contracts: AST 04-07368, AST-08-07215, AAPF AST 07-02923, DE-AC52-06NA25396, NASA LUNAR Science Institute (via cooperative Agreement NNA09DB30A), and NASA ATRP NNX09AD80G. Computing time has been provided by NSF and DOE resources through NRAC allocations MCA98N020, TG-AST090040 and TG-AST090095 as well as LANL Institutional Computing program. I also heavily thank the the University of Colorado's Research Computing team for their support. This work utilized the Janus supercomputer, which is supported by the National Science Foundation (award number CNS-0821794) and the University of Colorado Boulder. The Janus supercomputer is a joint effort of the University of Colorado Boulder, the University of Colorado Denver and the National Center for Atmospheric Research.

# Contents

## Chapter

<b>1</b>	Introduction	1
1.1	Big Bang Cosmology . . . . .	8
1.2	Large Scale Structure Formation . . . . .	10
1.2.1	Gravitational Instability . . . . .	11
1.2.2	Voids, Sheets, Filaments & Halos . . . . .	12
1.3	The ICM From Abell to Zel'dovich . . . . .	14
1.4	Plasma Physics of the ICM . . . . .	18
1.4.1	Heating Mechanisms . . . . .	19
1.4.2	Particle Acceleration . . . . .	20
1.4.3	Observational Signatures of the ICM . . . . .	22
1.5	Roadmap . . . . .	30
<b>2</b>	Methods: Simulation, Analysis, & Visualization	31
2.1	A Brief Introduction to Computational Cosmology . . . . .	31
2.1.1	Gravity . . . . .	31
2.2	Hydrodynamics . . . . .	34
2.2.1	Lagrangian Hydrodynamics: Smoothed Particle Hydrodynamics . . . . .	34
2.2.2	Eulerian Grid-Based Hydrodynamics . . . . .	35
2.3	Adaptive Mesh Refinement . . . . .	36

2.4	Enzo: A Community Code for Astrophysics . . . . .	37
2.4.1	Enhancements to Enzo . . . . .	40
2.5	yt: Data Analysis & Visualization . . . . .	42
<b>3</b>	<b>Cosmological Shocks</b>	<b>52</b>
3.1	Introduction . . . . .	52
3.2	Methodology . . . . .	56
3.2.1	The Enzo Code . . . . .	56
3.2.2	Shock-Finding Algorithm . . . . .	57
3.2.3	Cosmic Ray Acceleration Models . . . . .	61
3.2.4	Simulations . . . . .	64
3.3	Validation of Shock-Finding Method . . . . .	66
3.3.1	Shock Tube Test . . . . .	66
3.3.2	Comparison to Ryu et al. [204] . . . . .	67
3.4	Results for the Santa Fe Light Cone Volume . . . . .	73
3.4.1	Shock Frequencies . . . . .	73
3.4.2	Cosmic Ray Energy Injection . . . . .	78
3.5	Effect of Mass and Spatial Resolution on Cosmic Ray Acceleration Efficiency . . . . .	81
3.5.1	Spatial Resolution . . . . .	81
3.5.2	Mass Resolution . . . . .	82
3.6	Discussion . . . . .	84
3.7	Conclusions & Future Directions . . . . .	85
<b>4</b>	<b>Radio Relics</b>	<b>96</b>
4.1	Introduction . . . . .	96
4.2	Methods . . . . .	100
4.2.1	<i>Enzo</i> . . . . .	100
4.2.2	Simulations . . . . .	100

4.2.3	Shock Finding . . . . .	102
4.2.4	Synchrotron Emission . . . . .	103
4.3	Global Properties of Radio relics . . . . .	106
4.3.1	Full Box Projections . . . . .	106
4.3.2	Phase Diagrams . . . . .	109
4.3.3	Radio Emission as a Proxy for Cluster Accretion . . . . .	113
4.4	Individual Object Properties . . . . .	114
4.4.1	Cluster Projections . . . . .	114
4.4.2	Radio Power - Mass Relationship . . . . .	116
4.4.3	Radio Power-X-ray Relationship . . . . .	121
4.4.4	Luminosity Function . . . . .	125
4.5	Discussion . . . . .	127
4.5.1	Comparison To Previous Work . . . . .	127
4.5.2	Implications For Future Surveys . . . . .	129
4.5.3	Limitations of the Models . . . . .	130
4.6	Conclusions and Future Directions . . . . .	131
<b>5</b>	<b>Cosmological MHD Simulations of Galaxy Cluster Radio Relics: Insights and Warnings for Observations</b>	<b>133</b>
5.1	Introduction . . . . .	133
5.2	Methods . . . . .	135
5.2.1	Simulations . . . . .	135
5.2.2	Synchrotron Emission . . . . .	138
5.2.3	Analysis Tools . . . . .	138
5.2.4	Polarization . . . . .	139
5.3	Radio Relic Properties . . . . .	141
5.3.1	Simulated Radio & X-ray . . . . .	141

5.3.2	Density & Magnetic Field Strength Relationship . . . . .	146
5.3.3	Kinetic Energy & Radio Emission Distributions . . . . .	149
5.3.4	Merger Evolution . . . . .	151
5.4	Observational Implications . . . . .	155
5.4.1	Viewpoint . . . . .	155
5.4.2	Spectral Index . . . . .	157
5.4.3	Polarization Fraction & Direction . . . . .	160
5.5	Discussion & Future Directions . . . . .	163
<b>6</b>	<b>CRT: A Library for Cosmic Ray Transport</b>	<b>166</b>
6.1	Solving the Diffusion-Convection Equation for Cosmic Rays . . . . .	167
6.2	Introducing Cosmic Ray Transport (CRT) . . . . .	171
6.2.1	Structures . . . . .	172
6.2.2	Solvers . . . . .	173
6.2.3	Support . . . . .	176
6.2.4	Tests . . . . .	177
6.3	Hydrodynamic Tests with Enzo . . . . .	181
6.3.1	Cosmological Expansion . . . . .	181
6.3.2	Shock Tube . . . . .	183
6.4	Cosmic Ray Electrons in a Massive Galaxy Cluster . . . . .	187
6.4.1	Simulation Setup . . . . .	187
6.4.2	Time Evolution . . . . .	188
6.4.3	Radial Profiles . . . . .	198
6.4.4	Initial Conclusions & Future Work . . . . .	202
<b>7</b>	<b>Future Directions &amp; Conclusions</b>	<b>204</b>
7.1	Immediate Projects with CR Electrons . . . . .	204
7.2	CRT Micro-physics . . . . .	205

7.3	Other Applications of CRT . . . . .	207
7.4	Next Generation Galaxy Cluster Simulations . . . . .	209
7.4.1	Comparison to High-Resolution Sunyaev-Zel'dovich Imaging . . . . .	210
7.4.2	Turbulence and Cluster Cooling/Heating . . . . .	213
7.5	Conclusions . . . . .	214
	<b>Bibliography</b>	217
	<b>Appendix</b>	
A	Varying Magnetic Field Models	239
B	Polarized Emission Integration	243

## Tables

### Table

3.1	Simulation Parameters . . . . .	63
3.2	Mean Shock Quantities . . . . .	71
3.3	Temperature-Density Phase Space . . . . .	74
4.1	Best fit parameters for radio power scaling relationship with halo mass and 0.2-12 keV X-ray emission. Fitting functions are $10^B (M_{200}/10^{13} M_{\odot})^A$ and $10^B (L_x/10^{43} \text{ erg/s})^A$ for Mass and 0.5-12 keV X-ray luminosity, respectively. . . . .	121



## Figures

### Figure

- 1.1 Abell 1689, one of the most massive known galaxy clusters. Shown are both the cluster galaxies at optical wavelengths from the Hubble Space Telescope as well as the X-ray emission in blue from the intracluster medium. X-ray: NASA/CXC/MIT/E.-H Peng et al; Optical: NASA/STScI . . . . . 2
- 1.2 Galaxy cluster CIZA J2242.8+5301, which is currently undergoing a major merger. Shown in red is the radio relic emission thought to be from shock-accelerated electrons using the Giant Metrewave Radio Telescope in India. X-ray emission is shown in blue, observed with the ROSAT satellite. CREDIT: R.J. van Weeren, Leiden Observatory . . . . . 4
- 1.3 A three-color composite of the Perseus galaxy cluster core, showing optical, radio, and X-ray emission. Optical is shown in red, green, and blue, highlighting star formation, hydrogen filaments, and dark regions of dust lanes. The X-ray is shown in blue, and outlines the cavities blown out by the central active galactic nucleus. Radio lobes filling those cavities are shown in pink, and result from high energy electrons emitting synchrotron radiation. Credit: X-ray: NASA/CXC/IoA/A.Fabian et al.; Radio: NRAO/VLA/G. Taylor; Optical: NASA/ESA/Hubble Heritage (STScI/AURA) & Univ. of Cambridge/IoA/A. Fabian . . . . . 6

1.4	A volume rendering of gas density at $z = 0$ in a $(200\text{Mpc}/h)^3$ volume, illuminating the cosmic web of voids, filaments, and halos. Dark blue depicts the cosmic voids, while white illuminates the filaments and halos. This simulation was run on the Janus Supercomputer at the University of Colorado, Boulder. We use Enzo with WMAP7[131] cosmological parameters, and the rendering is created using yt. . . .	13
1.5	A cartoon depiction of Diffusive Shock Acceleration. Particle paths are shown in red, blue, and green. Magnetic field fluctuations impart energy on the left side to the particles, and steal energy from them on the right. Interactions between the fluctuations and particle paths are highlighted with jagged ellipses. Over time, the particles gain more energy than they lose due to the upstream velocity, $v_u$ , being larger than the downstream velocity, $v_d$ . . . . .	21
1.6	The function describing the total synchrotron power emitted as a function of $x = \nu/\nu_c = \omega/\omega_c$ . The dashed line corresponds to the location of the maximum value, and the solid line is drawn at $x = 1$ . . . . .	25
1.7	Left: Total power emitted as a function of frequency for a single electron for varying relativistic $\gamma$ factors and magnetic fields. Right: Total power at a fixed frequency as a function of relativistic $\gamma$ factors. Each line shows a $\gamma$ cutoff below which radiation at that given frequency drops off. . . . .	26
1.8	The spectral shape $f(x)$ for the thermal Sunyaev-Zel'dovich effect as a function of frequency. Shown in black are lines at 90 GHz, 150 GHz, 230 GHz, 275 GHz, 350 GHz, and 400 GHz, proposed bands for the CCAT telescope. . . . .	28
2.1	An example of using a gas density refinement criteria. Shown in the top panel is a slice through the galaxy cluster simulation at $z = 0.5$ presented in Chapter 6. The bottom shows the AMR level. In both cases the grid outlines are shown in black. Length units are comoving Mpc/h. . . . .	38

- 2.2 Left: Image-plane decomposition of a volume rendering. Right: Volume decomposition of a volume rendering. Each color represents a region that is “owned” by a different processor. If the viewing angle is changed, the data that each processor is responsible changes for the image-plane decomposition, while it stays constant for the volume decomposition. . . . . 43
- 2.3 Left: The original AMR structure of a small cosmology simulation, where the colors correspond to the average grid level along the line of sight and the black lines outline the grids. Right: The AMRKDTree constructed from the same dataset. . . . . 45
- 2.4 A simplified AMRKDTree structure with nodes labeled by their id. On the left is the full tree, and the 4 trees on the right depict how they are stored in each of the 4 processors. . . . . 46
- 2.5 The AMRKDTree parallel decomposition structure depicted by having each processor represented by a different color. Underlying simulation is a small AMR cosmology simulation. . . . . 47
- 2.6 Volume rendering of temperature of a radiation-hydrodynamics simulation of a  $(56Mpc/h)^3$  comoving volume at  $z = 7.5$ . Simulation credit: Michael Norman, Robert Harkness, Daniel Reynolds. Visualization credit: Samuel Skillman. Shown is gas temperature, chosen to highlight re-ionization bubbles during galaxy formation. Blue is  $10^4K$  and red is  $3 \times 10^4K$ . The top-right and bottom panels show zoom-in’s of the original  $4096^2$  pixels full rendering image. . . . . 50
- 2.7 Volume rendering of Temperature around a massive galaxy cluster, with a 30 Mpc/h field of view. This simulation has nearly a billion cells on the highest level of refinement. Green highlights gas at  $10^7K$ , and red shows the inner core of the cluster at  $10^8K$ . . . . . 51

- 3.1 A 2-D cartoon of our shock analysis algorithm. The shock centers are shown as dark blue cells, while the pre- and post-shock cells are outlined in thick black. The AMR resolution level is seen by varying grid-cell sizes. . . . . 60
- 3.2 Fractional efficiency of gas thermalization and cosmic ray acceleration, from the models by Kang and Jones [121].  $\delta_0(\mathcal{M})$  is the gas thermalization fraction expected from the Rankine-Hugoniot jump conditions.  $\delta(\mathcal{M})$  and  $\eta(\mathcal{M})$  are the gas thermalization fraction and cosmic ray acceleration fraction, respectively, from the non-linear calculations of Kang and Jones [121]. The two panels show results assuming different compositions of the pre-shock plasma. Top: thermal gas with no cosmic ray population. Bottom: thermal gas with a pre-existing cosmic ray population having  $P_{CR}/P_{gas} = 0.3$ , where  $P_{CR}$  and  $P_g$  are the cosmic ray and total gas pressure, respectively. . . . . 62
- 3.3 Distributions of the ratio of calculated Mach number to expected mach number from off-axis 3D AMR shock tube test problems. Shock surface area,  $S$ , distributions were averaged over all orientations for the each individual Mach number, and normalized so that the area under the curve is 1. Varying lines correspond to Mach numbers of 2 (dash-dotted), 5 (dashed), 30 (dotted), and 100 (solid). Sample standard deviations from 1.0 are all less than 0.06 . . . . . 68
- 3.4 Differential shock surface area normalized by the comoving volume of the simulation for external (left) and internal (right) shocks for  $z = 0$  in the ryu1024 simulation. The two methods of shock finding, coordinate split (dotted line) and coordinate unsplit (solid line), are shown. At low Mach numbers for external shocks and for all internal shocks we see a significant overprediction in the number of shocks when using the coordinate split method described in Ryu et al. [204] . . . . . 69

- 3.5 Projections of a  $2.8 \times 10^{15} h^{-1} M_{\odot}$  cluster from the “Santa Fe Lightcone.” Mach number (top-left) is weighted by the injected cosmic ray flux. Injected cosmic ray flux (top-right) is in units of  $ergs/(s h^{-2} Mpc^{-2})$ . Baryon column density (bottom-left) is in units of  $M_{\odot}/(h^{-2} Mpc^2)$ . Mass-weighted temperature (bottom-right) is in units of Kelvin. The total size of the projected volume is  $(32 h^{-1} Mpc)^3$ . All panels show logarithmic quantities. . . . . 72
- 3.6 Differential shock surface area as a function of logarithmic mach number bins for varying pre-shock gas phases. Pre-shock gas overdensity (top) is divided into several ranges that differentiate the overall distribution. Pre-shock gas temperature (bottom) differentiates the different types of shocks (i.e. accretion, merger). Both distributions are shown for three redshifts:  $z = 3$  (left),  $z = 1.5$  (middle) and  $z = 0$  (right). 75
- 3.7 Comoving shock surface area normalized by the simulation volume as a function of Mach number with varying redshifts. Three regions are suggested corresponding to internal cluster merger shocks (red), accretion shocks onto filaments (green), and accretion shocks onto clusters (blue). . . . . 88
- 3.8 Redshift evolution of the amount of kinetic energy processed by shocks as a function of Mach number. Redshift decreases from  $z = 3$  (red) to  $z = 0$  (black). The decrease in flux at late times for  $\mathcal{M} > 10$  signals the epoch at which dark energy becomes dominant. . . . . 89
- 3.9 Out of the incoming total kinetic energy of the shocks (solid line), the relative amount of energy devoted to the acceleration of cosmic rays for both models with (dashed line) and without (dotted line) a pre-existing CR population, as predicted by the Kang and Jones [121] diffusive shock acceleration model. . . . . 90

- 3.10 Differential kinetic energy flux processed by shocks as a function of Mach number and pre-shock gas phase. Pre-shock gas overdensity (top row) is divided into several ranges that differentiate the overall distribution. Each pre-shock temperature range (bottom row) roughly corresponds to a particular mach number. Both distributions are shown for three redshifts of  $z = 3$  (left column),  $z = 1.5$  (middle column) and  $z = 0$  (right column). . . . . 91
- 3.11 The effects of spatial resolution in different density regimes. Here we keep the mass resolution at the highest level ( $M_{dm} = 9.7 \times 10^8 M_\odot$ ) . The distribution function of shock Mach numbers in a  $(32 \text{ Mpc}/h)^3$  volume around a cluster weighted by surface area for three overdensity cuts is plotted against Mach number. Three cuts in overdensity are shown for  $\delta < 100$  (black lines),  $100 < \delta < 10^4$  (blue lines),  $\delta > 10^4$  (red lines). Varying spatial resolution are shown with dotted ( $62.4 \text{ kpc}/h$ ), dashed ( $15.6 \text{ kpc}/h$ ), and solid ( $3.9 \text{ kpc}/h$ ) linestyles. . . . . 92
- 3.12 Spatial resolution effects on kinetic energy flux for several density regimes. The kinetic energy flux is plotted against Mach number for varying spatial resolution denoted by linestyle. The shocks are grouped as external (black lines), clusters/filaments (blue lines), and rich clusters (red lines). . . . . 93
- 3.13 The effects of mass resolution in different density regimes. Here we keep the spatial resolution at the highest level of  $3.9 \text{ kpc}/h$ . Mass resolutions are shown by linestyles of dotted ( $6.2 \times 10^{10} M_\odot$ ), dashed ( $7.8 \times 10^9 M_\odot$ ), and solid ( $9.7 \times 10^8 M_\odot$ ). The shocks are grouped as external (black lines), clusters/filaments (blue lines), and rich clusters (red lines). . . . . 94
- 3.14 Spatial resolution effects on kinetic energy flux for varying dark matter particle masses. Mass resolutions are shown by linestyles of dotted ( $6.2 \times 10^{10} M_\odot$ ), dashed ( $7.8 \times 10^9 M_\odot$ ), and solid ( $9.7 \times 10^8 M_\odot$ ). The shocks are grouped as external (black lines), clusters/filaments (blue lines), and rich clusters (red lines). . . . . 95

4.1 Mass function of halos in *relic64* and *relic200* at  $z = 0$ . Halos are found using HOP with a minimum number of 30 dark matter particles. Conservative estimates of the low mass cutoff are  $10^{12}M_{\odot}$  and  $2 \times \sim 10^{13}M_{\odot}$  for *relic64* and *relic200*, respectively. This corresponds to 512 and 320 particles. The discrepancy at low mass for *relic200* is because of the lack of resolution of low-mass halos and poor force resolution at small scales. Dashed lines show the lower limit for the resolved halos for *relic64* and *relic200* in black and blue, respectively. Also shown are the fits from Warren et al. [247]. Because of the similarity between the two cosmologies, these fits differ by less than thickness of the line in this mass range. . . . . 99

4.2 Projection of several quantities through the entire *relic64* simulation volume at  $z = 0$ . Shown are mass-weighted density [ $\text{g cm}^{-3}$ ] (upper left), mass-weighted temperature [K] (upper right), radio emission-weighted Mach number (lower left), and radio flux density [ $\text{erg s}^{-1}\text{Hz}^{-1}\text{cm}^{-2}$ ] (lower right). . . . . 104

4.3 A zoom-in of Figure 4.2, now 16Mpc/h wide. . . . . 105

4.4 2D Phase Diagram of the relic radio emission in temperature-Mach number space for the *relic200*(left) and *relic64*(right) simulation. The temperature is that of the cell in the center of the shock. The color indicates the amount of 1.4 GHz radio emission [ $\text{erg s}^{-1}\text{Hz}^{-1}/(\text{Mpc}/h)^3/(d\log\mathcal{M} d\log T)$ ] for a given value of temperature and Mach number. . . . . 107

4.5 2D Phase Diagram of the relic radio emission in temperature-overdensity space for the *relic200*(left) and *relic64*(right) simulation. The color indicates the amount of 1.4 GHz radio emission [ $\text{erg s}^{-1}\text{Hz}^{-1}/(\text{Mpc}/h)^3/(d\log\delta d\log T)$ ] for a given value of temperature and overdensity. . . . . 109

4.6 2d Phase Diagram of the relic radio emission in temperature-Mach number space for the *relic200* simulation for varying redshifts. From top left to bottom right, we have  $z = 2.0, 1.5, 1.0, 0.5, 0.25, 0.00$  . . . . . 112

- 4.7 Density (top), temperature (middle) and 1.4GHz radio emission (bottom) for the 51 most massive halos in the *relic64* simulation at  $z = 0$ . Mass decreases from top left to bottom right ( $2.5 \times 10^{14} - 2.0 \times 10^{13} M_{\odot}$ ). Each individual image is 4 Mpc/h across. All images are projections down the x-axis. . . . . 115
- 4.8 1.4 GHz Radio Luminosity-Mass Relationship of halos in *relic64* (left) and *relic200* (right) for redshifts 2 (top), 1 (middle), and 0 (bottom). Shown in black are each individual halo. The lines represents a best power-law fit to all halos with  $M_{vir} > 10^{13} M_{\odot}$  and  $2 \times 10^{13} M_{\odot}$  for the *relic64* and *relic200* using a least-squares fitting routine. . . . . 117
- 4.9 1.4 GHz Radio emission overlaid on 0.2-12 keV X-ray emission for 20 snapshots during merger activity of the largest cluster in the *relic64* simulation from  $z=0.23$  to  $z=0.05$ , a time span of 2 .08 billion years. Length units are comoving. . . . . 119
- 4.10 Time evolution of 1.4 GHz radio and 0.2-12 keV X-ray luminosities of the merger shown in Figure 4.9, normalized to the luminosities at  $z = 0.229$ . The first frames are a result of a prior merger in its last stages. . . . . 120
- 4.11  $P_{1.4GHz} - L_X$  relationship for halos in *relic64* (left) and *relic200* (right) for  $z = 2, 1, 0$  from top to bottom. Both radio and X-ray emissivity are integrated out to the virial radius for each halo. A best fit line is found for halos with  $M_{vir} > 10^{13} M_{\odot}$  and  $2 \times 10^{13} M_{\odot}$  for the *relic64* and *relic200* using a least-squares fitting routine. For  $z = 0$ , we show fits to our data using a minimum mass (solid) as above and minimum X-ray luminosity of  $10^{44} \text{erg/s}$  (solid + crosses). Also shown are observational data (stars) from Feretti [73] along with a best fit (dashed). . . . . 122
- 4.12 (Left) 1.4 GHz Radio Luminosity Function for clusters in *relic64* and *relic200* for  $z = 0, 1$ , in units of inverse comoving  $(\text{Gpc}/h)^3$ . Shown in dashed lines are extrapolations using the Warren et al. [247] mass function and our  $P_{1.4GHz} - \text{Mass}$  scaling from Table 4.1. (Right) The Radio Luminosity Function for clusters in *relic64* as a function of magnetic field model. . . . . 124



4.13	Left Panels: <i>relic64</i> and <i>relic200</i> kinetic energy flux processed by shocks at $z = 0$ . Right Panels: 1.4 GHz radio emission. . . . .	128
5.1	Simulated X-ray and radio emission. The X-ray in the central regions shows a dynamic range of 100. The radio emission is calculated by placing the simulated cluster at $100Mpc/h$ , and masked to show a dynamic range of $10^4$ . . . . .	142
5.2	Projections of gas quantities. Upper left: Temperature, weighted by density. Upper middle: Sunyaev-Zel'dovich Compton- $y$ value converted to the maximum temperature decrement. Upper right: Mach number, weighted by radio emission. Lower left: Density, weighted by density. Lower middle: Integrated radio emissivity. Lower right: Magnetic field strength, weighted by density. Radio emission is overplotted on all panels except the Mach number, and is masked to show between $10^{-3} - 10$ mJy. Radio emission assumes cluster is at a distance of 100 Mpc/h. . . . .	144
5.3	Average magnetic field strength as a function of density, where each cell is weighted by the density, with the shaded area denoting the standard deviation. For reference, we show an analytic function that is linear with $\rho$ at low density and flattens at high density. . . . .	148
5.4	Phase plots of gas properties indicating the location of the kinetic energy flux and radio emission at shock fronts. The left plots show the kinetic energy distribution, while the right plots follow the radio emissivity. The top panels show the distributions as a function of magnetic field strength on the y-axis, and Mach number on the x-axis. The lower panels show them as a function of temperature on the y-axis, and density on the x-axis. . . . .	152

- 5.5 Time evolution of integrated gas properties in the volume surrounding the structures of interest. For density, temperature, and magnetic field, we calculate a weighted average, using density as the weight. For radio and X-ray values, we calculate the total emission within the innermost nested region of the simulation. Note the simulation was run beyond  $z = 0$  to allow the merger to finish. . . . . 154
- 5.6 180 degree rotation of radio emission. Flux computed by assuming a distance of 100 Mpc. Each panel is rotated by 10 degrees from the previous, moving left to right, top to bottom. Note that this panel of images acts as a autostereogram, and can be used to see the 3D structure of the radio emission. See video in the electronic journal. 156
- 5.7 Spectral index of simulated radio relic emission. The left portion of the image shows the “edge-on” view, whereas the right shows the “face-on” view. Both views are on the same scale. The left colorbar shows the mapping of color to the integrated spectral index including particle aging. The right colorbar shows the mapping of color to the prompt spectral index. Both colorbars apply to both views, providing a rough estimate of the uncertainty in our models of the spectral index. . . . . 157
- 5.8 A zoom in of the lower left radio relic. The left two panels show radio emission-weighted projections of the Mach number (left), and magnetic field strength (middle). The right panel shows a slice of the magnetic field strength, with black lines indicating the local magnetic field direction in the plane of the slice and the white overlay show the location of cells identified to be shocks. . . . . 158
- 5.9 Polarization fraction and direction. In each panel, the polarization direction is denoted by the black quivers, while the polarization fraction is represented by both the color scale as well as quiver length. The top panel shows the relic at full resolution (7.8kpc/h), while the lower panels show the same view at 4 times worse resolution. At  $z = 0.2$ , the redshift of CIZA J2242.8+5301, this corresponds to angular resolutions of 3.36'' and 13.44'', respectively. The left panels show the polarization for the “edge-on” (top) while the right shows the “face-on” view. . . . . 162

- 6.1 Code flow for one evolution of the cosmic rays. On the left is the evolution handled by Enzo, and on the right is the evolution handled by CRT. The reconstruction and cooling is subcycled based on a fraction of a cooling time until the final  $dt$  is reached. 173
- 6.2 Evolution of a converging flow of a single zone, due only to the momentum-space evolution. . . . . 178
- 6.3 Evolution of distribution of CR protons undergoing ion-coulomb and proton-proton interactions after  $t/15\text{Gyr} = 0.1, 0.3, 0.5, 0.8, 1.0$ . In each panel, the pentagons correspond to using 8 logarithmic bins and the squares correspond to using 80 logarithmic bins. The left panel shows the total number of protons in momentum bins defined by the low-resolution (8 bin) simulation. The right shows  $g_i$ , which is proportional to the energy density. . . . . 179
- 6.4 Evolution of distribution of CR electrons undergoing inverse Compton and electron-coulomb interactions after  $t/15\text{Gyr} = (5.0 \times 10^{-4}, 1.0 \times 10^{-3}, 3.0 \times 10^{-3}, 1.0 \times 10^{-2}, 2.0 \times 10^{-2}, 0.1, 0.25, 0.45, 0.6, 0.7)$ . In each panel, the pentagons correspond to using 8 logarithmic bins and the squares correspond to using 80 logarithmic bins. The left panel shows the total number of electrons in momentum bins defined by the low-resolution (8 bin) simulation. The right shows  $g_i$ , proportional to the energy density. . . . . 179
- 6.5 Evolution of distribution of CR electrons undergoing synchrotron cooling. Each line corresponds to a snapshot in time corresponding to fractions of 15Gyr,  $t/15\text{Gyr} = (0, 10^{-5}, 10^{-4.5} \dots 10^{-0.5}, 1.0)$ , starting from purple and moving to red. The vertical dashed shows the critical momenta for each time in the same color where all the electrons will have cooled at that point. The results from an 80 bin simulation are shown in solid lines, and the analytical results for each time is shown in dashed. . . 182

6.6	Evolution of the total number density of electrons in an adiabatically expanding, uniform density Enzo simulation (AdiabaticExpansion in the Enzo test problems). Shown are the baryon and cosmic ray number densities as a function of cosmological redshift, with the analytical solutions in dashed lines according to Equation 6.32 with and initial power-law slope to the CR distribution of $q_i = 4.3$ . . . . .	184
6.7	The magnetic field strength as a function of number density for a constant $\beta$ plasma.	185
6.8	Evolution of distribution of CR electrons behind a stationary $\mathcal{M} = 5$ shock, with gas entering from the left characterized by a post-shock temperature of $10^8\text{K}$ and pre-shock number density of $10^{-3}\text{cm}^{-3}$ . Shown are gas density (upper left) and temperature upper right), shock Mach number (lower left), and the number density of electrons in each of the 8 momentum bins, spanning from $\gamma = 100 - 2 \times 10^6$ . An equipartition magnetic field with $\beta = 100$ is chosen to determine the synchrotron cooling behind the shock. . . . .	186
6.9	A projection of baryonic gas density, weighted by cell mass in a $(10\text{Mpc}/h)^3$ comoving volume, shown at 6 different redshifts. A major merger occurs at $z = 0.5$ in the top right panel, and a second major merger is just beginning at $z = 0.0$ in the bottom right panel. . . . .	190
6.10	The same as Figure 6.9, except now gas temperature weighted by cell mass. . . . .	191
6.11	The same as Figure 6.9, except now 1.4 GHz Synchrotron emission projected along the line of sight. . . . .	192
6.12	The same as Figure 6.9, except now 74 MHz Synchrotron emission projected along the line of sight. Note the scale has shifted by an order of magnitude. . . . .	193
6.13	The same as Figure 6.9, except now 100 GHz Synchrotron emission projected along the line of sight. Though unlikely to be observed, this shows the rapid cooling of the high energy electrons, where now the emission is constrained around sites of acceleration (shocks). Note that the color scale has changed from the previous two figures. . . . .	194

6.14	The same as Figure 6.9, except now shows the integrated thermal Sunyaev-Zel'dovich effect y-parameter. . . . .	195
6.15	The same as Figure 6.9, except now shows the integrated Pseudo-Xray emission, which captures the $\rho^2 T^{-1/2}$ dependence. . . . .	196
6.16	Gas density radial profile for $z = 0.5$ (left) and $z = 0.0$ (right). The solid line indicates the average density, while the dashed line shows the standard deviation of the gas density. . . . .	199
6.17	Same as Figure 6.16, but for gas temperature. . . . .	200
6.18	Same as Figure 6.16, but for gas pressure. . . . .	200
6.19	Same as Figure 6.16, but for pseudo X-ray emissivity. . . . .	200
6.20	Cosmic ray electron number density radial profile for $z = 0.5$ (left) and $z = 0.0$ (right). Shown are three of the eight momentum bins, corresponding to $\gamma$ factors of $\sim 100, 3000, \text{ and } 10^5$ . . . . .	201
6.21	Synchrotron emission radial profile for $z = 0.5$ (left) and $z = 0.0$ (right). Shown are four different frequencies ranging from 100MHz to 100GHz. . . . .	201
6.22	Cosmic ray electron distribution power-law index radial profile for $z = 0.5$ (left) and $z = 0.0$ (right). Shown are two of the eight momentum bins, corresponding to $\gamma$ factors of $\sim 100$ and $3000$ . The shaded regions indicate the range of 1 standard deviation. . . . .	201
7.1	1.4 GHz (left) and 74 MHz (right) synchrotron emission from a 2D supernovae remnant simulation. . . . .	208
7.2	Evolution of the tSZE signal in a galaxy cluster merger simulation, showing the 150GHz for 6 different redshifts. Contours indicate integer multiplications of the signal-to-noise ratio. . . . .	212

- 7.3 The thermal Sunyaev-Zel’dovich emission seen at 150 GHz for various instrument configurations. In the top panels are the tSZE signals, while the bottom panels show an unsharp-masked processing of the signal to highlight gradients and shocks. The far right image shows the tSZE y-parameter at the resolution of the simulation. In each of the other four panels, this signal is convolved with a beam and added to background noise. The far left panel uses the expected South Pole Telescope 3G receiver specifications. The middle three show CCAT LW-Cam specifications for a “shallow” survey, “deep” survey and a “deep” survey with idealized sub-mm galaxy subtraction. . . . . 212
- A.1 Relative radio emission with respect to our fiducial magnetic field model for the *relic200* simulation at  $z = 0$ , shown in Figure 4.4. In the upper four panels, the reference magnetic field parameter,  $B_0$  is varied. In the bottom left panel, the magnetic field strength is flat at  $B = 0.1\mu G$ . In the bottom right panel, the magnetic field strength scales linearly with electron number density. . . . . 241
- A.2 As in Figure 4.8, but for varying magnetic field model parameters. In the upper four panels, the reference magnetic field parameter,  $B_0$  is varied. In the bottom left panel, the magnetic field strength is flat at  $B = 0.1\mu G$ . In the bottom right panel, the magnetic field strength scales linearly with electron number density. . . . . 242
- B.1 On and off-axis Faraday rotation test. The left panel shows the on-axis Faraday rotation through a magnetized sphere, with an image width equal to the domain size. The right panel shows the same rotation, but off-axis and with a width of 1.6 larger than the left, to show the off-axis nature of the domain. The electron number density and magnetic field strength of the sphere are chosen to rotate the polarization angle  $\pi$  radians for the rays passing through the center of the sphere. . . . . 246

- B.2 Dual plane polarization test. The polarization fraction as a function of image pixel across the mid-plane of the image, shown for varying viewing angles that are measured as an offset in the  $x - y$  plane from a viewing direction of  $\vec{L} = (1, 0, 0)$ . . . . 246

# Chapter 1

## Introduction

How did the Universe form? How has it evolved since the beginning of time from a hot, dense, singularity of space and time to what we see today, full of galaxies, stars, black holes, planetary systems, and life? These are the questions that not only drive my investigation of the Cosmos, but also have driven the work of philosophers and scientists since the earliest days of human kind. My role thus far has been a small one, and the work presented in this dissertation concerns only a small piece of the Cosmic puzzle. I have spent the last six years investigating the evolution and structure of objects known as clusters of galaxies. As their name suggests, galaxy clusters, as I will generally refer to them, are collections of a few tens to hundreds and sometimes thousands of galaxies. These galaxies are bound together in a gravitational potential formed by a collection of dark matter, hot diffuse gas, and the stars and galaxies themselves. These galaxy clusters are unique in that they are the largest gravitationally bound objects in the Universe, which potentially make them powerful probes of the structure of the Universe. They can help constrain what our Universe is composed of as well as probe the nature of two of the biggest mysteries in modern cosmology: dark matter and dark energy.

However, galaxy clusters are more than simply the most massive gravitationally collapsed objects in the Universe. While their abundance and bulk properties can be used to constrain cosmological parameters [102, 147, 243, 16], what makes them truly powerful tools in astrophysics is the wide array of complex phenomena occurring within them [127, 132]. In-falling gas from outside the cluster is shock-heated as it is accreted, becoming a hot, diffuse, magnetized plasma. These same



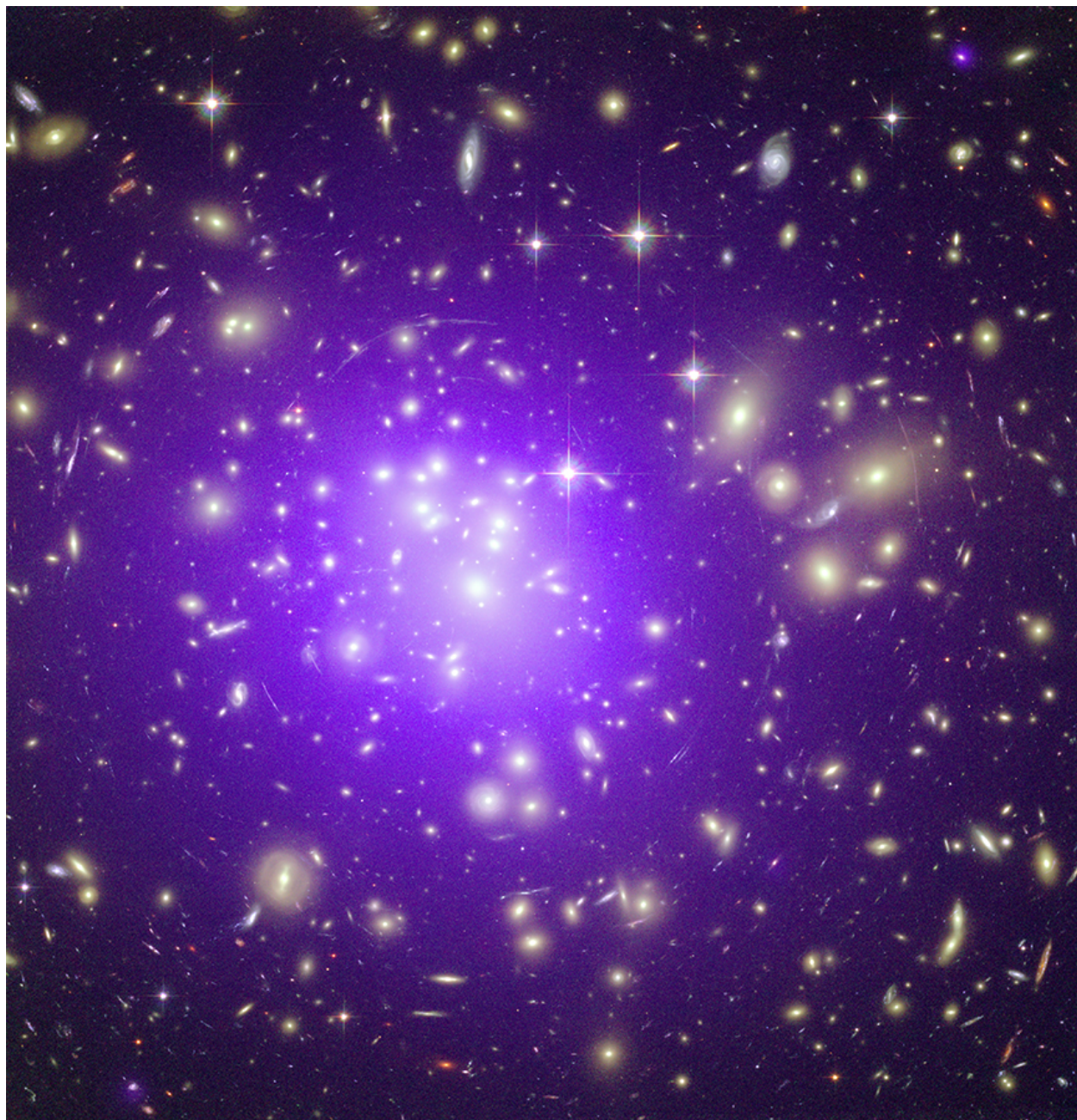


Figure 1.1 Abell 1689, one of the most massive known galaxy clusters. Shown are both the cluster galaxies at optical wavelengths from the Hubble Space Telescope as well as the X-ray emission in blue from the intracluster medium. X-ray: NASA/CXC/MIT/E.-H Peng et al; Optical: NASA/STScI

shocks are capable of accelerating cosmic ray electrons and ions [23, 204, 180, 109, 212, 239, 213]. Stars and galaxies form from cooling gas and return chemical, mechanical, thermal and non-thermal feedback to the intracluster medium (ICM) [119]. Active Galactic Nuclei accrete and expel gas within cores of galaxies, carving out X-ray cavities within the ICM and filling them with radio-emitting plasma threaded with magnetic fields [74, 253]. Magneto-hydrodynamic turbulence in the ICM is driven by both feedback from galaxies as well as merging sub-clusters traveling through the ICM at supersonic velocities [255].

For all of these reasons, we should consider clusters of galaxies to be astrophysical Swiss Army knives with which we can study an array of astrophysical and plasma physical phenomena. Throughout this dissertation, I focus on how we can leverage advances in simulation and theory together with current and next-generation telescopes to answer questions about both the thermal and non-thermal history of our Universe.

The technological advancements in radio astronomy have led a renaissance in probing the non-thermal populations of galaxy clusters. A number of NSF-funded national facilities, including the Jansky Very Large Array (JVLA) and Green Bank Telescope (GBT), are opening up new windows into the thermal and non-thermal landscape of clusters of galaxies. In particular, these telescopes are being used to map out synchrotron emission in clusters of galaxies. This diffuse emission is primarily classified as either a radio relic or radio halo. For a review of these objects, see Feretti et al 2012 [77]. Radio relics are characterized by extended radio emission near the cluster outskirts, have moderate ( $> 10\%$ ) polarized radio emission, and are often found in clusters with disturbed morphologies and coincident with shocks. As such, they are thought to be the result of shock acceleration [22]. Radio halos are instead often coincident with the central regions of galaxy clusters and follow the X-ray emission morphology. They are found to have low polarization fractions, and steeper spectral indices than those found in radio relics. The origin of this halo emission is debated [32] between turbulent re-acceleration models [30] and secondary production of electrons from proton-proton collisions[56]. In addition to US-based facilities, the Australian SKA Pathfinder (ASKAP), Westerbork Synthesis Radio Telescope (WSRT) and Low Frequency Array

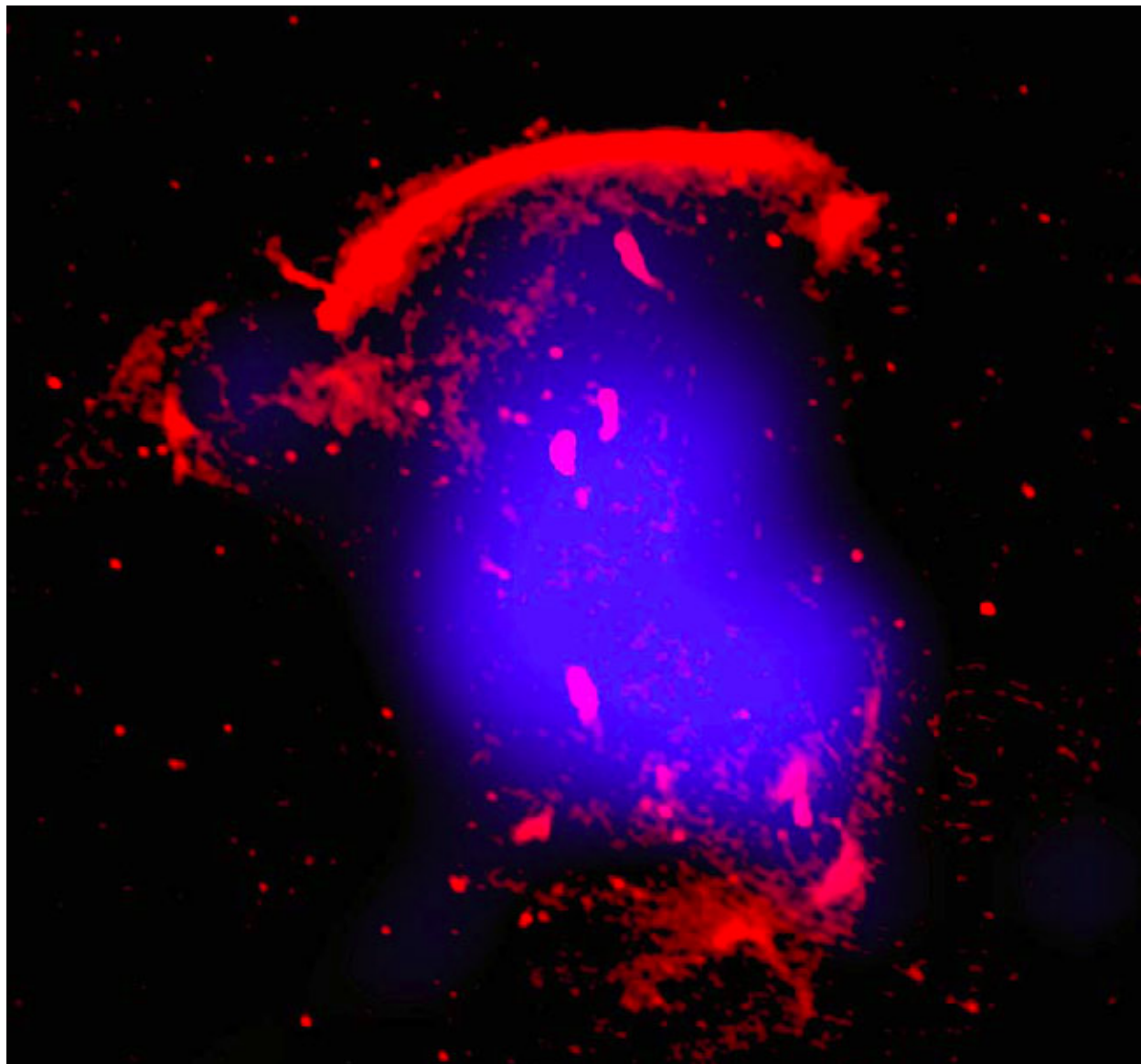


Figure 1.2 Galaxy cluster CIZA J2242.8+5301, which is currently undergoing a major merger. Shown in red is the radio relic emission thought to be from shock-accelerated electrons using the Giant Metrewave Radio Telescope in India. X-ray emission is shown in blue, observed with the ROSAT satellite. CREDIT: R.J. van Weeren, Leiden Observatory

(LOFAR) will provide very sensitive surveys of the radio sky at 1-2 GHz (ASKAP, WSRT) and 15 – 210 Mhz (LOFAR). Together, they are expected to observe 200-300 radio halos, a factor of  $\sim 10$  increase over today’s catalogs [44]. LOFAR has recently reported on their first observations of cluster radio emission in Abell 2256 [238]. Recently the Giant Metrewave Radio Telescope has been used to map the synchrotron emission in what is now known as the “Sausage” cluster, shown in Figure 1.2.

The Green Bank Telescope, using the MUSTANG 90 GHz imager [160], has produced exquisite maps of high-resolution thermal Sunyaev-Zel’dovich Effect (tSZE), which results from the inverse-Compton scattering of the cosmic microwave background (CMB) radiation by hot electrons in the ICM. Because of the simplicity of the physics behind the tSZE, it provides a complementary probe of the thermal and non-thermal ICM plasma. The tSZE signal is proportional to the line-of-sight integral of the pressure, and is therefore a sensitive probe of hydrostatic equilibrium and shocks in the ICM.

Similar advances in observational techniques have led to a myriad of data concerning the feedback from galaxies within clusters. Early on, evidence for feedback of energy into the ICM was seen at radio wavelengths, where radio jets and lobes were observed to move outward from a central Active Galactic Nuclei (AGN) [e.g. 177, 38, 175, 197]. Since then, advances in both radio and X-ray observations have revealed a complex interplay between the ICM and resident galaxies. Observations of the Perseus cluster [for a recent update, see 72] have unveiled X-ray cavities filled with radio emitting plasma, threaded with  $H\alpha$ -emitting gas [71], shown in Figure 1.3. These findings suggest a coordinated dance between in-falling cold gas, AGN feedback, shocks, sound waves, and magnetic fields. Further evidence for this feedback is found in a number of other galaxy clusters [94].

Together, these observations provide the puzzle pieces to understanding the physics within galaxy clusters. In order to put these pieces together, a large amount of work has been done in the past 30 years to develop and advance our capabilities of numerically simulating the formation and evolution of galaxy clusters. In some areas of research, we have made substantial progress, such as



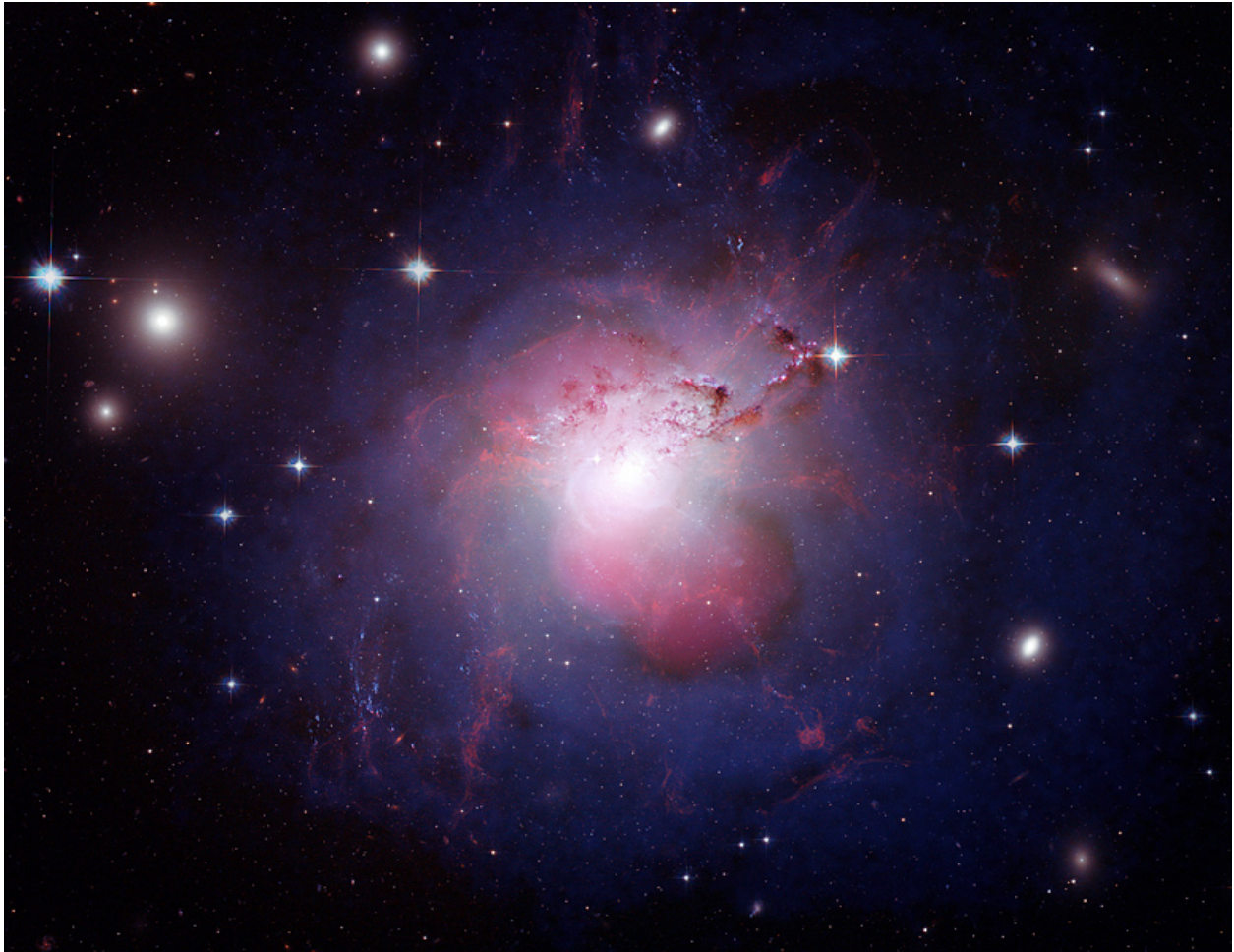


Figure 1.3 A three-color composite of the Perseus galaxy cluster core, showing optical, radio, and X-ray emission. Optical is shown in red, green, and blue, highlighting star formation, hydrogen filaments, and dark regions of dust lanes. The X-ray is shown in blue, and outlines the cavities blown out by the central active galactic nucleus. Radio lobes filling those cavities are shown in pink, and result from high energy electrons emitting synchrotron radiation. Credit: X-ray: NASA/CXC/IOA/A. Fabian et al.; Radio: NRAO/VLA/G. Taylor; Optical: NASA/ESA/Hubble Heritage (STScI/AURA) & Univ. of Cambridge/IOA/A. Fabian

the evolution of large scale structure dominated by the collapse of dark matter into sheets, filaments, and halos [221]. State-of-the art dark-matter simulations are breaching one trillion individual N-body particles used to sample the phase space of a collisionless dark matter fluid. However, we are still in our infancy of understanding the role that baryonic matter plays in galaxy cluster dynamics. This problem involves solving equations of compressible (magneto-)hydrodynamics. Several techniques, including smoothed particle hydrodynamics (SPH) Lagrangian [219], adaptive mesh refinement (AMR) Eulerian [34], and hybrid Voronoi Tessellation based [220] methods have been used to approach this problem. While this may be encouraging, the hydrodynamics are only the first piece in the puzzle. Further methods for including star and galaxy formation, metal and thermal feedback, cosmic ray acceleration, subgrid turbulence, and additional baryonic processes are still being developed, debated, and quantified.

This dissertation focuses on two primary questions regarding the evolution of galaxy clusters. The first is a question of how structure formation in the universe is imprinted on the distribution and appearances of shocks formed during accretion and merging. I will also discuss how these shocks may play a role in the acceleration of cosmic ray protons and electrons, and determine the types of shocks that are responsible for the bulk of the energy injected. The second question focuses on how a combination of simulations and observations can be used to investigate the plasma physical processes occurring in galaxy clusters. I will show that there are degeneracies that are present in observations that require the use of theory and simulations to disentangle, and comment on what the future might hold in terms of both new telescopes and computational abilities. A significant portion of this work sets the stage for my final dissertation project, which has been to implement a method of following the momentum-space distribution of cosmic ray electrons and ions in cosmological simulations. In Chapter 6 I outline how this is done, and showcase the first results of such simulations of a galaxy cluster. This initial simulation of a galaxy cluster is the highest resolution of its kind that has tracks the cosmic ray electrons in multiple momentum bins. Our initial findings suggest that there may be a more significant link between so-called radio relics and radio halos due to repeated merger shocks processing the central regions of a cluster.

In the remainder of this introduction, I will discuss the theoretical frameworks needed in order to study galaxy clusters, from cosmology to observational properties of galaxy clusters. Instead of a full review of each of these topics, I will focus on only what is needed to understand and interpret the results.

## 1.1 Big Bang Cosmology

It is widely believed that the Universe began its days at a singularity in time referred to as the Big Bang. At this moment in time, the Universe was composed of infinitely dense, hot plasma of quarks, gluons, and other fundamental particles. From this state, the Universe underwent rapid expansion during a phase referred to as “inflation” which leads to a causal disconnection between parts of the Universe that were once adjacent. This allows for the growth of a remarkably homogeneous and isotropic distribution of mass and energy, observed in every direction we look.

Throughout this dissertation, I assume that our Universe behaves according to the “concordance” Lambda Cold Dark Matter ( $\Lambda$ CDM) cosmology. Rather than justify its use as opposed to any other cosmological model, which is far outside of this work, I will simply describe the fundamental assumptions and results of the model.

Modern cosmology relies on two fundamental concepts: the Cosmological Principle and Einstein’s Theory of General Relativity (GR). The Cosmological Principle states that the Universe is homogeneous and isotropic. This principle allows for GR to be applied in a simplified fashion that leads to the Friedmann-Robertson-Walker (FRW) metric that describes the expansion history of the Universe. In its most basic form,  $\Lambda$ CDM cosmology assumes that Einstein’s theory of General Relativity applies and that the Cosmological Principle holds. There are 4 types of matter and energy in our Universe: radiation; baryonic “normal” matter; non-baryonic “dark” matter, and dark energy. The relative abundances of each of these at a given point in time determine the large scale growth of the Universe. Within this framework, the expansion of the Universe can be described by

the evolution of the scale factor,  $a$ , and its growth rate  $\dot{a}$ . We define

$$H(t) = \frac{\dot{a}(t)}{a(t)} \quad (1.1)$$

as the Hubble expansion rate. The evolution of  $H(t)$  can be recast into cosmological redshift using  $z = \frac{\Delta\lambda}{\lambda}$ , where  $\lambda$  is the rest-frame wavelength of a photon emitted at a redshift  $z$ . In this case the redshift is due to the expansion of space-time itself, and can be described in terms of the scale factor as  $a = \frac{1}{1+z}$ , where  $a = 1$  at redshift  $z = 0$ . The expansion rate is described by the fractional densities of each species of energy and density as:

$$H(z) = E(z)H_0 \quad (1.2)$$

$$E(z) = \sqrt{(1+z)^3\Omega_m + (1+z)^2\Omega_K + (1+z)^{3*(1+w)}\Omega_\Lambda + (1+z)^4\Omega_\gamma}, \quad (1.3)$$

where  $H_0 = 70h_{70}$  km/s/Mpc is Hubble's Constant at  $z = 0$ , and

$$\rho_c = \frac{3H_0^2}{8\pi G}. \quad (1.4)$$

Each  $\Omega_s$  corresponds to the fractional density of each species with respect to the critical density,

$$\Omega_s = \frac{\bar{\rho}_s}{\rho_c} \quad \forall s \in (m : \text{Matter}, K : \text{curvature}, \Lambda : \text{Dark Energy}, \gamma : \text{radiation}). \quad (1.5)$$

The contribution to  $E(z)$  due to dark energy is parameterized using the Dark Energy equation of state relating the pressure and energy density,

$$P = \omega\rho, \quad (1.6)$$

which in the  $\Lambda$ CDM cosmology takes on the value of  $\omega = -1$ .

At the time of this writing, these values are [106, 18]  $\Omega_m = 0.288$ ,  $\Omega_\Lambda = 0.712$ ,  $\Omega_K \approx 0$ ,  $\Omega_r = 5 \times 10^{-5}$ , and  $H_0 = 69.33$ km/s/Mpc. This corresponds to a flat Universe given  $\Omega_K$  is so small.

From the Big Bang forward the Universe expanded and cooled, during which there were many interesting phase transitions which are of little direct importance to the remainder of our



discussion. We will assume that what we begin with is a dark, neutral universe composed of only the lightest elements dictated by Big Bang Nucleosynthesis, and that have an underlying set of fluctuations in their density and velocity structure. These fluctuations lead to gravitational instabilities, causing the beginning of structure formation. As the first structures begin to collapse, gravitational potentials with halo masses of  $O(10^5 M_\odot)$  begin to form, leading to the eventual cooling, and collapse to the first stars in the Universe.

These first stars are likely massive due to inefficient cooling mechanisms. Their radiation as well as eventual deaths lead to a Cosmic Dawn in which the Universe begins the long and arduous path to reionization. Through further collapse of structure, galaxies begin to form, aiding in the reionization process through their supernovae and black hole feedback. After these first two stages in the hierarchical structure formation take place, these galaxies begin to merge and collapse into ever deeper gravitational potential wells until objects referred to as clusters of galaxies, or galaxy clusters, begin to form.

Galaxy clusters are the latest stage of the gravitational collapse forming at the intersection of filaments, growing to total masses of over  $10^{15} M_\odot$  for the most massive clusters. Typical galaxy clusters have masses of a few  $10^{14} M_\odot$ . These exceedingly deep gravitational potentials lead to virial temperature of  $\sim (10^8 K)$ , with typical gas number densities of  $10^{-5} - 10^{-3} cm^{-3}$ .

## 1.2 Large Scale Structure Formation

Through observations of the cosmic microwave background [176, 106], we can infer several key properties of the universe only 300,000 years after the Big Bang. One of the most useful results is that of the power spectrum of low-level fluctuations against the mean temperature. These fluctuations describe the inhomogeneities in the Universe that will eventually lead to the gravitational collapse into stars, galaxies, and large scale structures. Under the influence of gravity, regions of the universe will progress through several stages of collapse. In this section I will walk through the process of gravitational collapse and define the terminology that will be used throughout this dissertation to describe such structures.

### 1.2.1 Gravitational Instability

Fundamentally, the structures present in our universe are due to gravitational instability, seeded by very small scale fluctuations in the early Universe. We believe that before the inflationary epoch, each field (density, velocity, etc.) could be described as a Gaussian random field, governed by quantum fluctuations. During inflation, these fluctuations were “frozen-in” as the Universe rapidly expanded. This is due to the cosmological horizon shrinking with respect to the wavelengths of the initial perturbations. Once this happened, these perturbations would form the seeds for what is now the cosmic web.

Once the expansion began to slow the horizon began to grow with respect to the perturbations, allowing larger and larger scales to influence each other, beginning the process of gravitational collapse. Before the time of radiation-matter equality ( $z_{req} \approx 3200$ ) any perturbation in the baryon matter would be quickly erased by the propagation of sound waves through the radiation-dominated fluid, acting to delay the onset of gravitational instability in the gas. However, the non-baryonic dark matter component is not susceptible to such pressure waves, and therefore the gravitational instability can proceed far before the gas starts to collapse. After  $z_{req}$ , the gas begins to fall into the already-forming dark matter potentials. At this point, the evolution the gravitational collapse is captured by following the evolution of three fundamental equations: the continuity equation; the Euler equation for acceleration driven by gravity, dark and baryonic matter, and pressure forces; and the Poisson-Newton equation for relating the gravitational potential to the matter density.

These three equations can be cast to describe an over-dense region of the universe defined as an overdensity,

$$\delta(\vec{r}, t) = \frac{\rho(\vec{r}, t) - \bar{\rho}}{\bar{\rho}}, \quad (1.7)$$

where  $\bar{\rho}$  is the mean density of the Universe. After defining the peculiar velocity  $\vec{v}(\vec{r}, t)$  as part of the total velocity  $\vec{u}(\vec{r}, t)$ ,

$$\vec{u}(\vec{r}, t) = \frac{da(t)\vec{r}}{dt} = H(t)a(t)\vec{r} + \vec{v}(\vec{r}, t), \quad (1.8)$$

we can write the set of three equations as:

$$\frac{\partial \delta}{\partial t} + \frac{1}{a} \nabla \cdot (1 + \delta) \vec{v} = 0 \quad (1.9)$$

$$\frac{\partial \vec{v}}{\partial t} + \frac{\dot{a}}{a} \vec{v} + \frac{1}{a} (\vec{v} \cdot \vec{\nabla}) \vec{v} = -\frac{1}{a} \nabla \Phi - \frac{1}{\rho a} \nabla p \quad (1.10)$$

$$\nabla^2 \Phi = 4\pi G \bar{\rho}_m(t) a(t)^2 \delta(\vec{r}, t). \quad (1.11)$$

These three equations describe the continuity equation, momentum equation, and Poisson's equation. Assuming spherical symmetry one can analytically solve the above set equations for the evolution of over-dense perturbations to determine whether or not the overdensity will collapse or expand. A seminal paper using this technique is Gunn & Gott 1972, [99]. For a spherical collapse it can be shown that the overdensity needed within a given radius has to exceed  $\approx 1.68$ , in order to detach from the Hubble flow and collapse. These (semi-)analytical approaches led the way to modern numerical simulations, providing key results to compare to, and providing a language to describe the large scale structure evolution.

### 1.2.2 Voids, Sheets, Filaments & Halos

Gravitational instability leads to the collapse and formation of a hierarchy of structures present in our Universe. To help our definitions, we use the critical density (Equation 1.4) and assume mass fractions of dark and baryonic matter of  $\Omega_{cdm}$  and  $\Omega_b$ , which are combined to be  $\Omega_m$ . I also define the overdensity as

$$\delta = \frac{\rho_m - \Omega_m * \rho_{crit}}{\Omega_m * \rho_{crit}} \quad (1.12)$$

as the ratio of local total mass over-density to the average matter density. Using this definition, we now define **voids** as all regions in the Universe with  $\delta < 1.0$ . These are regions which have been locally depleted of matter.

The first structures with  $\delta > 1.0$  to collapse are **sheets**, regions that are planar in nature that act as membranes between adjacent voids. These sheets have small overdensities from  $1.0 <$

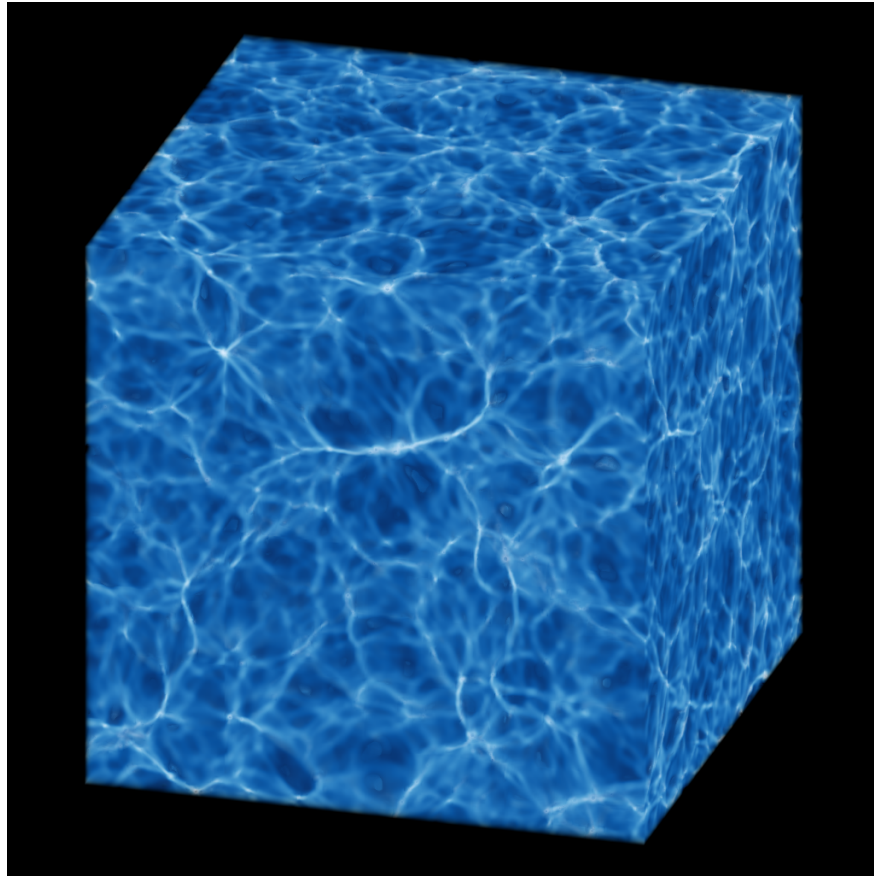


Figure 1.4 A volume rendering of gas density at  $z = 0$  in a  $(200\text{Mpc}/h)^3$  volume, illuminating the cosmic web of voids, filaments, and halos. Dark blue depicts the cosmic voids, while white illuminates the filaments and halos. This simulation was run on the Janus Supercomputer at the University of Colorado, Boulder. We use Enzo with WMAP7[131] cosmological parameters, and the rendering is created using yt.

$\delta < 10$ . At the intersection of two sheets lie **filaments**, cylinder-like strands of matter that form the underlying cosmic web. Filaments have typical overdensities of  $10 < \delta < 10^3$ , and are often in a temperature range of  $10^4 - 10^6 K$ , having gone through an accretion shock from the sheet onto the filament. Finally, halos sit at the intersection of two or more filaments. In this dissertation we define halos as being regions where  $\delta > 100$ . This process leads to a hierarchy of structure in the Universe, with halos nested inside of filaments forming at the intersection of sheets, surrounded by voids. See Chapter 3 for a further description of the shock structure onto filaments and halos. Figure 1.4 shows a volume rendering from a  $(200\text{Mpc}/h)^3$  simulation volume at redshift  $z = 0$ , produced using the Enzo code and rendered using the yt analysis toolkit, described further in Chapter 2.

In a way, the cosmic flow of structure formation can be thought of as a city drainage system. Incoming matter flows out of the voids like rain falling from the sky. When the rain hits the road (a sheet) it slowly migrates towards the street gutters (filaments). At this point the speed of flow increases dramatically due to the water depth (mass density), and rushes towards the storm drain into the sewer (halos). Like in sewers, matter gets mixed up and allows for the creation of new and interesting species, both chemical and possibly biological in nature.

### 1.3 The ICM From Abell to Zel’dovich

Over the past 50 years our telescopes, theoretical models, and simulations have progressed dramatically to unveil the structure of the ICM. While there have been significant advances in optical wavelength telescopes, I will only briefly discuss their implications and results. The majority of this dissertation will completely circumvent the complicated physics needed to reproduce galaxy clusters in the optical, such as star and galaxy formation and evolution. Instead, we will see that the nature of the ICM is best probed through a combination of X-ray, radio, and sub-mm wavelength astronomy.

The first observation of what would later be known to be a galaxy cluster came in 1784 by Charles Messier, when he observed a concentration of “nebulae” that would soon be found to

be the Virgo cluster of galaxies. Several years later F. Wilhelm Herschel, after receiving a grant from the King of England to build what was at the time the world's largest telescope[21] at 1.47 meters. He also found nebulae that were seemingly clustered together, verifying what Messier had found earlier. While Messier was uninterested in determining the nature of these nebulae that were not comets, Herschel continued his investigation, and even passed on his passion to his son, John F.W. Hershel. They were able to develop the first northern and southern catalogs of nebulae, and critically noted that there seemed to be more nebulae in the north than in the south in 1864. This was partly due to the larger foreground emission in the galactic plane visible in the Southern hemisphere.

By the early 20th century the Coma, Virgo and Perseus clusters of galaxies [186, 222, 251, 52] had been discovered, at which point more than 300 “nebulae” were seen in the Coma cluster alone. At this point there began to be many references to the local supercluster and an interconnectedness between the local group and the Virgo cluster, forming structures as large as perhaps even 100Mpc. Optical astronomy has progressed significantly with the advent of 10-meter class optical ground-based telescopes, as well as the widely known success of the Hubble Space Telescope. Optical light and optical spectroscopy can uncover a wealth of data concerning the chemical makeup of galaxy clusters.

One of the biggest surprises in the study of galaxy clusters was the observation of diffuse X-ray emission coming from the central regions of galaxy clusters. The first observation of X-rays in an astrophysical context was from a sounding rocket that observed the X-ray background in 1962[89]. In the next few years, there were several disputed claims (see [64] for a historical perspective), before the first real detection from the Virgo Cluster (M87) in 1966 [41]. The first detection of the extended emission in the Coma cluster was in 1971 by Meekins et al.[150].

This diffuse X-ray emission was confirmation of very hot, diffuse, baryonic matter that we now refer to as the Intracluster Medium (ICM). The X-rays are produced through free-free interactions between electrons and ions, also known as thermal Bremsstrahlung (braking) radiation. This process gives rise to a continuum emission at X-ray energies ( $0.1 - \sim 10keV$ ). On top of this

continuum emission, there are a forest of X-ray emission lines that are primarily due to  $L\alpha$  and  $K\alpha$  series lines, which can dominate the emission for hot clusters. The details of these processes are discussed in 1.4.3.1. We define the X-ray emission luminosity and surface brightness,

$$L_x[\text{erg/s}] = \int e_\nu(\vec{x})dV \quad (1.13)$$

$$S_x[\text{erg/s/cm}^2] = \int e_\nu(\vec{x})dl \quad (1.14)$$

where  $e_\nu$  is the X-ray emissivity,  $\vec{x}$  is the position, and the integral is taken over the volume and along the line of sight, respectively.

By obtaining X-ray spectra it is possible to further constrain the bulk plasma properties of the emitting gas. Additional insight can be gained if the galaxy cluster is close to spherical symmetry, where one can then use a method of de-projection [206] to constrain the density, temperature, and entropy of the cluster as a function of radius. These techniques are useful but also limited, as we will see the bulk of this dissertation investigates the aspherical, non-hydrostatically relaxed parts of galaxy clusters, which warrant a much more detailed model to describe their atmospheres.

An early catalog of clusters was obtained in the X-ray through the ROSAT all-sky [245], where over 200 galaxy clusters were found serendipitously. This was the first X-ray catalog of clusters at this scale. This sample would be used extensively in follow up observations with modern satellites. There are currently three work-horses for X-ray astronomy: Chandra, XMM-Newton, and Suzaku. These three telescopes each have their strengths and weaknesses. Chandra provides unprecedented (0.5 arcsecond) resolution while simultaneously providing moderately high spectral resolution of 60 – 1000 depending on the energy. XMM-Newton EPIC cameras have a spatial resolution of 6 arcseconds and moderate spectral resolution of 20 – 50, but a slightly larger collecting area and lower background noise than Chandra. Suzaku has fairly low collecting area, low resolution (1.5 – 2.0 arcminutes), similar spectral resolution to Chandra, but considerably lower background noise, making it popular for searching for diffuse X-ray emission[210].

X-ray observations have traditionally been most useful in studying the cores of galaxy clusters. This is due primarily to the strength of the X-ray emission being proportional to  $\rho^2T^{-1/2}$ . Therefore,

the contrast from the cores to the outskirts can be many orders of magnitude in surface brightness. Recently, Suzaku has been used to begin to study the outskirts of galaxy clusters, utilizing a low noise background and very long integration times [210]. This has been used to probe the temperature, density, and pressure profiles out to the virial radius. These have been compared with simulation results quite favorably from some of our work in Burns et al. [40].

On the opposite end of the spectrum, in 1959 an extended radio source was detected in the Coma cluster at 408 MHz [137]. It took another 10 years to show that this emission was not a result of multiple radio galaxies and instead must be coming from the ICM itself [250], and Wilson referred to the emission as the “halo”. As more observations were taken, it became clear that this halo emission was quite rare, and even today only a small fraction of galaxy clusters seems to show evidence for halo emission.

Since then, there has been tremendous progress in the imaging of low surface brightness diffuse cluster emission. The primary turning point was the introduction of the NRAO VLA Sky Survey (NVSS) [51]. In the next year, Giovannini and collaborators released a survey of galaxy cluster radio emission, where an additional 18 sources were identified, compared to just 11 prior to that [92]. For an excellent review of the history of the discoveries of diffuse radio emission, see Feretti 2012 [77].

In this dissertation I will primarily compare our simulations with radio “relics,” of which there are of order 25 known relic sources in galaxy clusters. Recently van Weeren and collaborators have led the field in observations of previously unknown relics using an observational campaign involving the VLA, WSRT, and GMRT telescopes [232] (see Figure 1.2). Even more recently, LOFAR in the Netherlands has come online, providing incredible images of low-frequency radio emission [238].

Finally, due to advances in sub-mm detector technology, it is possible to observe distortions in the CMB spectrum due to the Sunyaev-Zel’dovich Effect. This effect describes the up-scattering of CMB photons off the hot pool of ICM electrons through the inverse Compton effect. As described in the next section, this process is capable of probing the integrated gas pressure along the line of sight. There have been a number of telescopes both on the ground and in space that are attempting



to map out the pressure profiles of galaxy clusters using this effect, such as ACT, SPT, SZA, and very recently Planck. We will discuss what is possible using high resolution SZ imaging telescopes in Chapter 7, where we create mock CCAT observations in preparation for its construction.

## 1.4 Plasma Physics of the ICM

The intracluster medium is a hot, diffuse, magnetically-threaded plasma. On top of the cluster atmosphere there is a constant influx of in-falling subclusters, constantly mixing and stirring the resident fluid. As such, the ICM is the host of a tremendous variety of plasma physical processes that can only be studied, and likely only exist, in their environments. Galaxy clusters are also very large and bright, making them some of the best plasma physics laboratories in the Universe. In this section we will detail the important thermal and non-thermal processes that are present in galaxy clusters that lend themselves to be studied observationally and numerically. For an excellent review of the study of galaxy clusters and their thermal properties, see [12]. For a review of the outskirts of galaxy clusters, see [190].

First, it is important to consider the conditions of the ICM to set the context for our calculations. The ICM is very diffuse, having number densities of  $10^{-6} - 10^{-3}$  particles/cm<sup>3</sup>. The ICM is also very hot, normally having temperatures in the range of  $10^6 - 10^8$  K. This very high temperature sets a correspondingly very high thermal sound speed,

$$c_s = \sqrt{\frac{\gamma k_B T}{\mu m_p}} \approx 1513 \sqrt{\frac{T}{10^8 \text{K}}} \text{ km/s} \quad (1.15)$$

where  $T$  is the temperature of the gas,  $\mu$  is the mean molecular weight in units of  $amu$ ,  $m_p$  is the mass of a proton,  $k_B$  is the Boltzmann constant, and  $\gamma$  is the adiabatic index of the gas. The gas flow velocities are similar to this speed, which is also comparable to the velocity measured for cluster galaxies. Given the very hot temperatures, it is expected that the majority of atoms will be either completely or heavily ionized, leading to a population of electrons and ions, forming a two-fluid plasma. As such, there is an array of thermal, non-thermal, ionization, hydrodynamic, and magnetohydrodynamic processes occurring in the ICM. This plasma is dominated at the 99%

level by Hydrogen and Helium, and topped off with an array of heavier elements, which we will refer to from here on out using the theorists' favorite term, "metals."

#### 1.4.1 Heating Mechanisms

A well-known problem of numerical simulations is that of accurately capturing the thermal balance in the cores of galaxy clusters, where a complex interplay of extreme radiative cooling is seemingly balanced by a yet-to-be-determined heat source. Otherwise, the gas, having cooling times less than the Hubble time, would quickly form massive amounts of stars in the central cores, which is not observed. There are a few possible heat sources including heat conduction combined with sound waves or turbulence[246, 202, 54], cosmic-ray heat conduction[142, 100], or feedback from active galactic nuclei[19, 192, 149].

If thermal conduction is efficient enough, it is thought that heat from outside the core would be capable of stopping this cooling catastrophe. This has gained a lot of interest in the past decade, and there is now a large effort into understanding the micro- and nano-physics of the interplay between conduction, magnetic fields, thermal gradients, and instabilities[187, 170, 148, 171, 24, 172, 201]. In recent work, I have collaborated with Britton Smith, Brian O'Shea, and Mark Voit to investigate the effects of thermal conduction in Enzo simulations (Smith et. al. in prep), where the conduction may have an impact on the shock structures as well.

On the other hand, we know that AGN can provide thermal and kinetic feedback to the cluster core by examining images such as that in Figure 1.3. However, we do not yet understand how the primarily radio-mode feedback is then coupled to the thermodynamics of the gas. We also do not yet understand what regulates the duty cycle of the AGN, describing how often the jets are being powered. AGN feedback has been used by our group [215] as well as other groups[209] to attempt to regulate the cooling in cluster cores.

### 1.4.2 Particle Acceleration

One of the fundamental physical processes that this dissertation investigates is that of the ability to accelerate ions and electrons at shock fronts. As such, I will give a broad overview of how we think this process may be operating, as well as outline what general questions still remain. The idea that shocks can be accelerated at shock fronts originated from what Enrico Fermi thought might happen if a charged particle encountered a magnetic cloud[79]. He postulated that if the cloud was moving in a preferential direction, on average ions and electrons would be boosted by a factor proportional to the velocity ( $v/c$ ) of the cloud. If the cloud was moving randomly, then the average gain would instead be a stochastic process, leading to a gain proportional to  $(v/c)^2$ . These two variations are referred to as “First Order” and “Second Order” Fermi Acceleration.

It wasn't until the late 1970's that several independent groups began to apply Fermi's work to a system that involves a shock, where the scattering of the particle occurs through resonant scattering off Alfvén waves. Because of the diffuse process that the particles undergo as they scatter back and forth across the shock and eventually escape, this process was coined Diffusive Shock Acceleration or DSA [134, 10, 14, 15, 23], with a number of excellent reviews following a few years later [61, 22]. A cartoon depiction of this process is shown in Figure 1.5. Particles, on average, gain more energy from interactions in the upstream gas than they lose from the downstream gas, and therefore slowly gain energy.

One method of modelling DSA is to follow the distribution function of the particle population as it is modified due to momentum-space diffusion near shocks. This approach is taken by [124, 9, 244, 121, 123, 122], the most recent of which focuses on the re-acceleration of cosmic rays at weak shocks. A more fundamental approach to this problem can be taken through the use of Particle-in-Cell (PIC) simulations of individual ions and electrons in a magneto-hydrodynamic shock. Until recently it was computational infeasible to approach such a problem. However, recent studies by Anatoly Spitkovsky and collaborators [218, 88] have begun to probe the individual particle orbits and the transition from thermal to non-thermal populations of ions/electrons. There is still

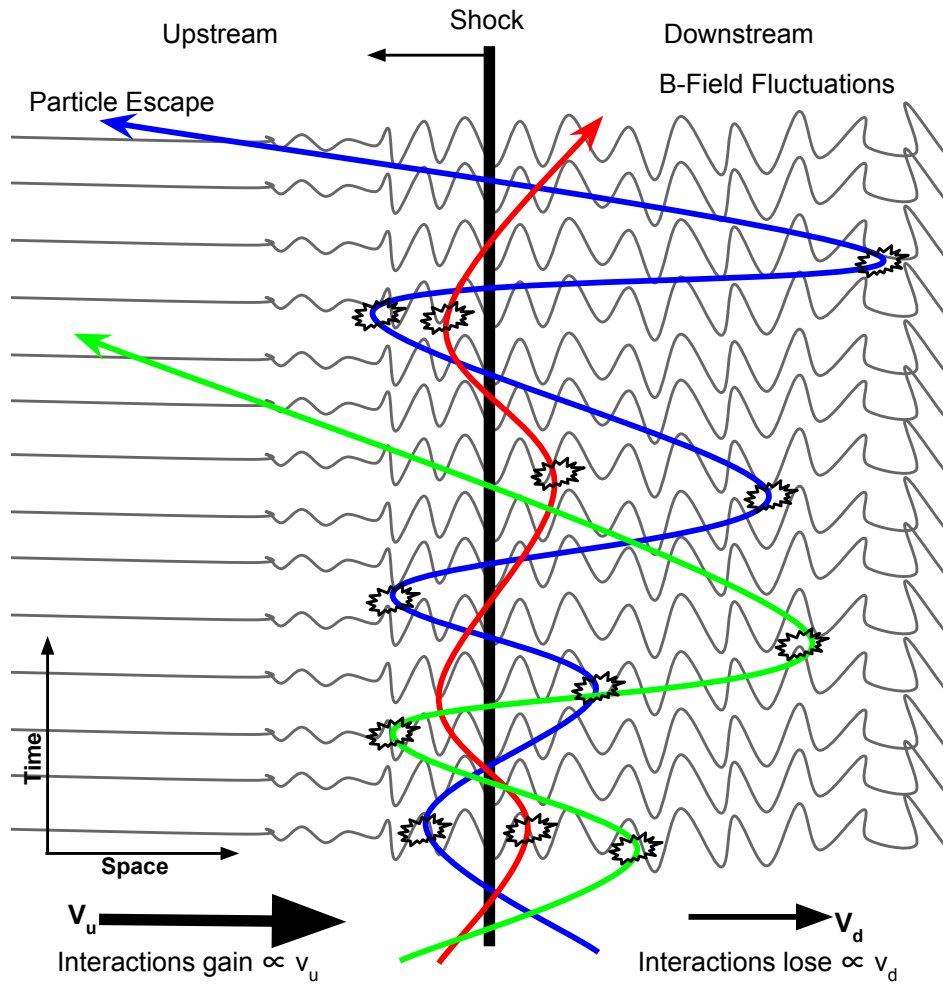


Figure 1.5 A cartoon depiction of Diffusive Shock Acceleration. Particle paths are shown in red, blue, and green. Magnetic field fluctuations impart energy on the left side to the particles, and steal energy from them on the right. Interactions between the fluctuations and particle paths are highlighted with jagged ellipses. Over time, the particles gain more energy than they lose due to the upstream velocity,  $v_u$ , being larger than the downstream velocity,  $v_d$ .

much work to be done in these studies to include a realistic ion-electron mass ratio and fully-3D calculations, but early signs suggest this will be a rich tool for investigating particle acceleration from first principles.

For the purposes of this dissertation it is useful to outline a few models that will be used in the context of ion and electron acceleration. For ion acceleration, we primarily use the results of Hyesung Kang and collaborators’ work on deriving acceleration efficiencies from their DSA simulations [121]. In this work, they find that the fraction of energy injected into the cosmic ray protons increases asymptotically to  $\sim 50\%$  at  $\mathcal{M} = 100$ , with little or no acceleration below  $\mathcal{M} = 3$ . For details on the exact shape see Chapter 3.

For the electrons, we use a model developed by Hoeft and Brüggén [109], where instead of following the electron acceleration using DSA or PIC techniques, they assume that a fixed fraction of electrons are injected into the non-thermal tail power-law tail of the energy distribution, and that the acceleration is in equilibrium with the synchrotron cooling rate of the electrons. This imparts a spectral steepening into the electron distribution, which shows up as a steepening in the overall spectral shape of the radio emission. Further details of this model will be discussed in Chapters 4 and 5. Until Chapter 6, we will not explicitly include the effects of DSA in our simulations, but instead use the results of DSA to make estimates for the proton/electron populations in a post-processing step. In Chapter 6, however, we will use DSA to predict the momentum-space distribution function in the post-shock regions for injecting cosmic rays.

### 1.4.3 Observational Signatures of the ICM

#### 1.4.3.1 X-ray: Bremsstrahlung & Metal Line Cooling

Bremsstrahlung emission is also known as “free-free” emission, meaning that the radiation results from the interaction between a free electron and a positively charged ion. The term Bremsstrahlung is German for “braking” and hints at the nature of the process, which is due to very fast moving electrons being slowed by the electromagnetic force of the ions as they pass by. It can be

shown that the X-ray emissivity of this process as a whole can be calculated using a weighted sum over the ion species:

$$e_{\nu}^{ff} = \frac{2^5 \pi e^6}{3 m_e c^3} \left( \frac{2\pi}{3 m_e k_B} \right)^{1/2} n_e T^{-1/2} e^{-h\nu/k_B T} \sum_i Z_i n_i g_{ff}(Z_i, T, \nu) \quad (1.16)$$

where  $Z_i$  is the charge of the ion, and  $g_{ff}$  is the Gaunt factor, which accounts for quantum mechanical effects and extended collisions. It has a slow dependence on frequency and temperature, so it does not strongly affect the emission properties.

The important aspects of this emission are that the emission is only weakly inversely proportional to the square root of the temperature of the gas, and is proportional to the product of the electron and ion number densities. Hence this is referred to as an “n-squared” process, and means that the X-ray emission is expected to be highly peaked towards the cores of galaxy clusters and that there may be large scatter due to over-dense sub-clumps in the cluster atmosphere.

The next most important X-ray emission mechanism is that of metal line cooling, which makes up for the majority of the remaining X-ray emission. In particular, the hot ICM allows for a forest of keV lines present in highly ionized metals. The 6.7keV  $K\alpha$  line of Fe (meaning an  $n=1$  to 0 transition) is present in massive galaxy clusters and provides a key constraint in observations. If an observation has the spectral resolution to do so, distinguishing different lines makes it possible to use a combination of the line ratios and shape of the thermal spectrum to constrain the bulk temperature of the gas. At the same time, using the ratios of the line emission to the thermal emission it is possible to constrain the abundances of each metal species. There is an entire industry of X-ray spectroscopic modelling, starting with [189].

#### 1.4.3.2 Radio: Synchrotron Radiation

While the X-ray emission gives us insight into the thermal plasma of the ICM, radio emission opens the door to many non-thermal processes. The most prominent effect is that of synchrotron radiation from high energy, “cosmic ray” electrons. Synchrotron emission results from the acceleration of a relativistic electron during its orbit about a magnetic field line. Here we quote the results

of the full derivation of synchrotron emission, which can be found in many textbooks such as [203], which we roughly outline here. The fundamental motion of the electron is a helical motion about the magnetic field line at the gyrofrequency,

$$\omega_B = \frac{eB}{\gamma m_e c} \quad (1.17)$$

where  $B$  is the magnetic field strength and  $e$  is the charge of the electron. From this motion, it can be shown that the critical frequency above which the spectrum of the synchrotron emission drops rapidly is

$$\omega_c = \frac{3}{2} \gamma^3 \omega_B \sin \theta = \frac{3eB \sin \theta}{2m_e c} \gamma^2 \quad (1.18)$$

$$\nu_c = \frac{3eB \sin \theta}{4\pi m_e c} \gamma^2 \approx 4.2 \times 10^6 (B \sin \theta) \gamma^2 \text{ Hz} \quad (1.19)$$

where  $\theta$  is the pitch angle of the electron in its helical motion. The radiation from a single electron, characterized by an energy  $E = \gamma m_e c^2$  using now the relativistic  $\gamma$  factor, is a strongly peaked spectrum continuum emission that peaks near the characteristic synchrotron frequency. The total power emitted as a function of frequency is

$$P(\omega) = \frac{\sqrt{3} e^3 B \sin \theta}{2\pi m_e c^2} F(x) \quad (1.20)$$

$$P(\nu) = \frac{\sqrt{3} e^3 B \sin \theta}{m_e c^2} F(x) \quad (1.21)$$

where  $x = \nu/\nu_c = \omega/\omega_c$  and  $F(x)$  is defined as

$$F(x) = x \int_x^\infty K_{\frac{5}{3}}(x') dx' \quad (1.22)$$

and  $K_{\frac{5}{3}}$  is the modified Bessel function of order  $\frac{5}{3}$  [1].  $F(x)$  is shown in Figure 1.6. If one were to integrate over the entire range of frequencies, the total power emitted by a single electron is [203]

$$P_{syn} = \frac{2e^4 (B \sin \theta)^2 \beta^2 \gamma^2}{3m_e^2 c^3} \quad (1.23)$$

where here we have included  $\beta = v/c \approx 1$ .

Example spectra of single electrons for several relativistic  $\gamma$  factors and varying magnetic fields (assuming  $\sin \theta = 1$ ) are shown in Figure 1.7. In many cases, the population of electrons can

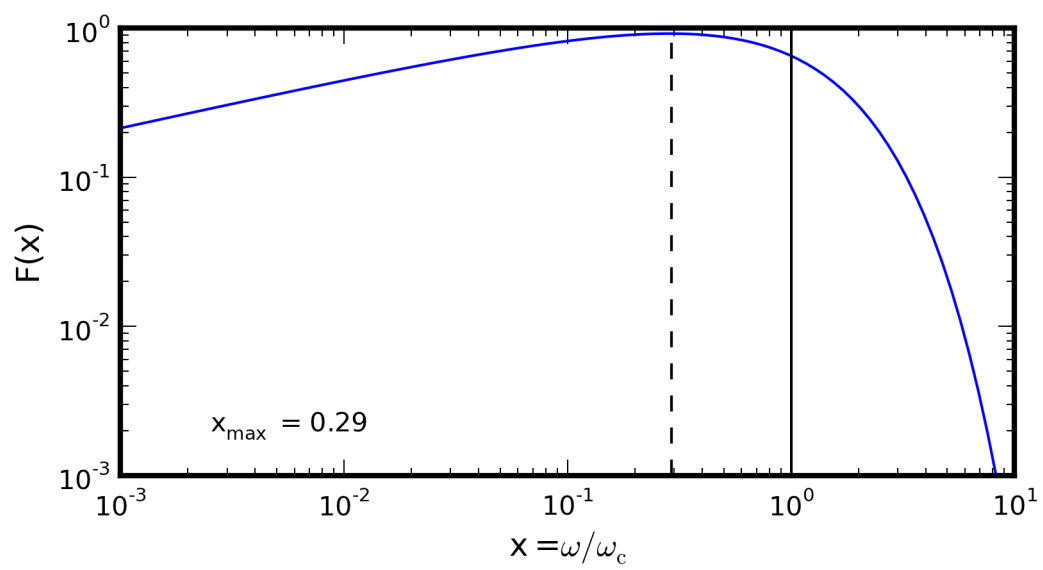


Figure 1.6 The function describing the total synchrotron power emitted as a function of  $x = \nu/\nu_c = \omega/\omega_c$ . The dashed line corresponds to the location of the maximum value, and the solid line is drawn at  $x = 1$ .



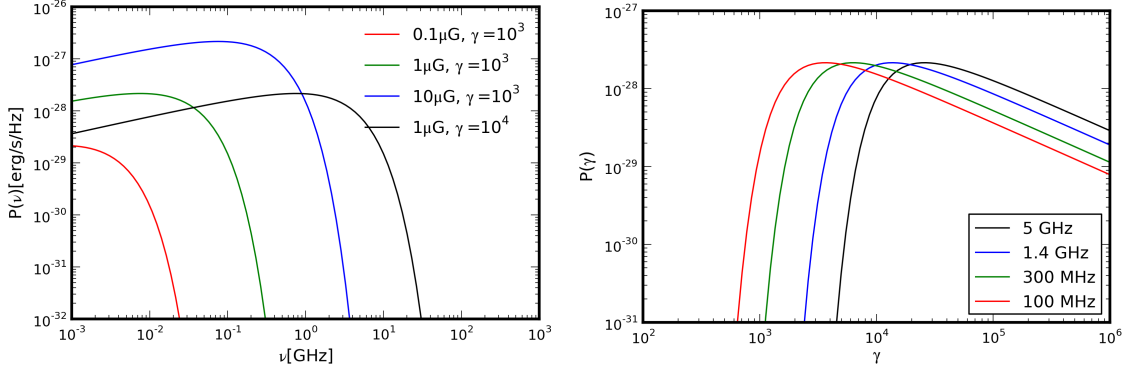


Figure 1.7 Left: Total power emitted as a function of frequency for a single electron for varying relativistic  $\gamma$  factors and magnetic fields. Right: Total power at a fixed frequency as a function of relativistic  $\gamma$  factors. Each line shows a  $\gamma$  cutoff below which radiation at that given frequency drops off.

be well approximated by a power law distribution where the number of electrons in a given energy bin is described by

$$N(E)dE = N_0 E^{-\delta} dE \quad (1.24)$$

where  $N_0$  is the normalization factor. In this case, it can be shown that the total emission from the population is also a power law, with index  $\alpha = (\delta - 1)/2$ , and scales as:

$$J(\nu) \propto N_0 (B \sin \theta)^{1+\alpha} \nu^{-\alpha} \quad (1.25)$$

This relationship between the observed spectral index of the radiation and the underlying electron spectrum is an important link to determine what type of source could accelerate such electrons. As we will see later in this dissertation, it will help differentiate between various classes of radio emission in galaxy clusters.

The synchrotron emission not only acts as a source of energy, but of course that energy comes from the electron's energy and therefore provides a cooling (energy-loss) term for the electrons. It happens to be the case that in cluster-like environments, the cooling time of a typical electron is comparable to many other timescales relevant for cluster evolution. Using the total power emitted in 1.21, the energy of an electron can be integrated to calculate the characteristic lifetime of an

electron to lose half of its energy to be [203]:

$$t_{syn} = \frac{3m_e^3 c^5}{2e^4 (B \sin \theta)^2} \frac{1}{\gamma_0} \approx 1.6 \left( \frac{\gamma_0}{10^4} \right)^{-1} * \left( \frac{B \sin \theta}{\mu G} \right)^{-2} Gyr \quad (1.26)$$

where  $\gamma_0$  is the initial gamma factor of the electron. This timescale is similar to that of many cluster timescales such as the sound crossing time, which is the time for a sound wave to propagate across the cluster. We can parameterize it in terms of the temperature,  $T$ , and distance,  $D$ , with

$$t_{sound} = D/c_s \approx 6.6 \times 10^8 \left( \frac{T}{10^8 K} \right)^{-1/2} \left( \frac{D}{1 Mpc} \right) yrs \quad (1.27)$$

As we will see in Chapter 5, these two timescales will be intimately linked in determining the behavior of shock-accelerated radio emission in galaxy clusters.

### 1.4.3.3 Sunyaev Zel'dovich Effect

The final observational signature that we will discuss here in the context of galaxy clusters is in the sub-mm wavelengths, where a unique and powerful mechanism leaves its mark. In 1970, Sunyaev and Zel'dovich postulated that one method of determining the source of the X-ray's observed in clusters (whether it was Bremsstrahlung or Inverse Compton X-ray emitting electrons), would be to look for a decrement in the "Relic Radiation" now known as the CMB[227]. If the emission is from inverse Compton interactions, the low energy photons of the CMB would be upscattered by the  $10^7 K$  electrons, and the spectrum of the CMB would change.

The result of such an interaction would be to boost the CMB photon energy while retaining the total number of photons, modifying the nearly perfect blackbody radiation. This modification shows up as a decrement for frequencies below a cross-over point and an increment for frequencies above it. It can be shown in the low temperature limit that the modification to the incoming

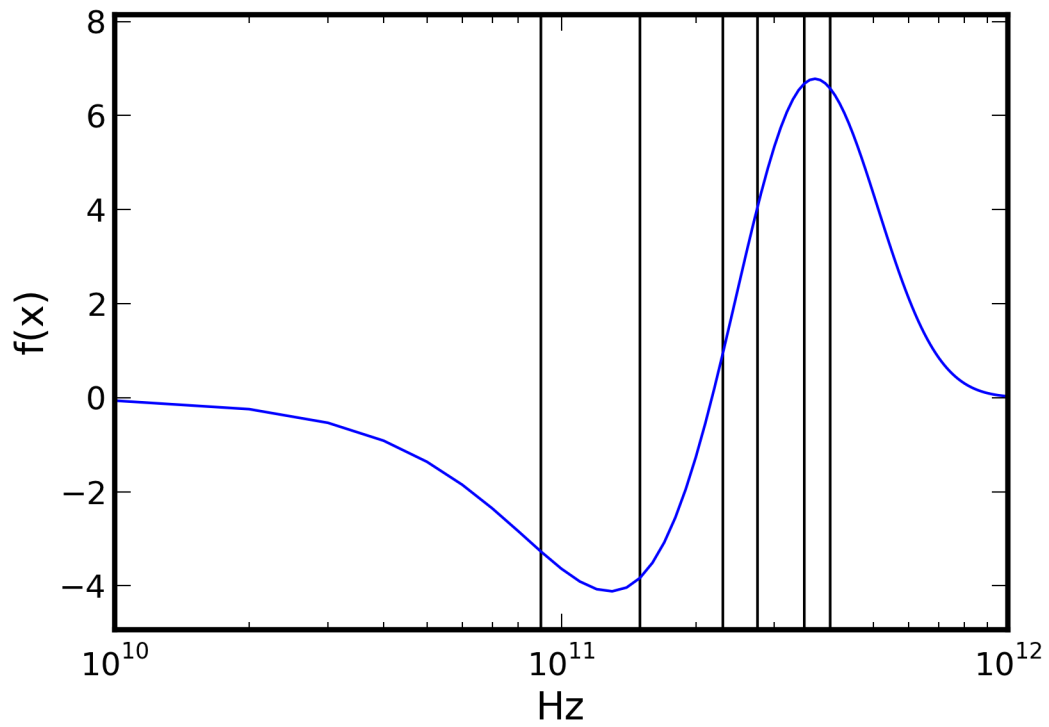


Figure 1.8 The spectral shape  $f(x)$  for the thermal Sunyaev-Zel'dovich effect as a function of frequency. Shown in black are lines at 90 GHz, 150 GHz, 230 GHz, 275 GHz, 350 GHz, and 400 GHz, proposed bands for the CCAT telescope.

background intensity is [20]:

$$\begin{aligned}
\Delta I_T(\nu) &= \Delta I_{T0} * f(x) \\
f(x) &= \frac{x^4 e^x}{(e^x - 1)^2} (x \coth(x/2) - 4) \\
x &= \frac{h\nu}{k_B T_{rad}} \\
\Delta I_{T0} &= I_0 y_{SZ} \\
&= I_0 \int n_e \sigma_T \frac{k_B T_e}{m_e c^2} dl \\
I_0 &= \frac{2h}{c^2} \left( \frac{k_B T_{rad}}{h} \right)^3 \approx 2.7 \times 10^{-8} \text{WHz}^{-1} \text{m}^{-2} \text{sr}^{-1}
\end{aligned} \tag{1.28}$$

where  $I_0$  is the initial intensity of CMB,  $y_{SZ}$  is the Comptonization parameter, and  $f(x)$  is the functional form as a function of frequency, shown in Figure 1.8.

There are several important features to the thermal SZ effect (tSZE):

- Since it is a modification of the CMB and not an intrinsic source, the signal is redshift and distance independent, allowing for studies of very high redshift galaxy clusters unlike at X-ray and optical wavelengths.
- It is linearly proportional to the product of the density and temperature, meaning that relative brightness of the effect does not fall off radially in a cluster as quickly as, for example, the X-ray surface brightness. This allows for investigations in the outskirts of galaxy clusters.

There are currently several ongoing projects looking to observe the tSZE in clusters at ever higher angular resolutions. One particularly powerful tool in the tSZE is collecting multi-frequency observations both below and above the null in the spectrum. Doing so can help constrain both the overall integrated signal as well as any deviations due to gas motions and relativistic effects (for particularly hot clusters this can be a major deviation, e.g. [113]). Using the tSZE to constrain the ICM properties is very promising, particularly given the ability to probe farther out in the cluster atmosphere, as is already being done with the MUSTANG, SPT, ACT, and Planck experi-

ments. Future telescopes such as CCAT will be revolutionary because of its resolution and ability to subtract sources using spectral information.

## 1.5 Roadmap

In the next chapter, we will outline some of the numerical methods used in this dissertation, focusing on the aspects most important for the remainder of the work. The following three chapters after that are each individually published chapters, reproduced here in their entirety. The first is focused the distribution and properties of cosmological shocks and how they might be responsible for a large population of cosmic ray protons. Chapter 4 attempts to take a large distribution of galaxy clusters and relate their synchrotron emission from shock-accelerated electrons to their other bulk properties such as mass and X-ray emission. After that, we change gears from strictly hydrodynamics simulations and use, for the first time, a cosmological magnetohydrodynamic adaptive mesh refinement simulation of a galaxy cluster to study the radio emission properties of a massive merging system.

Chapter 6 represents unpublished work first incorporating the capability to follow a distribution of electrons as they evolve within Enzo. After providing the background and tests of this method, we introduce the highest resolution simulation of a galaxy cluster that follows the spectral behavior of electrons in multiple energy/momentum bins. We will show that including the effects of aging has a profound effect on the interpretation of large-scale diffuse radio emission in galaxy clusters. We end with a future look to what is possible with this new framework in the final chapter, as well as showcase preliminary work on predictions for high-resolution tSZE experiments with our simulated clusters.

## Chapter 2

### Methods: Simulation, Analysis, & Visualization

‘There is a computer disease that anybody who works with computers knows about. It’s a very serious disease and it interferes completely with the work. The trouble with computers is that you “play” with them!’ – Richard P. Feynman

This chapter provides a description of the computational backbone around which the bulk of this dissertation relies upon. I will first give a brief outline of techniques that have been used in numerical cosmology. From there, I will introduce Enzo, the primary tool used in this work. Afterwards, I will describe some of the challenges in the analysis of such work, giving a brief introduction to yt, a simulation analysis toolkit. Finally, I will describe a parallel domain decomposition algorithm that I developed to enable the visualization of some of the largest astrophysical simulations run to date.

#### 2.1 A Brief Introduction to Computational Cosmology

In this section I will review the various ways in which we can attempt to model and simulate the Universe from the largest structures down to galaxies. Fundamentally, we are interested in following the evolution and interplay between dark matter, dark energy, baryonic matter, and electromagnetic radiation.

##### 2.1.1 Gravity

First and foremost, gravitational interactions dominate the formation and evolution of the large scale structures in the Universe. Current measurements [106] place  $\Omega_m = 0.27$ ,  $\Omega_\lambda =$

0.73,  $\Omega_b = 0.0445$ , meaning that the ratio of dark to baryonic matter is  $\frac{0.2255}{0.0445} \sim 5$ . We note here that Planck has recently released their first cosmological parameter results that differ from the WMAP results considerably[183]. We will continue to use the WMAP results until these new results are verified. As such, the process of structure formation is driven primarily by the dark matter evolution. This dark matter is, as far as we can tell, collisionless in nature, and is governed by the collisionless Boltzmann equation,

$$\frac{\partial f}{\partial t} + \vec{v} \cdot \nabla f + \frac{\vec{F}}{m} \cdot \nabla_v f = 0, \quad (2.1)$$

where  $f = f(\vec{x}, \vec{v}, t)$  is the distribution function and  $\vec{F}$  are the forces acting on the fluid.

Attempting to solve for the full distribution function is quite demanding, as it requires the solution to a 6-spatial + 1-temporal dimensional problem. Except for a few cases (see [257] for a recent implementation), the computational cost of solving this 6+1 dimensional problem is prohibitively high. Instead, what is usually done is to average over the velocity-space and reduce the problem to a 3+1 dimensional system. Under these assumptions, one can sample the phase space using point-like particles that react to forces using Newtonian dynamics. Given that the force in such a system is entirely due to gravity,  $F_g = -\nabla\Phi$  where  $\Phi$  is the gravitational potential, all that is needed to update the positions of the particles is to know the gravitational potential. To then solve for the gravitational potential, we solve the Poisson equation,

$$\nabla^2\Phi = 4\pi G\rho, \quad (2.2)$$

where  $\rho$  is the mass density and  $G$  is Newton's gravitational constant. There are several popular methods for solving this elliptic equation, each of which have performance and accuracy trade-offs. The simplest method is to define an initial set of points that sample the mass distribution and directly solve for the gravitational interactions between each of the particles. This is equivalent to replacing the mass density with a sum over Dirac Delta functions. However, this procedure results in an  $N^2$  algorithm because of the need to calculate the interaction between every particle with all  $N - 1$  other particles.

To improve performance, Hockney and Eastwood [107] introduced the “Particle-Mesh” (PM) N-body method that discretizes the volume into a uniform grid of cells, and discretizes the mass into uniform-mass particles, having roughly equal numbers of cells and particles. At each step in the evolution, each particle is first deposited onto the grid using a second-order cloud-in-cell (CIC) interpolation routine. Once the mass is deposited, a 3-D Fast Fourier Transform (FFT) is used to transform into k-space, where Poisson’s equation takes on a form that is easily solved using finite-difference equations. Once the potential is updated, an inverse FFT is performed to return the system to real space, where the spatial derivative of the potential is calculated to determine the acceleration at each point. Particles are then pushed by this acceleration, and the process is repeated. The fundamental limitation to this approach is its static force resolution. However as the Universe evolves, we expect to form large scale clustering of structures, where in principle we would rather have higher resolution to follow their formation. PM techniques only allow for uniform spatial resolution, and therefore are incapable of doing so. The benefit to PM methods is that they scale as  $N \log(N)$ , and therefore allow for higher uniform resolution than direct N-body studies.

By combining the direct and PM methods, Hockney et al. [108] developed a “Particle-Particle/Particle-Mesh” (P<sup>3</sup>M or P3M) method that decomposes the potential into long-range and short-range contributions. On large scales, it uses a PM method on an initial grid, but then uses direct N-body calculations for the short-range interactions. This has the advantage of both speed on large scales and accuracy in collapsed structures.

Finally, there are fully-unstructured methods that often rely on a tree-based data structure to then use a fast multipole method [97] approach to separate out the short and long-range forces. For each particle, the tree data structure is traversed, accumulating the forces by grouping far away particles together, reducing the number of force calculations. For an excellent review on the state-of-the art in dark matter simulations, see Kuhlen et al. [136]



## 2.2 Hydrodynamics

It was not until relatively recently that researchers began to follow the hydrodynamic evolution of the baryonic component large scale structure. There are two primary methods for discretizing the baryonic gas that is evolved during a cosmological solution: by mass or by volume.

### 2.2.1 Lagrangian Hydrodynamics: Smoothed Particle Hydrodynamics

Smoothed particle hydrodynamics is a method that models a system by first discretizing the mass in the simulation. Therefore a parcel of gas is discretized into point masses that are characterized by position, velocity, and internal energy. To recover spatial quantities such as density, one must then average over a number of nearest neighbor particles, usually through the use of an integration kernel that falls off with radius. For a review of the intricacies of kernel selection and the SPH method in general, see [185].

One can then show that the time evolution of the density,  $\rho$ , velocity  $\vec{v}$  and internal energy  $u$  can be given by[185]:

$$\rho_a = \sum_b m_b W(\vec{r}_a - \vec{r}_b, h_a); h = h(\rho), \quad (2.3)$$

$$\frac{d\vec{v}_a}{dt} = - \sum_b m_b \left[ \frac{P_a}{\Omega_a \rho_a^2} \nabla_a W_{ab}(h_a) + \frac{P_b}{\Omega_b \rho_b^2} \nabla_a W_{ab}(h_b) \right], \quad (2.4)$$

$$\frac{du_a}{dt} = \frac{P_z}{\Omega_a \rho_a^2} \sum_b m_b (\vec{v}_a - \vec{v}_b) \cdot \nabla_a W_{ab}(h_a), \quad (2.5)$$

where  $a, b$  refer to particle indices,  $W$  is a smoothing kernel,  $h$  is the smoothing length,  $P$  is the pressure determined from an equation of state,  $\vec{v}$  is the velocity,  $u$  is the internal energy, and  $\Omega$  here denotes a term relating to the gradient of the smoothing length. These equations are a result of analyzing the Lagrangian of particle motion, rather than the equations of hydrodynamics. It also assumes that there is no change in entropy, meaning that these assumptions will need to be re-examined when dealing with discontinuities such as shocks in the flow. One of the advantages to using a Lagrangian approach is that as structures collapse, the spatial resolution naturally increases

as particles fall into the potential well. However, it is difficult/impossible to otherwise control the resolution in a given region in space.

### 2.2.2 Eulerian Grid-Based Hydrodynamics

The other widely used method for solving the equations of hydrodynamics is to discretize the volume, and directly address the continuum equations of hydrodynamics. If we include terms that arise in a comoving coordinate system (used in cosmological simulations), we can write down the Eulerian equations for ideal magnetohydrodynamics:

$$\frac{\partial \rho}{\partial t} + \frac{1}{a} \nabla \cdot (\rho \vec{v}) = 0 \quad (2.6)$$

$$\frac{\partial \rho \vec{v}}{\partial t} + \frac{1}{a} \nabla \cdot \left( \rho \vec{v} \vec{v} + \vec{I} p^* - \frac{\vec{B} \vec{B}}{a} \right) = -\frac{\dot{a}}{a} \rho \vec{v} - \frac{1}{a} \rho \nabla \phi \quad (2.7)$$

$$\frac{\partial E}{\partial t} + \frac{1}{a} \nabla \cdot \left[ (E + p^*) \vec{v} - \frac{1}{a} \vec{B} (\vec{B} \cdot \vec{v}) \right] = -\frac{\dot{a}}{a} \left( 2E - \frac{B^2}{2a} \right) - \frac{1}{a} \vec{v} \cdot \nabla \phi - \Lambda + \Gamma + \frac{1}{a^2} \nabla \cdot F_{cond} \quad (2.8)$$

$$\frac{\partial \vec{B}}{\partial t} - \frac{1}{a} \nabla \times (\vec{v} \times \vec{B}) = 0 \quad (2.9)$$

where  $E$  is the comoving total fluid energy,  $\rho$  is the comoving baryonic density,  $\vec{v}$  is the peculiar velocity,  $\vec{B}$  is the comoving magnetic field strength,  $\vec{I}$  is the identity matrix,  $a$  is the cosmological expansion factor,  $\Lambda$  and  $\Gamma$  are the cooling and heating terms,  $F_{cond}$  is the thermal conduction flux, and  $p^*$  is the total isotropic pressure,

$$p^* = p + \frac{B^2}{2a}. \quad (2.10)$$

Note that the total comoving fluid energy can be expressed in terms of a sum of the internal energy, kinetic energy, and magnetic energy,

$$E = e + \frac{\rho v^2}{2} + \frac{B^2}{2a}. \quad (2.11)$$

In order to close this system of equations, you need to add Poisson's equation from Equation 2.2 and an equation of state relating the pressure to the internal energy and density of the gas. While in principle this can be a complex relationship, for all the applications in this dissertation, we will

assume an ideal gas equation of state with a ratio of specific heats,  $\gamma_{ad}$ :

$$e = \frac{p}{(\gamma_{ad} - 1)\rho}. \quad (2.12)$$

This set of equations are then discretized on a (usually) Cartesian grid, and solved using a variety of finite difference and finite volume techniques, though the enumeration and comparison of is far beyond the scope of this dissertation. For a good introduction to finite volume methods, see LeVeque [139].

When dealing with cosmological simulations it is necessary to place the equations of (magneto-)hydrodynamics in a comoving expanding coordinates, governed by the formulae for the expansion history of the Universe as in the previous chapter, Equations 1.1 and 1.3. There are extensive code comparisons between grid and particle based hydrodynamics, and is far outside the scope of this dissertation[82, 168, 228, 240].

## 2.3 Adaptive Mesh Refinement

An unfortunate aspect of Eulerian hydrodynamics is that for a uniform static mesh, the spatial resolution does not vary (by definition!) and therefore it is difficult to capture the dynamics of collapsed or inhomogeneous volumes when the relevant scales vary by more than a few orders of magnitude. For example, currently even the highest resolution fixed-grid cosmology simulations are only approaching  $\sim 6400^3$  elements. The common solution to this problem is to either statically or adaptively refine the mesh in regions of interest. Mechanisms to do so are broadly labeled as adaptive mesh refinement (AMR) methods, and broadly are split into 2 primary types: cell-based and patch-based. Cell-based AMR examines each computational element and determines (through a variety of refinement criteria) whether or not the cell should be split into (usually 8 in 3 dimensions) higher resolution cells. Patch-based AMR instead selects a rectangular prism of cells, some number of which satisfy the refinement criteria, and create a new grid at twice the resolution that covers that region. There are benefits to both methods; Patch-based AMR is well suited to applying hydrodynamic solvers that were designed for rectangular grids in the first place, whereas

cell-based AMR can be more flexible and carries a more consistent memory footprint, allowing for efficient load-balancing mechanisms for parallel processing.

The method aside, the primary benefit to an AMR method is that it allows one to define the resolution of the simulation in a fairly arbitrary method. In order to follow the gravitational collapse of an object, for example, one can choose to refine based on baryonic/non-baryonic density. If instead one is simulating the evolution of an instability interface, refinement can be based on the first or second derivatives of any of the fluid quantities. In Chapter 5, we show how refining on magnetic field strength can also be very useful. This is a strong advantage over SPH codes that are only capable of “refining” on density, which can lead to difficulties in capturing instabilities or thermal properties in under-dense regions[228].

## 2.4 Enzo: A Community Code for Astrophysics

All simulations discussed in this dissertation were run using the Enzo cosmology code [33, 34, 163, 167]. While a full description can be found in the cited papers, we will review the key aspects that are of importance to this work. Additionally, there is a highly anticipated method paper describing the capabilities of Enzo, hopefully to be published in 2013 (Bryan, O’Shea, et. al. in prep).

Enzo solves the comoving equations of gravity and Eulerian magnetohydrodynamics on top of a block-structured (patch-based) adaptive mesh refinement [AMR; 17] method. Enzo utilizes an array of hydrodynamic (HD) and magnetohydrodynamic (MHD) solvers. The most often-used HD solver is the piecewise parabolic method [PPM; 49] with cosmological modifications by Bryan et al. [35]. The second is the method from the ZEUS magnetohydrodynamics code [223, 224]. Enzo is now capable of including the effects of magnetohydrodynamics, as described in Collins et al. [50]. The solver is spatially second order, while the PPM solver [49] commonly used in Enzo is spatially 3rd order.

The AMR algorithm within Enzo partitions the simulation volume into 3D rectangular solid grids. The refinement criteria is quite flexible, and new methods can be implemented with relative

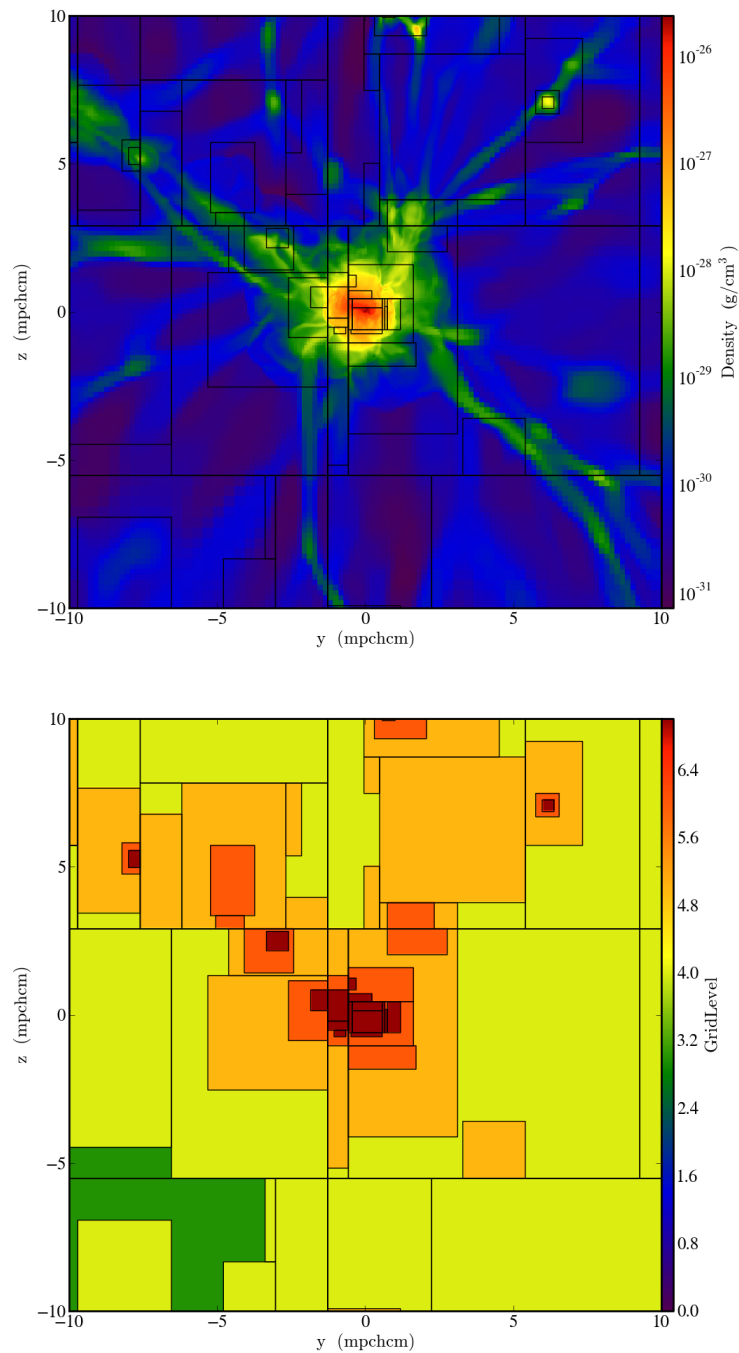


Figure 2.1 An example of using a gas density refinement criteria. Shown in the top panel is a slice through the galaxy cluster simulation at  $z = 0.5$  presented in Chapter 6. The bottom shows the AMR level. In both cases the grid outlines are shown in black. Length units are comoving Mpc/h.

ease. For the bulk of this dissertation, I will primarily refine based on dark matter and baryonic density. However, in some test problems as well as in more recent work, I have begun to refine based on the second derivative of various fields, as outlined in Löhner et al. [143]. In structure formation the dynamic range is quite immense, and due to computational limitations Enzo implements a maximum refinement level,  $l_{max}$ .

Enzo is also adaptive in time, advancing each level of grids by the maximum timestep allowed by a combination of limiters such as the Courant-Friedrichs-Lewy condition,

$$\Delta t \leq C_{CFL} \frac{\Delta x}{c_s + |\vec{v}|}, \quad (2.13)$$

where  $c_s$  is the sound speed,  $\vec{v}$  is the velocity, and  $C_{CFL}$  is the Courant number that is specific to each hydrodynamic method (0.8 for PPM). This is done until the grids are advanced to the same time as their parent grid. This requires the careful book-keeping of hydrodynamical fluxes to be exchanged between child, parent, siblings, and all other jumps in levels across a spatial boundary.

Enzo utilizes the Message Passing Interface (MPI) for parallelization. We use this to program a Single Program Multiple Data (SPMD) pipeline, decomposing the full simulation volume into relatively equal portions and executing the same code on each processor. Each processor updates its portion of the simulation, exchanging information with neighboring regions as necessary. Enzo has been used on some of the nation’s largest supercomputing centers, utilizing up to  $\sim 10,000$  cores when running with AMR and up to  $\sim 100,000$  cores for fixed-resolution simulations that are more scalable than their AMR counterparts. This parallelism is being augmented by a shared-memory parallelism, discusses more in the next section.

Enzo is open-source and released under the BSD licence. It is openly-developed using the Mercurial distributed version control system, with current development occurring through Bitbucket<sup>1</sup>. Contributions are welcomed and encouraged, and are curated through a system of code review and answer testing.

---

<sup>1</sup> <http://bitbucket.org/enzo/>

### 2.4.1 Enhancements to Enzo

I have made several enhancements to Enzo during the course of this dissertation, both in terms of physical models as well as performance. First of all, as described in the following chapter, I added the ability to locate and characterize hydrodynamic shocks by their Mach number.

The next two developments are related to the code performance and scalability. First, prior to this work, it was difficult to obtain a quick status of how well the code is performing at either a particular AMR level or by physical solver routine. Motivated by this, I led the development of a timing framework that was designed to provide a lightweight registering system that tracked many of the commonly used methods in Enzo. For example, we automatically track the time spent on each level of the simulation, as well as the time spent in the hydrodynamic solver, gravity solver, AMR hierarchy rebuild, and data output. However, since Enzo is such a flexible framework with many methods implemented we also made it simple to add custom times by simply calling `TIMER_START('Your Routine Name')` and `TIMER_END('Your Routine Name')` at the beginning and end of the routine. These timers are automatically registered in a C++ Standard Template Library “map” container<sup>2</sup>. These timers are created and managed individually on each processor in an asynchronous fashion.

At each complete update of the simulation (or less often if specified), each timer is then communicated to the root processor where it calculates the mean, standard deviation, minimum, and maximum for each of the timers across all processors. For level timers, there are also attributes such as the number of cell updates, the current number of grids, and the average cells/s/MPI process. This information is then output to a “performance.out” logfile. This provides a simplified interface to the user that can be used to diagnose performance issues as well as estimate a given problem type’s scalability. In addition to the logfile, we have developed a plotting interface for quickly producing figures that process the data from the logfile. An example logfile is copied below:

```
# This file contains timing information
# For instructions on how to decipher this information,
```

---

<sup>2</sup> <http://www.cplusplus.com/reference/map/map/>

```

# see [enzo base directory]/src/performance_tools/README.
# Times are collected across MPI processes and presented as:
# Level_N/Total, mean time, std_dev time, min time, max time, cell updates, grids, cell updates/processor/sec
# Routine, mean time, std_dev time, min time, max time
# Starting performance log. MPI processes: 64

Cycle_Number 1
ComputePotentialFieldLevelZero 2.239623e-01 9.822534e-02 2.101960e-01 1.003597e+00
Group_WriteAllData 2.231031e+00 6.441905e-04 2.229430e+00 2.232325e+00
Level_0 1.383130e+00 3.873529e-01 1.039812e+00 1.840182e+00 2.097152e+06 64 2.369119e+04
Level_1 6.662001e-01 3.620463e-01 4.037309e-02 9.334538e-01 3.329280e+05 32 7.808465e+03
Level_2 9.788156e-01 2.241700e-02 9.142530e-01 1.002886e+00 1.080000e+06 93 1.724022e+04
Level_3 2.879420e+00 7.087654e-02 2.683918e+00 2.950934e+00 4.505600e+06 151 2.444937e+04
RebuildHierarchy 1.517866e+00 4.560974e-05 1.517668e+00 1.517965e+00
SetBoundaryConditions 2.522391e+00 5.951711e-01 1.473226e+00 3.918054e+00
SolveCRs 1.504842e+00 2.463377e-01 1.046746e+00 1.984637e+00
SolveForPotential 4.534562e-01 6.475919e-02 3.941810e-01 5.721302e-01
SolveHydroEquations 1.458573e+00 2.636861e-01 9.762454e-01 1.971736e+00
Total 7.750820e+00 4.456098e-05 7.750759e+00 7.751011e+00 8.015680e+06 340 1.615893e+04

```

By examining such data one can see that the simulation is spending the majority of the time on Level 3, and that the 3 most time-consuming functions are the hydrodynamics, cosmic rays, and setting “SetBoundaryConditions”, which also includes the multi-grid gravity solver.

Because of what is referred to as the “multi-core revolution,”<sup>3</sup> the natural increase in computational power due to increased clock frequency on a given CPU has been stifled. Instead, industry has shifted to placing more cores on a single chip, increasing the parallelism but at a cost of flattening clock frequency. In order to take advantage of these new processors, I have collaborated with Dr. John Wise (Georgia Tech) to implement a hybrid parallelism within Enzo. This takes the existing Message Passing Interface (MPI) approach and combines it with an Open Multi-Processing (OpenMP) shared-memory implementation. This allows users to take advantage of increased core counts in modern supercomputers, without introducing the overhead and load-balancing limitations associated with each additional MPI process. This has allowed some of the later simulations in this dissertation to run at a total application speedup of 2.5x when using 6 OpenMP threads per MPI task (total of 3072 cores compared to 512). While ideally this speedup would be 6.0x, communication and input/output overhead (which are not OpenMP parallelized) takes up a substantial amount of runtime. For the routines which are parallelized with OpenMP we see nearly ideal speedup. For example, the time spent inside the hydrodynamic solver is 38 seconds vs the

---

<sup>3</sup> <http://www.scidacreview.org/0904/html/multicore.html>



original 284 seconds, a speedup of 7.5x. This super-linear speedup is likely due to the decreased number of MPI tasks per node as well as better memory access. Further improvement is almost certainly possible, as this was the first attempt at optimization.

## 2.5 yt: Data Analysis & Visualization

For all of the work in this dissertation after Chapter 3, I utilized the astrophysical visualization and analysis toolkit, yt[229]. Simulations utilizing AMR have the exquisite benefit of providing us a way to span many orders of magnitude in dynamic range. Until recently, however, it was excruciatingly painful to analyze such simulations. Creating simple analysis tasks such as slicing or projecting required fairly intimate knowledge of the AMR hierarchy structure. In addition, most of these tools were written in C++ to handle the complex masking and construction of the AMR hierarchy, requiring new analysis tools to be compiled, run, tested, re-compiled, and so-on.

This motivated Matthew Turk during his PhD to lay the groundwork for yt, a python-based analysis tool that has eventually grown into an exciting community and need-driven project. The driving philosophy behind yt is to provide simple and fast access to your simulation data without having to worry about all the book-keeping of complex data structures. For AMR datasets, only the highest resolution data for that region of space is returned, thereby simplifying analysis pipelines. For example, to access a sphere of data and calculate its mass-weighted average temperature, the entire pipeline looks like:

```
from yt.mods import *
dataset = load('path_to_dataset')
value, center_position = dataset.h.find_max('Density')
sphere = dataset.h.sphere(center_position, (1.0, 'mpc'))
avg_temp = sphere.quantities['WeightedAverageQuantity']('Temperature', 'CellMass')
```

In this dissertation, I use yt for 2D slices and projections, volume rendering, radial profiles, 1D and 2D probability distribution functions, as well as to define and create derived fields such as

emissivities and energy flux.

During this dissertation I developed a number of new features for `yt`, but my primary contribution has been the development of a parallel AMR volume decomposition framework within `yt` for volume rendering. Volume rendering is the process of displaying volumetric quantities using a transfer function that relates properties of the volume such as density or temperature to luminance that is then cast from the volume to an image plane used to represent the viewer. This process can be quite expensive, as it requires ray-tracing through a volume, solving a form of the radiative transfer equation for both optically thin and optically thick environments depending on how transparent the transfer function is. As such, it is desirable to have a parallel-capable volume renderer that can handle the domain decomposition of arbitrarily large datasets.

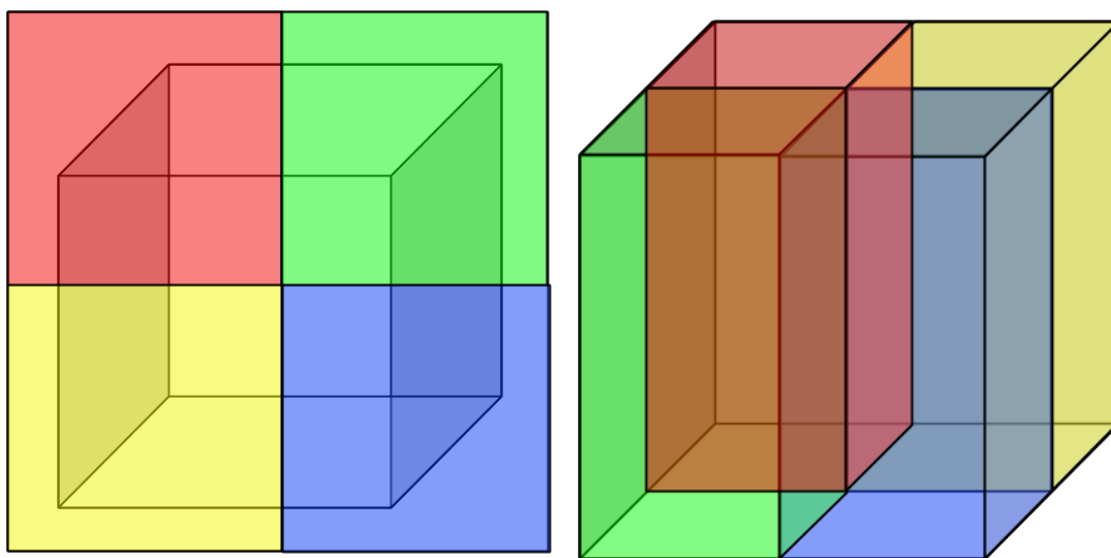


Figure 2.2 Left: Image-plane decomposition of a volume rendering. Right: Volume decomposition of a volume rendering. Each color represents a region that is “owned” by a different processor. If the viewing angle is changed, the data that each processor is responsible changes for the image-plane decomposition, while it stays constant for the volume decomposition.

This motivated the original implementation of a parallel volume renderer that handled domain decomposition by first splitting the image plane into  $N_{proc}$  equally sized sub-images, and decomposing the 3D data into inclined rectangular prisms that extend from the image plane through the dataset. See Figure 2.2 for an illustration. This method has the advantage that for very large

images, the image plane can be partitioned into smaller images, reducing the memory footprint of the image itself. However, it also has several disadvantages. First, there may be data input/output overlap due to multiple processors needing access to the same blocks of data due the way an image plane overlaps with the data. Second, if the viewpoint changes, the data has to be re-loaded (assuming the dataset doesn't fit completely in memory for each processor) from the disk, resulting in a large overhead. Third, for highly clustered AMR simulations, the load balancing between image planes may be very poor, especially for deeply nested simulations.

These disadvantages led to the need for a volume-based decomposition of the volume rendering, as depicted in the right panel of Figure 2.2. For these reasons, we implemented a new domain-decomposition method that utilizes a kD-Tree data structure, originally suggested for AMR volume rendering by Kreylos et al. [133]. A kD-Tree is a binary, self balancing tree that is used to partition a  $k$  dimensional space. Each leaf in the tree represents a point in the  $k$  dimensional space. The non-leaf nodes can be thought of as hyperplanes that divide the space into two halves; the left children of the node are the points on the left side of the hyperplane and vice-versa for the right child. To build a kD Tree the algorithm finds the best dimension to split the space in, and then the algorithm splits it so that an equal number of points end up on both sides of the hyperplane. After that, the algorithm recurses on each side of the hyperplane treating it as its own space. This continues until the algorithm reaches a point where there is only one point in the space, in which case it returns a leaf node associated with that point. The motivation behind using a kD-Tree structure is that for a given orientation of an image plane, a volume can be uniquely traversed through a straightforward comparison between the viewing location and each splitting hyperplane position, yielding either a back-to-front or front-to-back traversal.

However, since we don't necessarily want to decompose our simulation data down to the point/cell level, we modified the traditional kD-Tree structure to handle the partitioning of regions that also may have overlapping, higher-resolution regions due to the AMR nature. We also want to implement this in a way such that not only is the volume decomposed, but the kD-Tree itself is decomposed and allows for the parallel, independent construction of the tree. In yt, this is currently

referred to as the `AMRKDTree`, so we will use that term to describe our implementation. The first iteration of the `AMRKDTree` was written and implemented for my High Performance Scientific Computing (CSCI5576) class project with Wil St. Charles, and existed in the `yt` codebase for several years. Recently I was motivated to re-write the `AMRKDTree` in order to allow for more flexible data inputs. I will therefore only describe the current implementation. There are three main parts of the `AMRKDTree` framework: construction, traversal, and compositing.

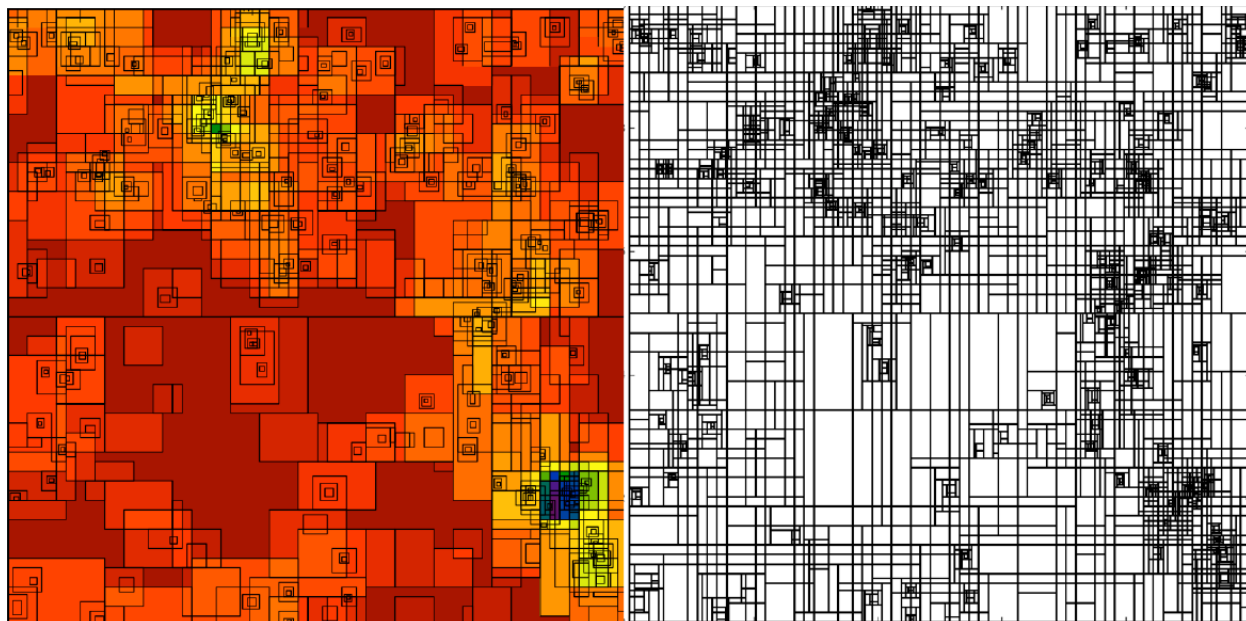


Figure 2.3 Left: The original AMR structure of a small cosmology simulation, where the colors correspond to the average grid level along the line of sight and the black lines outline the grids. Right: The `AMRKDTree` constructed from the same dataset.

The construction phase of the `AMRKDTree` is the most complex phase. In principle, the input to the construction is a set of AMR grids that are described by its dimensionality (number of cells in a given direction), and left and right edges in space that define the rectangular prism. The output is the `AMRKDTree` that begins with the head node of the tree, and is then defined by a series of splitting nodes with left and right child nodes, each of which are either a leaf node or additional splitting node. To explain the parallel construction, assume that each processor has rank *myrank* and that there are a total of *nprocs* processors. We start by defining a node id that begins with 1 for the head node, and uses the following for calculating child/parent id's:

```

def lchild_id(node_id): return (node_id<<1)
def rchild_id(node_id): return (node_id<<1) + 1
def parent_id(node_id): return (node_id-1) >> 1

```

We then only build the tree necessary for each processor by building up to an id of  $nprocs$  on all processors, and then only build the subtree that begins with the id of  $myrank$  on each separate processor. This also defines the domain decomposition to be that of a breadth-first decomposition rather than depth-first, but this has several advantages discussed below. By recursively adding grids AMR level-by-level, we build up the full tree. This tree does not have to be volume-filling, in that disconnected sets of grids can just as easily be added as full hierarchies. A simplified example is also shown in Figure 2.4, whereas how it is applied to a small simulation is visualized in Figure 2.5.

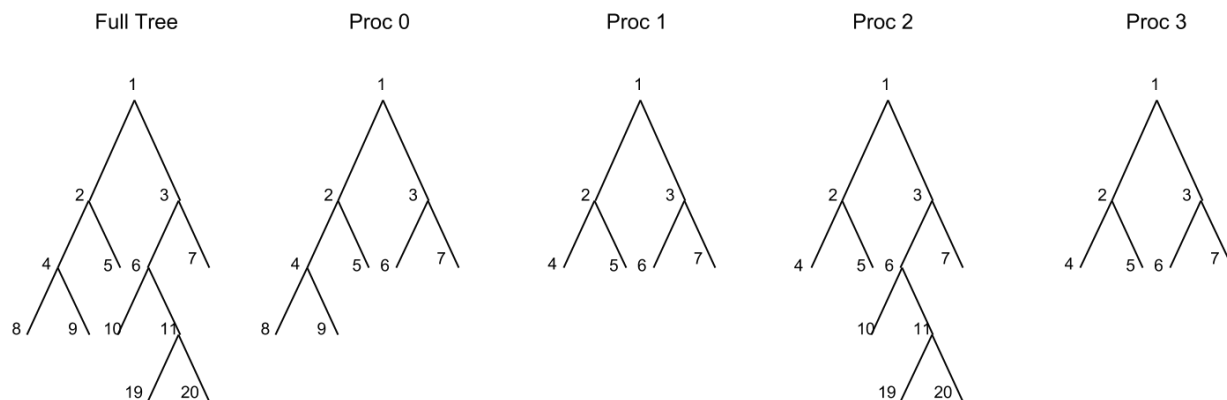


Figure 2.4 A simplified `AMRKDTree` structure with nodes labeled by their id. On the left is the full tree, and the 4 trees on the right depict how they are stored in each of the 4 processors.

During the traversal phase, called by the volume rendering functions in `yt`, the `AMRKDTree` is traversed from either back-to-front or front-to-back. It then yields a brick of data to the volume renderer to be processed by the ray-caster. This adds luminance to the r,g,b,a channels of the image. This phase is fairly straightforward, and each processor traverses its own piece of the full `AMRKDTree`. One of the key features of the `AMRKDTree` traversal is that once built, each processor owns the same portion of the dataset regardless of viewing angle. Therefore once the first snapshot

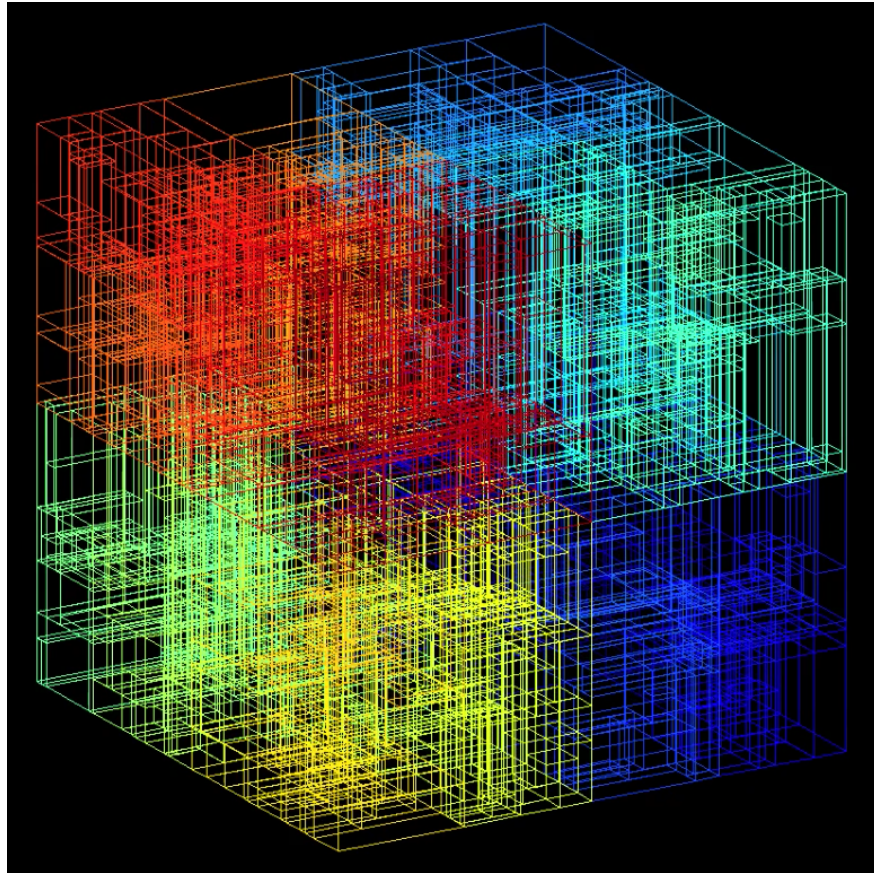


Figure 2.5 The AMRKDTree parallel decomposition structure depicted by having each processor represented by a different color. Underlying simulation is a small AMR cosmology simulation.

is taken, rotating and zooming is significantly faster and can result in a large performance boost over reading in the data each time. All that changes is the final composition of the image, described next.

The final phase is that of compositing. Unlike the image plane decomposition technique, the combination of each processor’s image into the final image takes more care. In the default configuration, each processor has the entire image plane, but it needs to be composited along the line of sight in the same order as it would be done in serial. Therefore, we traverse the `AMRKDTree` once more during the compositing phase. At each node, we send the right child’s image to the left child, and composite it from either back to front or front-to-back. This results in a butterfly-like image reduction, though due to the arbitrary number of processors the reduction can take on a slightly asymmetric behavior.

The result of this framework is the capability to render some of the largest AMR datasets available using the same processors that were used to run the simulation. We show two examples. The first example is a  $3600^3$  unigrid simulation of galaxy formation, where each field takes nearly  $350GB$  of memory. We choose an image size of  $4096^2$  to highlight our capability of not only handling large data, but also in creating high resolution images. The snapshot shown in Figure 2.6 is of the simulation at  $z = 7.5$ , and by choosing the temperature range to go from  $1 - 3 \times 10^4 K$ , we are able to see how bubbles of ionized gas form around galaxies that are “turning on” for the first times in cosmic history. This type of visualization at high resolution is a unique tool for scientists that need to explore their data in order to truly understand it. When running on 64-128 cores, each frame of the renders take 5-15 seconds once the data has been loaded into memory for the first snapshot.

Figure 2.7 shows one of my own simulations run on the Janus Supercomputer at the University of Colorado, Boulder, while testing the performance of the hybrid MPI+OpenMP parallelism. This simulation uses aggressive refinement criteria to refine a massive galaxy cluster all the way out from the core to the near its accretion shock at high uniform resolution. While normally simulations of galaxy clusters have a relatively small number of cells at the highest level of refinement, here our simulation had nearly  $10^9$  cells at 30kpc resolution. This poses many problems for conventional

volume rendering techniques that must uniformly sample a dataset at some specified frequency. Our ability to partition the AMR hierarchy and integrate along the highest resolution elements allows us to visualize the gas temperature in exquisite detail. Future improvements to this capability are possible through optimization of the `AMRKDTree` construction and load balancing.



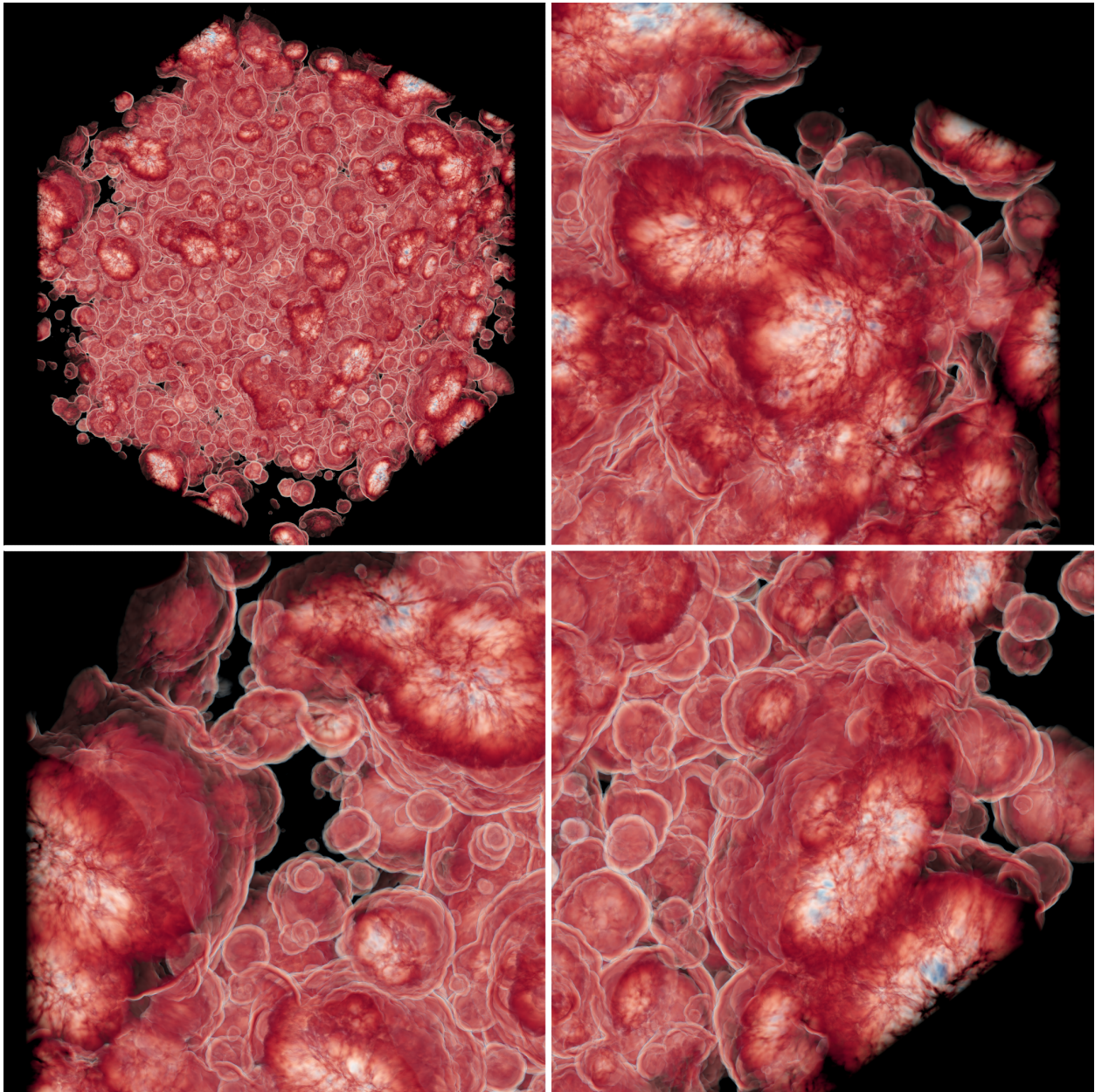


Figure 2.6 Volume rendering of temperature of a radiation-hydrodynamics simulation of a  $(56Mpc/h)^3$  comoving volume at  $z = 7.5$ . Simulation credit: Michael Norman, Robert Harkness, Daniel Reynolds. Visualization credit: Samuel Skillman. Shown is gas temperature, chosen to highlight re-ionization bubbles during galaxy formation. Blue is  $10^4\text{K}$  and red is  $3 \times 10^4\text{K}$ . The top-right and bottom panels show zoom-in's of the original  $4096^2$  pixels full rendering image.

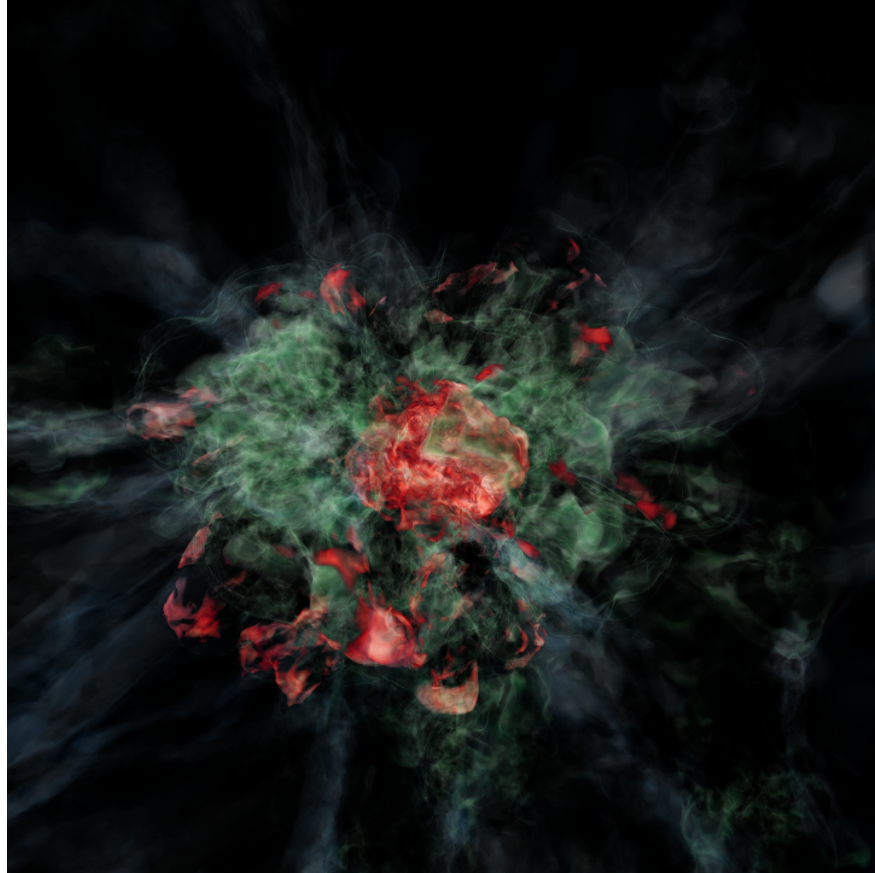


Figure 2.7 Volume rendering of Temperature around a massive galaxy cluster, with a 30 Mpc/h field of view. This simulation has nearly a billion cells on the highest level of refinement. Green highlights gas at  $10^7 K$ , and red shows the inner core of the cluster at  $10^8 K$ .

## Chapter 3

### Cosmological Shocks

As published in S. W. Skillman, B. W. OShea, E. J. Hallman, J. O. Burns, and M. L. Norman. *Cosmological Shocks in Adaptive Mesh Refinement Simulations and the Acceleration of Cosmic Rays*. *ApJ*, 689:1063-1077, December 2008. doi: 10.1086/592496. Reproduced by permission of the AAS. [212]

#### 3.1 Introduction

What determines the thermal history of galaxy clusters? On large scales, it is governed by the in-fall of material onto dark matter halos and the conversion of gravitational potential energy into thermal energy. This process occurs through the heating of the gas via strong accretion shocks surrounding galaxy clusters and filaments [204, 158, 179, 174]. Once inside collapsed structures, complex flows associated with the merging of subhalos continue to create moderate-strength shocks that allow the halos to virialize. Because of this, shocks encode information about structure formation and its thermal effects on the gas.

Cosmological shocks affect three important realms of structure formation and leave feedback on the surrounding medium. First, shocks thermalize the incoming gas, providing much of the pressure support in baryons. This process is the basis upon which clusters are able to virialize. Additionally, the thermalization of gas at the standing accretion shocks surrounding large-scale filaments produces the warm-hot intercluster medium (WHIM) at temperatures of  $10^5 K - 10^7 K$  [53, 45]. The history of the mass flux through these shocks describes the evolution of gas in the

WHIM phase [181].

Second, the strength of the outer accretion shocks onto halos, characterized by the Mach number, is dependent upon the mass of the gravitating object. This is because the higher mass generates larger acceleration and velocity in the diffuse gas while the sound speed of the upstream gas is uniform for previously unshocked gas, corresponding to a temperature of  $\approx 10^4 K$ . This temperature floor is created by the reionization from stars. Thus, the Mach number of accretion shocks can be used as an independent measure of cluster mass. This could conceivably be a powerful new tool for cluster mass estimation if we are able to observe the accretion shock with radio observations [e.g. 90].

Finally, because these shocks are collisionless features whose interactions in the hot plasma are mediated by electromagnetic fields, it is possible for a portion of the thermal distribution of particles to be accelerated and transformed into non-thermal populations of cosmic rays (CRs) through the process of diffusive shock acceleration [DSA; e.g. 62, 22]. This process results in a fraction of the kinetic energy of shocking gas being converted into both thermal and non-thermal components [152, 155, 124, 120, 121]. The cosmic ray electron populations are likely sources of radio halos and radio relics in galaxy clusters [128, 91, 157, 181], while the cosmic ray protons may be sources of  $\gamma$ -ray emission through their interactions with gas protons [153, 154]. If a significant portion of the gas pressure resides in cosmic rays, then it will likely affect gas mass fraction estimates as well as the assumption of hydrostatic equilibrium. Because of the importance of these mass estimates in measuring dark energy, we must include the underlying physics in order to perform precision cosmology [8].

To date, studies of cosmological shocks have included observational, theoretical, and numerical techniques. Observationally, the majority of the work surrounding cosmic shocks are related to radio relics, of which only a few have been studied in depth [e.g. 198, 47, 166]. Using the spectral index of the non-thermal particle distribution, we can infer a Mach number if the acceleration is due to first order Fermi acceleration [90]. Additionally, GLAST will begin observing  $\gamma$ -rays and will likely see signatures from galaxy clusters due to hadronic cosmic ray interactions with pions

[178].

On the theoretical side, the majority of analyses are based upon manipulating the Press-Schechter formalism [184, 208] to deduce first the mass function of accreting objects and then their interactions with infalling material. Pavlidou and Fields [174] extended these analyses to calculate the energy and mass flux through accretion shocks. Furthermore, several analytical attempts have been made to describe merger shocks, including those by Fujita and Sarazin [84] and Gabici and Blasi [87, 86]. However, it is quite difficult to account for the complex morphologies that arise during structure formation using purely analytical frameworks. For this reason, multiple numerical techniques have been developed using hydrodynamical simulations.

There have been numerical studies of shocks using both Eulerian “single-grid” codes [e.g. 156, 204, 121] as well as smoothed particle hydrodynamics (SPH) codes [179, 180, 181, 178]. There are advantages and disadvantages of both methods. In previous work using grid-based codes, shocks were analyzed during post-processing by examining temperature jumps for a given point in time [204]. However, it was impossible to cover the spatial dynamic range needed to describe both the complex flow within halos and their coupling to large scale structures because of the use of a uniform grid. Therefore, even the largest simulations, with  $1024^3$  cells in a  $100h^{-1}Mpc$  volume, has a comoving spatial resolution of only  $97.7h^{-1}kpc$  [204]. There have been recent attempts at prescribing hybrid models to study turbulent generation, but full resolution convergence of the results have still not yet been achieved [205]. The advantage of a grid code is its superb shock-capturing algorithms that do not rely on the use of artificial viscosity when using higher-order methods [168].

In contrast, SPH codes are implicitly adaptive in space due to the Lagrangian nature of the method, e.g. high density regions are resolved by a larger number of particles than low-density regions. This approach conserves hydrodynamic quantities exactly when they are advected with the flow. However, because the properties of the gas are determined by a weighted average over neighboring particles, formally discontinuous shocks are spread over a length determined by the smoothing length. Additionally, SPH relies on artificial viscosity to dissipate flows and produce

the correct amount of entropy. Because of these restrictions, Pfrommer et al. [179] developed a method that is able to identify shocks by examining the time-evolution of the entropy of individual SPH particles. Comparing the instantaneous entropy injection rate to the characteristic time it takes a particle to cross the broadened shock surface, they are able to identify and calculate the instantaneous Mach number of shocks while remembering the pre-shock conditions. Therefore, the analysis can be performed on-the-fly and shock quantities were traced along with the usual hydrodynamic properties. These calculations use calibrations against “shock tube” simulations to derive the correct relationship between entropy injection rate and Mach number, which may vary with respect to different artificial viscosity implementations.

To address all of the problems listed above, we have developed a novel numerical algorithm capable of detecting and identifying shocks in the 3-D adaptive mesh refinement (AMR) grid-based code, *Enzo*. The use of AMR allows us to analyze unprecedented dynamic ranges with an advanced hydrodynamic code that is able to capture shocks exceedingly well. In this work we explore simulations with dynamic range of up to  $2^{16} = 65,536$ , but we are not limited from going further in future work. Because of the complexity of the structure of AMR simulations, it was necessary to develop several new numerical algorithms to identify the shocks. This shock-finding analysis algorithm will be presented and compared to previous methods [e.g. 204, 179]. In order to validate and quantify the robustness of our method, we carry out a resolution study that includes both mass and spatial resolutions that vary by factors of 16 and 64, respectively.

We also propose a new method of characterizing shocks by their pre-shock overdensity and temperature. This then allows analysis that goes beyond the traditional internal vs. external (of filaments/clusters) shocks classification suggested by Ryu et al. [204]. By refining the temperature and density ranges examined, we are able to identify shocks that reside in voids, filaments, and halos. Additionally, by using temperature cuts, we can identify the population of gas that is being shocked into the warm-hot intercluster medium (WHIM).

After calculating the shock structure in a given simulation, we are able to compute the amount of shock kinetic energy that is transferred to high-energy cosmic ray protons through diffusive shock

acceleration. While the surface area of the large scale structure shocks are dominated by low pre-shock temperature and density, the bulk of the cosmic ray energy generation occurs in the centers of collapsed structures. Since stronger shocks will produce harder spectra [22], we expect that the strong accretion shocks could be the source of high energy cosmic rays.

In Section 3.2 we describe the numerical methods used for both the cosmological simulations as well as the analysis of the shock-finding process. In Section 3.3, we compare our algorithm to that of Ryu et al. [204] and test it using 3-D “shock tube” tests. Section 3.4 contains the main results of analyzing a large,  $(512 \text{ Mpc}/h)^3$ , cosmological simulation with a peak spatial resolution of  $7.8 \text{ kpc}/h$ . Section 3.5 describes the effects of spatial and mass resolution on the shock populations and cosmic ray acceleration. In Section 3.6, we discuss the limitations of our analysis, and in Section 3.7 we summarize our findings and discuss potential future directions.

## 3.2 Methodology

### 3.2.1 The Enzo Code

All simulations were run using the Enzo cosmology code [33, 34, 163, 167]. While a full description can be found in the cited papers, we will review the key aspects that are of importance to this work.

Enzo is a block-structured adaptive mesh refinement [AMR; 17] code that couples an Eulerian hydrodynamics method that follows the gas dynamics with an N-Body particle mesh (PM) solver [65, 107] to follow the dark matter component. Enzo implements two hydrodynamic solvers. The first is a piecewise parabolic method [PPM; 49] with cosmological modifications by Bryan et al. [35]. The second is the method from the ZEUS magnetohydrodynamics code [223, 224]. In this work we restrict ourselves to the PPM method because of its superior shock-capturing ability and lack of artificial viscosity.

The AMR scheme within Enzo is handled by partitioning the simulation volume into 3D rectangular solid grids. Each of these grids contain a number of grid cells that set the spatial

scale on which the hydrodynamics is solved. If a region of cells within a grid is determined to require higher resolution, as judged by a number of refinement criteria including gas/dark matter overdensity, minimum resolution of the Jeans length, local gradients of density, pressure, or energy, shocks, or cooling time, then a minimum enclosing volume around those cells is created at the appropriate level of refinement. These newly created “child grids” can then themselves recursively become “parent grids” to yet another more highly refined region. This recursive nature does not set any restrictions to the number of grids or level of refinement. However, because structure formation leads to an enormous dynamic range we are limited by available computational resources, a maximum level of refinement  $l_{max}$  is instituted.

In addition to being adaptive in space, Enzo implements an adaptive time stepping algorithm. All grids on a given level are given advanced simultaneously with a maximum timestep such that the Courant condition is satisfied by all the cells on that level. This results in a hierarchy of timesteps: a parent grid on level  $l$  is advanced  $\Delta t(l)$ , and then its subgrid(s) on level  $l + 1$  are advanced by one or more timesteps until they reach the same physical time as their parent grid. At this point, flux information is exchanged from child to parent grid in order to provide a more accurate solution to the hydrodynamics on the parent grid. This procedure is done recursively until all grids are at the same physical time as the root grid, at which point the process is repeated until the stopping point of the calculation is reached.

### 3.2.2 Shock-Finding Algorithm

The bulk of our analysis relies on accurately identifying and quantifying the strength of shocks. After finding a shock, we would like to calculate its Mach number, which characterizes the strength of the shock. There are several methods that can be used in order to calculate the Mach number, including density, temperature, velocity, or entropy jumps across the shock. As in Ryu et al. [204], we use the Rankine-Hugoniot temperature jump conditions to calculate the Mach number. The temperature jump is preferable to density because it is more sensitive to Mach number, whereas the density jump quickly asymptotes for strong shocks. The Mach number is



solved for by

$$\frac{T_2}{T_1} = \frac{(5\mathcal{M}^2 - 1)(\mathcal{M}^2 + 3)}{16\mathcal{M}^2}, \quad (3.1)$$

where  $T_2$  and  $T_1$  are the post-shock (downstream) and pre-shock (upstream) temperatures, respectively.  $\mathcal{M}$  is the upstream Mach number.

A cell is determined to have a shock if it meets the following requirements:

$$\nabla \cdot \vec{v} < 0 \quad (3.2)$$

$$\nabla T \cdot \nabla S > 0 \quad (3.3)$$

$$T_2 > T_1 \quad (3.4)$$

$$\rho_2 > \rho_1, \quad (3.5)$$

where  $\vec{v}$  is the velocity field,  $T$  is the temperature,  $\rho$  is the density, and  $S = T/\rho^{\gamma-1}$  is the entropy. In our analysis, as in Ryu et al. [204], we have set a minimum preshock temperature of  $T = 10^4 K$  since the low-density gas in our cosmological simulations is assumed to be ionized (a reasonable assumption at  $z \lesssim 6$ ). Therefore, any time the pre-shock temperature is lower than  $10^4 K$ , the Mach number is calculated from the ratio of the post-shock temperature to  $10^4 K$ . This introduction of a temperature floor prevents us from drastically overestimating the accretion shock strength in adiabatic simulations. Future work will incorporate a self-consistent UV ionizing background radiation.

Now the task is to identify all of the shocks and their corresponding Mach numbers. The method that has been previously used in unigrid simulations [e.g. 204] is to loop through rows of cells along each of the coordinate axes and identify 1-D shock structures in each direction. Contiguous cells that meet the requirements above in Eqs. 2-5 are then combined into a single shock structure with the cell of maximum convergence marked at the center. The pre- and post-shock cells are identified as first cells outside of the shock structure. If a center is marked in more than one direction, the maximum calculated Mach number of the three possible is taken to be the true Mach number. Because of this, we would expect errors to arise when examining shocks whose

direction of motion is not oriented along a coordinate axis. To address this issue, we have designed an algorithm that does not suffer from this limitation.

In our method, we first determine the direction of shock propagation from the local temperature gradients, making the assumption that the shock-induced temperature gradient overwhelms the background temperature gradient. We then search the cells along the temperature gradient for the pre- and post-shock cells. If we find a neighboring cell to have a more convergent flow, that cell is marked as the center and we move outwards from it. This guarantees that the analysis is anchored to the center of the shock. Once the furthest pre- and post-shock cells are found, the temperatures are taken and the Mach number is calculated from Equation 1. A two-dimensional analog of this process is shown in Figure 3.1. Because our algorithm is not confined to operate along coordinate axes, the calculated Mach numbers provide a more accurate description of the underlying shock properties than the Ryu et al. [204] method.

Specifically, in situations where there are weak shocks or complex flow velocities, using the coordinate-split approach may allow for an excess of shocks since the direction of the shockwave is not taken into account. Our method picks a single direction that a shock could be propagating, given a specific temperature gradient. Ryu et al. [204] claim that their shocks are spread out over 2-3 cells, of which one is marked as the center. For the other 1-2 cells, the coordinate split approach may mis-identify these other 1-2 cells as low Mach number shocks due to normal temperature gradients. This would lead to an over-prediction of low Mach number shocks.

This process is further complicated by the use of adaptive mesh refinement (AMR), primarily because neighboring cells are not necessarily at the same level of refinement. This occurs most often at the site of accretion shocks onto halos and filaments where the density gradient, upon which the refinement criteria are based, is largest. Therefore, knowledge of the grid hierarchy must be used. We incorporate this into our algorithm and allow for a neighboring cell to be any cell at the same or lower level of refinement. We do not allow the algorithm to search for neighbors at higher levels (smaller grid cells) since one cell will have multiple neighbors. If this situation occurs, we use the neighboring cell on the same level. Because of this requirement, we must perform our analysis on

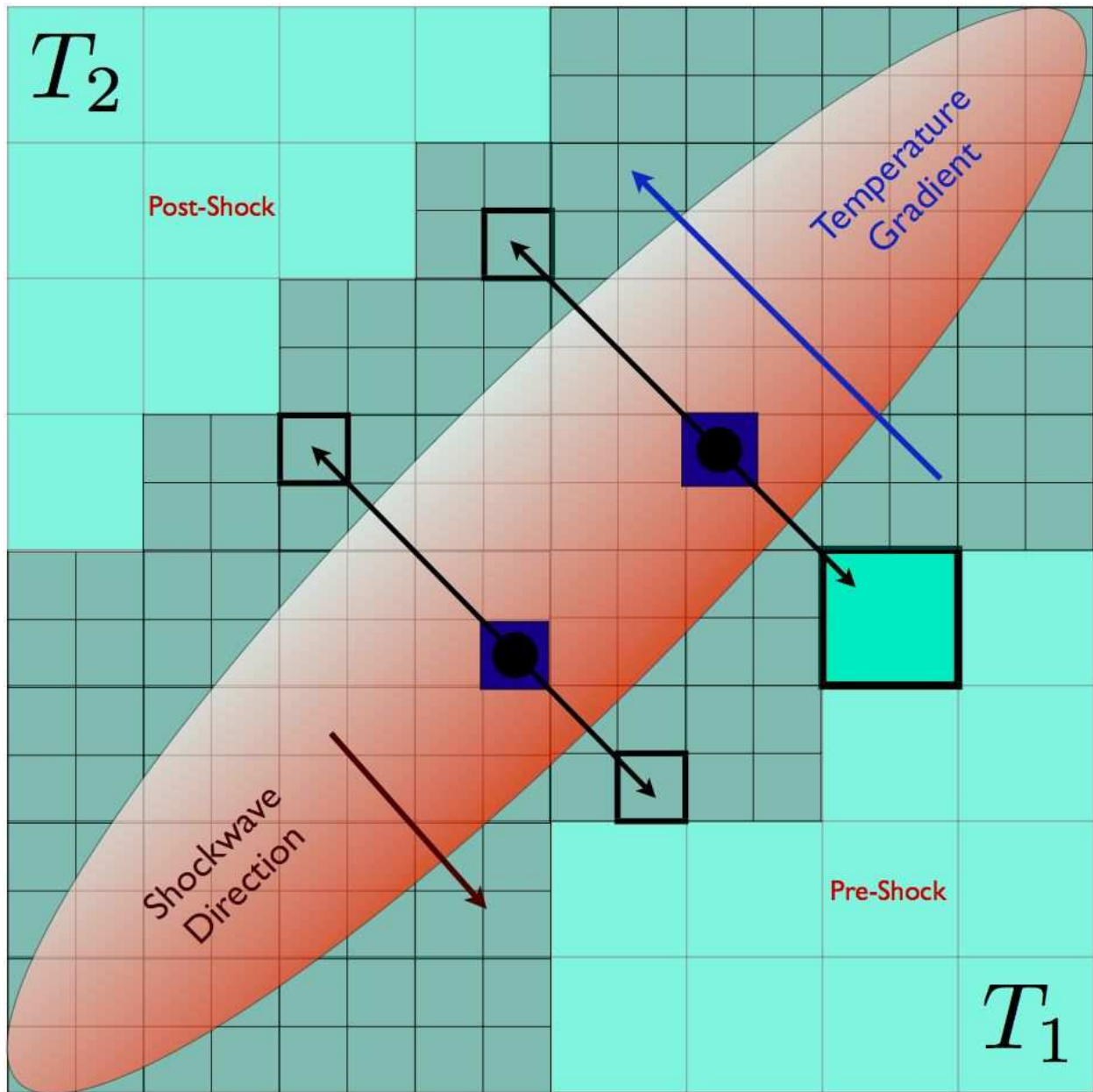


Figure 3.1 A 2-D cartoon of our shock analysis algorithm. The shock centers are shown as dark blue cells, while the pre- and post-shock cells are outlined in thick black. The AMR resolution level is seen by varying grid-cell sizes.

the most highly refined grids first, and move to progressively coarser levels of resolution.

### 3.2.3 Cosmic Ray Acceleration Models

Following the method proposed in Ryu et al. [204], we now seek to determine the amount of kinetic energy that is converted into heating of the gas and accelerating cosmic rays. We begin with calculating the total kinetic energy flux through a shock surface. The kinetic energy flux associated with a mass flux of  $\rho_1 \mathcal{M} c_s$  is:

$$f_{KE} = \frac{1}{2} \rho_1 (\mathcal{M} c_s)^3, \quad (3.6)$$

where  $\rho_1$  is the pre-shock density and  $c_s$  is the sound speed in the pre-shock gas. From this total incoming kinetic energy flux, a fraction will be used in the thermalization of the gas and the acceleration of cosmic rays. In keeping with [204], we will denote the amount of energy per unit time used to heat the gas and accelerate cosmic rays as  $f_{TE}$  and  $f_{CR}$ , respectively. In the case of a purely hydrodynamical shock without the inclusion of cosmic ray feedback, the fractional thermalization  $\delta_0(\mathcal{M})$  can be determined by the Rankine-Hugoniot jump conditions,

$$\delta_0(\mathcal{M}) = \frac{\left[ e_{TE,2} - e_{TE,1} \left( \frac{\rho_2}{\rho_1} \right)^\gamma \right] v_2}{\frac{1}{2} \rho_1 v_1^3}, \quad (3.7)$$

where  $e_{TE,1}$  and  $e_{TE,2}$  are the thermal energy densities in the pre and post-shock regions, respectively.

With the inclusion of cosmic rays, there is no simple analytical form for the fractional thermalization of the gas, which depends on magnetic field orientation, turbulence, and the pre-shock cosmic ray population. Instead, we adopt the results of 1D diffusive shock acceleration (DSA) simulations by Kang and Jones [121]. The time-asymptotic values of the fractional thermalization,  $\delta(\mathcal{M}) = f_{TE}/f_{KE}$ , and fractional CR acceleration,  $\eta(\mathcal{M}) = f_{CR}/f_{KE}$ , were found to be nearly self-similar for the temperatures and shock velocities considered. These simulations also accounted for whether or not the pre-shock medium had preexisting cosmic rays. With a preexisting cosmic ray population, the fractional energy deposited into CRs increases dramatically at low Mach numbers because it is much easier to accelerate an existing power-law distribution of particles than a

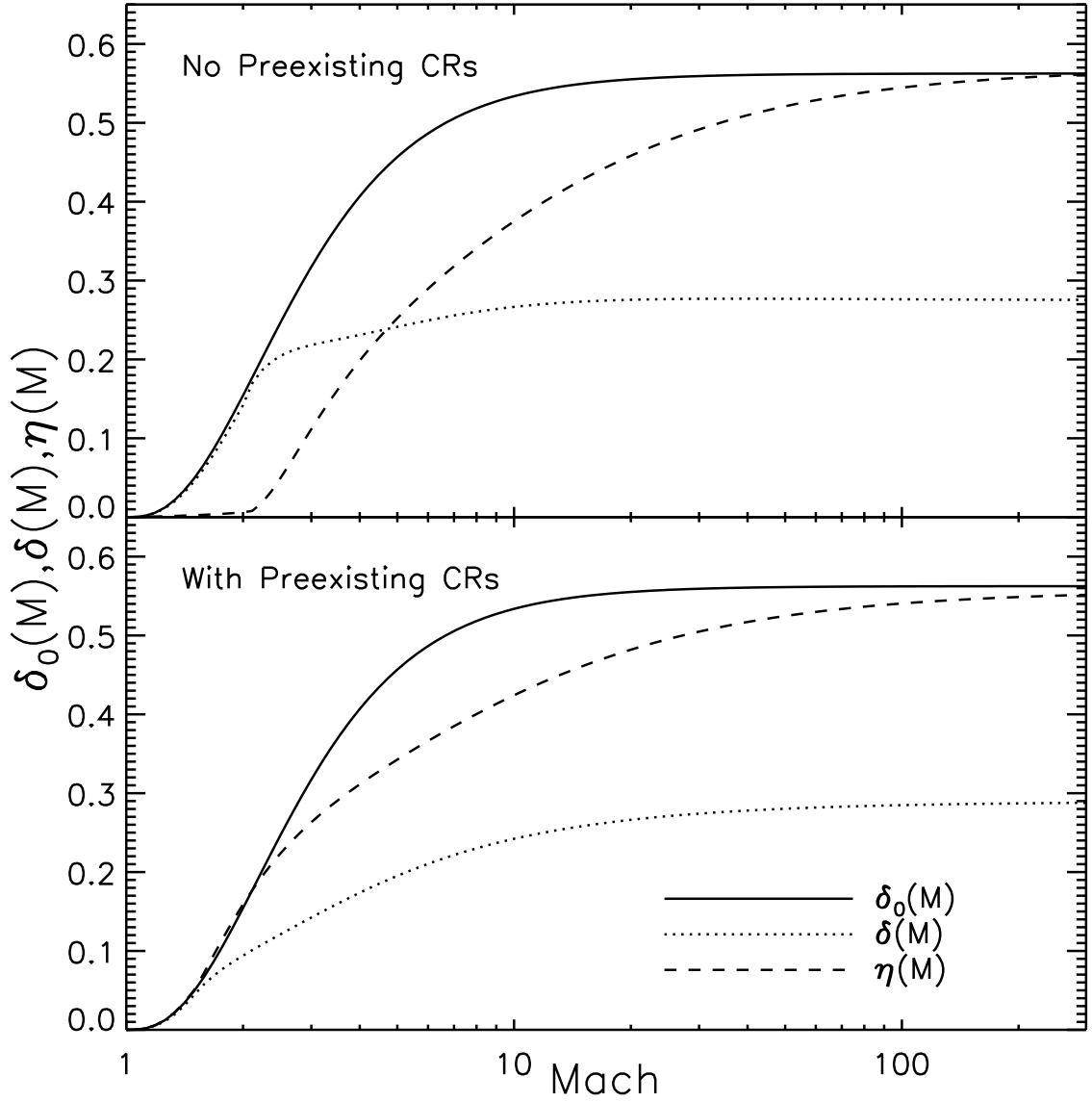


Figure 3.2 Fractional efficiency of gas thermalization and cosmic ray acceleration, from the models by Kang and Jones [121].  $\delta_0(\mathcal{M})$  is the gas thermalization fraction expected from the Rankine-Hugoniot jump conditions.  $\delta(\mathcal{M})$  and  $\eta(\mathcal{M})$  are the gas thermalization fraction and cosmic ray acceleration fraction, respectively, from the non-linear calculations of Kang and Jones [121]. The two panels show results assuming different compositions of the pre-shock plasma. Top: thermal gas with no cosmic ray population. Bottom: thermal gas with a pre-existing cosmic ray population having  $P_{CR}/P_{gas} = 0.3$ , where  $P_{CR}$  and  $P_g$  are the cosmic ray and total gas pressure, respectively.

Table 3.1. Simulation Parameters

Name	$L_{box}$	$\Delta x_{RG}$	$l_{max}$	$M_{dm}$	$\Delta x_{max}$	$\Omega_b$	$\Omega_m$	$\sigma_8$
<i>ryu1024</i>	100	97.7	0	$5.877 \times 10^7$	97.7	0.043	0.27	0.8
<i>SF Light Cone</i>	512	1	7	$7.228 \times 10^{10}$	7.8	0.04	0.3	0.9
<i>m1_l8</i>	256	1	8	$6.224 \times 10^{10}$	3.9	0.0441	0.268	0.9
<i>m1_l6</i>	256	1	6	$6.224 \times 10^{10}$	15.6	0.0441	0.268	0.9
<i>m1_l4</i>	256	1	4	$6.224 \times 10^{10}$	62.4	0.0441	0.268	0.9
<i>m4_l8</i>	256	500	8	$7.781 \times 10^9$	3.9	0.0441	0.268	0.9
<i>m4_l6</i>	256	500	6	$7.781 \times 10^9$	15.6	0.0441	0.268	0.9
<i>m4_l4</i>	256	500	4	$7.781 \times 10^9$	62.4	0.0441	0.268	0.9
<i>m16_l8</i>	256	250	8	$9.726 \times 10^8$	3.9	0.0441	0.268	0.9
<i>m16_l6</i>	256	250	6	$9.726 \times 10^8$	15.6	0.0441	0.268	0.9
<i>m16_l4</i>	256	250	4	$9.726 \times 10^8$	62.4	0.0441	0.268	0.9

Note. —  $L_{box}$  is the simulation box size in comoving Mpc/h.  $\Delta x_{RG}$  is the effective root grid resolution (the m4 and m16 series of calculations use one and two static nested grids, respectively).  $l_{max}$  is the maximum level of AMR allowed in the simulation.  $M_{dm}$  is the dark matter particle mass (in the static nested grids for the m4 and m16 series of runs) in  $M_\odot/h$ .  $\Delta x_{max}$  is the peak spatial resolution in comoving  $kpc/h$ .  $\Omega_b$  and  $\Omega_m$  are the fractional densities of baryons and matter compared to the critical density ( $\Omega_\Lambda \equiv 1 - \Omega_m$  in all simulations, so  $\Omega_0 = 1$ ).  $\sigma_8$  is the power spectrum normalization of the mass fluctuation in a comoving 8 Mpc sphere.

thermal distribution of particles. Shown in Figure 3.2 are the results of the Kang & Jones DSA simulations for a population with no preexisting cosmic rays and one in which CRs existed initially with  $P_{CR}/P_g \approx 0.3$ , where  $P_{CR}$  and  $P_g$  are the cosmic ray and total gas pressure, respectively. The sum of  $\delta(\mathcal{M})$ ,  $\eta(\mathcal{M})$ , and the remaining fraction of kinetic energy in the gas is equal to one, conserving energy.

We do not track the cosmic ray population in our simulations at present, and as a result we are unable to constrain the amount of preexisting CRs in the pre-shock medium. Therefore, we can think of our results from the two scenarios shown in Figure 3.2 as bracketing the likely range of efficiencies. Additionally, these efficiency models are only valid for situations where the shock normal is parallel to the magnetic field. Any deviation from these ideal conditions will likely reduce the efficiency of cosmic ray acceleration [121], so one can view the results described later in this paper as upper limits on cosmic ray injection efficiency.

### 3.2.4 Simulations

We constructed three distinct sets of cosmological simulations for this project. A summary of some of the simulation parameters is given in Table 3.1. First, we have a simulation that was devised as an analog of the unigrid numerical simulation by Ryu et al. (2003). For this simulation, we used identical cosmological parameters to Ryu et al. [204] in order to provide a reference simulation to compare our new shock-finding method with previous work. The cosmological parameters for this simulation, *ryu1024*, are:  $\Omega_{BM} = 0.043$ ,  $\Omega_{DM} = 0.227$ ,  $\Omega_{\Lambda} = 0.73$ ,  $h = H_0/(100 \text{ km s}^{-1}\text{Mpc}^{-1}) = 0.7$ , and  $\sigma_8 = 0.8$ , which are broadly consistent with WMAP Year 5 results [130]. The comoving size of the simulation volume is  $(100 \text{ Mpc}/h)^3$  and is discretized into  $1024^3$  cells, giving a comoving spatial resolution of  $97.7 \text{ kpc}/h$ . It also employs  $512^3$  dark matter particles with a  $1024^3$  grid. In order to reproduce the Ryu et al. results as closely possible, we did not use AMR techniques. The simulation was initialized with an Eisenstein & Hu (1999) power spectrum with a spectral index of  $n = 1.0$  at  $z=99$  and the simulation states were output in 20 times between  $z = 10$  and  $z = 0$ . The analysis of this simulation is described in Section 3.2.

Our main results in this work focus on the analysis of a  $(512 \text{ Mpc}/h)^3$  volume that utilizes a  $512^3$  root grid and up to 7 levels of AMR. It is referred to as the “Santa Fe Light Cone,” and has been previously described by Hallman et al. [104]. This simulation has a peak spatial resolution of  $7.8 \text{ kpc}/h$  and a dynamic range of 65,536. The cosmological parameters used were:  $\Omega_M = 0.3$ ,  $\Omega_{BM} = 0.04$ ,  $\Omega_{CDM} = 0.26$ ,  $\Omega_\Lambda = 0.7$ ,  $h = H_0/(100 \text{ km s}^{-1} \text{ Mpc}^{-1}) = 0.7$ , and  $\sigma_8 = 0.9$ , and employs a Eisenstein & Hu (1999) power spectrum with a spectral index  $n = 1.0$ . Cells are refined whenever the baryon or dark matter density increased by a factor of 8 beyond the previous level. Because the simulation then refines by a factor of 8 in volume, the average mass per grid cell stays roughly constant. The simulation was initialized at  $z = 99$  and was run to  $z = 0$ . The analysis of this simulation is described in Section 4.

In order to study the effects of spatial and dark matter mass resolution, we have performed a suite of simulations that vary these factors, and illustrate their results in Section 5. These simulations are known as “nested grid” simulations. An initial cosmological simulation is run at low resolution. The most massive halo at  $z = 0$  is found and the simulation is re-centered at the final location. The simulation is then re-run, while only adaptively refining a region that bounds all dark matter particles that eventually are inside the most massive halo. Therefore, the focus of the simulation is only on the inner portion of the initial volume. With this capability, we are able to modify the root grid and peak spatial resolution for this subvolume and study their direct effects on the evolution of a single cluster. In our simulations, we initialize a  $(256 \text{ Mpc}/h)^3$  volume with  $256^3$  root grid cells. From that, we only adaptively refine in a  $(32 \text{ Mpc}/h)^3$  subvolume. Within the subvolume, we add up to two static nested grids, with more highly refined dark matter particles and gas cells. A list of all simulation parameters used is given in Table 3.1. The cosmological parameters used are:  $\Omega_M = 0.268$ ,  $\Omega_{BM} = 0.0441$ ,  $\Omega_{CDM} = 0.2239$ ,  $\Omega_\Lambda = 0.732$ ,  $h = H_0/(100 \text{ km s}^{-1} \text{ Mpc}^{-1}) = 0.704$ , and  $\sigma_8 = 0.9$ . These parameters are the WMAP year 3 parameters [217] but with a somewhat higher  $\sigma_8$ .



### 3.3 Validation of Shock-Finding Method

#### 3.3.1 Shock Tube Test

In order to verify that our shock-finding algorithm is accurate, we have performed a suite of 3-D AMR shock tube tests. In these tests we have varied the Mach number as well as orientation with respect to the coordinate axis. The setup of this test problem is described in Mihalas and Weibel Mihalas [151]. It consists of a stationary, uniform pre-shock medium. The shock is then introduced via boundary conditions that match the Rankine-Hugoniot Jump conditions for a given Mach number. The volume is then allowed to adaptively refine up to 2 levels, using shocks as a criteria for refinement. We have chosen to adaptively refine based on shock locations (i.e. strong pressure jumps) instead of density because this should introduce a complicated AMR topology in order to test the robustness of our algorithm. This forces us to traverse different levels of refinement for pre- and post-shock quantities.

In order to change the direction of shock propagation, we change the time at which a given boundary cell changes from uniform to “shocked.” Using this procedure, we vary the shock propagation vector over both  $\theta$  and  $\phi$ , which are angles off of the x-z and x-y planes, respectively. In addition to the three on-axis scenarios, we vary  $\theta$  and  $\phi$  over all permutations of the angles 0,  $\pi/8$ ,  $\pi/6$ , and  $\pi/4$ . For each shock propagation direction, we then vary the input Mach number over  $\mathcal{M} = 2, 5, 30, \text{ and } 100$ .

The general result from this study is that our shock-finding algorithm is very accurate. As shown in Figure 3.3, if we make a histogram of the ratio of calculated Mach number to expected Mach number, and normalize it so that the area under the curve is equal to 1, the result is both accurate and precise. In Figure 3.3, we created the histogram by summing over all orientations of the shock of a given Mach number. As one can see, the peak is centered around 1.0, with an average sample standard deviation of less than 0.06. We have examined the average Mach number and standard deviation as a function of angle and have found no discernible trend or bias.

Additionally, due to the manner in which we set up the propagating shock, small inhom-

geneities arise that are likely the cause of much of the calculated scatter. This is because we introduce the shock from the boundary conditions which do not explicitly keep the leading edge of the shock as a perfect discontinuity. Therefore the accuracy of our shock finding algorithm is likely better than that shown in Figure 3.3.

### 3.3.2 Comparison to Ryu et al. [204]

In order to test our analysis against previous work done by Ryu et al. [204], we generated a  $1024^3$  fixed grid simulation with identical cosmological parameters and spatial resolution as their most highly-resolved calculation. This simulation is described in detail in Section 2.4. We expect to see a difference in results from the shock-finding method and from underlying differences in the hydrodynamical solvers. Enzo uses the Piecewise Parabolic Method, which captures shocks across a single zone, whereas Ryu et al. [204] use the total variation diminishing (TVD) method, which spreads shocks over approximately two cells.

In order to study the differences between our shock-finding methods and those of Ryu et al. [204], we mimic the top half of Figure 5 from Ryu et al. [204] in our Figure 3.4. However, in addition to using our new shock-finding algorithm that searches along temperature gradients, we include a coordinate-split analysis that is similar to that of Ryu et al. [204]. As we claimed in Section 2.2, using a coordinate-split approach overpredicts the number of low Mach number and internal shocks. For external, low Mach number shocks, the difference is roughly a factor of 3, which agrees with our hypothesis that the coordinate-split approach identifies cells that are associated with a strong shock to the center of a weak shock. The difference in the internal shocks spans all Mach numbers because the flow to be very complex, making it easy to mistake a normal temperature gradient with that of a shock. We have also studied the integrated kinetic flux through shock surfaces and find it to be in general agreement with Ryu et al. [204]. We will study this in more detail in the future when we include this analysis “on-the-fly.”

While the shock surface area distributions are good indicators of qualitative differences, we now quantify these results. This is done by recreating Table 1 from [204] in our Table 3.2. For this

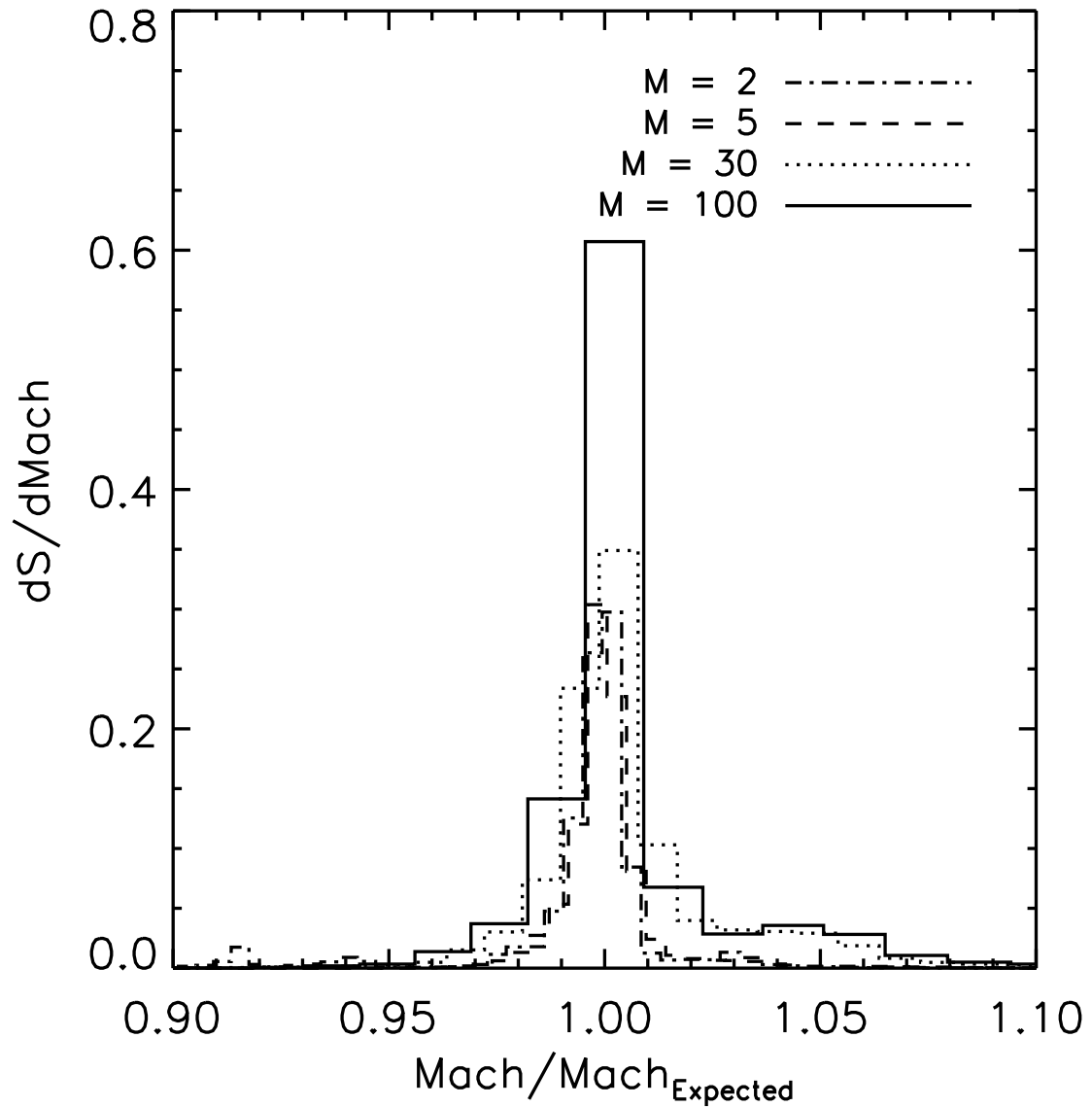


Figure 3.3 Distributions of the ratio of calculated Mach number to expected mach number from off-axis 3D AMR shock tube test problems. Shock surface area,  $S$ , distributions were averaged over all orientations for the each individual Mach number, and normalized so that the area under the curve is 1. Varying lines correspond to Mach numbers of 2 (dash-dotted), 5 (dashed), 30 (dotted), and 100 (solid). Sample standard deviations from 1.0 are all less than 0.06

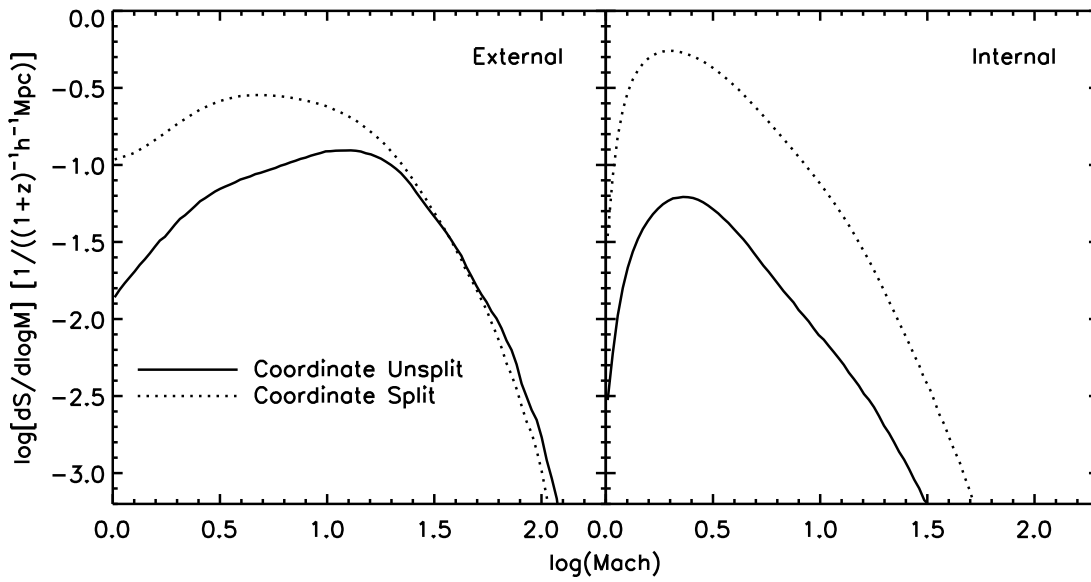


Figure 3.4 Differential shock surface area normalized by the comoving volume of the simulation for external (left) and internal (right) shocks for  $z = 0$  in the ryu1024 simulation. The two methods of shock finding, coordinate split (dotted line) and coordinate unsplit (solid line), are shown. At low Mach numbers for external shocks and for all internal shocks we see a significant overprediction in the number of shocks when using the coordinate split method described in Ryu et al. [204]

portion of the analysis, we mimic the Mach number floor requirement that  $\mathcal{M} > 1.5$ , which was used to reduce the effects of complex flow in the Ryu et al. [204] analysis. First, it is instructive to give a physical motivation for these parameters. The quantity  $1/S$  can be thought of as a mean separation of shocks because it is the simulation volume divided by the total shock surface area. This gives it units of comoving  $Mpc$ . The ratio of external and internal shocks gives the reader an intuition as to where the majority of the shocks are occurring. Note that as the redshift decreases, the relative amount of internal shocks increases, indicative of the increase in shocks within halos and the measured amount of matter in large halos. The average quantities are surface area weighted means of the quantity in question. A subscript of *ext* or *int* denotes that only external or internal shocks were used, respectively. External shocks are those with pre-shock temperatures less than  $10^4 K$  while internal shocks are those with pre-shock temperature greater than  $10^4 K$ .

In comparing our Table 3.2 to Table 1 in Ryu et al. (2003), we find that we predict a higher average Mach number and higher mean comoving distances between shocks for both internal and external shocks. The ratio between our average external Mach number and that found in Ryu et al. ranges between 1.54 and 1.6, while that of the internal Mach number (disregarding  $z = 2.0$ ) ranges between 1.3 and 1.5. We have disregarded  $z = 2.0$  because there is a large amount of merging between  $z = 2.0$  and 1.75, significantly raising the internal temperature of many of the large clusters, increasing the sound speed and decreasing the Mach number. Therefore, we believe that our particular realization of this volume had later mergers than that of Ryu et al. [204].

The differences in the average Mach numbers as well as the increase in mean comoving distance between shocks is almost entirely due to the use of a coordinate split algorithm vs. a coordinate unsplit algorithm. The identification of many more low Mach number shocks increases the frequency, thus decreasing the comoving length between shocks. Therefore for future studies, this difference must be taken into account.

Table 3.2. Mean Shock Quantities

$z$	$1/S$	$S_{ext}/S_{int}$	$\langle M_{ext} \rangle$	$\langle M_{int} \rangle$	$1/S_{ext}$	$1/S_{int}$
0.0	6.235	3.550	12.65	3.767	7.992	28.37
0.25	6.519	4.312	13.02	3.961	8.030	34.63
0.50	6.886	5.196	12.86	4.119	8.211	42.67
0.75	7.301	6.248	12.61	4.225	8.470	52.92
1.0	7.767	7.442	12.26	4.310	8.811	65.57
1.25	8.297	8.743	11.81	4.399	9.246	80.84
1.50	8.884	10.18	11.34	4.412	9.756	99.38
1.75	9.546	11.59	10.89	4.411	10.37	120.2
2.0	10.31	13.04	10.50	7.679	11.10	144.8

Note. — Mean shock quantities.  $z$  is the redshift of the simulation.  $1/S$  is the mean comoving length between shock surfaces in units of  $h^{-1}Mpc$ .  $S_{ext}/S_{int}$  is the ratio of shock surface area for external to internal shocks.  $\langle M_{ext} \rangle$  and  $\langle M_{int} \rangle$  are the surface area-weighted mean of the external and internal shock Mach number, respectively.  $1/S_{ext}$  and  $1/S_{int}$  are the average comoving distance between external and internal shocks, respectively, in  $h^{-1}Mpc$ .

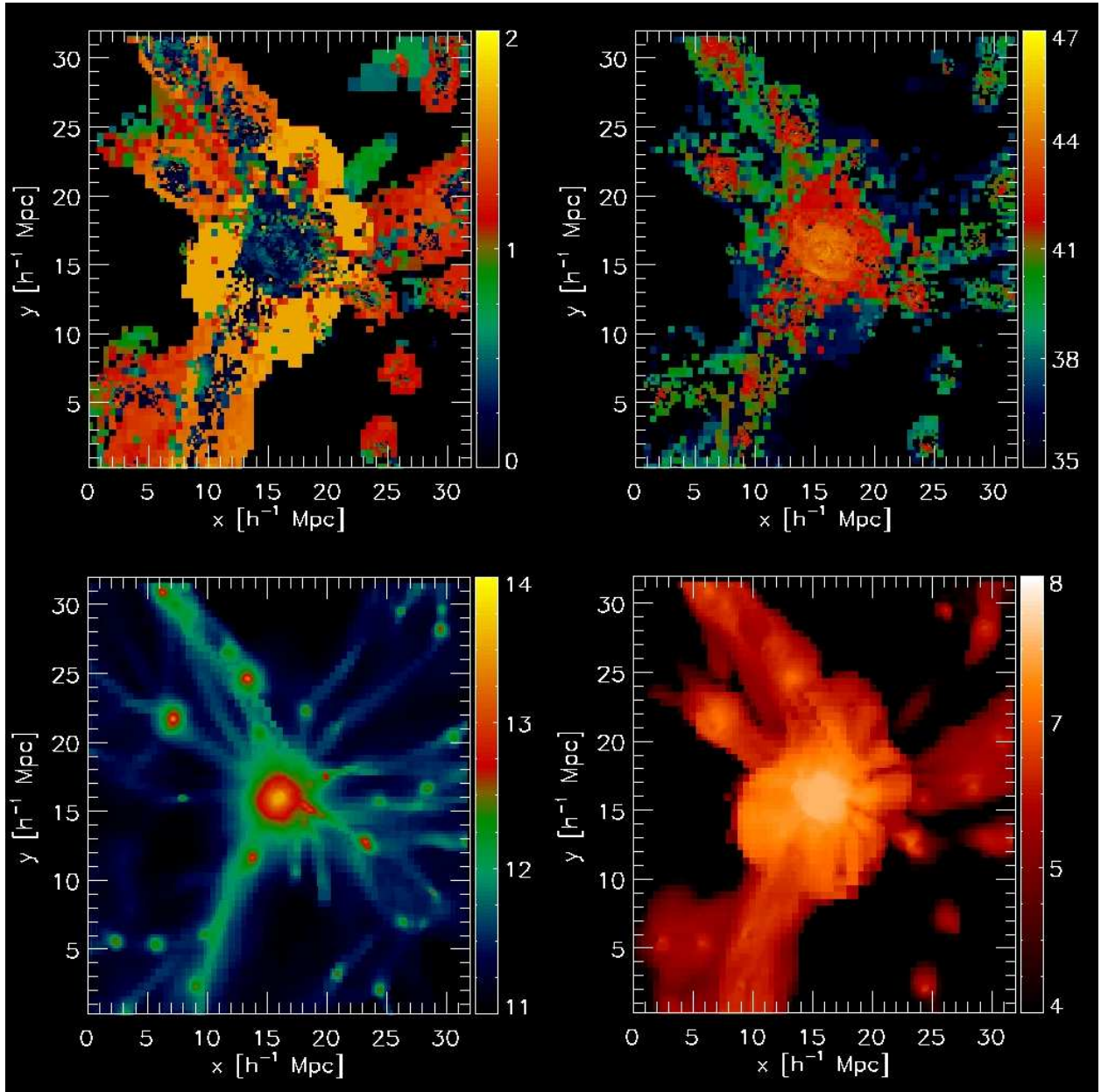


Figure 3.5 Projections of a  $2.8 \times 10^{15} h^{-1} M_{\odot}$  cluster from the “Santa Fe Lightcone.” Mach number (top-left) is weighted by the injected cosmic ray flux. Injected cosmic ray flux (top-right) is in units of  $\text{ergs}/(s h^{-2} \text{Mpc}^{-2})$ . Baryon column density (bottom-left) is in units of  $M_{\odot}/(h^{-2} \text{Mpc}^2)$ . Mass-weighted temperature (bottom-right) is in units of Kelvin. The total size of the projected volume is  $(32 h^{-1} \text{Mpc})^3$ . All panels show logarithmic quantities.

### 3.4 Results for the Santa Fe Light Cone Volume

Now that we have outlined our improved shock finding algorithm, we apply it to a large cosmological simulation encompassing a volume of  $(512 \text{ Mpc}/h)^3$ . This simulation, called the “Santa Fe Light Cone,” was described previously by Hallman et al. (2007). This represents the first time that a large cosmological volume with superb spatial resolution has been studied for its shock and cosmic ray properties. Whereas previous studies were only able to study a small number ( $\sim 10$ ) of clusters due to a small cosmological box [179], we have over 9000 halos with  $M_{halo} > 5 \times 10^{13} M_{\odot}$ , and over 200 with  $M_{halo} > 5 \times 10^{14} M_{\odot}$ . This allows us to perform a statistical study of cosmological shocks unlike any that has been done previously. Both the increase in volume (by a factor of  $\sim 125$ ) and an enhanced spatial resolution over previous unigrid/SPH simulations allow unprecedented detail in our calculations.

We begin by outlining the shock distribution and how it can be thought of as a new way to view large scale structure formation in the Universe. We do this by breaking the distributions down by temperature and density cuts, which further illuminates the underlying dynamics. From there, we apply the DSA cosmic ray acceleration model and determine what phase of gas will contribute most to the acceleration of cosmic rays. Finally, we estimate the global fraction of kinetic energy that is processed through shocks that is devoted to the acceleration of cosmic rays in an effort to determine their possible dynamical effects on gas behavior in galaxy clusters.

#### 3.4.1 Shock Frequencies

As was done in Ryu et al. [204], we calculate the surface area of all shocks in a given logarithmic Mach number interval. However, instead of only classifying shocks as internal or external depending on their preshock temperature, we break the distribution into logarithmic temperature and density cuts that can be postprocessed to examine any subset of the  $\rho$  or  $T$  phase space for the entire computational volume. Primarily, we create several physically motivated temperature and density cuts, which are outlined in Table 3.3. Note that the gas in the  $T < 10^4 K$  heading is



Table 3.3. Temperature-Density Phase Space

Location	Temperature Range	Overdensity Range
Voids	$T < 10^4 K$	$\delta < 1$
Filaments	$10^4 K < T < 10^6 K$	$1 < \delta < 100$
Clusters	$10^6 K < T < 10^8 K$	$100 < \delta < 10^3$
Cluster Cores	$T > 10^8 K$	$\delta > 10^3$

Note. — Approximate ranges for pre-shock temperature  $T$  or pre-shock overdensity  $\delta = \rho_b / \langle \rho_b \rangle$  for general large scale structures.

artificial since we do not include a UV background. This temperature range traces gas that has not been previously shock heated. In addition to studying the physical properties of the preshock region, we study the evolution of the distributions as a function of redshift.

Figure 3.5 shows a projection of the Mach number for the largest cluster in the simulation ( $2.8 \times 10^{15} M_\odot$ ), weighted by cosmic ray acceleration rate. This allows us to see the structure of cosmological shocks. By weighting the projection by cosmic ray acceleration rate, we see both the external high-Mach number shocks and the internal shocks, since the internal shocks' weights are higher. In the other three panels, we show the injected cosmic ray flux, density, and mass-weighted temperature.

#### 3.4.1.1 Density & Temperature Ranges

We now expand the classification of external and internal shocks Ryu et al. [204] by examining the shock Mach number distributions in varying temperature and density ranges. This will provide a more complete description of where these shocks arise in structure formation than in previously published analyses. In Figure 3.6, the shock frequency is plotted for a range of density and temperature cuts. At  $z = 3$ , we see that shock surface area distribution is dominated by shocks with low temperature/low overdensity pre-shock quantities. These represent the accretion shocks

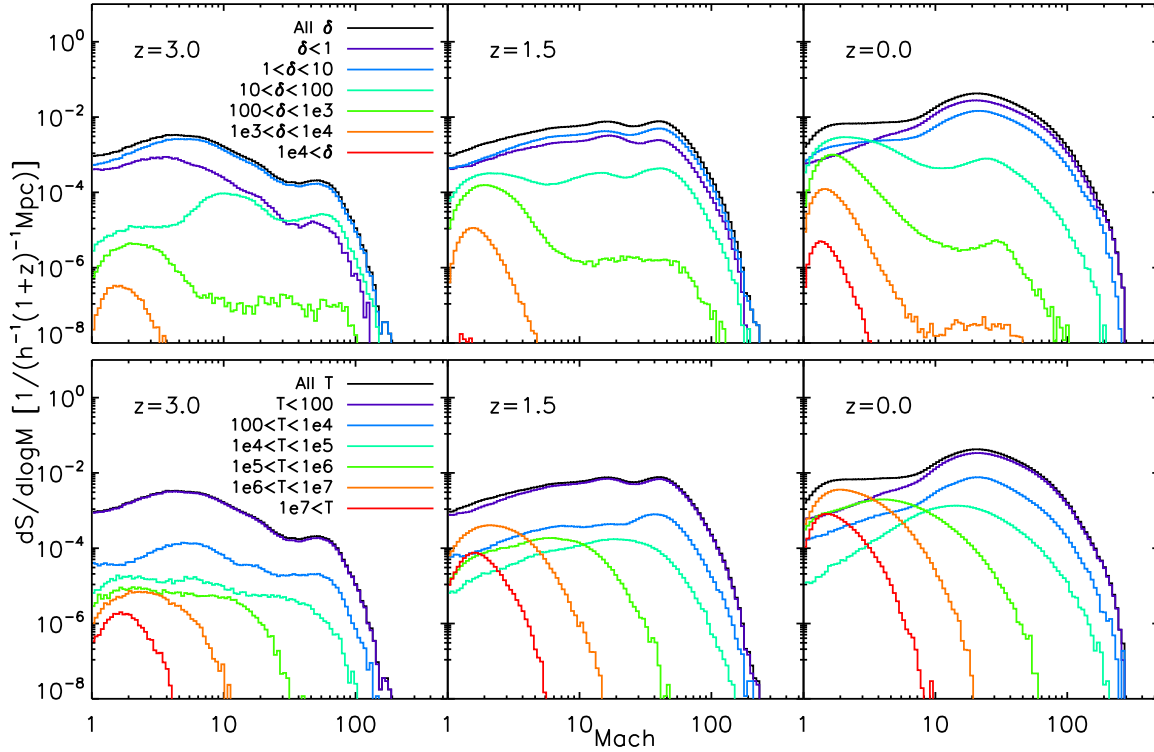


Figure 3.6 Differential shock surface area as a function of logarithmic mach number bins for varying pre-shock gas phases. Pre-shock gas overdensity (top) is divided into several ranges that differentiate the overall distribution. Pre-shock gas temperature (bottom) differentiates the different types of shocks (i.e. accretion, merger). Both distributions are shown for three redshifts:  $z = 3$  (left),  $z = 1.5$  (middle) and  $z = 0$  (right).

onto filaments and proto-clusters. As the simulation evolves, the distribution becomes bimodal with components from both low pre-shock temperature, high-Mach number accretion shocks and high-temperature, low-Mach number merger shocks.

The temperature cuts each have a characteristic Mach number cutoff that increases with decreasing temperature. This cutoff is due to the maximum temperature jump that is possible with a given pre-shock temperature. Therefore, since the maximum temperature in the simulation is  $\sim 10^8 K$  (determined by the mass of the largest cluster), a temperature jump from  $10^6 K$  will result in a  $\mathcal{M} \approx 18$ , very close to the cutoff seen at  $z = 0$  for  $10^6 K < T < 10^7 K$ . Similarly, the cutoffs for lower pre-shock temperatures indicate the largest temperature jumps for each population. At higher redshifts, these temperature cutoffs decrease due to the lower maximum temperatures present in the simulation. Therefore, the movement of these cutoffs tell us about the temperature evolution of the simulation.

Additionally, the Mach number associated with the peaks in the shock frequency distribution can be used to determine the mathematical mode of the post-shock temperature distribution. For  $z = 0$ , these peaks correspond to post-shock regions with  $T_2 \sim \text{few} \times 10^6 K$  for pre-shock temperatures  $T_1 < 10^6 K$ . Therefore the majority of these shocks are heating the pre-shock gas to WHIM temperatures in filaments. For  $T_1 > 10^6 K$ , the peak Mach numbers correspond to post-shock temperatures of  $T_2 \approx 2 \times 10^7 - 1.5 \times 10^8 K$ . These are complex flow and subhalo merger shocks in the interior regions of clusters.

If we instead examine the varying density cuts, similar results are observed. At high redshifts, we see that the dominating accretion shocks (high Mach number shocks) have pre-shock overdensities of  $\delta \sim 1 - 10$ . This is because of the relative paucity of large-scale halos and filaments and, thus, relatively shallow gravitational potential wells. The infalling gas will get much closer to the accretor and therefore denser before shocking. As we move to lower redshift, the  $\delta < 1$  shocks begin to dominate because we are shocking further out into the voids.

For the interior cluster shocks, there are three regimes that present themselves in the analysis. If we examine  $z = 3$  with  $10 < \delta < 100$ , there are plateaus near  $\mathcal{M} \approx 2 - 4$  and  $\mathcal{M} \approx 10 - 70$ . It is

difficult to determine what the post-shock density will be because of the insensitivity of the density contrast at high Mach numbers ( $\rho_2/\rho_1 \rightarrow 4$  for  $\mathcal{M} \gg 3$ ). However, it is likely that the two high Mach number shock plateaus correspond to filaments for  $\mathcal{M} \approx 10$  and clusters at the virial radius for  $\mathcal{M} \approx 70$ . The low Mach number shocks are most likely interior flow shocks.

At late times, all of the intermediate pre-shock density regions have bimodal distributions. The high Mach peak corresponds to density contrasts of 4, while the low  $\mathcal{M}$  corresponds to jumps of  $\sim 2$ . Therefore, we are likely looking at merger and complex flow shocks, respectively.

### 3.4.1.2 Redshift Evolution of Shock Properties

There are three primary populations of shocks that we see evolve through time, as seen in Figure 3.7. There are accretion shocks onto clusters, accretion shocks onto filaments, and merger and complex flow shocks within clusters and filaments. These are outlined by the blue, green, and red shadings in Figure 3.7, and their qualitative behavior can give useful insights as to the evolution of large scale structure. Let us analyze each of these populations separately. To determine the origin of these populations, we have examined slices and projections of the data and compared the Mach number of the cell to its location with respect to large scale structure.

First, at early times we see a small peak at very high Mach numbers that denotes shocks onto collapsing halos. This corresponds to gas that has previously been untouched by shocks falling directly onto the proto-cluster gas, with temperature jumps from hundreds of Kelvin to  $10^6 K$  (Note the Mach numbers are still calculated with a temperature floor of  $10^4 K$ ). We see that as the universe evolves, the strongest shocks in the simulation become stronger. This is due to the mass of the clusters increasing with time, providing a larger gravitational force pulling the material onto the halo. We also see that this peak increases in shock frequency while slowly moving to slightly lower Mach numbers. Because the mass function cuts off exponentially at high mass, the number of small halos heavily outweighs the large halos. These smaller halos have lower free-fall speeds at the radius of the accretion shock, leading to a smaller Mach number. Therefore the large number of weaker shocks dominate the net surface area distribution.

Second, the shocks onto filaments begin at Mach numbers of  $\mathcal{M} \sim 6$  and move towards  $\mathcal{M} \sim 20$  at late times. The surface area of these shocks are much larger at early times because the surface area of a cylinder per unit volume is larger than that of a sphere as well as an increased number of filaments with respect to halos (there are several filaments that feed into a single halo). The strength of these shocks grow with the increase in size of the filaments.

Finally, the low Mach number shocks ( $\mathcal{M} < 3$ ) due to halo mergers and complex flow are nearly non-existent at high redshifts. However, as large halos collapse and start to merge, the shock surface area also increases. Therefore this evolution traces the strength and frequency of merger shocks.

### 3.4.2 Cosmic Ray Energy Injection

The thermal history of the large scale structure in the Universe is primarily determined by the conversion of gravitational potential energy into kinetic energy, which is subsequently converted to heating gas and the acceleration of cosmic rays. Here we present results of our application of the cosmic ray acceleration model described in Section 2.3 to the “Santa Fe Light Cone.”

#### 3.4.2.1 Function of Redshift

The first result is that, as in previous studies [e.g 204, 179, 125], the most important Mach number shocks in terms of cosmic ray acceleration are at  $\mathcal{M} \approx 2 - 4$ . This may seem surprising given that the surface area of shocks is dominated by high Mach shocks. However, the amount of energy dissipation is the product of the mass flux through the shocks and the Mach number. The large accretion shocks at early times ( $z < 3$ ) have already consumed a large fraction of the gas in voids. This leaves very little mass at low densities to be processed by the most massive halos. This is in contrast to the low Mach complex flow shocks within the clusters. These process very large amounts of mass and kinetic energy, and therefore experience very high thermalization and acceleration of cosmic rays even with lower efficiency. Cosmic rays from these low Mach number shocks will, however, have a steep energy spectrum and dissipate their energy relatively quickly

compared to strong accretion shocks [e.g. 158].

Figure 3.8 shows a distribution function of the kinetic energy processed through shocks per comoving  $(Mpc/h)^3$  as a function of redshift where the height of the distribution function gives the differential amount of kinetic energy processed by shock for a given Mach number bin. As the simulation evolves to  $z = 0.5$ , there is a monotonic increase in the average kinetic energy density processed. Both the low-Mach complex flow and high-Mach accretion shocks increase by factors of 10 – 100. This monotonic increase stops at  $z \sim 0.5$  because of the dominance of dark energy in a  $\Lambda$ CDM universe at this epoch, resulting in a decreased merger of, and accretion onto, the highest-mass halos. Therefore, the number of accretion shocks characterized by high Mach numbers will decrease. Compounding this effect is the slow evacuation of the voids and the lack of additional mass to accrete.

By applying the diffusive shock acceleration model, we can estimate how much of this energy is put into gas thermalization versus the acceleration of cosmic rays within the confines of the model. This acts as a first estimate of the energy injection into cosmic rays, and should not be taken as the final word on the subject. Cosmic ray injection is a highly non-linear process that is not fully understood. Further work on this model is needed.

Figure 3.9 shows the relative amounts of energy dissipated for the two different models involving either no pre-existing cosmic rays or an initial amount of cosmic rays such that  $P_{CR}/P_g \approx 0.3$ . As one can see, the relative amount of cosmic ray acceleration vs. thermalization heavily depends on the assumed inputs of the underlying DSA model. Until we are able to track the cosmic ray pressure within our simulations, we are resigned to give these rough limits of cosmic ray acceleration.

### 3.4.2.2 Variation of Cosmic Ray Injection Efficiencies With Gas Properties

Separation of distribution functions showing thermalization as a function of both temperature and density provides valuable insight into the physical processes occurring in the simulation. In Figure 3.10, we see that there are two primary modes of kinetic energy flux at  $z = 3$ . For  $\mathcal{M} < 2$ ,

the thermalization is dominated by shocks at  $100 \lesssim \delta \lesssim 10^4$  and  $T \gtrsim 10^6 K$ . These shocks are likely within the largest filaments and the first clusters. At higher Mach numbers,  $\mathcal{M} > 6 - 7$ , the thermalization is dominated by gas at  $T < 10^6 K$  and  $\delta \sim 10 - 100$ . This points towards accretion shocks onto filaments and the heating of the WHIM. If we use the peaks in each temperature cut up to  $T \sim 10^6 K$  to estimate the Mach number, we can calculate the post-shock temperature for these shocks to be  $1 - 3 \times 10^6 K$ . This reinforces the thought that these shocks are heating the WHIM. Shocks in this range of Mach numbers are also seen in Figure 3.5 as surrounding the filaments.

At later times, the entire distribution shifts to higher thermalization rates due to the collapse of structures. Low Mach numbers are again dominated by complex flows within clusters. By examining the shocks with pre-shock temperature of less than  $10^5 K$  as well as the redshift evolution from Figure 3.8, we are able to verify that the high Mach number accretion shocks are becoming less important due to the separation of the voids from the clusters after  $z \approx 0.5$ . In the overdensity cut that corresponds to  $1 < \delta < 10$ , we see a shift from a peak at high Mach numbers to small Mach numbers as the relative importance of accretion and mergers switch.

If we compare our results to those of Pfrommer et al. [179], we see a good agreement at low Mach numbers. Pfrommer et al. [179] found shocks as strong as  $\mathcal{M} \sim 10^3$ . However, we never see shocks above  $\mathcal{M} \approx 200$ . This is likely due to the lack of a temperature floor in their simulation, which thus allows a higher numerical value for the Mach number. These shocks are likely not realized in the real universe due to the presence of a ubiquitous ionizing radiation background that will keep gas above  $10^4 K$ .

Finally, we can compare our results to recent work by Kang et al. (2007), who used a unigrid calculation similar to that of Ryu et al. [204], but included radiative processes, star formation, and a relaxed minimum temperature floor. Again, this relaxation of the temperature floor to (in their case) the CMB temperature resulted in very high Mach numbers – up to  $\mathcal{M} > 10^4$ . This corresponds to a temperature jump by a factor of  $\sim 3 \times 10^7$ , a jump from  $3K$  to  $10^8 K$  (the minimum and maximum temperatures in the simulation). At low Mach numbers, our results are very similar to those of Kang and Jones [121].

### 3.5 Effect of Mass and Spatial Resolution on Cosmic Ray Acceleration Efficiency

In order to quantify the robustness of our simulations with respect to mass and spatial resolution, we perform a series of simulations where the mass and spatial resolution of a single galaxy cluster are varied over a wide range of parameter space. Two parameters are varied in this study. The first is the maximum level of refinement, which affects the spatial resolution and, ultimately, the accuracy of the hydrodynamic solver. The second parameter is the dark matter particle mass resolution, which affects the accuracy with which the gravitational potential is calculated.

#### 3.5.1 Spatial Resolution

Our maximum spatial resolution ranges from  $62.4 \text{ kpc}/h$  to  $3.9 \text{ kpc}/h$  (see Table 3.1). Since this only limits the maximum resolution, one expects to see a strong dependence on this parameter only at high densities. Figure 3.11 shows the dependence of shock surface area on level refinement for three overdensities. For shocks with pre-shock overdensities less than  $\sim 100$ , the main difference in the multiple resolutions is at low Mach numbers (below  $M \sim 2$ ) and only appears in the lowest resolution simulation.

At overdensities above  $10^3$ , we not only see that the low Mach number complex flow shocks are lost at low resolution, but also a drop in the number of high Mach number shocks. At this density and spatial refinement, it is thought that the absence of sufficient spatial resolution leads to the artificial smoothing of the gas, creating an inability to capture shocks. The main result of this spatial resolution study is that a resolution between  $3.9 \text{ kpc}/h$  and  $15.6 \text{ kpc}/h$  should be sufficient in all but the most dense regions of the simulations. Therefore, our “Santa Fe Light Cone” simulation presented in Section 3 had an adequate peak resolution of  $7.8 \text{ kpc}/h$ .

To examine the effect of spatial resolution on cosmic ray acceleration, we study the kinetic energy flux through shocks as a function of spatial resolution. Figure 3.12 shows a distribution function measuring the thermal dissipation rate as a function of Mach number with varying spatial



resolution. This study is performed with the maximum mass resolution,  $M_{dm} = 9.7 \times 10^8 M_{\odot}$ . At low overdensities ( $\delta < 100$ ), the effect of spatial resolution is very small. At moderate to high overdensities ( $100 < \delta < 10^4$ ), there are differences on the order of a factor of 2 that are likely due to the smoothing of high density gas as the resolution is decreased. The primary difference in the dissipation rates occur for low Mach numbers when we do not have sufficient spatial resolution to resolve all of the complex flow shocks. There are also large differences at  $\mathcal{M} \geq 10$  for the lowest resolution simulation. However, the difference between 3.9 *kpc/h* and 15.6 *kpc/h* is negligible.

At very high overdensities ( $\delta > 10^4$ ), there is a very large difference between the varying spatial resolutions. One reason is that if a cell has an overdensity of  $10^4$ , the grid would normally be on the 5th level of refinement. With a maximum refinement level of 4 for the poorest resolution simulation, any gas at this overdensity would be very poorly resolved. The difference between the 15.6 *kpc/h* and 3.9 *kpc/h* resolution simulations is likely small number statistics for the former simulation. The 3.9 *kpc/h* resolution simulation will resolve these high densities with roughly 64 times more cells compared to the 15.6 *kpc/h* simulation.

### 3.5.2 Mass Resolution

The mass resolution of each simulation is set by the resolution of the root grid (or highest-level static nested grid). The size of each root cell determines the amount of mass given to each dark matter particle. Therefore, if the root grid doubles in resolution, the mass resolution increases by a factor of  $2^3$ . In principle, there should be two effects of increased mass resolution. First, one would expect that since we are extending our mass function to a lower limit, the number of subhalos and our resolution of complex fluid flow should increase. This should manifest itself in an increase of shocks in the low Mach number regime. Second, the increased mass resolution also corresponds to an increase in the static grid spatial resolution. This may affect the calculated surface area of shocks that reside in voids. Since the temperature jumps in the voids are likely to be much higher than those within clusters, we would expect this effect to show up in the high Mach number regime.

In order to test these hypotheses, we varied the mass resolution from  $6.2 \times 10^{10} M_{\odot}/h$  to

$9.7 \times 10^8 M_\odot/h$ . The results of this study are shown in Figure 3.13. At  $\delta < 100$ , we see that as the mass resolution increases, the number of low Mach number shocks increase, while the high Mach number shocks decrease. At high densities, the situation is more complicated. For  $\mathcal{M} < 2$ , the surface area likely increases because of the increase in the number of subhalos and complex flow. For  $M > 7 - 8$ , the differences seem to be largely due to statistical uncertainties. For  $\delta > 10^4$ , the disparity at  $\mathcal{M} < 2$  is again likely due to the number of subhalos and their effects on turbulence. At  $2 < M < 5$ , there is a large difference between the highest mass resolution simulation and the other two. Because we believe these shocks are merger shocks, it may be because there are just too few dense subhalos that merge with large halos to create this surface area.

As with the spatial resolution, we now study the effects of mass resolution on the thermal dissipation rates at shock fronts. Figure 3.14 shows the effect of varied mass resolutions with a fixed spatial resolution of  $3.9 \text{ kpc}/h$ . Again, we break the analysis down into overdensity regimes. Low overdensity, high Mach number shocks exhibit a strong dependence on the mass resolution. This is because of the ability to better resolve shocks in the voids and low density filaments. The disparity in high overdensity ( $100 < \delta < 10^4$ ), low Mach number shocks is less apparent, but also suggests that the mass resolution of the simulation has an effect on the thermal dissipation of gas through shocks. At  $\delta > 10^4$ , we again see the effect of a decreased number of subhalos available to merge.

Contrary to the effects of spatial resolution, the biggest differences due to mass resolution appear in the high Mach number regime. This is again due to the overestimate of Mach number at low root grid resolution. One evident result is that while the spatial resolution seems to be fairly well converged, it is not clear that the mass resolution has converged. Therefore, we can only claim a fairly weak precision in the thermal dissipation and cosmic ray acceleration rates for the current simulations.

There are several key results to this resolution study. We appear to have converged in terms of maximum spatial resolution in all but the densest cluster gas. However, our convergence upon the various quantities with respect to dark matter mass resolution is not clear. The differences in the

cosmic ray acceleration rate are not larger than the underlying uncertainty in the results of diffusive shock acceleration simulations, suggesting that both mass resolution and our understanding of the physical mechanisms of cosmic ray acceleration must be improved in the future.

### 3.6 Discussion

There are several topics that warrant discussion with respect to the results that we have presented thus far. These include the variation of results with respect to  $\sigma_8$ , the inclusion of non-adiabatic physics, the limitation of the diffusive shock acceleration model, and the implications of the mass resolution in the “Santa Fe Light Cone” Simulation.

If our goal is to do large statistical studies of galaxy clusters, changing the value of  $\sigma_8$  will have significant effects. First, a higher  $\sigma_8$  will greatly increase the number of massive clusters in a given volume. By comparing the *ryu1024* simulation with the “Santa Fe Light Cone,” with values of  $\sigma_8$  of 0.8 and 0.9, respectively, we see that this increases the frequency and strength of the high Mach number shocks. Additionally, this should increase the amount of kinetic energy that is processed by shocks since mergers will be more frequent.

In all of our simulations thus far we have only used adiabatic physics. Previous studies, such as those done by Kang et al. [125], have found that when including radiative cooling and star formation that the shock properties are still governed primarily by gravitational physics and that additional physics have little effect on overall distributions at scales larger than  $\sim 100h^{-1}kpc$ . However, Pfrommer et al. [180] found that at smaller scales, on the inside of clusters, the cosmic ray contribution to the overall pressure is greatly increased with the inclusion of radiative cooling. Additionally, we currently adopt a temperature floor of  $10^4K$  because of the lack of an ionizing background. This should instead be done in a self-consistent manner.

While we are using results of recent diffusive shock acceleration simulations by Kang and Jones [121], there are assumptions and limitations that may have an effect on our results. We assume that the magnetic field is parallel to the shock normal, which yields the largest efficiency for accelerating cosmic rays. Any deviation from this will likely cause decreases in the overall

efficiency of the shocks as particle accelerators. Additionally, for low Mach numbers, knowledge of the pre-shock composition is very important and can lead to orders of magnitude differences in the acceleration efficiency. Therefore, being able to track the cosmic ray pressure in “on-the-fly” calculations will allow us to provide a more self-consistent estimate. Finally, we are assuming that the only method for cosmic ray production is through first-order Fermi acceleration, and therefore we ignore other potential sources of cosmic rays, such as second-order acceleration by turbulence, galaxies, and AGN.

The results of the resolution study provided in Section 4 have suggested that we have not yet seen a convergence with respect to the dark matter particle mass in the “Santa Fe Light Cone” simulation. This likely results in an under-prediction in the number of merging subhalos and the kinetic energy flux associated with them.

### 3.7 Conclusions & Future Directions

Our study of cosmological shocks has resulted in several advances in both scientific understanding and numerical algorithms. We now summarize the key findings:

- We have developed a novel numerical scheme that is capable of detecting and accurately characterizing the Mach number of shocks in an adaptive mesh refinement simulation. This method has relaxed the previous restriction of using a coordinated axis-based approach and now allows us to accurately characterize shocks that have any orientation with respect to the coordinate grid.
- Using our new shock-finding technique on a unigrid cosmological simulation that is identical to the highest-resolution calculation in Ryu et al. [204], we have shown that previous methods resulted in an overestimate of the number of low Mach number shocks by a factor of  $\sim 3$  due to confusion of the direction of shock propagation, and that this underestimate is consistent with using shock-finding algorithms that only sweep along coordinate axes.
- We have analyzed the largest AMR cosmological simulation to date that includes adiabatic

gas physics, the “Santa Fe Light Cone.” This simulation has an effective spatial dynamic range of 65,536 and resolves both large scale structure and small-scale features within galaxy clusters. Whereas previous studies were able to study on the order of 10 high mass clusters, we have thousands within a single simulation volume. Our study of this simulation has led to a new technique for conceptualizing structure formation because we are able to analyze the evolution of three different populations of shocks: cluster accretion, filament accretion, and internal merger and complex flow shocks.

- By applying the results of 1-D Diffusive Shock Acceleration models, we calculate the amount of kinetic energy at shock fronts that is used to accelerate cosmic rays, and find it to be in agreement with previous studies. These cosmic rays will make up a significant fraction of the total pressure in the intracluster medium and therefore their dynamical effects need to be studied.
- We have performed a resolution study that varies both the dark matter particle mass and peak spatial resolution. From the results of this study, we believe that the spatial refinement in the “Santa Fe Light Cone” simulation is adequate. The state of mass resolution convergence is less clear, suggesting that for future studies we should focus on higher mass resolution.

While our numerical technique of characterizing shocks has been proven to be robust, our results are still somewhat limited by the physics. We have not yet included potentially important effects such as radiative cooling, star formation and feedback, AGN heating, or a photoionizing UV background. These physics will be included in future work. Second, our results are based upon a post-processing of the simulation output. Ideally, the shocks would be identified in an “on-the-fly” manner during simulation runtime. Additionally, the cosmic ray acceleration would be traced in a self-consistent manner that allowed for a back-reaction on the gas. Attempts at tracing the cosmic ray pressure have been made by Pfrommer et al. [179, 180] using an SPH code, and we will be working towards the same goal in the near future within *Enzo*. Finally, the acceleration of cosmic

rays is still dependent on the underlying magnetic field strength and orientation. Cosmological MHD has been implemented within *Enzo*, and in the near future we will include magnetic fields and their coupling to cosmic rays within a cosmological AMR volume.

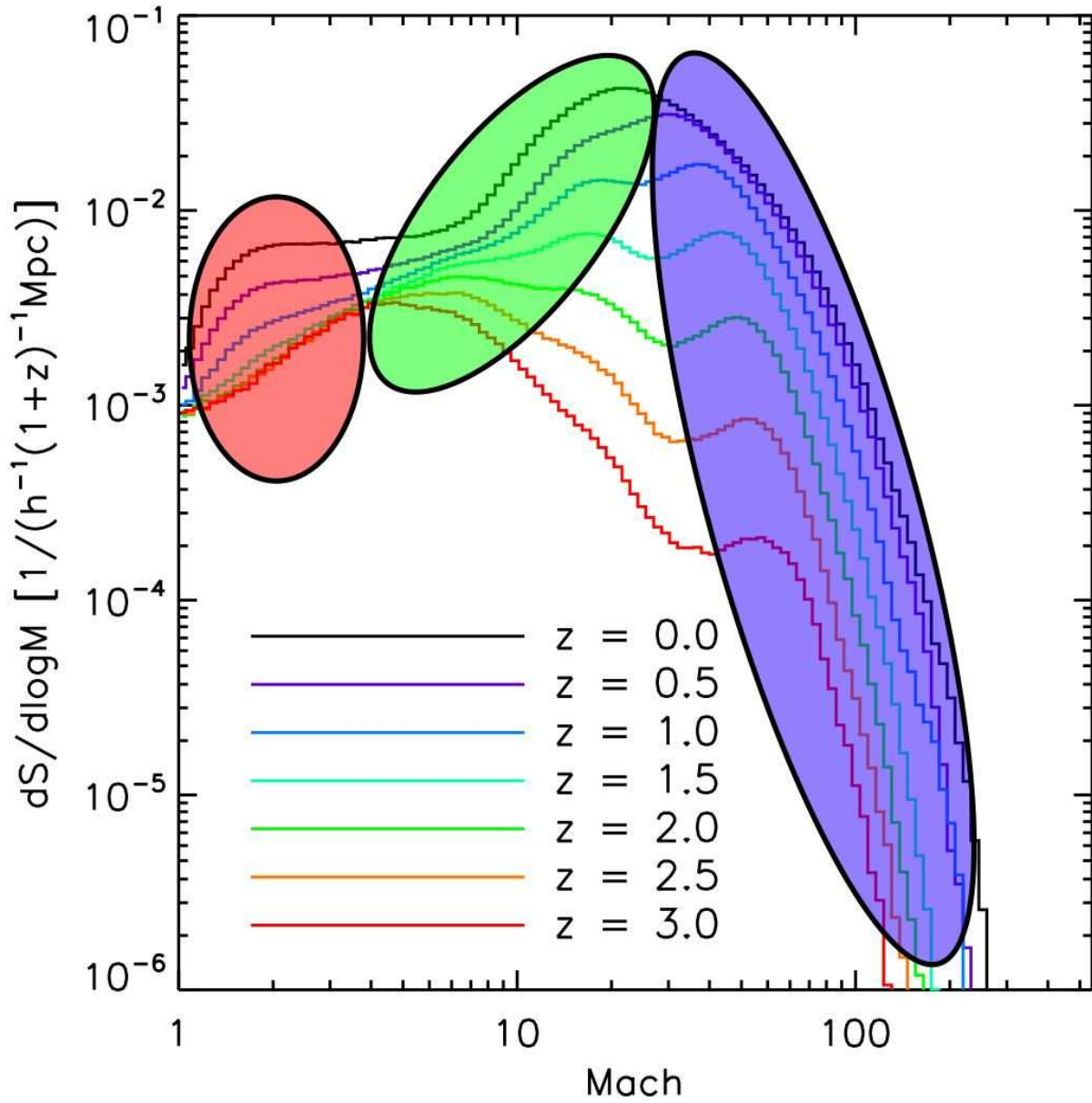


Figure 3.7 Comoving shock surface area normalized by the simulation volume as a function of Mach number with varying redshifts. Three regions are suggested corresponding to internal cluster merger shocks (red), accretion shocks onto filaments (green), and accretion shocks onto clusters (blue).

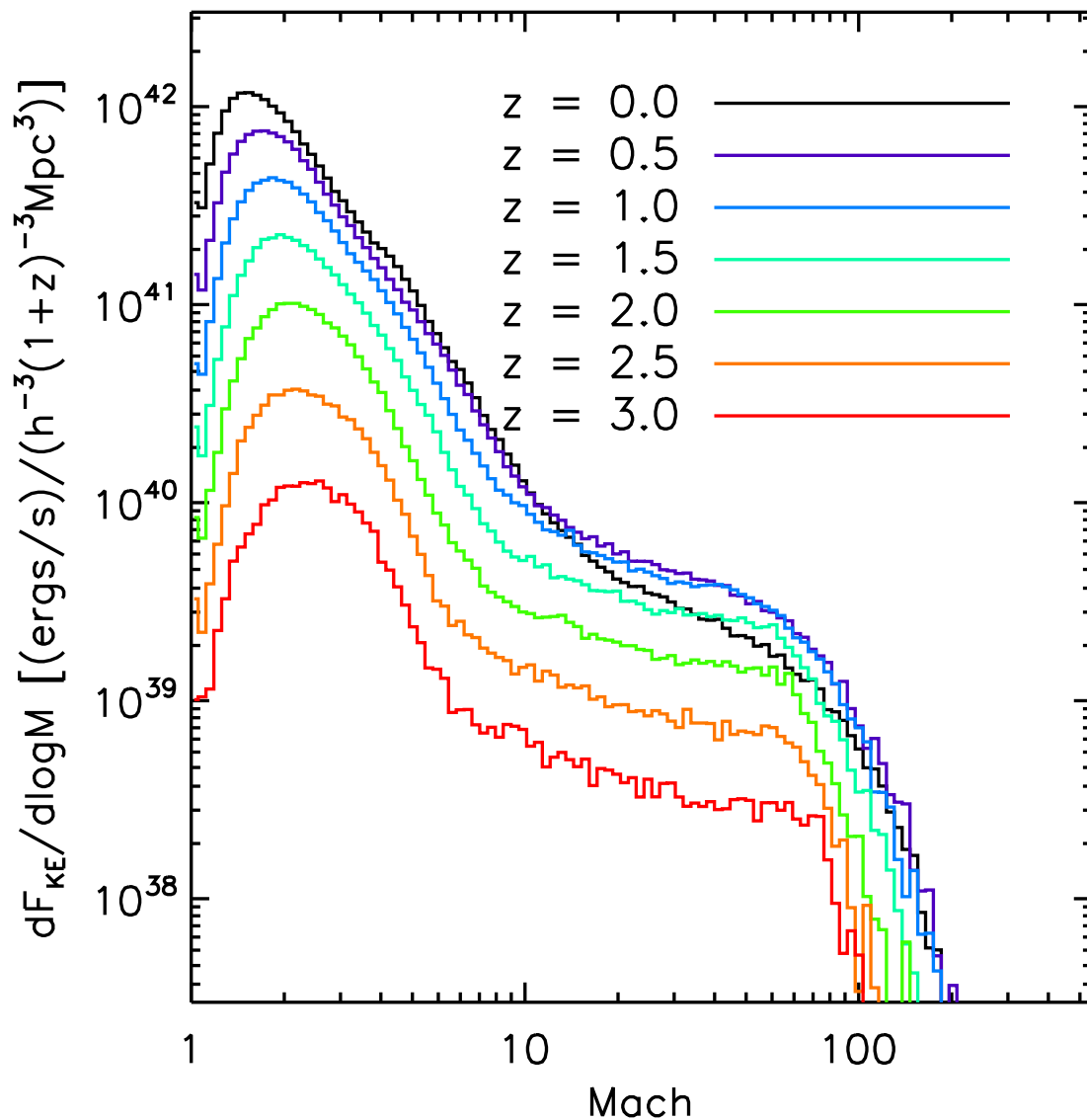


Figure 3.8 Redshift evolution of the amount of kinetic energy processed by shocks as a function of Mach number. Redshift decreases from  $z = 3$  (red) to  $z = 0$  (black). The decrease in flux at late times for  $\mathcal{M} > 10$  signals the epoch at which dark energy becomes dominant.



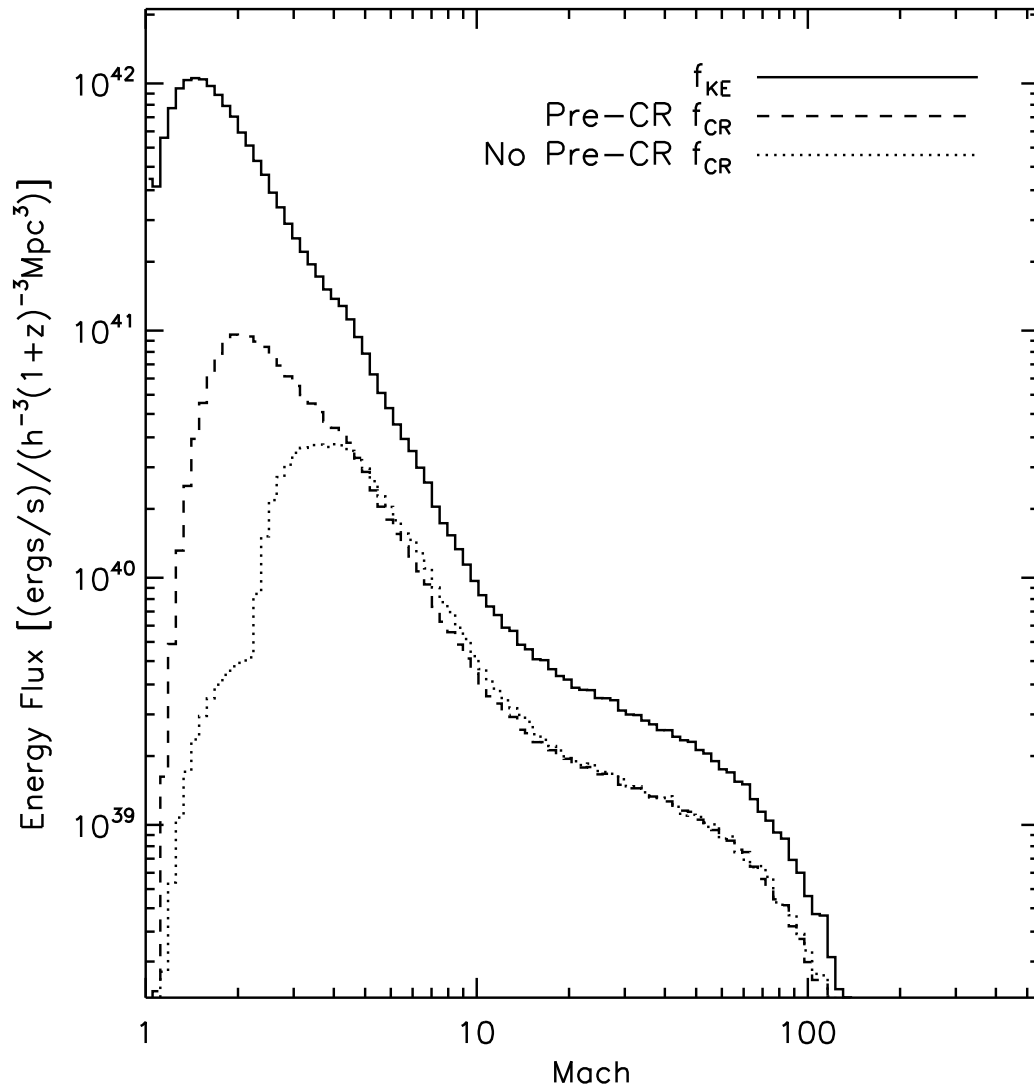


Figure 3.9 Out of the incoming total kinetic energy of the shocks (solid line), the relative amount of energy devoted to the acceleration of cosmic rays for both models with (dashed line) and without (dotted line) a pre-existing CR population, as predicted by the Kang and Jones [121] diffusive shock acceleration model.

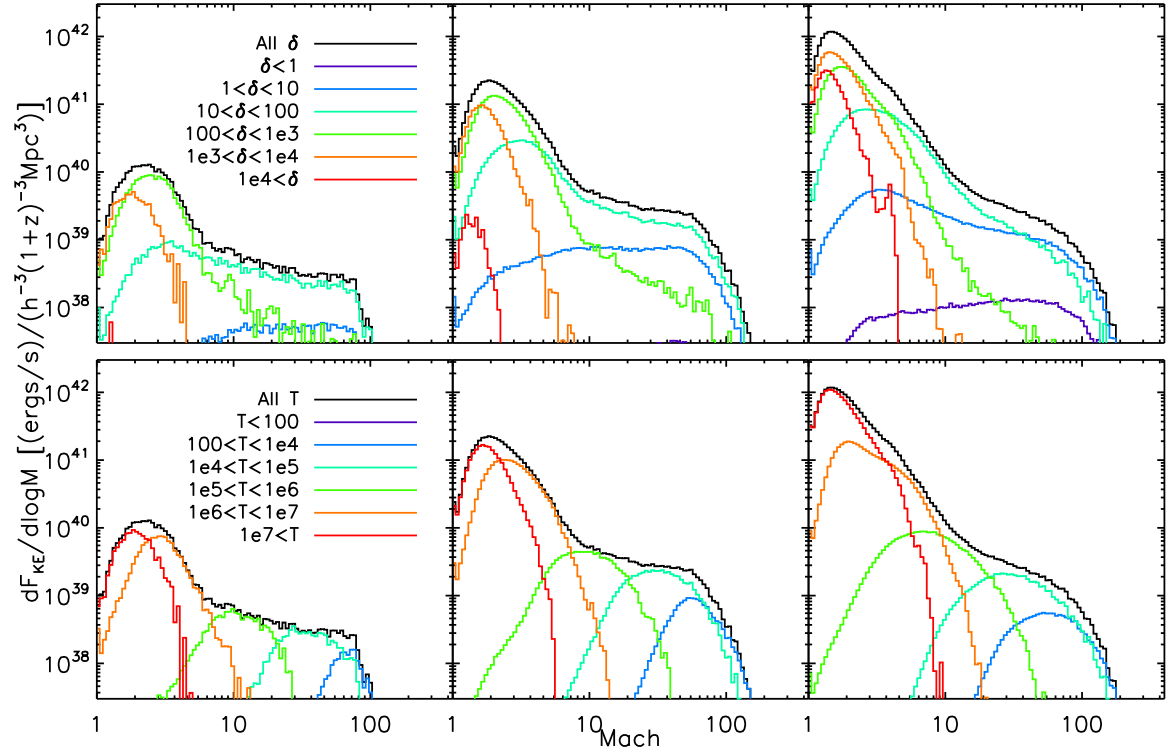


Figure 3.10 Differential kinetic energy flux processed by shocks as a function of Mach number and pre-shock gas phase. Pre-shock gas overdensity (top row) is divided into several ranges that differentiate the overall distribution. Each pre-shock temperature range (bottom row) roughly corresponds to a particular mach number. Both distributions are shown for three redshifts of  $z = 3$  (left column),  $z = 1.5$  (middle column) and  $z = 0$  (right column).

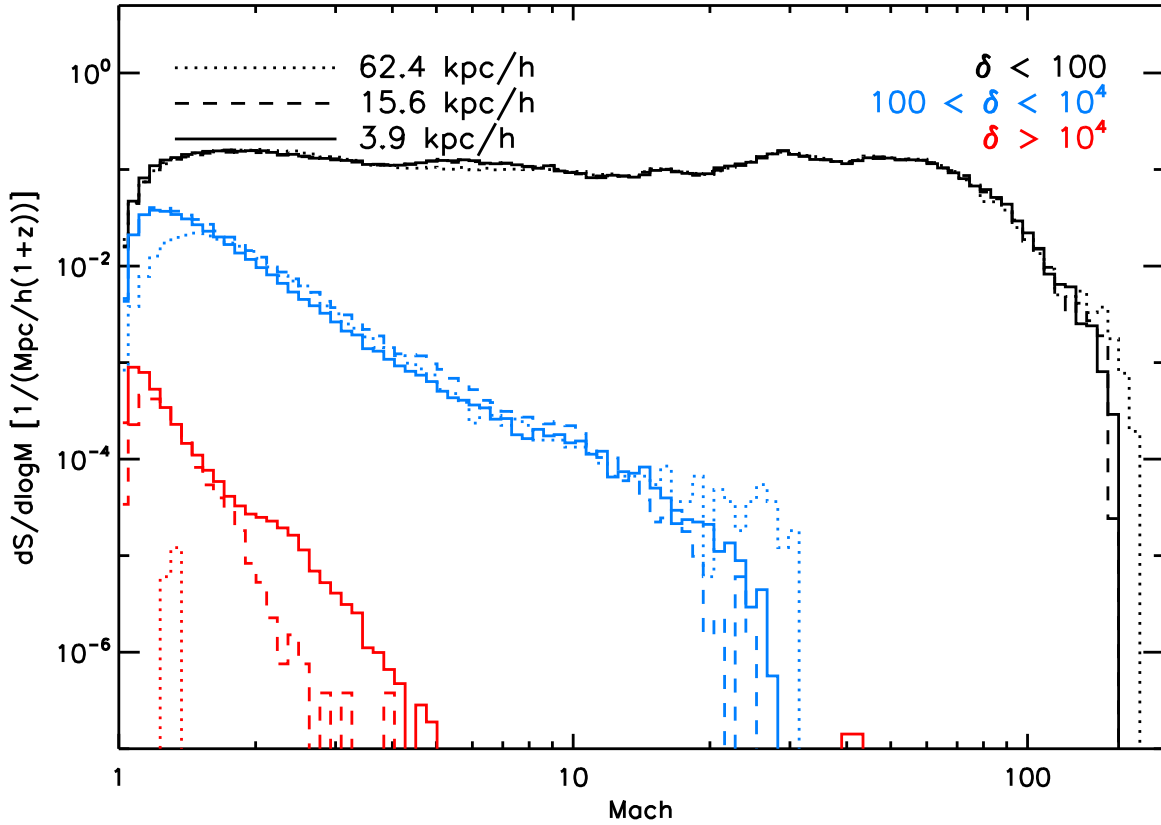


Figure 3.11 The effects of spatial resolution in different density regimes. Here we keep the mass resolution at the highest level ( $M_{dm} = 9.7 \times 10^8 M_{\odot}$ ). The distribution function of shock Mach numbers in a  $(32 \text{ Mpc}/h)^3$  volume around a cluster weighted by surface area for three overdensity cuts is plotted against Mach number. Three cuts in overdensity are shown for  $\delta < 100$  (black lines),  $100 < \delta < 10^4$  (blue lines),  $\delta > 10^4$  (red lines). Varying spatial resolution are shown with dotted (62.4  $\text{kpc}/h$ ), dashed (15.6  $\text{kpc}/h$ ), and solid (3.9  $\text{kpc}/h$ ) linestyles.

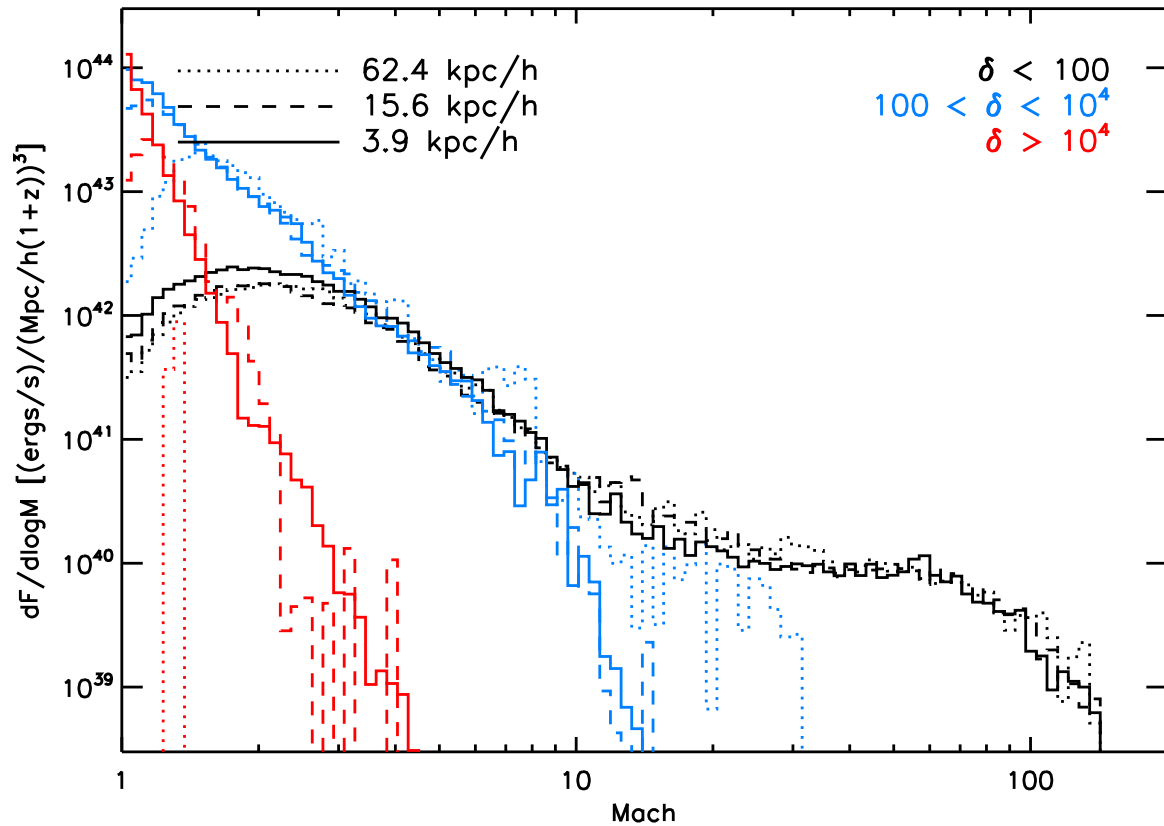


Figure 3.12 Spatial resolution effects on kinetic energy flux for several density regimes. The kinetic energy flux is plotted against Mach number for varying spatial resolution denoted by linestyle. The shocks are grouped as external (black lines), clusters/filaments (blue lines), and rich clusters (red lines).

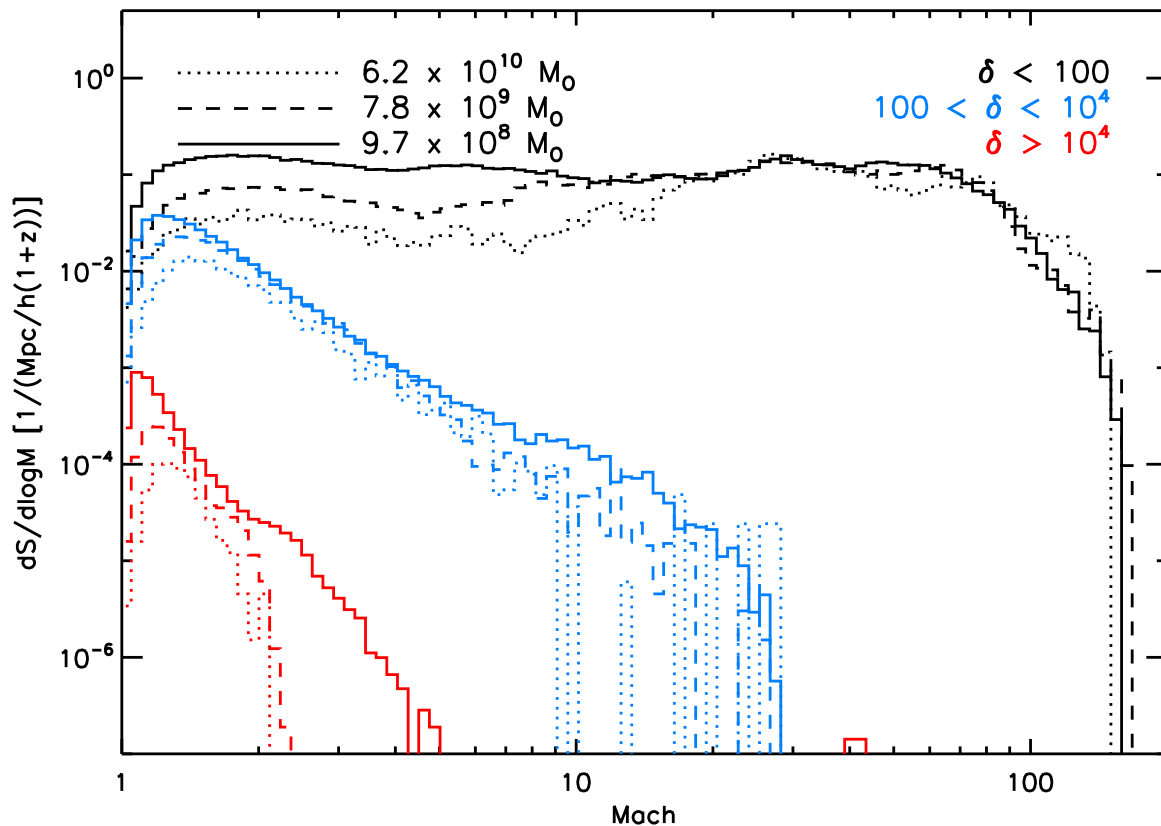


Figure 3.13 The effects of mass resolution in different density regimes. Here we keep the spatial resolution at the highest level of  $3.9kpc/h$ . Mass resolutions are shown by linestyles of dotted ( $6.2 \times 10^{10} M_{\odot}$ ), dashed ( $7.8 \times 10^9 M_{\odot}$ ), and solid ( $9.7 \times 10^8 M_{\odot}$ ). The shocks are grouped as external (black lines), clusters/filaments (blue lines), and rich clusters (red lines).

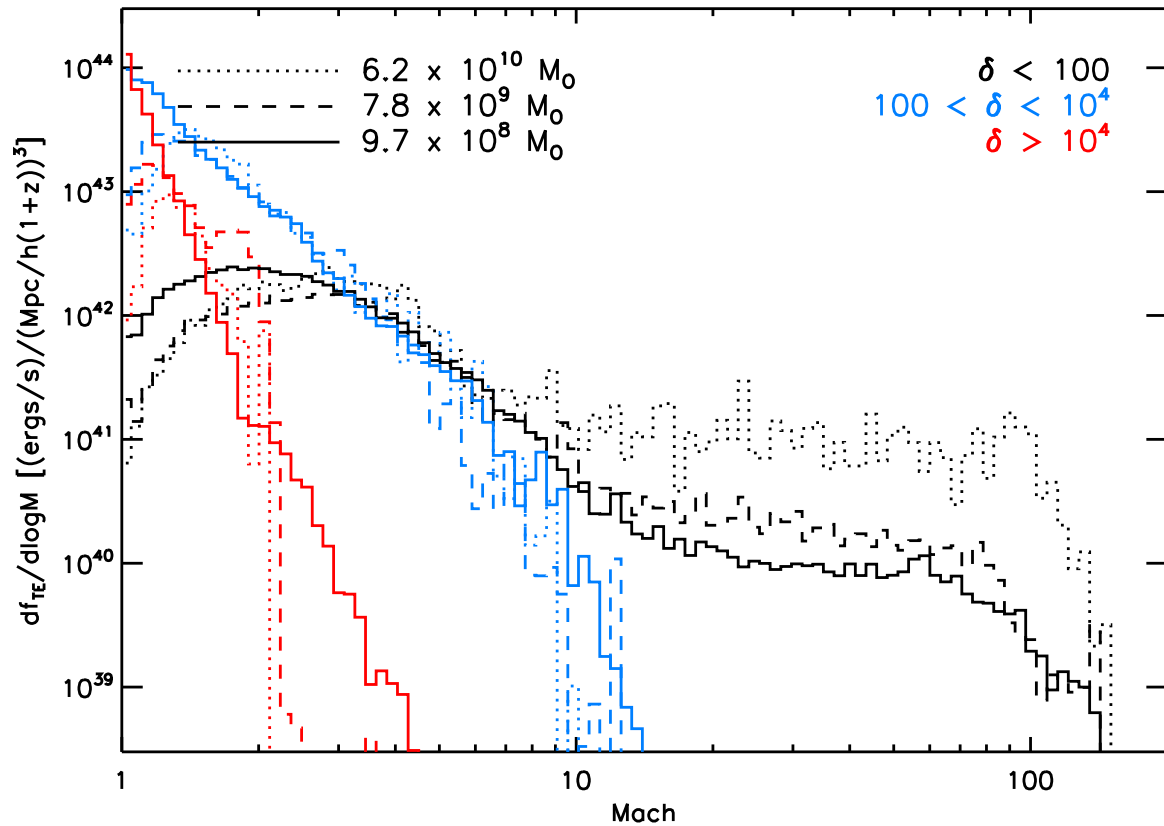


Figure 3.14 Spatial resolution effects on kinetic energy flux for varying dark matter particle masses. Mass resolutions are shown by linestyles of dotted ( $6.2 \times 10^{10} M_{\odot}$ ), dashed ( $7.8 \times 10^9 M_{\odot}$ ), and solid ( $9.7 \times 10^8 M_{\odot}$ ). The shocks are grouped as external (black lines), clusters/filaments (blue lines), and rich clusters (red lines).

## Chapter 4

### Radio Relics

As published in S. W. Skillman, E. J. Hallman, B. W. OShea, J. O. Burns, B. D. Smith, and M. J. Turk. Galaxy Cluster Radio Relics in Adaptive Mesh Refinement Cosmological Simulations: Relic Properties and Scaling Relationships. *ApJ*, 735:96, July 2011. doi: 10.1088/0004-637X/735/2/96. Reproduced by permission of the AAS. [213]

#### 4.1 Introduction

The assembly history of galaxy clusters are wrought with violent mergers, high Mach-number flows, and extreme plasma physical interactions. Much of this results from a wide range of cosmological structure formation shocks [156, 204, 179, 125, 110, 212, 239, 173]. These shocks, however, do more than simply heat the inflowing plasma. They also accelerate electrons and ions to relativistic speeds [14, 23]. See Drury [61], Blandford and Eichler [22], and Jones and Ellison [115] for reviews. These relativistic particles then act as signatures of merger and shock activity. The relativistic protons have radiative loss (e.g. collisions, pion decay, inverse Compton scattering) times comparable to the Hubble time, and therefore remain in the intracluster medium and contribute to the total pressure of the gas [156, 179]. On the other hand, relativistic electrons have relatively short lifetimes, on the order of a few hundred million years, and spend the remaining part of their life emitting synchrotron radiation as they gyrate about magnetic field lines.

Relativistic protons in the intracluster medium are, in principle, most easily observed through their collisional interactions with thermal ions, leading to pion decays that end in gamma-ray

emission [179]. This emission is being studied with the Fermi satellite, and while preliminary results hint at low levels of relativistic ions, long integrations of individual clusters are still forthcoming [6].

Relativistic electrons have been more extensively studied in several galaxy clusters through their synchrotron radiation [198, 166, 26, 230]. These electrons are most frequently associated with objects called radio *relics* [70], which have extended radio emission in the cluster exterior, are associated with shocks, and have moderately polarized radio emission with spectral indices of  $\alpha \approx 1 - 2$  for surface brightness  $S \sim \nu^{-\alpha}$ . They are also, by definition, not associated with active galactic nuclei (AGN). This spectral shape most likely indicates that these electrons were recently shock-accelerated [22]. Radio *halos*, on the other hand, have low polarization and usually follow the X-ray morphology in the centers of clusters. They are thought to be associated with turbulent acceleration and/or older populations of previously shock-accelerated electrons [e.g. 31].

The origin of the shock-accelerated electrons is believed to be primarily due to diffusive shock acceleration (DSA), as described in Blandford and Eichler [22]. This is a first-order Fermi mechanism in which electrons are accelerated by reflecting off magnetic field perturbations created by plasma effects in shock waves. Recent numerical studies by Spitkovsky [218] have shown success in reproducing this mechanism through ab-initio simulations using particle-in-cell (PIC) methods, though the incoming plasma flow was at a much higher velocity than the shocks discussed here. Studies of non-relativistic flow are ongoing because of the difficulty associated with the range in relevant timescales in such simulations [218].

If these electrons are capable of reaching high enough energies, they will emit synchrotron radiation in the presence of magnetic fields. It is widely believed that the cluster surroundings are magnetized at relatively low field strengths, on the order of microgauss in the ICM [85, 191, 193, 205], although measurements made by Faraday rotation indicate  $\sim 10\times$  larger values [96, 48]. Because the shock-accelerated electrons are expected to have a power-law distribution in energy, the synchrotron emission will also have a power-distribution in frequency. There have been a number of recent studies of these radio *relics* in interferometric observations of nearby galaxy



clusters [198, 166, 26, 230]. However, the total number of clusters with known relics is still fairly small ( $\sim 22$ ) [230]. This is in part due to the low surface brightness of these extended sources.

Studies of these objects comes at a critical point in time with a number of upcoming improvements in radio astronomy capabilities. The VLA is currently being upgraded to the “Expanded VLA” (EVLA), which will be roughly a factor of 10 better in terms of surface brightness sensitivity due primarily to an increase in bandwidth of up to 1 GHz at 1.5 GHz [162]. Several other telescopes will be coming online in the near future, such as LOFAR, possibly the SKA, and even lunar farside low frequency arrays [39] allowing an unprecedented view of the synchrotron Universe [199]. Given the low surface brightness and spectrum of the emission, low frequency observations ( $\sim 1$  GHz and below) are most effective in providing information on the radio relics and halos.

Here we set out to model these radio relics using high resolution, adaptive mesh refinement (AMR) cosmological simulations. These simulations include both dark matter and adiabatic baryonic physics, and allow us to model the shock acceleration of electrons and produce observationally-relevant radio luminosity functions and scaling relationships between cluster parameters such as synchrotron power, mass, and X-ray luminosity. By using large simulation volumes, we are able to show statistics for thousands of objects, from which individual morphological and evolutionary analyses can be carried out.

In Section 4.2, we introduce our simulation and galaxy cluster sample set and describe our shock finding method and synchrotron emission models. In Section 4.3, we study the global statistics of radio relics through projections and phase diagrams. Then, in Section 4.4, we describe the properties of individual halos, and use their statistics to generate radio luminosity scaling relationships and luminosity functions. We end with Section 4.5 where we discuss the implications for future surveys, the limitations of our model, and future directions.

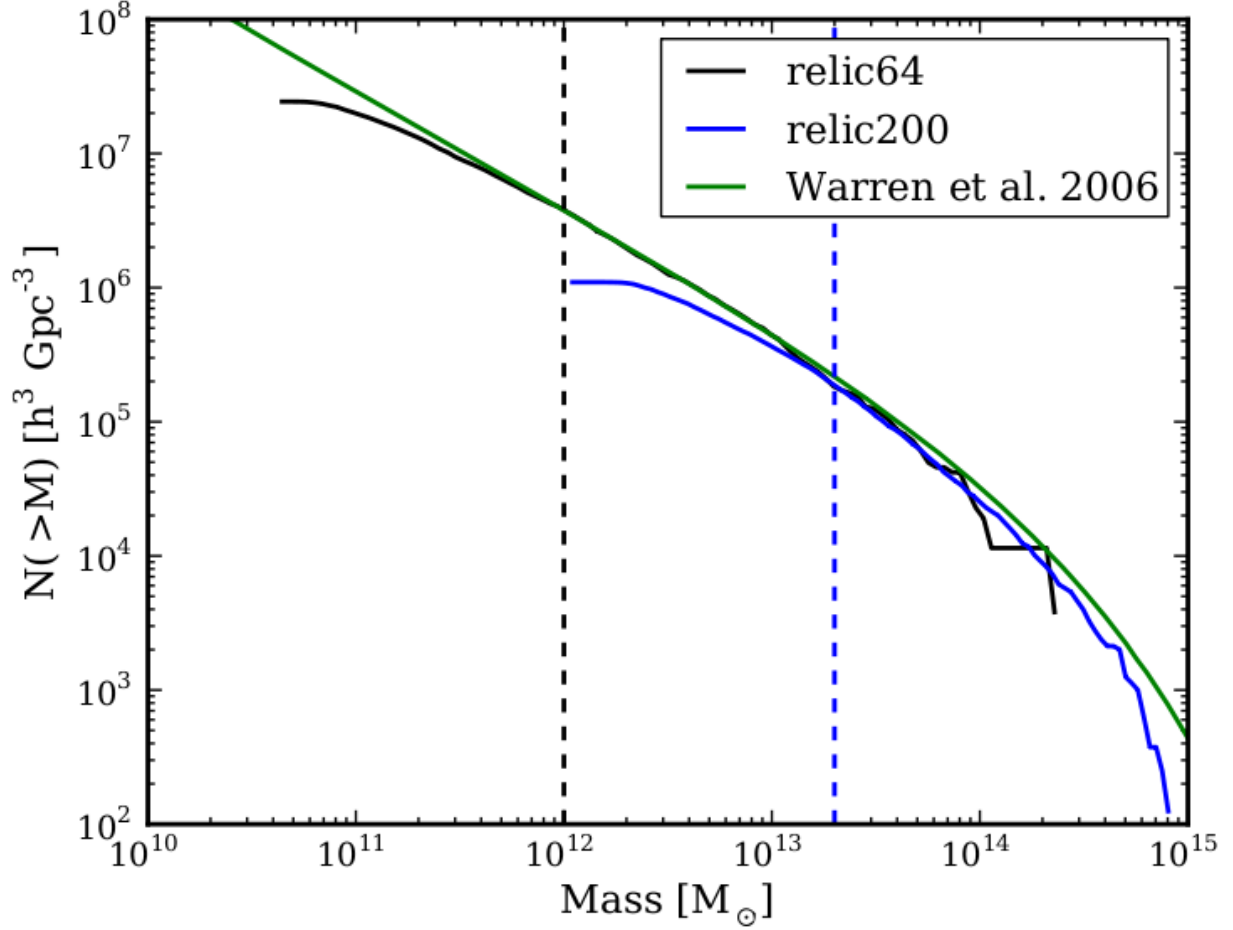


Figure 4.1 Mass function of halos in *relic64* and *relic200* at  $z = 0$ . Halos are found using HOP with a minimum number of 30 dark matter particles. Conservative estimates of the low mass cutoff are  $10^{12} M_\odot$  and  $2 \times \sim 10^{13} M_\odot$  for *relic64* and *relic200*, respectively. This corresponds to 512 and 320 particles. The discrepancy at low mass for *relic200* is because of the lack of resolution of low-mass halos and poor force resolution at small scales. Dashed lines show the lower limit for the resolved halos for *relic64* and *relic200* in black and blue, respectively. Also shown are the fits from Warren et al. [247]. Because of the similarity between the two cosmologies, these fits differ by less than thickness of the line in this mass range.

## 4.2 Methods

### 4.2.1 *Enzo*

All simulations were run using the *Enzo* cosmology code [34, 33, 163, 167, 168]. While a full description can be found in the cited papers, we will review the key aspects that are of importance to this work.

*Enzo* uses block-structured adaptive mesh refinement [AMR; 17] as a base upon which it couples an Eulerian hydrodynamic solver for the gas with an N-Body particle mesh (PM) solver [65, 107] for the dark matter. Users have the choice of solving the hydrodynamics with several methods including the piecewise parabolic method [PPM; 49, 252] extended for cosmological applications by Bryan et al. [35] and the ZEUS finite-difference method [223, 224]. In this work we utilize both methods, and restrict our studies to adiabatic gas physics.

The AMR method that *Enzo* uses breaks the simulation domain into rectangular solid volumes called *grids*. These *grids* contain many computational elements called *cells* that set the resolution scale. Each grid exists on a *level* of refinement determined by the spatial resolution of its cells that ranges from 0 –  $l_{max}$ , where  $l_{max}$  is defined by the user. Once *cells* within a given *grid* satisfy the refinement criteria (based on overdensity, minimum resolution of the Jeans length, local gradients of hydrodynamical quantities, shocks, or cooling time), a new *grid* is created at the next higher level. In our simulations, we refine on overdensity of the gas and dark matter fields.

### 4.2.2 Simulations

We will focus on two simulations that both use N-body dynamics for the dark matter and adiabatic baryonic physics. The first simulation, hereby denoted as *relic64*, has a comoving volume of  $(64 h^{-1}\text{Mpc})^3$  with  $256^3$  root-grid cells and up to 6 levels of additional refinement. The AMR is done by inserting a higher-resolution region wherever a cell satisfies the refinement criteria. Here we require a gas or dark matter overdensity ( $\delta \equiv \rho/\bar{\rho}$  where  $\bar{\rho}$  is the average density of gas or dark matter, respectively) of 8 to refine. Because refinement effectively splits a cell into

8 cells, this ensures that cells on each level have similar amounts of mass. This allows for a peak spatial resolution of  $3.9 h^{-1}\text{kpc}$  (comoving). The simulation uses the ZEUS hydrodynamic solver, with initial conditions from an Eisenstein and Hu [66] power spectrum with a spectral index  $n_s = 0.97$ . The cosmological parameters used are  $\Omega_M = 0.268$ ,  $\Omega_B = 0.0441$ ,  $\Omega_{CDM} = 0.2239$ ,  $\Omega_\Lambda = 0.732$ ,  $h = H_0/(100 \text{ km s}^{-1}\text{Mpc}^{-1}) = 0.704$ , and  $\sigma_8 = 0.82$ . The dark matter mass resolution is  $1.96 \times 10^9 h^{-1}M_\odot$ . The simulation was started at a redshift of  $z = 99$  and run until  $z = 0$ , using approximately 300,000 cpu-hours on the Texas Advanced Computing Center (TACC) Ranger supercomputer.

We use a second simulation with a larger volume  $(200 h^{-1} \text{ Mpc})^3$  with more modest resolution, *relic200*, to capture a higher mass range for our simulated galaxy clusters. As before, it uses  $256^3$  root-grid cells and up to 5 levels of AMR. It has a peak resolution of  $24.4 h^{-1}\text{kpc}$  (comoving) and a dark matter mass resolution of  $6.23 \times 10^{10} h^{-1}M_\odot$ . The simulation uses a slightly different cosmology of  $n_s = 0.96$ ,  $\Omega_M = 0.279$ ,  $\Omega_B = 0.046$ ,  $\Omega_{CDM} = 0.2239$ ,  $\Omega_\Lambda = 0.721$ ,  $h = H_0/(100 \text{ km s}^{-1}\text{Mpc}^{-1}) = 0.701$ , and  $\sigma_8 = 0.817$ , consistent with WMAP Year-5 results [130]. This simulation uses the PPM hydrodynamic solver, was also run on the TACC Ranger, and took approximately 100,000 cpu-hours to complete.

The mass functions of the two simulations are shown in Figure 4.1. To calculate the mass function we begin by finding all the halos using the halo-finding algorithm HOP Eisenstein and Hut [67], implemented in *yt*<sup>1</sup>, an analysis and visualization system written in Python, designed for use with the adaptive mesh refinement codes including *Enzo* [229]. This method finds halos by “hopping” from one dark matter particle to its most dense neighbor until a particle is its own highest density neighbor. All particles that find the same densest particle are then grouped into a single halo. The *relic64* simulation contains  $10^{11}M_\odot - 10^{14}M_\odot$  halos, but in our analysis we only consider objects with masses above  $10^{12}M_\odot$ , corresponding to  $\sim 510$  dark matter particles. This run was primarily designed to have superb resolution capable of capturing the morphology and structure of the relics and shocks. The *relic200* simulation contains  $5 \times 10^{12}M_\odot - 8 \times 10^{14}M_\odot$

---

<sup>1</sup> <http://yt.enzotools.org>

halos. For this simulation, we consider only halos above  $2 \times 10^{13} M_{\odot}$ , corresponding to  $\sim 320$  dark matter particles. This simulation is designed to study the statistics of medium-sized clusters. While neither of these simulations capture the most massive clusters in the Universe (e.g. Coma), they provide insight to radio relic origins, structure, and evolution. Studies of very large volume simulations are reserved for future work.

### 4.2.3 Shock Finding

To identify the shocks that ultimately accelerate the electrons that emit synchrotron radiation, we need an accurate shock identification algorithm. For this we use the temperature-jump method given in Skillman et al. [212]. Here we present an overview of the method for completeness. We use the Rankine-Hugoniot temperature jump conditions to derive the Mach number:

$$\frac{T_2}{T_1} = \frac{(5\mathcal{M}^2 - 1)(\mathcal{M}^2 + 3)}{16\mathcal{M}^2}, \quad (4.1)$$

where  $T_2$  and  $T_1$  are the post-shock (downstream) and pre-shock (upstream) temperatures, respectively.  $\mathcal{M}$  is the Mach number using the upstream (pre-shock) gas.

A cell is determined to have a shock if it meets the following requirements:

$$\nabla \cdot \vec{v} < 0, \quad \nabla T \cdot \nabla S > 0, \quad T_2 > T_1, \quad \rho_2 > \rho_1, \quad (4.2)$$

where  $\vec{v}$  is the velocity field,  $T$  is the temperature,  $\rho$  is the density, and  $S = T/\rho^{\gamma-1}$  is the entropy. In our analysis, as in Skillman et al. [212], we have set a minimum preshock temperature of  $T = 10^4$  K since the low-density gas in our cosmological simulations is assumed to be ionized (a reasonable assumption at  $z < 6$ ). Therefore, any time the pre-shock temperature is lower than  $10^4$  K, the Mach number is calculated from the ratio of the post-shock temperature to  $10^4$  K.

Once a shock is found, we identify the cell with the most negative flow divergence, choosing from a ray aligned with the temperature gradient. Therefore, even if several cells in a row qualify as a shock, only the “center” of the shock is marked as a shock, and the temperature jump is taken from the full jump across all the shocked cells. This relieves problems when shocks are spread

out over several cells, especially when not aligned with the coordinate axes. In addition, this method has been implemented to run “on-the-fly” in *Enzo* so that post-processing of the data is not needed. This method then saves the Mach number and quantities such as the pre-shock density and temperature directly along with the other hydrodynamical quantities during simulation output. The unique feature of this shock-finder is its ability to accurately identify off-axis shocks within AMR simulations and quantify their Mach number even if the shock is identified as being spread out across several cells.

#### 4.2.4 Synchrotron Emission

In order to estimate the synchrotron emission from the shock waves, we follow the method of Hoeft and Brüggén [109]. Here we summarize the main features of the model. The first assumption is that the electrons are accelerated to a power-law distribution that is related to the Mach number from diffusive shock acceleration theory. These accelerated electrons form an extension to the thermal, Maxwellian distribution that has a power-law form and exponential cutoff related to balancing the acceleration and cooling times of the electrons.

The accelerated electrons then emit in the radio through synchrotron radiation. Since we are not performing magnetohydrodynamic simulations, we assume that the magnetic field is governed by flux freezing such that the magnetic field strength is related to the density by  $B = 0.1\mu G(\frac{n}{10^{-4}\text{cm}^{-3}})^{2/3}$ , where  $n$  is the number density. This is a reasonable assumption even in merging clusters, as was found by Roettiger et al. [196]. In Section 4.4.4 and Appendix A we explore the effect of a modified magnetic field model.

The total radio power from a shock wave of area  $A$ , frequency  $\nu_{obs}$ , magnetic field  $B$ , electron acceleration efficiency  $\xi_e$ , electron power-law index  $s$  ( $n_e \propto E^{-s}$ ), post-shock electron density  $n_e$  and temperature  $T_2$  is [109]

$$\frac{dP(\nu_{obs})}{d\nu} = 6.4 \times 10^{34} \text{ erg s}^{-1} \text{ Hz}^{-1} \frac{A}{\text{Mpc}^2} \frac{n_e}{10^{-4}\text{cm}^{-3}} \frac{\xi_e}{0.05} \left(\frac{\nu_{obs}}{1.4\text{GHz}}\right)^{-s/2} \times \left(\frac{T_2}{7\text{keV}}\right)^{3/2}$$

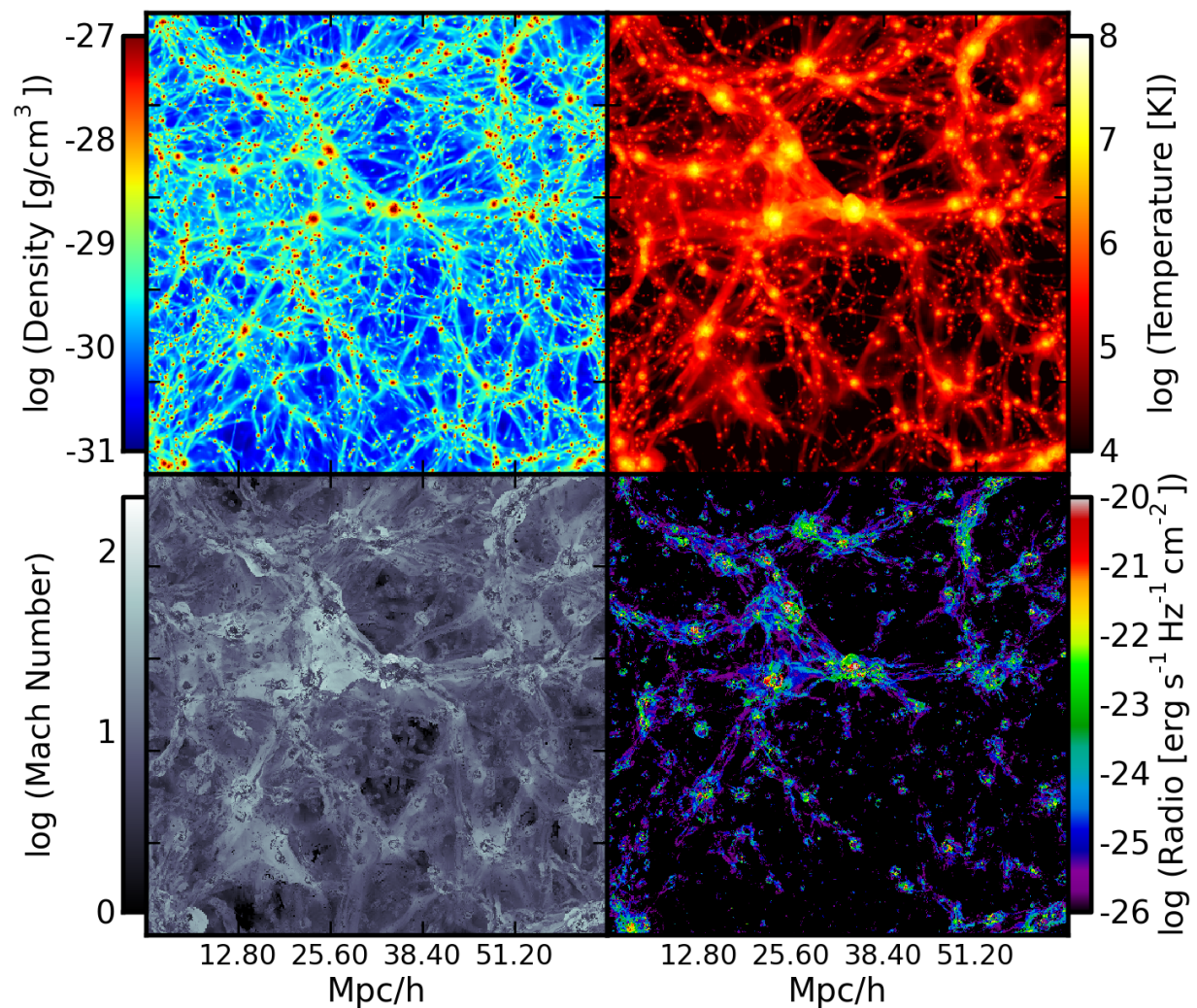


Figure 4.2 Projection of several quantities through the entire *relic64* simulation volume at  $z = 0$ . Shown are mass-weighted density [ $\text{g cm}^{-3}$ ] (upper left), mass-weighted temperature [K] (upper right), radio emission-weighted Mach number (lower left), and radio flux density [ $\text{erg s}^{-1}\text{Hz}^{-1}\text{cm}^{-2}$ ] (lower right).

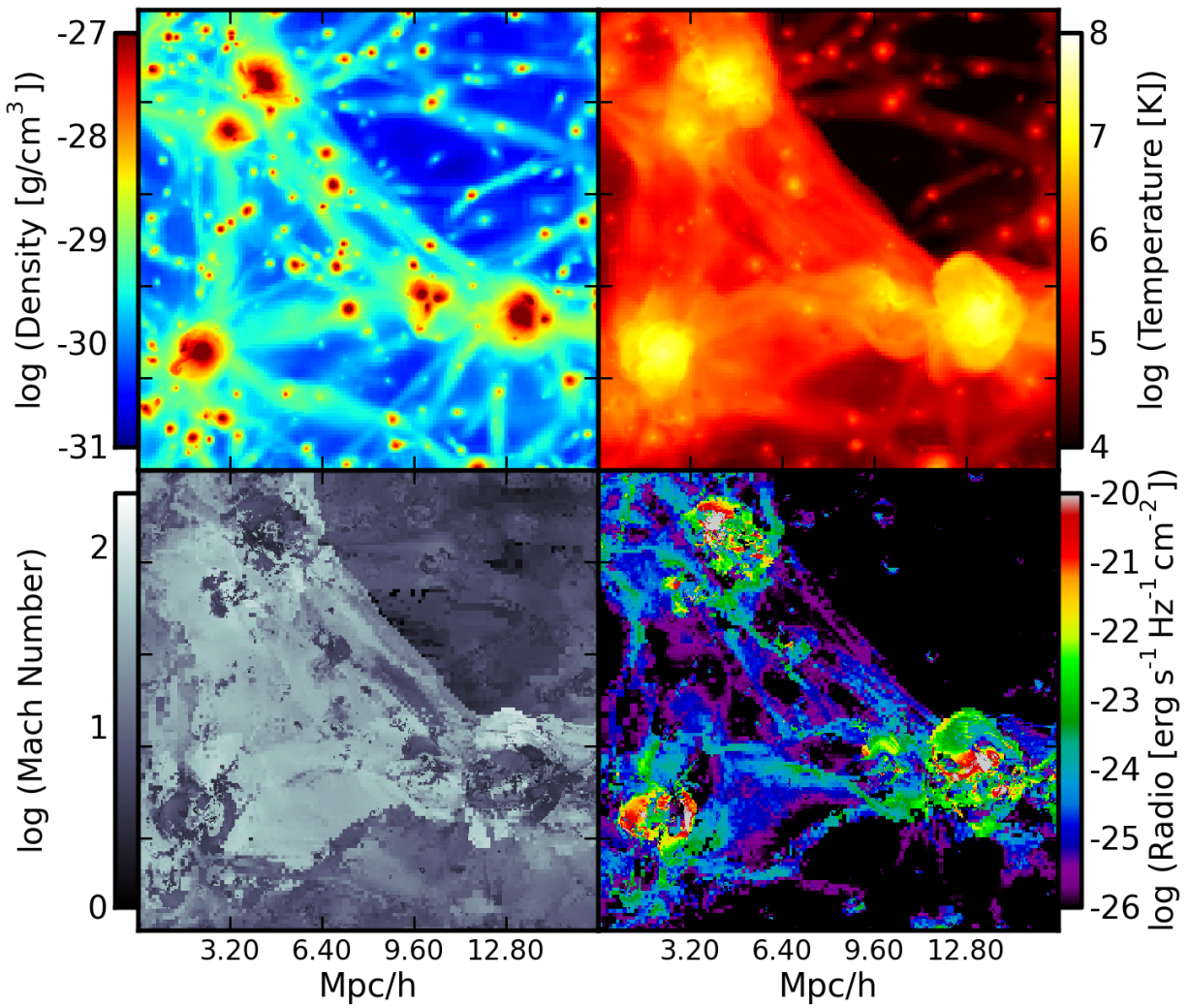


Figure 4.3 A zoom-in of Figure 4.2, now 16Mpc/h wide.



$$\frac{(B/\mu G)^{1+(s/2)}}{(B_{CMB}/\mu G)^2 + (B/\mu G)^2} \Psi(\mathcal{M}). \quad (4.3)$$

Note that the radiation spectral index is related to the electron spectral index by  $\alpha = (s - 1)/2$ .  $B_{CMB}$  is defined as the magnetic field corresponding to the energy density of the CMB. It has a value of  $B \equiv 3.47\mu G(1+z)^2$ , and accounts for the inverse Compton emission that is simultaneously cooling the electrons along with their synchrotron emission. The final term,  $\Psi(\mathcal{M})$ , is a dimensionless quantity that contains dependencies on the shock Mach number such that at  $\Psi(2.5) \sim 10^{-3}$  and approaches 1 for  $\mathcal{M} > 10$ . It can be thought of as a shape factor that, together with  $\xi$ , defines the acceleration efficiency as a function of Mach number. Note that for calculations with  $z > 0$ , we modify  $\nu_{obs} \rightarrow \nu_{obs} \times (1 + z)$  since we observe the redshifted emission.

In all of our analysis, we use  $\xi_e = 0.005$ , which was found by Hoeft et al. [110] to match radio emission in known relics to similar mass clusters in their simulation. While the true value of this parameter is quite uncertain from current observational and theoretical constraints, the relationship between it and the total radio power is linear. Therefore, if we underestimate the electron acceleration efficiency by a factor of 10, it will lead to a derived radio power that is low by a factor of 10, and thus all relationships between radio power and other quantities (e.g. mass, x-ray luminosity) simply need to be rescaled. While we have chosen the dimensionless shape factor  $\Psi(\mathcal{M})$  from Hoeft and Brüggen [109], there are still uncertainties in the efficiency of acceleration as a function of Mach number. However, exploration of the effects of these uncertainties are beyond the scope of this work. We also ignore the effects of re-accelerated  $\gamma \sim 200$  electrons from radio galaxies.

## 4.3 Global Properties of Radio relics

### 4.3.1 Full Box Projections

To begin our study of radio relics, we first performed simple projections of the radio emission through the entire simulation volume. An example is shown in Figure 4.2 along with projections of density, temperature and Mach number. For quantities such as density, temperature and Mach

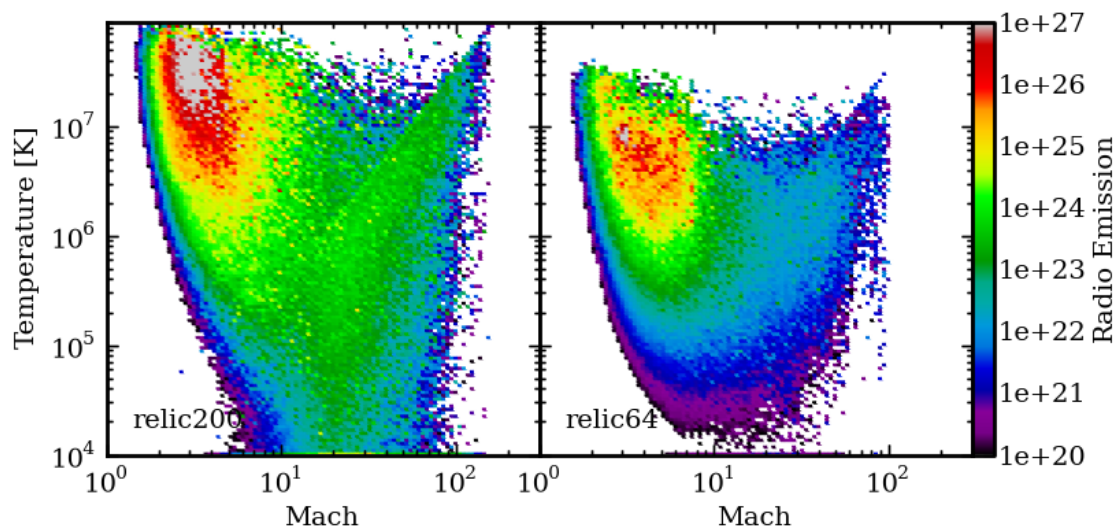


Figure 4.4 2D Phase Diagram of the relic radio emission in temperature-Mach number space for the *relic200* (left) and *relic64* (right) simulation. The temperature is that of the cell in the center of the shock. The color indicates the amount of 1.4 GHz radio emission [ $\text{erg s}^{-1}\text{Hz}^{-1}/(\text{Mpc}/h)^3/(d\log\mathcal{M} d\log T)$ ] for a given value of temperature and Mach number.

number in an AMR simulation, we choose to weight each cell by a secondary quantity since a simple average along the line of sight for each cell would bias the most highly refined regions because of their increased number of cells. Therefore, we choose to weight the density and temperature fields by cell mass, and the Mach number by the radio emission. This has the effect of pulling out the values of density and temperature from the densest regions, and the shocks that contribute the most to the radio emission. For radio and X-ray fields, we project the emissivities [energy/time/volume] without a weight, leading to final values with units of [energy/time/area]. Mathematically, a weighted projection (here along the  $z$ -axis) is defined by:

$$P_z(x, y) = \frac{\int w(x, y, z)v(x, y, z)dz}{\int w(x, y, z)dz} \quad (4.4)$$

where  $w(x, y, z)$  is the weight quantity at that location and  $v(x, y, z)$  is the value of the projected quantity. To evaluate this integral in our AMR setting, the integral traverses the box along cells that are at the highest refinement for a given point in space, and ignores cells that are covered by more highly refined regions. This, like the bulk of our analysis, is done using  $yt$ , detailed above.

In Figures 4.2-4.3, we see that in general the radio emission traces out the large scale structure seen in the density projection. Additionally, the emission is also highly correlated with the temperature structure. However, the correlation with Mach number is more interesting. In the projection of Mach number, we see shocks with strengths up to  $\mathcal{M} \sim 10 - 100$  throughout the volume in filaments and cluster edges, whereas the peak radio emission only shows up in small, curved arcs within clusters. At the location of these arcs, the value of the Mach number projection drops to values between  $\mathcal{M} \sim 3 - 10$ . This shows that the strongest shocks which are most likely external, accretion, shocks are not responsible for the bright radio emission, and that it is instead the interior shocks [204, 212], as was found by Hoeft et al. [110] with moderate strengths, that shine in the radio. This can be understood by the fact that it is the mass flux of gas through shocks that is most important since that determines the number of electrons that can be accelerated. Therefore, while the Mach number is much lower for the interior shocks, the shock velocity stays roughly constant while the pre-shock density is much higher, yielding more accelerated electrons.

In the projection of Mach number, this results in the appearance of “veins” lining the interior of the filaments, “arcs” in the periphery of the clusters, and “holes” in the centers of the clusters. While they are decrements in the projection of Mach number, they are the bright areas in the radio emission.

The lack of strong emission in the accretion shocks suggests that having a hot, dense plasma is more important than the Mach number of the shock. This can be understood by Equation 4.3. Since  $\frac{dP}{dv} \propto A n_e \xi \nu T^{3/2} \frac{B^{1+s/2}}{B_{CMB}^2 + B^2}$  and in most cluster situations  $B_{CMB}^2 > B^2$  and  $s = 2\alpha + 1 = 3$ , we have that  $\frac{dP}{dv} \propto n_e B^{5/2} \propto n_e (n_e^{2/3})^{5/2} \propto n_e^{8/3}$ . This implies that since the density in the accretion shocks is  $\approx 10^2 - 10^3$  times lower than that in a merger shock, the power emitted will be down by a factor of  $\approx 2 \times 10^3 - 10^5$ . Therefore the features we see observationally are more likely to be related to merger shocks than accretion shocks.

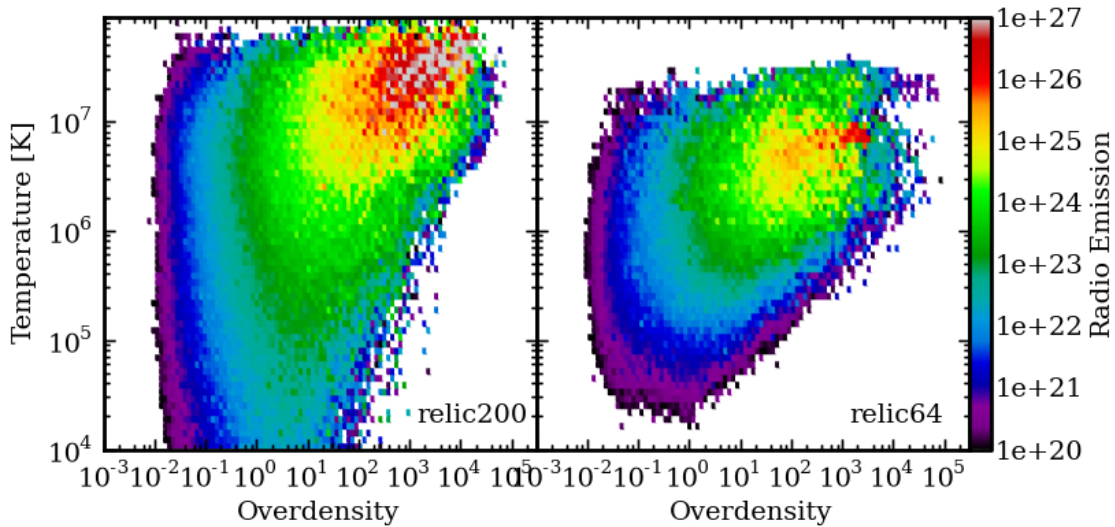


Figure 4.5 2D Phase Diagram of the relic radio emission in temperature-overdensity space for the *relic200*(left) and *relic64*(right) simulation. The color indicates the amount of 1.4 GHz radio emission [ $\text{erg s}^{-1}\text{Hz}^{-1}/(\text{Mpc}/h)^3/(d\log\delta d\log T)$ ] for a given value of temperature and overdensity.

### 4.3.2 Phase Diagrams

The second method we use to study the bulk properties of the radio emitting plasma is phase diagrams. Such diagrams are the equivalent of a two-dimensional histogram. Here we use them to

study the gas properties of the radio emitting regions.

The structure of these diagrams is as follows. For a given simulation output, we construct x and y-axis bins that are equally spaced logarithmically in two fields. Within each of these 2D bins, we integrate the total amount of a given quantity such as radio emission. This integrated value is normalized by the comoving volume of the simulation in order to give a comparable value between different physical size simulations. We have found three particularly insightful quantities to examine in a range of permutations: temperature, overdensity, and Mach number.

We have constructed one such phase diagram, seen in Figure 4.4, in which the x-axis is the Mach number, the y-axis is temperature, and the bins are colored by the total radio emission in that bin. The total integrated emission is normalized by the volume of the simulation and the size of the bins. As such, one reads this figure as “At Mach number  $x$  and temperature  $y$ , there is  $z$  amount of radio emission per comoving Mpc/h per  $\Delta \log \mathcal{M} \Delta \log T$ .” The utility of these diagrams is demonstrated in Figure 4.4, where it is immediately clear that the bulk of the radio emission in both simulations originates from hot gas with  $T = 10^6 - 5 \times 10^7 \text{K}$ , and Mach number  $\mathcal{M} = 3 - 10$ . This reinforces our earlier hypothesis that the radio features are generated from interior shocks associated with merging subclusters that have low Mach numbers but high mass and energy flux due to the high relative density, and therefore shock velocity, of cluster cores. Second, it points out that shocks with  $\mathcal{M} = 20 - 100$  have little role at  $z = 0$  in producing appreciable radio emission. In fact, their integrated luminosity is a factor of 500 – 1000 less than their low-Mach number counterparts.

At first glance, one also picks out a diagonal structure in the *relic200* phase diagram that seems to be an upper limit on the temperature for a given Mach number. This is a very interesting feature that has a simple explanation. We calculate our Mach number using a minimum pre-shock temperature of  $10^4 \text{K}$ . Now, while the gas at the location of the shock is not necessarily the pre- or post-shock temperature, it is bounded by those two values. This is because the shock location is based on the cell with the most convergent flow, not the location of the pre- or post-shock gas. Because of this, if gas with pre-shock temperature  $T_1 < 10^4 \text{K}$  is being accreted, the gas at the

location of the shock will have a maximum temperature of  $T_{max} \leq \frac{(5\mathcal{M}^2-1)(\mathcal{M}^2+3)}{16\mathcal{M}^2} 10^4 \text{K}$ . This maximum coincides perfectly with the diagonal feature. Therefore, any gas below this line is likely pristine gas (that is, gas that has not been previously shocked) being accreted onto filaments or clusters for the first time. This gives us a proxy for the relative amount of accretion in a simulation.

We can then use this diagnostic to study the role of accretion in the *relic64* and *relic200* simulations. While *relic64* does have a small amount of accretion, it is far below that of *relic200*. This is because of the different mass clusters present in each of the two simulations; *relic200* has clusters that are up to an order of magnitude more massive than in *relic64*. Recalling that the accretion radius  $r_s = \frac{GM}{c_s^2}$  scales with mass [29], the clusters in *relic200* are able to pull in and accrete more gas than those in *relic64*. This behavior will be studied as a function of redshift below.

As we did in the temperature-Mach number phase space, we now examine the behavior in the temperature-overdensity plane in Figure 4.5, where overdensity is defined as  $\rho/\bar{\rho}$ , where  $\bar{\rho}$  is the mean matter density of the Universe,  $\Omega_M \rho_{crit}$ . Here our earlier findings are reinforced - the strongest emission is coming from the densest, hottest regions in the simulations.

Both simulations exhibit the same general properties, though *relic200* has hotter gas again due to the larger clusters. This suggests that not only will the most massive clusters likely be associated with the strongest radio emission, but that the strongest features will arise from merger shocks passing through the centers of cluster, which seems to be the case observationally. Below an overdensity of  $\sim 10-30$ , the radio emission greatly decreases. This strongly disfavors the possibility of seeing cluster accretion shocks in agreement with Hoeft et al. [110]. This is compounded by the fact that these accretion features are more diffuse and therefore have reduced surface brightness compared to the more compact merger shocks, making them difficult to study observationally. If we then compare *relic64* to *relic200*, we see that there is a relative absence of accreting gas in the *relic64* simulation, reinforcing our earlier findings that *relic64* has less accretion due to the smaller mass halos compared to *relic200*. In the following section we study this accretion as an evolutionary tracer in more depth.

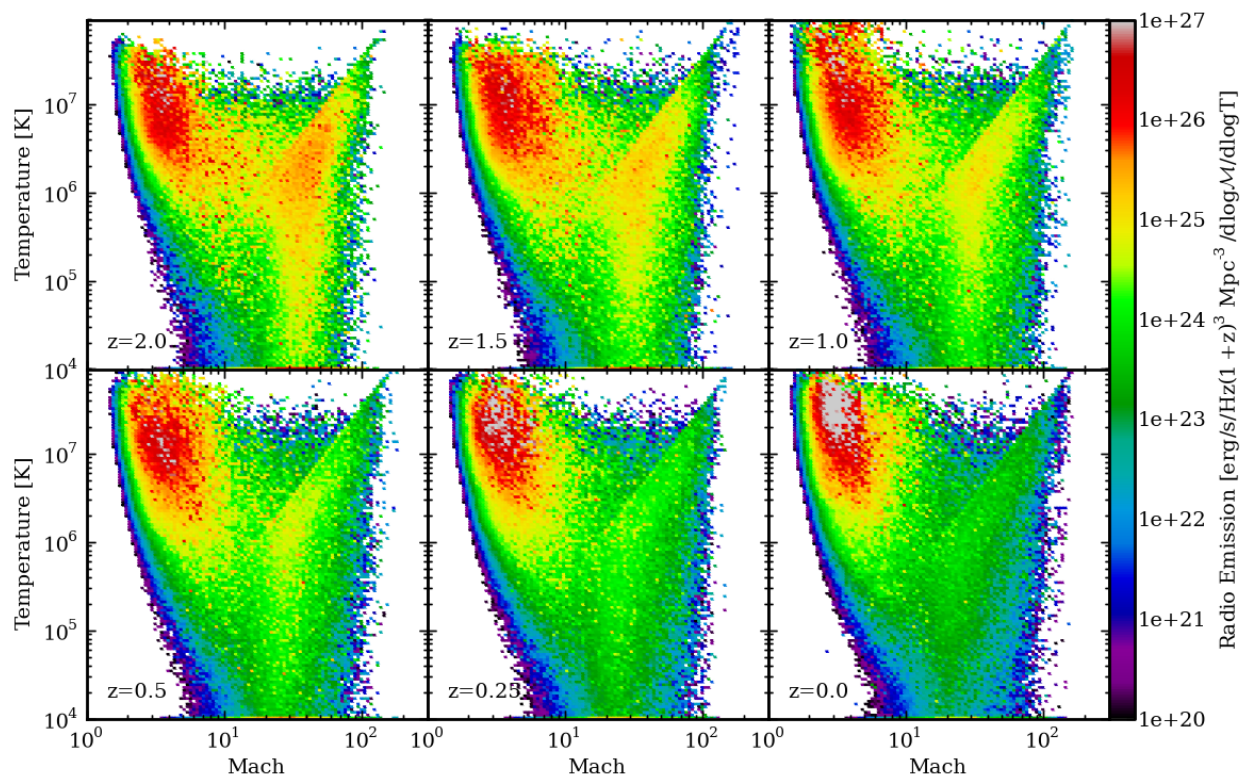


Figure 4.6 2d Phase Diagram of the relic radio emission in temperature-Mach number space for the *relic200* simulation for varying redshifts. From top left to bottom right, we have  $z = 2.0, 1.5, 1.0, 0.5, 0.25, 0.00$

### 4.3.3 Radio Emission as a Proxy for Cluster Accretion

We have seen at  $z = 0$  that there is a relatively small amount of radio emission coming from cluster and filament accretion shocks. We now investigate whether or not this holds for earlier times. Figure 4.6 is an analog to our prior phase diagrams, but we now show the evolution of this phase diagram for *relic200* back to  $z = 2.0$ . We have normalized the emission by comoving volume in order to avoid confusion with the expansion of space. Even with this taken out, we see that there is a strong evolutionary trend in the origin of the radio emission.

At  $z = 2$ , we see that the emission from accretion shocks is comparable to, if not above, that of the interior merger shocks. This roughly translates to an equal amount of thermal energy being processed by mergers and accretion shocks at  $z = 2$  since the efficiency of acceleration does not differ dramatically between the two cases. The line that we previously identified with accretion shocks is now quite strong, and there is even a dominant population within the accretion regime, centered around  $10^6\text{K}$  and Mach numbers of  $40 - 60$ .

By  $z = 1$ , the emission from accretion shocks has dropped by a factor of 10 while the merger shocks have increased by a factor of  $2 - 3$ . Finally, by  $z = 0$ , nearly all of the radio emission due to accretion shocks has disappeared while the interior shocks have increased by a factor of 10 from  $z = 2$ . This drop in radio emission from accretion shocks coincides with the Universe beginning to accelerate due to 'dark energy' at  $z = 0.75 - 1.0$ . This process manifests itself by both depleting the voids leading to less mass to accrete, and decoupling of clusters from the cosmic expansion. Therefore, instead of growing in mass, and growing the radius of influence, dark energy dominates and pulls all the remaining matter away from the cluster faster than it can grow. We note here that this assumes that there is no evolution in the relative magnetic field strengths or acceleration efficiencies between merger and accretion shocks. It may be the case that the magnetic field strength at accretion shock locations is lower or higher at early times compared to the interior of proto-clusters. However, since we do not have conclusive evidence to this evolution, we have chosen to adopt the simplest model that assumes no evolution.



This decrease in radio emission from accretion shocks is similar to the depletion of cosmic ray proton acceleration at  $z < 1$  from accretion shocks, found in Skillman et al. [212]. This behavior is a novel perspective to view the effects of Dark Energy. If the radio relics from these accretion shocks are observable in the future, one should see a decrease in their frequency and power as  $z$  decreases.

## 4.4 Individual Object Properties

### 4.4.1 Cluster Projections

In this section, we take the opposite approach from the previous section and examine projections of individual objects. We begin with our list of halos and make radial profiles that start at the density peak and continue to the previously found  $r_{200}$ , defined here as the radius where  $\delta \equiv \rho/\bar{\rho} = 200$ . We call the mass enclosed within this radius the *virial mass*, and also record several other quantities, such as X-ray luminosity and radio power within the virial radius.

We begin by demonstrating the power of having a large sample of clusters in a single simulation by projecting *only* the 51 most massive clusters at  $z = 0$  along the x-axis in *relic64* in Figure 4.7. The width and depth of each individual projection here is 4 Mpc/h.

The most important result gleaned from these images is the morphological properties of cluster structure. If we first examine the gas density (top), we see that while there is some amount of substructure, the density is centrally concentrated. Since X-ray emission closely follows the density distribution of the gas, this implies that the X-ray emission will be brightest in the centers of clusters. However, the radio emission (bottom) is brightest on the edges of the clusters and has very little correlation with the density structure. Instead, it more closely follows the temperature structure (middle). This is because the temperature is more strongly affected by shocks than the density (recall  $\rho_2/\rho_1 \leq 4$  from shock jump conditions for  $\gamma = 5/3$ ). Note, however, that the emission is still confined within high density regions inside the virial radius. Immediately from these images, we expect radio emission to be anti-coincident with the X-ray emission, as is seen in existing *relic*

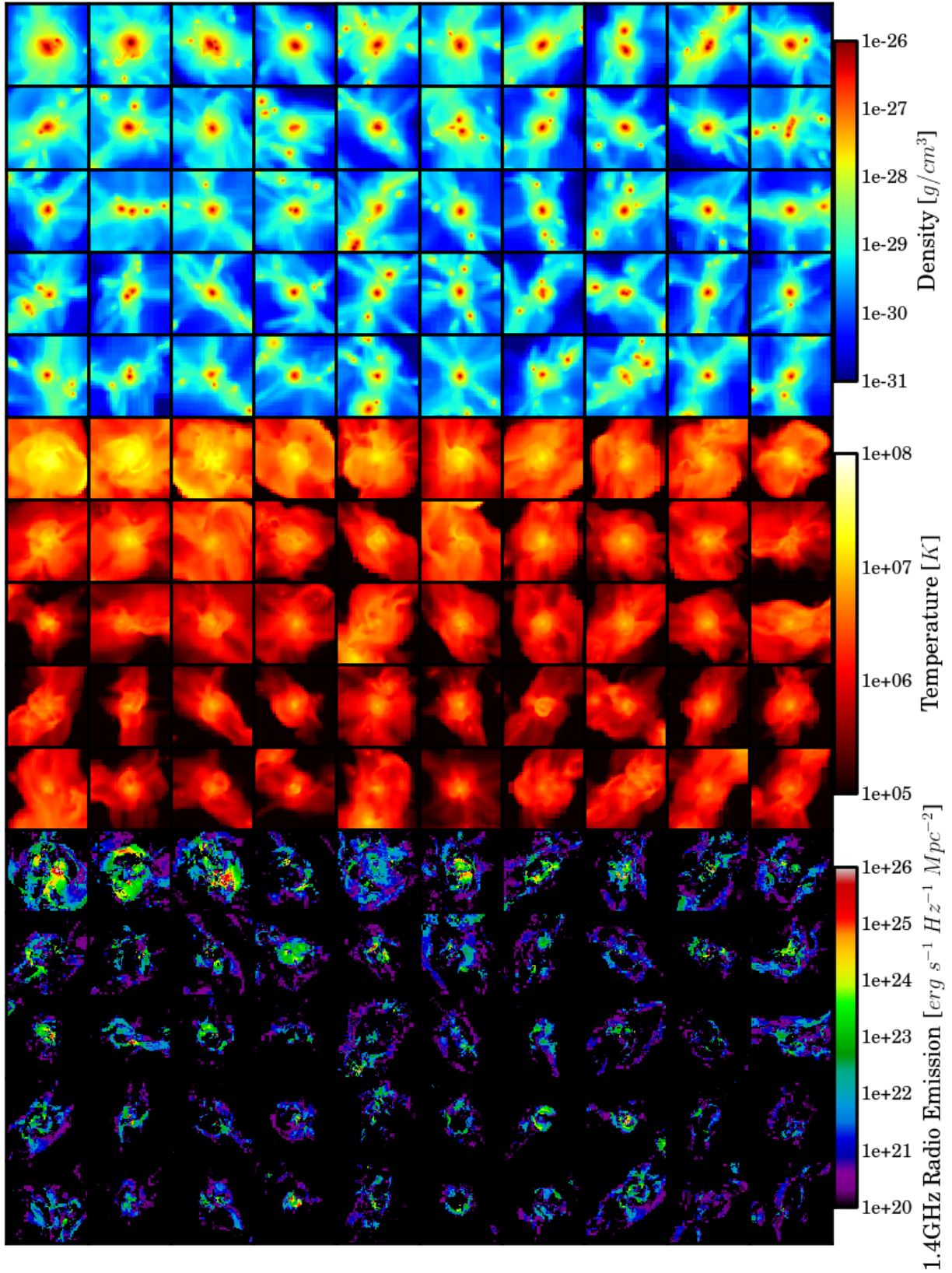


Figure 4.7 Density (top), temperature (middle) and 1.4GHz radio emission (bottom) for the 51 most massive halos in the *relic64* simulation at  $z = 0$ . Mass decreases from top left to bottom right ( $2.5 \times 10^{14} - 2.0 \times 10^{13} M_{\odot}$ ). Each individual image is  $4\ Mpc/h$  across. All images are projections down the x-axis.

examples [90, 230, 26, 47]. This behavior implies that shocks are more likely to appear in radio imaging than in X-ray surface brightness maps.

Also visible in the radio emission are common features such as arcs and rings. These features are due to merging subclusters as their bow shocks propagate through the ICM. These shapes are similar to what is seen in observed radio relics. This similarity supports our claim that the morphology of these objects is related to the location of shocks, as was originally suggested in Ensslin et al. [70]. In a few rare situations (here in 2-3 clusters), these arcs appear in the very center of the cluster. Because the surrounding medium is both hot and quite dense in these cases, the radio emission is very strong. This agrees with our previous results from Section 4.3.2, where we found the bulk of the emission at late times to be in the hot, dense phase of the gas.

#### 4.4.2 Radio Power - Mass Relationship

From the projections of individual halos in Figure 4.7, we can see that there is a general trend for the more massive halos to have higher radio emission (note masses decrease from the top left to bottom right). We now want to quantify this scaling relationship by studying the radio luminosity-mass relationship for the halos in our simulations. We begin with the earlier list of halos and use the virial quantities of each halo. For each halo, we use their total mass and 1.4 GHz radio power (integrated out to  $r_{200}$ ) to populate Figure 4.8. Second, for the distribution of halos, we now determine the linear-least squares fit to  $\log(P_{1.4GHz}) = A \log(M_{200}) + B$  for all halos with  $M_{200} > 10^{13} M_{\odot}$  and  $2 \times 10^{13} M_{\odot}$  for the *relic64* and *relic200* simulations, respectively. We choose to only fit halos above this minimum mass because at smaller scales additional physics such as cooling not included in our simulations would possibly strongly affect the emission. Additionally, we do not capture small mass halos that are likely moving through these small clusters possibly creating a large fraction of the total radio emission. Because our simulation data does not have a measurable uncertainty for a given radio power, we have to use an alternate method of determining the error estimates of our parameters. We first find the best fit parameters using a uniform weighting. By calculating the residuals for each point from this best-fit relation, we estimate the uniform error for

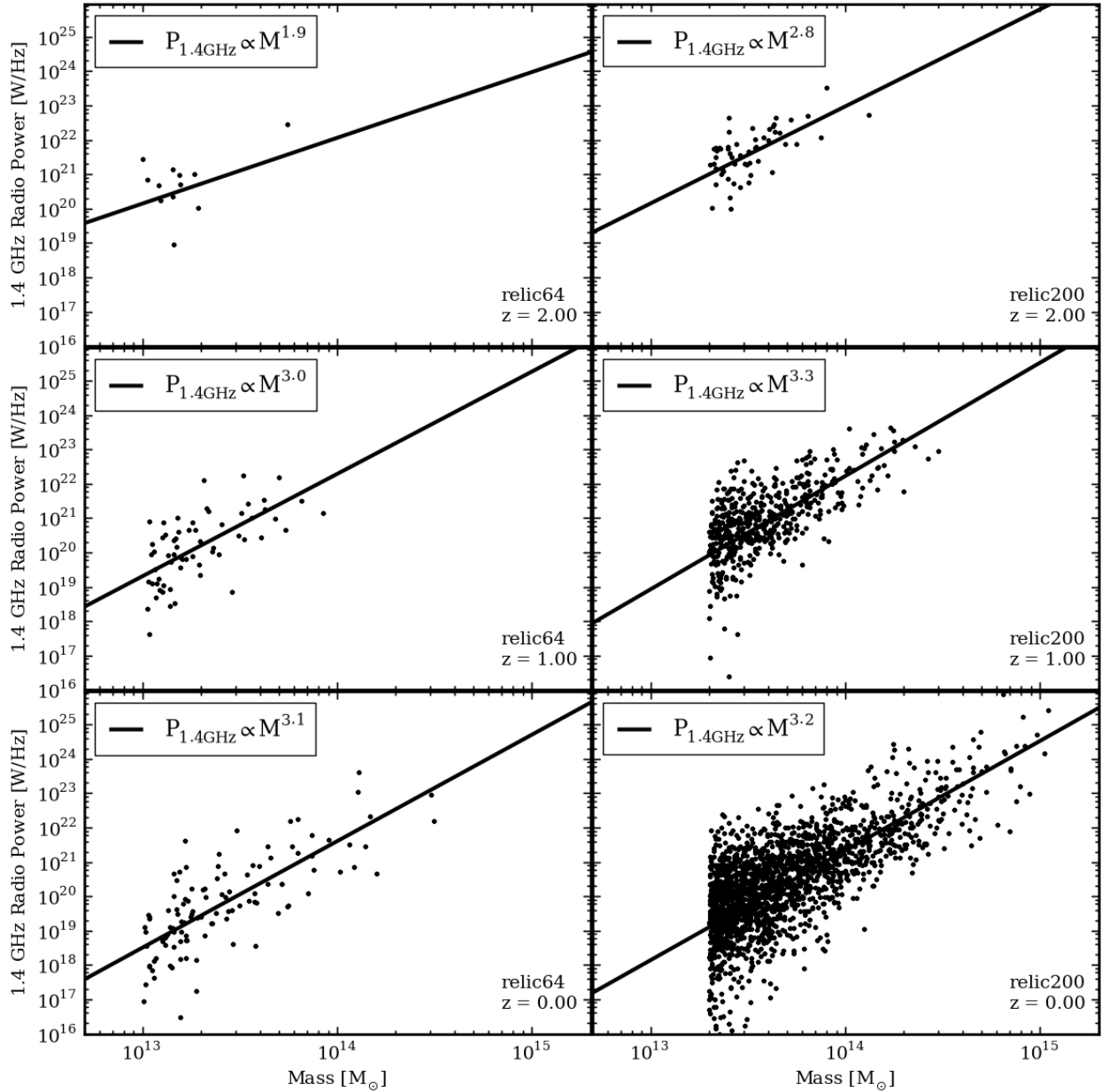


Figure 4.8 1.4 GHz Radio Luminosity-Mass Relationship of halos in *relic64* (left) and *relic200* (right) for redshifts 2 (top), 1 (middle), and 0 (bottom). Shown in black are each individual halo. The lines represents a best power-law fit to all halos with  $M_{vir} > 10^{13} M_{\odot}$  and  $2 \times 10^{13} M_{\odot}$  for the *relic64* and *relic200* using a least-squares fitting routine.

each point as the standard deviation of this residual. We then fit the data again using this error to obtain the uncertainty estimates in each parameter. The values of these parameters are shown in Table 4.1.

Perhaps the most interesting result from Figure 4.8 is the normalization as a function of redshift. At  $z = 0$ , a  $10^{14}M_{\odot}$  mass halo emits  $\sim 10^{20}erg/s/Hz$ , while a similar mass halo at  $z = 2$  emits  $\sim 10^{22}erg/s/Hz$ . This amplifies our hypothesis that the merger state of the halo is very important. The  $10^{14}M_{\odot}$  halo at  $z = 2$  is one of the most massive objects at that time and has likely recently formed, whereas the same mass halo at  $z = 0$  is a fairly common object that was likely formed some time ago. Additionally, the probability of a merger with a 1 : 1 mass ratio is very low for the largest halos at a given time. For both simulations at multiple redshifts, the radio power is correlated with the mass of the halo. This dependence is expected since the radio emission is a function of the temperature, density and magnetic field strength of the halo, all of which scale positively with the mass.

The second result of these radio luminosity-mass relationships is the large scatter around the best fit. We see that there can be scatter of up to 2 – 3 orders of magnitude for a given mass cluster. This suggests that while the radio emission is correlated with mass, the merger state of the halo plays a major role in determining the radio power. As can be seen from the projections of these halos in Figure 4.7, the most radio luminous objects have very disturbed morphology and are undergoing major mergers.

In Figure 4.9, we show the evolution of the most massive cluster in *relic64*, and track the total radio and X-ray luminosity as a function of redshift. The X-ray emission is calculated using outputs of the Cloudy code [78] where we have adapted the method of Smith et al. [216] for radiative cooling to calculate frequency-dependent emission. This yields an X-ray emission for given temperature and density of the gas, and is shown in gray. The radio emission, shown in color, has been masked such that all values below  $10^{-21}erg/s Hz^{-1}cm^{-2}$  are transparent, allowing for a view of the X-ray data and masking out radio features that are too faint to be observed. To help follow the evolution of the total radio and X-ray luminosities from the cluster, we plot their relative luminosities with

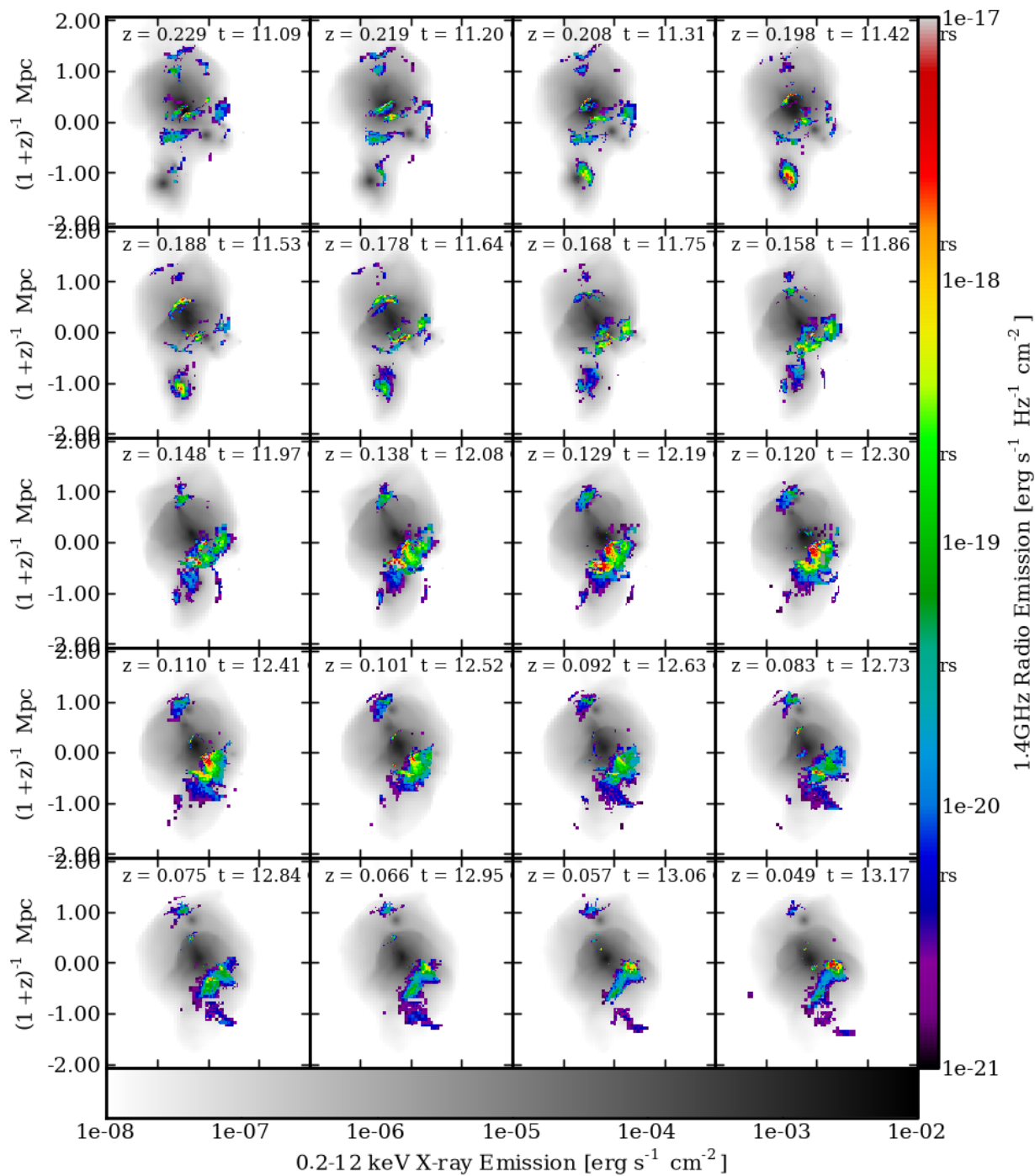


Figure 4.9 1.4 GHz Radio emission overlaid on 0.2-12 keV X-ray emission for 20 snapshots during merger activity of the largest cluster in the *relic64* simulation from  $z=0.23$  to  $z=0.05$ , a time span of 2.08 billion years. Length units are comoving.

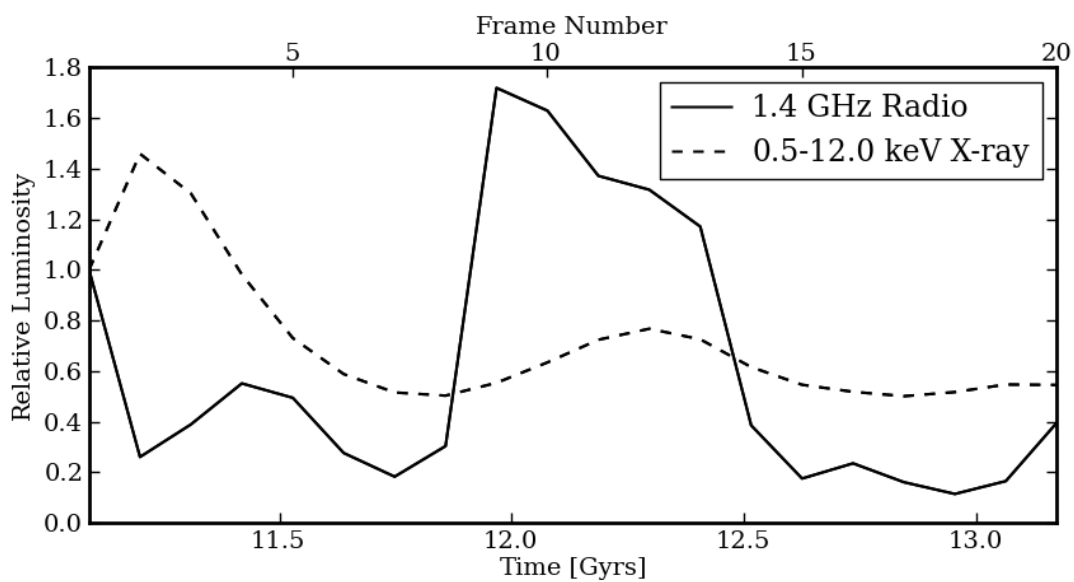


Figure 4.10 Time evolution of 1.4 GHz radio and 0.2-12 keV X-ray luminosities of the merger shown in Figure 4.9, normalized to the luminosities at  $z = 0.229$ . The first frames are a result of a prior merger in its last stages.

respect to their values at  $z = 0.23$  in Figure 4.10.

As we follow the evolution from  $z = 0.23$ , we see the evolution of a major merger where the two cores pass through each other at  $z = 0.22$ . The smaller halo is moving from the center towards the upper-right. As the shockwave builds through  $z = 0.17$ , the radio emission closely follows the X-ray brightness jump, as we would expect. By  $z = 0.16$ , the radio emission from the initial shock has decreased dramatically. While the initial shock has disappeared in the radio, a secondary shock has been created that moves in from the hot ICM into the wake the merger left behind from the middle towards the lower-right. By  $z = 0.15$  (frame 9), this is the most luminous feature in the radio. At this time, the image is 7-8 times brighter in the radio than it was at  $z = 0.16$  (frame 8), illustrating how strongly radio emission depends on the merger state of the cluster. As the halo evolves further, additional smaller objects fall into the ICM, but don't get nearly as bright as major merger. By  $z = 0.1$  (frame 14), the integrated radio luminosity has dropped back to pre-merger levels.

During this merger, the X-ray luminosity also increases, but the total X-ray emission only increases by 50%, which again illustrates the difference in the X-ray and radio emission mechanisms. A detailed analysis of cluster evolution and merger state is reserved for a later study.

#### 4.4.3 Radio Power-X-ray Relationship

Simulation		<i>relic64</i>				<i>relic200</i>			
$z$	Var	A	$\sigma_A$	B	$\sigma_B$	A	$\sigma_A$	B	$\sigma_B$
$z = 0$	Mass	3.1	0.1	18.51	0.07	3.19	0.04	18.14	0.02
$z = 1$	Mass	3.0	0.2	19.38	0.08	3.30	0.08	18.93	0.04
$z = 2$	Mass	1.9	0.4	20.1	0.1	2.8	0.2	20.2	0.1
$z = 0$	X-ray	1.32	0.08	19.32	0.06	1.34	0.02	19.49	0.02
$z = 1$	X-ray	0.9	0.2	19.6	0.2	1.28	0.04	19.52	0.04
$z = 2$	X-ray	1.0	0.3	19.8	0.2	1.0	0.1	20.2	0.1

Table 4.1 Best fit parameters for radio power scaling relationship with halo mass and 0.2-12 keV X-ray emission. Fitting functions are  $10^B(M_{200}/10^{13}M_{\odot})^A$  and  $10^B(L_x/10^{43}erg/s)^A$  for Mass and 0.5-12 keV X-ray luminosity, respectively.

While the X-ray and radio emission may not be coincident in projection, we expect to see



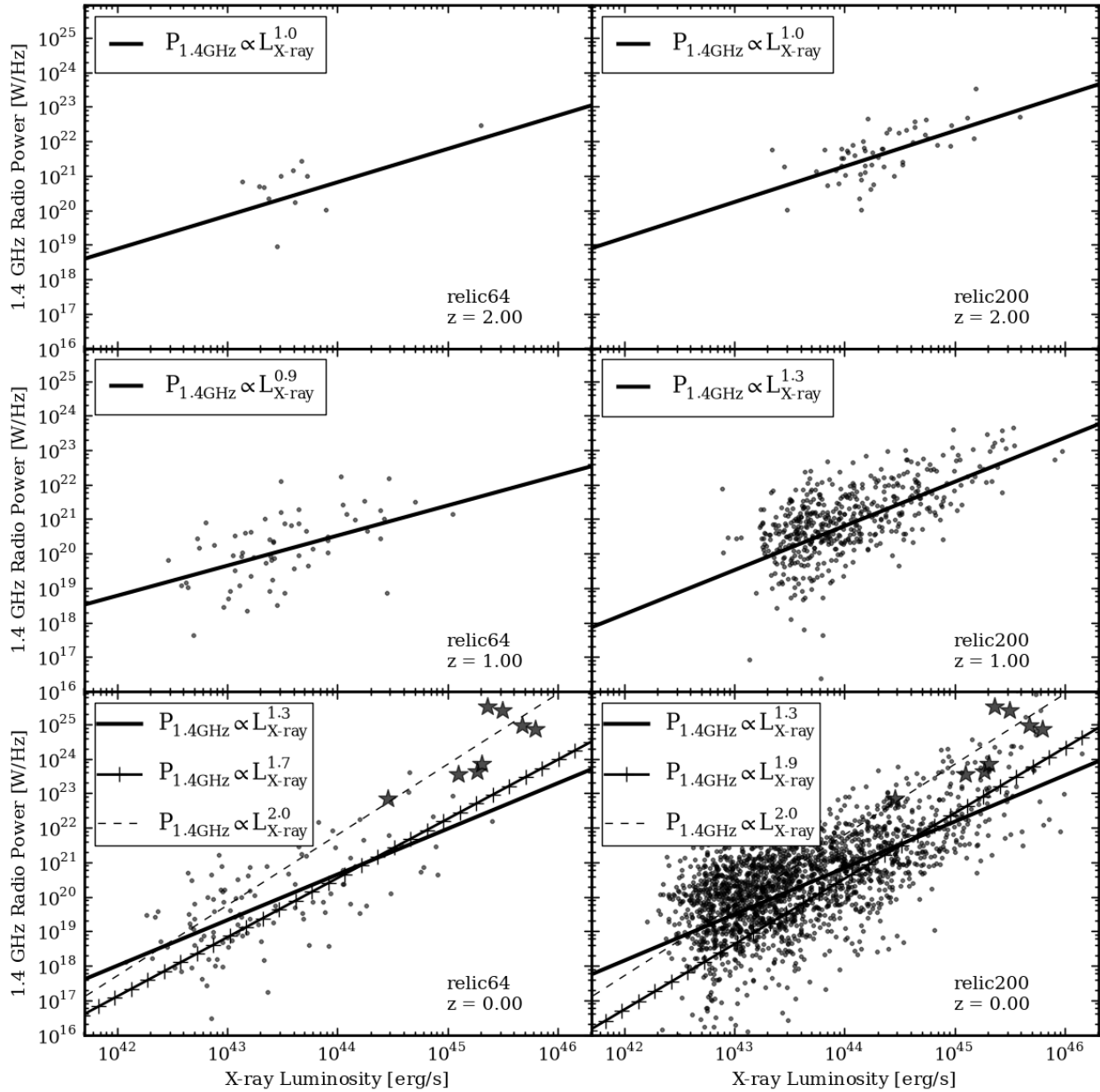


Figure 4.11  $P_{1.4\text{GHz}} - L_X$  relationship for halos in *relic64* (left) and *relic200* (right) for  $z = 2, 1, 0$  from top to bottom. Both radio and X-ray emissivity are integrated out to the virial radius for each halo. A best fit line is found for halos with  $M_{\text{vir}} > 10^{13}M_{\odot}$  and  $2 \times 10^{13}M_{\odot}$  for the *relic64* and *relic200* using a least-squares fitting routine. For  $z = 0$ , we show fits to our data using a minimum mass (solid) as above and minimum X-ray luminosity of  $10^{44}\text{erg/s}$  (solid + crosses). Also shown are observational data (stars) from Feretti [73] along with a best fit (dashed).

a correlation between the total X-ray and radio luminosity since they both sample hot, dense gas. We start our analysis from the results of our radial profiles and examine the  $0.2 - 12\text{keV}$  X-ray and  $1.4\text{ GHz}$  radio emission within  $r_{200}$  for *relic64* and *relic200* in Figure 4.11.

We again use a method of linear-least squares regression described above to obtain a scaling relationship between the X-ray and radio luminosity, the results of which are shown in Table 4.1. Again we see that while there is a clear trend with X-ray luminosity, large scatter in the individual clusters can dominate the relationship. This scatter likely comes from two sources. First, a cluster that is relatively relaxed will have significant X-ray emission, whereas the lack of shocks in such a scenario will necessarily lead to zero radio emission in this model. Second, the fractional increase in X-ray luminosity across a shock front is much less than the radio emission because the X-ray primarily depends on the density of the gas at cluster temperatures, whereas the radio scales with density *and* temperature.

As a function of redshift, the scaling relationship between radio power and X-ray luminosity evolves much like the radio power-mass relationship. Objects with the same X-ray luminosity at early times are more likely to have much higher radio power than their low-redshift counterparts. Additionally, the strength of the relationship increases at low redshift significantly due to the stronger correlation with larger mass halos.

Even though our constraints on the fit parameters seem quite small, one can argue the due to the large scatter there should be a broad range of values capable of producing “acceptable” fits. To give a basic understanding of how our fit parameters can vary, for our two simulations at  $z = 0$ , we have shown the results of fitting using two cuts on our underlying data. The solid line is the result of fitting the points using all halos with a mass greater than  $10^{13}M_{\odot}$  and  $2 \times 10^{13}M_{\odot}$  for the *relic64* and *relic200* simulations, respectively. The solid line with hash marks shows the result of only fitting points with  $L_X > 10^{44}\text{erg/s}$ . As one can see, the slope varies quite dramatically. Therefore when comparing to observational constraints, the selection function of the observed/simulated clusters is very important.

We can compare our derived scaling relationships with observational estimates from known

radio relics. Feretti [73] found X-ray luminosities and  $1.4\text{GHz}$  radio power for 9 Abell clusters. If we fit their data using our same least-squares regression technique, we obtain  $P_{1.4\text{GHz}} \propto L_X^{2.0 \pm 0.5}$ , agreeing quite well within the uncertainties in our  $z = 0$  simulation data. However, the normalization for the real relics are much higher than our simulated relics. We explicitly plot these clusters on Figure 4.11. A very important point from this is that the observed relics land on the high end of both the X-ray luminosity and radio power. This demonstrates the selection effects coming in to play, as we have only observed the brightest objects as of yet. This suggests that deeper observations of radio-quiet clusters should lead to the discovery of low power radio relics. As another constraint, Cassano et al. [43] study this relationship for giant radio halos and find  $P_{1.4\text{GHz}} \propto L_X^{1.74 \pm 0.21}$ . While these giant radio halos are thought to be from turbulent re-acceleration of electrons, their origin is likely linked to the same driving forces (i.e. mergers) as the radio relics. We note here that our X-ray emission is likely underestimated due to our lack of radiative physics in our simulations. However, properly modeling galaxy formation, metal pollution, cooling, and thermal feedback is beyond the scope of this study.

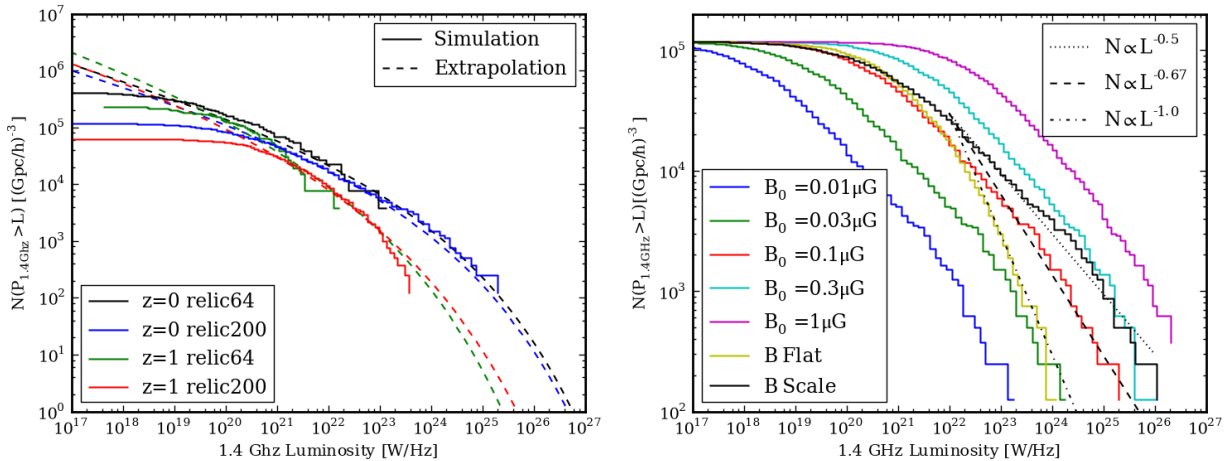


Figure 4.12 (Left) 1.4 GHz Radio Luminosity Function for clusters in *relic64* and *relic200* for  $z = 0, 1$ , in units of inverse comoving  $(\text{Gpc}/h)^3$ . Shown in dashed lines are extrapolations using the Warren et al. [247] mass function and our  $P_{1.4\text{GHz}} - \text{Mass}$  scaling from Table 4.1. (Right) The Radio Luminosity Function for clusters in *relic64* as a function of magnetic field model.

#### 4.4.4 Luminosity Function

Now that we have explored how the radio emission varies as a function of mass and X-ray luminosity, we ask the question: “How many radio relics do we expect at a given luminosity in the Universe?” Here we attempt to answer this question by constructing an observationally-motivated radio luminosity function. This is done by calculating the cumulative number of objects brighter than a given luminosity. We have done so in Figure 4.12, and normalized the count rates by  $h^3(1+z)^3 \text{ Gpc}^{-3}$ .

As we expect from our radio luminosity-mass relationship, the overall shape of the luminosity function is similar to the cluster mass function presented in Section 4.4.2. At first glance this luminosity function is not very encouraging for observational studies because even our most luminous objects are difficult or impossible to capture with current radio telescopes. However, this is primarily a result of the mass range in our current simulations. The known radio relics are associated with massive clusters with  $M > 10^{15} M_{\odot}$ , and our largest clusters in *relic200* only begin to reach the  $10^{15} M_{\odot}$  mark. Obtaining spatial resolution needed to capture the relics in a volume large enough to capture these very rare clusters is computationally difficult. We address this by combining best estimates of the halo mass function with our radio luminosity-mass relationship.

We begin by calculating the best fits for the radio luminosity-mass relationships for both of our simulations. Next, we take fits from Warren et al. [247] for the mass function at redshift 0 and 1. We then convert the mass in the mass function to the expected radio luminosity from our fits in Table 4.1. The results of this fitting are shown in the left panel of Figure 4.12. Because of the scatter in the radio-mass luminosity function, we are able to place rough lower and upper limits on the luminosity function. This scatter will be constrained by future simulations that cover a larger mass scale of galaxy clusters.

As we have done for our other results in Appendix A, we varied the magnetic field model to examine its effects on the luminosity function. The first parameter we changed is the normalization of the magnetic field,  $B_0$ . In Figure 4.12, we show  $B_0 = \{0.01, 0.03, 0.1, 0.3, 1.0\} \mu\text{G}$ . Since the

emitted power is roughly proportional to  $B^{5/2}$  (see Section 3.1), as we increase  $B_0$  the luminosity function shifts quite dramatically to larger luminosities. At low values of  $B_0$  the increase is close to the expected increase of  $B^{5/2}$ , while at higher values  $B$  approaches  $B_{CMB}$ , reducing the effect of the increased local field strength. The second variation was in the scaling of the magnetic field with respect to the electron density. The line labeled “B-Flat” corresponds to  $B = B_0$ , whereas “B-Scale” denotes  $B \propto B_0 n_e$ . In both cases we set  $B_0 = 0.1\mu G$ . With a uniform magnetic field, we see that the number of high-luminosity objects decreases dramatically, while the number of low luminosity objects increases slightly. This is understandable given that the highest luminosity objects come from the most massive clusters, which have the highest densities. In this case, the density doesn’t correspond to higher magnetic fields, and the radio luminosity is diminished with respect to the adiabatic scaling. Similarly, in the “B-Scale” case, the magnetic field strength is even higher in the dense parts of the largest clusters, leading to a shallower slope in the luminosity function. By comparison, Hoeft et al. [110] also found a slope of  $-2/3$  using the same model as the  $B_0 = 0.1\mu G$  line in 4.12, adding verification to both results.

To determine the number of clusters for a given survey area and redshift depth, we integrate the cosmological volume out to  $z = 0.5$  for a given survey area  $d\Omega$ ,

$$\frac{dV}{dzd\Omega}(z) = \frac{c}{H_0} \frac{(1+z)^2 D_A^2}{E(z)} \quad (4.5)$$

with

$$E^2(z) = \Omega_{m,0}(1+z)^3 + \Omega_\Lambda, \quad (4.6)$$

where  $D_A$  is the angular diameter distance. The result of this is that an all-sky survey out to  $z = 0.5$  covers  $26.1 (\text{Gpc}/h)^3$ . In combination with our estimates from the *relic200* simulation in Figure 4.12, we expect to find 180 (conservative) to 1000 (optimistic) clusters with a total radio luminosity of  $10^{25} W/Hz$  within this cosmological volume.

We also see from Figure 4.12 that the luminosity function of halos increases from  $z = 1$  to  $z = 0$ . However, if plotted using proper volumes, the factor of 8 brings the two luminosity

functions much closer together. Therefore the proper number density of radio relics seems to be fairly constant through cosmic time. This is an unexpected result, and encouraging for moderate redshift studies of radio relics. We note here that the frequency at which telescopes receive this synchrotron emission changes as a function of the emitter’s redshift. Therefore when deriving the radio luminosity of an object at redshift  $z$ , we use  $\nu = 1.4 \text{ GHz} (1 + z)$ . Because of this, the emitted power is actually decreased since  $P_{1.4\text{GHz}} \propto \nu^{-s/2}$  where  $s \approx 2$  for strong shocks. The power emitted in the cluster’s frame is therefore substantially larger than what is shown in Figure 4.12. The similar luminosity function is therefore a product of the increased merger and accretion activity at higher redshift compared to that at  $z = 0$ .

## 4.5 Discussion

### 4.5.1 Comparison To Previous Work

In order to compare our results to previous shock studies, we have calculated the kinetic energy flux through shocks, as shown in figure 4.13. The left two panels show the kinetic energy flux as a function of Mach number in the *relic64* and *relic200* simulations, respectively. The right panels instead show the radio emission as a function of Mach number. While the black lines denote all temperatures, we also show the breakdown in terms of the pre-shock temperature. The kinetic energy flux results here can be directly compared to Figure 6 of Ryu et al. [204], Figure 10 of Skillman et al. [212], Figure 11 of Vazza et al. [239], and can also be compared after unit conversions to Figure 6 of Pfrommer et al. [179]. Even though these simulations all vary in size and adopted cosmological parameters, the similarities in the kinetic energy flux processed by shocks is quite strong. This suggests that the underlying shock characteristics are quite well understood even if the particular radio emission models vary.

In the right panels of 4.13, we can see that there is a larger difference between the two simulations presented here in terms of the radio emission. This is likely due to the varying mass scales present in the simulations. We have also subsampled the *relic200* simulation into random

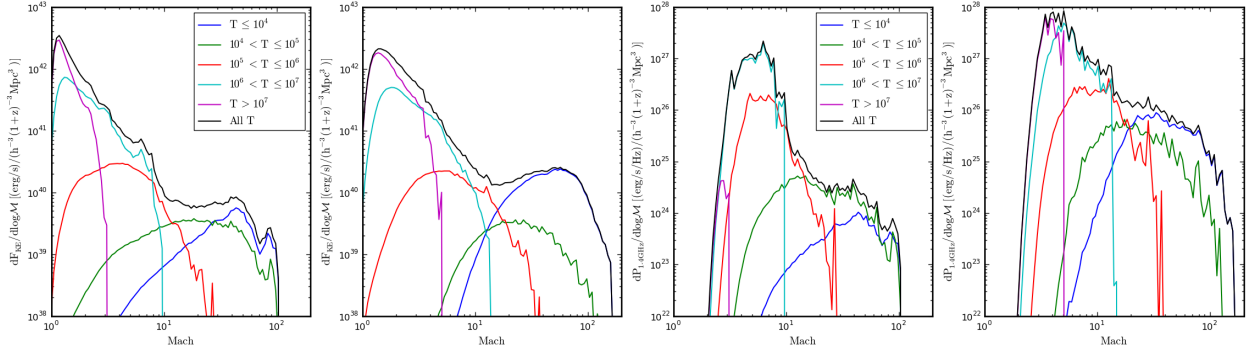


Figure 4.13 Left Panels: *relic64* and *relic200* kinetic energy flux processed by shocks at  $z = 0$ . Right Panels: 1.4 GHz radio emission.

$(64\text{Mpc}/h)^3$  domains and found that a major contribution is confined to one of these subdomains.

One of the earliest studies of shocks in a cosmological context is found in Miniati et al. [156], where the authors found similar shock structure and kinetic energy flux trends as is seen in this study, though in a unigrid context. They, too, found that intermediate Mach number shocks are responsible for processing the majority of kinetic energy. In a pioneering work, Miniati et al. [157] studied the injection and evolution of cosmic ray electrons. Using a framework to follow the cosmic ray distribution, they presented a radio power - core temperature relationship that shows strong similarity to what we have found with respect to cluster mass and X-ray luminosity, including a larger amount of scatter from cluster-to-cluster. Even though the resolution was modest compared to studies here, many of the primary characteristics of the radio emission are similar.

Much of our work presented here can be compared with that of Hoeft et al. [110]. We use the same radio emission model, but instead apply it to AMR simulations as opposed to smoothed particle hydrodynamic simulations. In particular, we can compare our radio relic luminosity function in Figure 4.12 to their Figure 9. After accounting for the different normalization, we find that we have more objects at  $\sim 10^{25} W/Hz$ . However, this result is from a small number of objects in our simulations and therefore future simulations with a larger sample of galaxy clusters are needed.

In Pfrommer et al. [181], the authors studied the acceleration and emission properties of cosmic ray electrons and protons in a smoothed particle hydrodynamics setting which focused on a set of high resolution galaxy clusters. Many of the same characteristics of galaxy cluster radio

relic emission that we found in this study are consistent with their results. The morphology of the radio relic emission is very similar to our results, though since they follow the electron population through time the emission is more diffuse compared to our simulated clusters. In another paper in the same series, Pfrommer [178] study the scaling relationship between the radio synchrotron, gamma-ray, and inverse Compton emission from the same set of galaxy clusters. Their results when fitting the scaling relationship between radio synchrotron emission and cluster mass give a significantly shallower slope of  $1 - 1.5$ . However, due to the small number of clusters in their study, it is difficult to tell if there is a meaningful difference between their results and the ones presented here. In future work it would be useful to run a series of high resolution AMR simulations using our methods to compare to their results.

#### 4.5.2 Implications For Future Surveys

Our study has shown that nearly every cluster has radio emission and displays signs of radio relics at some stage in their evolution. When and where this radio emission occurs, however, is very sensitive to the merger and evolutionary state of the cluster. Current studies of radio relics have been confined to pointed observations of nearby, massive clusters, often based on strong X-ray emission. While this observational strategy does conform to our general results found in mass and X-ray scaling relationships, we have determined that not all X-ray luminous or massive clusters have significant relic emission. It is instead heavily biased towards disturbed, merging clusters. Because the surface brightness of these relics is low due to their extended nature, large surveys with near-future telescopes are unlikely to yield serendipitous discoveries of cluster radio emission. Instead, the focus should be on deep, multiwavelength, large field-of-view observations with sensitivity to extended diffuse radio emission of disturbed X-ray clusters.

Additionally, studies must include regions away from the peak X-ray emission. As was seen in Section 4.4, radio emission from shocks is generally brightest at the edges of clusters, surrounding the X-ray emission. This prescribes a fairly difficult observational roadmap, but the potential benefits include studying fundamental plasma physics phenomena such as in-situ shock electron



acceleration and magnetic field structure. By combining statistical and morphological studies of these objects, we can readily compare them with the high-resolution hydrodynamical simulations presented here.

Our luminosity function, derived from the Warren et al. [247] mass function, suggests what can be expected in future observational studies. With surface brightness sensitivity improvements of a factor of 10, we can expect to see an increase of a factor of 10-100 in the number of clusters with radio relics. Alternatively, an all-sky survey out to  $z = 0.5$  should result in the discovery of  $\sim 200$  clusters above a luminosity of  $10^{25} W/Hz$ .

### 4.5.3 Limitations of the Models

There are several limitations to this study. First, we have not performed self-consistent MHD simulations, and instead adopted a scaling relationship between the post-shock density and magnetic field. This leads to the absence of any magnetic field configurations imprinting their structure on the radio relics. We plan to incorporate MHD simulations in future work. However, since  $B \sim B_{CMB}$  in the cluster environments we study here, the magnitude of our radio emission should not change dramatically. We are also not presenting a self consistent view of magnetic field generation, evolution, and non-linear interactions with shocks or particle acceleration, all of which are poorly understood in a cosmological context.

Second, due to our relatively small box sizes, we have not captured the largest objects in the universe, which are likely to produce the brightest radio signatures. To account for this, we have provided an estimate using an analytic mass function combined with mass-luminosity scaling relationships. However, self-consistently capturing these very massive clusters is important, and will be explored in future work. Third, we also only follow recently accelerated electrons and ignore the aging of electron populations or re-accelerated electrons, which is likely to be important for radio halos and steep-spectrum objects. A more realistic model would follow the electron population “on-the-fly” and modify the acceleration efficiency as a function of pre-existing electron populations. Given that we assume radio emission only comes from electrons that have just been accelerated,

this means that the radio relic luminosities shown are lower limits.

While our spatial and mass resolutions are quite good in the *relic64* simulation, it is likely that increasing the resolution would have an affect on our results. Skillman et al. [212] found that in terms of the kinetic energy processed by shocks, a peak spatial resolution of  $3.9kpc/h$  and a mass resolution of roughly  $10^9 M_\odot$  was approaching a converged result, though perfect convergence was not seen. In *relic64* our spatial resolution matches this value, while we are a factor of two above this mass resolution. For *relic200*, we are likely not capturing all of the kinetic energy flux in low Mach number shocks, which would suggest a higher spatial and mass resolution simulation would lead to somewhat higher radio luminosity emission. This will likely always be the case since any increase in mass resolution will lead to a greater sampling of the mass function, allowing one to follow the merger assembly of galaxy clusters more accurately. This should increase the frequency of merger shocks, increasing overall radio emission.

Finally, the electron acceleration efficiency in Equation 4.3 is poorly constrained at present. With additional radio observations, particularly using next generation low frequency radio telescopes, along with new PIC simulations, we may be able to calibrate  $\xi_e$  to more accurate values. This could be important in scaling the radio luminosity function in Figure 4.12 and estimating the number of radio relics expected in clusters and/or sky surveys.

## 4.6 Conclusions and Future Directions

We have carried out high resolution AMR cosmological simulations using our accurate shock finding algorithm with a radio emission model for shock-accelerated electrons to examine the properties of radio relics in galaxy clusters. From this model, our main results are:

- We have produced synthetic radio maps of the large scale structure and cluster environments, showing the variety of radio relic morphologies and locations.
- Through the use of 2D phase diagrams, we have found that while there is radio emission from both merger (internal) and accretion shocks, the emission from the hot, dense in-

tracluster medium associated with the merger shocks dominate the total emission. This balance is redshift-dependent, with accretion shocks being more important at high redshift.

- We have generated scaling relationships using over 2000 simulated halos that give insight to how radio emission scales with mass and X-ray luminosity. These relationships evolve with redshift and there is a large scatter for individual halos as a result of merger state.
- By studying the time evolution of a cluster undergoing a merger, we find that the radio emission is highly dependent on the merger state, varying on time scales of a few hundred million years.
- We have produced a synthetic radio luminosity function that gives observational predictions for the number of clusters with radio relics. This can be used to compare to future observed cluster luminosity functions and as a test of synchrotron emission models.

In future studies we plan to examine the merger history and morphology of these objects in greater detail. The redshift evolution of individual clusters is likely to be heavily correlated with merger state, and a statistical study of this relationship is vital to future observational studies. Finally, in order to correctly model these radio relics, we need to self-consistently follow the electron population, taking into account effects of particle aging and re-acceleration. Future studies will also examine larger cosmological volumes and implement techniques such as light cones.

## Chapter 5

### Cosmological MHD Simulations of Galaxy Cluster Radio Relics: Insights and Warnings for Observations

As published in S. W. Skillman, H. Xu, E. J. Hallman, B. W. OShea, J. O. Burns, H. Li, D. C. Collins, and M. L. Norman. Cosmological Magnetohydrodynamic Simulations of Galaxy Cluster Radio Relics: Insights and Warnings for Observations. *ApJ*, 765:21, March 2013. doi: 10.1088/0004-637X/765/1/21. Reproduced by permission of the AAS. [214]

#### 5.1 Introduction

Galaxy clusters are hosts to a variety of thermal and non-thermal phenomena, many of which are the result of cosmological structure formation. The study of relativistic particles in galaxy cluster environments was motivated by the observation of the radio halo in the Coma cluster by Large et al. [137], and has since grown into an industry of observations, theory, and simulation. For a review on current radio observations of galaxy clusters see Ferrari et al. [80], Feretti et al. [77], and for a review on the non-thermal processes see Dolag et al. [59]. Here we review the basic characteristics of galaxy cluster radio “halos” and giant radio “relics,” to use the classification in Ferrari et al. [80]. Radio halos are usually  $\sim$  Mpc-sized features in galaxy clusters, closely following the X-ray morphology in the central regions of the cluster. They are generally characterized by very low ( $<$  few percent) linear polarization fractions, and are found in galaxy clusters with disturbed morphology and no evidence for a cool core [80, 93, 77]. The origin of the emission is thought to be from relativistic ( $\gamma \sim 10^4$ ) electrons emitting synchrotron radiation. The source of the energy in

these electrons, however, is debated. It may originate from the decay of pions (the “secondary” or “hadronic” model), created by interactions between cosmic ray protons and the thermal population [55, 56, 157], which would be strengthened by the observation of gamma-ray emission in cluster cores. However, initial studies of many galaxy clusters using the FERMI satellite [3], as well as for fewer objects with other instruments, e.g. MAGIC observations of Perseus[6, 7], combined with radio data [114, 32] constrain the energy in cosmic rays to be very low ( $\ll 10\%$ ) of the thermal energy in most cases. Others believe that the electrons are turbulently accelerated either from the thermal population or from aging populations of electrons either from shock acceleration or AGN/supernova injection [30].

Radio relics, on the other hand, are thought to be accelerated by first-order Fermi acceleration through the process of Diffusive Shock Acceleration (DSA) [23]. They have a relatively steep radio, and therefore inferred electron, spectrum where  $S \propto \nu^{-\alpha}$  with  $\alpha \approx 1 - 2$ . These radio sources are not associated with any of the cluster galaxies or AGN bubbles. They are also not associated with any point sources in other wavelengths, and are usually found in the outskirts of clusters. Their location can be up to  $\sim 2$  Mpc from the cluster core, and can be extended up to  $\sim 1.5$  Mpc in length [232, 235, 237]. In some cases these radio features are coincident with X-ray surface brightness and temperature jumps, potentially indicating the presence of a shock front [81, 5]. Early work by Ensslin et al. [70], Roettiger et al. [195], Venturi et al. [242] originally proposed that cosmological structure formation shocks may be responsible for the acceleration of these relativistic electrons. The original source of these electrons may be from the ICM itself or from prior outburst in radio galaxies [69, 68]. While more rare, double radio relics are observed in several systems. Double radio relics are unique in that they provide tighter constraints on the geometry and kinematics of the merging clusters[233]. Upcoming radio telescopes such as LOFAR, the Jansky VLA, and eventually the SKA will provide an increase in sensitivity and resolution (both spectral and spatial) that will allow for discoveries in blind surveys. Because of this, we are at an important time to use simulation and theory to predict the number and the properties of relics in cosmological samples. Past simulations have focused on both single clusters [195, 181, 13] as well as ensembles of clusters

[110, 213, 241, 164]. Both are needed in order to constrain the plasma physics and how varying environments lead to observational quantities such as luminosity functions.

In this paper we investigate the origins, properties, and observational implications of a merging galaxy cluster using a numerical simulation. For the first time, we start from cosmological initial conditions and self-consistently evolve the cluster magnetic field from an AGN source the equations of magnetohydrodynamics rather than assuming a magnetic field strength and topology. This allows us to explore one scenario in which the magnetic field forms, evolves, and interacts with the radio relic emission. We describe, in detail, the plasma environment of the radio-emitting regions.

After investigating the properties of the cluster gas, we analyzed the resulting radio emission using novel approaches to explore systematic effects present in current radio observations. We used a new tool to view this Eulerian grid simulation from arbitrary directions in order to demonstrate the effect of viewing angle on the derived properties. We then developed the capability to integrate the polarized radio emission along the line of sight to provide the closest comparison to observations. We then use this technique to produce polarization fraction and position angle maps from our MHD AMR simulation, and provide comments on the relevance of our results to current observations of radio features in galaxy clusters. Finally, we discuss the impact of using previous assumptions about the magnetic field compared to the values that are self-consistently evolved from an AGN source. We use this to provide insight into observational results.

## 5.2 Methods

### 5.2.1 Simulations

Our simulation was run using a modified version of the *Enzo* cosmology code [34, 33, 163, 167]. *Enzo* uses block-structured adaptive mesh refinement [AMR; 17] as a base upon which it couples an Eulerian hydrodynamic solver for the gas with an N-Body particle mesh (PM) solver [65, 107] for the dark matter. In this work we utilize the MHD solver described in Collins et al. [50]. The

solver employed here is spatially second order, while the PPM solver [49] commonly used in *Enzo* is spatially 3rd order. The net effect on the shock-finding algorithm will be to broaden a single shock by a small amount. However it will be impossible to disentangle this effect from the changes in shock structure due to the addition of magnetic forces in the evolution. None of the results we present here will be sensitive to these small differences. We have extended this version of *Enzo* to include temperature-jump based shock-finding as described in Skillman et al. [212] and used in Skillman et al. [213].

The galaxy cluster studied in this work is the same as cluster U1 in Xu et al. [256]. In this work, clusters were formed from cosmological initial conditions, and magnetic fields were injected by the most massive galaxy at a variety of stages in the cluster evolution. It was found that different injection parameters of magnetic fields have little impact on the cluster formation history. This simulation models the evolution of dark matter, baryonic matter, and magnetic fields self-consistently. The simulation uses an adiabatic equation of state for gas, with the ratio of specific heat being  $5/3$ , and does not include heating or cooling physics or chemical reactions. While studies have been done including these physical models and their role in characterizing shocks [125, 180], we chose to ignore them due to both computational cost as well as possible confusion between structure formation shocks and those arising from star/galaxy feedback. Additionally, Kang et al. [125] found little effect on the overall kinetic energy dissipation between simulations with adiabatic gas physics and those including cooling and feedback, and while Pfrommer et al. [180] show changes at high Mach number, as we will see these have little consequence for the shocks involved with producing radio relics.

The initial conditions of the simulation are generated at redshift  $z = 30$  from an Eisenstein and Hu [66] power spectrum of density fluctuations in a  $\Lambda$ CDM universe with parameters  $h = 0.73$ ,  $\Omega_m = 0.27$ ,  $\Omega_b = 0.044$ ,  $\Omega_\Lambda = 0.73$ ,  $\sigma_8 = 0.77$ , and  $n_s = 0.96$ . These parameters are close to the values from WMAP3 observations [217]. While these parameters differ from the latest constraints, it is largely irrelevant for this particular project. The simulated volume is  $(256 h^{-1}\text{Mpc})^3$ , and it uses a  $128^3$  root grid and 2 nested static grids in the Lagrangian region where the cluster forms.

This gives an effective root grid resolution of  $512^3$  cells ( $\sim 0.69$  Mpc) and dark matter particle mass resolution of  $1.07 \times 10^{10} M_{\odot}$ . During the course of the simulation, 8 levels of refinements are allowed beyond the root grid, for a maximum spatial resolution of  $7.8125 h^{-1}$  kpc. The AMR is applied only in a region of  $(\sim 43 \text{ Mpc})^3$  where the galaxy cluster forms near the center of the simulation domain. The AMR criteria in this simulation are the same as in Xu et al. [256]. During the cluster formation but before the magnetic fields are injected, the refinement is only controlled by baryon and dark matter density, refining on overdensities of 8 for each additional level. After magnetic field injections, in addition to the density refinement, all the regions where magnetic field strengths are higher than  $5 \times 10^{-8} \text{ G}$  are refined to the highest level. The importance of using this magnetic field refinement criterion in cluster MHD simulations is discussed in Xu et al. [255].

The magnetic field initialization used is the same method in Xu et al. [253, 254] as the original magnetic tower model proposed by Li et al. [140], and assumes the magnetic fields are from the outburst of AGN. The magnetic fields are injected at redshift  $z = 3$  in two proto-clusters, which belong to two sub-clusters. The injection locations are the same locations in simulations U1a and U1b in Xu et al. [256]. There is  $\sim 6 \times 10^{59}$  erg of magnetic energy placed into the ICM from each injection, assuming that  $\sim 1$  percent of the AGN outburst energy of a several  $10^8 M_{\odot}$  SMBH is in magnetic fields. Previous studies [255] have shown that the injection redshifts and magnetic energy have limited impact on the distributions of the ICM magnetic fields at low redshifts.

The simulated cluster is a massive cluster with its basic properties at redshift  $z = 0$  as follows:  $R_{\text{virial}} = 2.5$  Mpc,  $M_{\text{virial}}(\text{total}) = 1.9 \times 10^{15} M_{\odot}$ ,  $M_{\text{virial}}(\text{gas}) = 2.7 \times 10^{14} M_{\odot}$ , and  $T_{\text{virial}} = 10.3$  keV. This cluster is in an unrelaxed dynamical state at  $z = 0$  with its two magnetized sub-clusters of similar size undergoing a merger. The total magnetic energy in the simulation at  $z = 0$  is  $9.6 \times 10^{60}$  erg, nearly all of which is within the cluster virial radius. The details about the cluster formation are described in Xu et al. [256].



### 5.2.2 Synchrotron Emission

We use the same technique as was presented in Skillman et al. [213] and based on Hoeft and Brüggén [109], except we no longer rely on the assumption that the magnetic field is a simple function of density and instead use the magnetic field from the simulation. This method assumes that a fraction of the incoming kinetic energy of the gas is accelerated by the shock up to a power-law distribution in energy, which extends from the thermal distribution. This distribution is that predicted by diffusive shock acceleration theory in the test-particle limit [61, 14, 146, 2, 23, 165]. At the high energy end, it also assumes that there is an exponential cutoff determined by the balance of acceleration and cooling. The total radio power from a shock wave of area  $A$ , frequency  $\nu_{obs}$ , magnetic field  $B$ , electron acceleration efficiency  $\xi_e$ , electron power-law index  $s$  ( $n_e \propto E^{-s}$ ), post-shock electron density  $n_e$  and temperature  $T_2$  is [109]

$$\frac{dP(\nu_{obs})}{d\nu} = 6.4 \times 10^{34} \text{ erg s}^{-1} \text{ Hz}^{-1} \frac{A}{\text{Mpc}^2} \frac{n_e}{10^{-4} \text{ cm}^{-3}} \frac{\xi_e}{0.05} \left(\frac{\nu_{obs}}{1.4 \text{ GHz}}\right)^{-s/2} \times \left(\frac{T_2}{7 \text{ keV}}\right)^{3/2} \frac{(B/\mu\text{G})^{1+(s/2)}}{(B_{CMB}/\mu\text{G})^2 + (B/\mu\text{G})^2} \Psi(\mathcal{M}). \quad (5.1)$$

where  $\Psi(\mathcal{M})$  is a dimensionless shape function that rises steeply above  $\mathcal{M} \sim 2.5$  and plateaus to 1 above  $\mathcal{M} \sim 10$ . In all work presented we use a fiducial value of  $\xi_e = 0.005$ , as suggested in Hoeft et al. [110], and the same as used in Skillman et al. [213].

There are several important things to notice about this model, which will help guide our interpretations of the results throughout this paper. First, the emission scales linearly with the downstream electron density, and with the downstream temperature to the 3/2 power. Additionally, in regions where the magnetic field is less than the equivalent magnetic field strength from the CMB energy density,  $B_{CMB}$ , the emission scales with  $B^{1+s/2}$ , where  $s \sim 3$  for most relic situations.

### 5.2.3 Analysis Tools

In this work we relied heavily on the data analysis and visualization toolkit, *yt* [229], to produce the derived data products presented. Here we describe the tools used specifically in our

analysis, and leave further description to the *yt* documentation <sup>1</sup>. Derived Quantities<sup>2</sup>, such as `WeightedAverageQuantity` and `TotalQuantity`, are used to calculate weighted averages and totals of fluid quantities. For example, we use `WeightedAverageQuantity` to calculate the average temperature, weighted by cell mass. To analyze properties such as the radio and X-ray emission from our simulations, we use `Derived Fields` <sup>3</sup> to define the functional form of our new fields, which is then calculated on a grid-by-grid basis as needed. To calculate distribution functions, either as a function of position or fluid quantity, we utilize `1-D Profiles` and `2-D Phase Plots`<sup>4</sup>. By specifying a binning field, we are then able to calculate either the total of another quantity or the average (along with the standard deviation). These are used to create radial profiles as well as characterize quantities such as the average magnetic field strength as a function of density and temperature. We also take advantage of adaptive slices and projections. `Slices`<sup>5</sup> sample the data at the highest resolution data available, and return an adaptive 2D image that can then be re-sampled into fixed resolution images. Similarly, we use weighted and unweighted projections<sup>6</sup> of quantities to provide average or total quantities integrated along the line of sight. Again, these adaptive 2D data objects can then be re-sampled to create images at various resolutions. We also utilize and extend off-axis projections for use in integrating the polarization vectors of radio emission, to be described further in Section 5.2.4. Finally, we use the spectral frequency integrator to calculate the X-ray emission based on the `Cloudy` code, as was done in Skillman et al. [213] and Hallman and Jeltama [103], and was described in detail in Smith et al. [216].

#### 5.2.4 Polarization

In addition to calculating the synchrotron emission, in this paper we investigate the polarization fraction and position angles of the emission. In order to compare our simulations to observations, we have developed several new tools, including the ability to calculate the polariza-

---

<sup>1</sup> <http://yt-project.org/doc>

<sup>2</sup> <http://yt-project.org/doc/analyzing/objects.html#derived-quantities>

<sup>3</sup> [http://yt-project.org/doc/analyzing/creating\\_derived\\_fields.html](http://yt-project.org/doc/analyzing/creating_derived_fields.html)

<sup>4</sup> <http://yt-project.org/doc/visualizing/plots.html#d-profiles>

<sup>5</sup> <http://yt-project.org/doc/visualizing/plots.html#slices>

<sup>6</sup> <http://yt-project.org/doc/visualizing/plots.html#projections>

tion properties of the radio emission. In this section, we describe how we calculate Stokes I, Q, and U parameters from any viewing angle of our simulation. For a review of these topics, see Burn [36], Longair [144], Heiles [105]. While previous analyses of polarized emission were capable of viewing along the coordinate directions, to our knowledge, **this is the first presentation of off-axis polarized radio emission from AMR simulations**<sup>7</sup>. This capability presents several challenges. Whereas the total radio emission is calculated as a direct sum of the emission multiplied with the path length, the calculation of the polarized emission requires simultaneous integration of each polarized component along the line of sight due to their mixing through Faraday rotation.

We have built this capability on top of the analysis package *yt*. We began with the “off-axis projection”<sup>8</sup> operation, which is an off-axis ray-casting mechanism. It operates by creating a fixed-resolution image plane for which each pixel is then integrated through the simulation volume. To do this correctly, first the AMR hierarchy is homogenized into single-resolution bricks that uniquely tile the domain. This ensures that only the highest resolution data is used for a given point in space. These bricks are ordered and traversed by the image plane. The result of this is that we are able to integrate along the line of sight through the AMR hierarchy sampling only the highest-resolution cells for that given point in space.

We have furthermore modified this framework such that the RGB channels of the image act as the total emission, I, and polarized emission along the x,  $I_x$ , and y,  $I_y$ , axes.  $I_x$  and  $I_y$  can be thought of as the emission-weighted electric field. The details of this calculation can be found in Appendix A. We first create derived fields that correspond to the magnetic field projected onto the unit vectors  $\vec{v}_x$ ,  $\vec{v}_y$  and  $\vec{v}_\parallel$ , where  $\vec{v}_x$  and  $\vec{v}_y$  are defined with respect to east and north vectors defined by the viewing direction,  $\vec{v}_\parallel$ . We label these magnetic fields as  $B_x$ ,  $B_y$ , and  $B_\parallel$ , respectively. We then define the polarization angle  $\chi$  of the electric field as the angle made between  $B_x$  and  $B_y$  rotated by  $\pi/2$ . Finally, we define a Faraday rotation field  $\Delta\phi = 2.62 \times 10^{-17} \times \lambda^2 n_e B_\parallel dl$ , where all variables are in cgs units. Using a similar notation to [169], we then integrate along the line of

<sup>7</sup> Hoeft et al. [110] studied the view dependence on the total radio emission

<sup>8</sup> <http://yt-project.org/doc/cookbook/index.html#cookbook-offaxis-projection>

sight the  $I$ ,  $I_x$ , and  $I_y$  values using the following discrete step:

$$\begin{bmatrix} I_{i+1} \\ I_{x,i+1} \\ I_{y,i+1} \end{bmatrix} = \begin{bmatrix} dl & 0 & 0 \\ dl f_p (\vec{v}_x \cdot \vec{E}) & \cos(\Delta\phi) & -\sin(\Delta\phi) \\ dl f_p (\vec{v}_y \cdot \vec{E}) & \sin(\Delta\phi) & \cos(\Delta\phi) \end{bmatrix} \begin{bmatrix} \epsilon_i \\ I_{x,i} \\ I_{y,i} \end{bmatrix} \quad (5.2)$$

where  $\Delta\phi$  is the Faraday rotation,  $\vec{v}_x$  and  $\vec{v}_y$  are the image plane coordinate vectors,  $f_p$  is the fractional polarization of the synchrotron radiation of a given power-law slope of electrons,  $dl$  is the ray segment length between the incoming and outgoing face of each cell, and  $\vec{B}$  is the magnetic field. Once integrated through the volume, we are then able to create intensity, polarization fraction, and polarization direction maps. This capability is available to download using the changeset with hash fc3acb747162 here: <https://bitbucket.org/samskillman/yt-stokes>.

### 5.3 Radio Relic Properties

In this section we describe the general properties of the simulated galaxy cluster. We begin by comparing the morphological similarities between our simulated cluster and several observed clusters. We then move on to describe the other gas properties in an effort to constrain the properties of the radio-emitting plasma. Finally, we will look at the time evolution of these quantities in order to understand their coupling during the merger process.

#### 5.3.1 Simulated Radio & X-ray

We begin by comparing the radio and X-ray emission from our simulation with the radio relics present in A3376 (see Figure 1a. in Bagchi et al. [11]) and CIZA J2242.8+5301 (see Figure 1 in van Weeren et al. [232]). In this work we calculate the X-ray emission using Cloudy to integrate the emission from 0.5 – 12 keV assuming a metallicity of  $Z/Z_{solar} = 0.3$ . The resulting 1.4 GHz radio and 0.5 – 12 keV X-ray emission is overlaid in Figure 5.1. The X-ray is shown in color with a dynamic range of 100. The radio flux is calculated by placing the simulated cluster at a distance of  $100Mpc/h$ . We then mask the radio emission such that  $10^{-3} - 10^1$  mJy is visible. The total

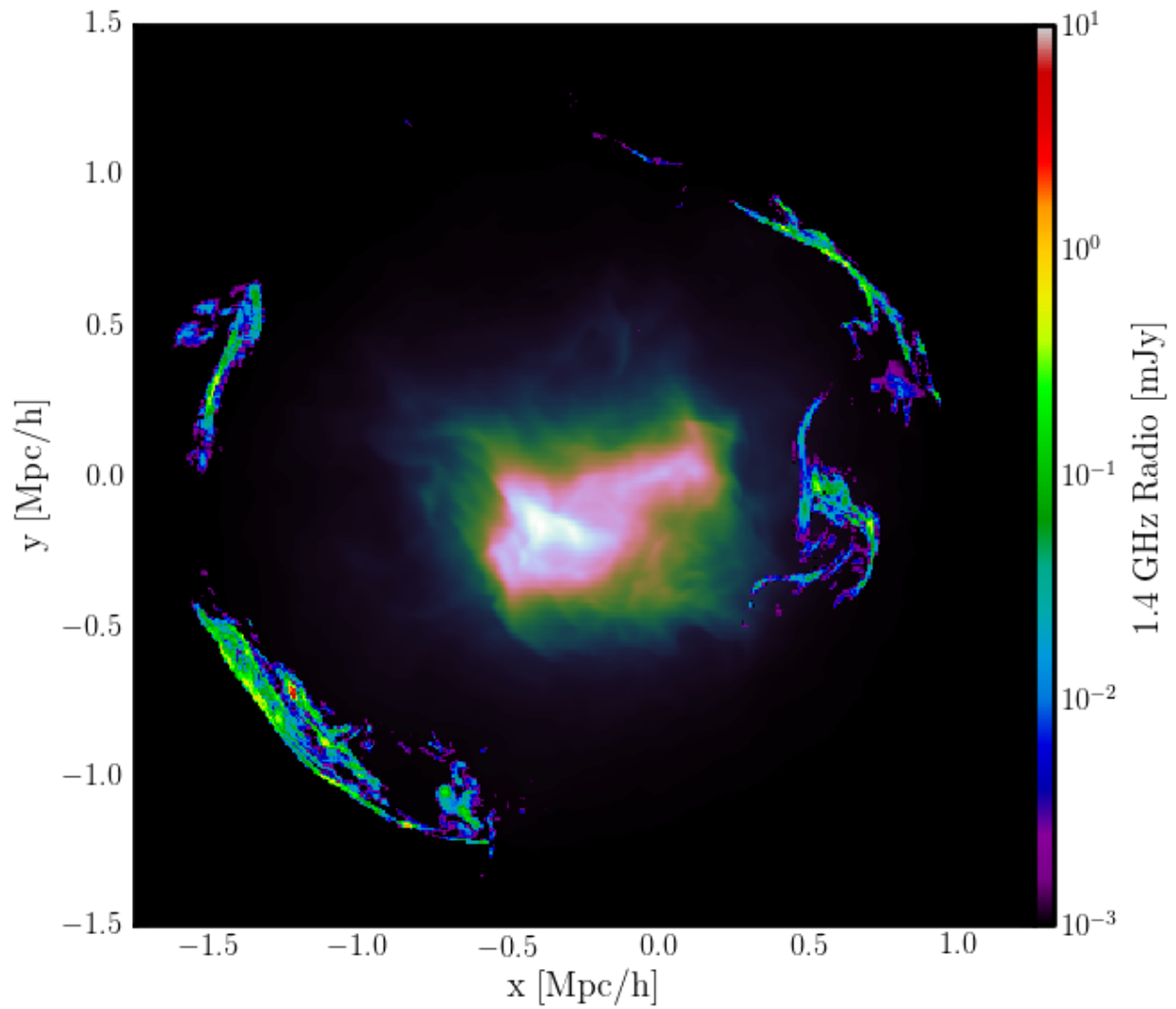


Figure 5.1 Simulated X-ray and radio emission. The X-ray in the central regions shows a dynamic range of 100. The radio emission is calculated by placing the simulated cluster at  $100 Mpc/h$ , and masked to show a dynamic range of  $10^4$ .

integrated flux for the left and right relics are  $9.67 \times 10^{24}$  and  $3.11 \times 10^{24} W/Hz$  at  $1.4GHz$ , which is similar to many of the observed single and double radio relics [77].

There are a few specific details that we highlight here due to their similarities to many observed radio relics. First, we note that this appears as a double radio relic. These are relatively rare compared to their single-sided counterparts. This snapshot is following a major merger roughly 300 Myr after core passage. The primary cluster is moving to the lower-left, with the secondary moving primarily to the right. After core passage, a merger shock develops, moving both to the lower left and upper right, and as will be seen in later figures, aligns with strong jumps in temperature and density. The two relic features are aligned with the direction of the merger as well as the shape of the X-ray emission. This alignment of the X-ray morphology and radio emission is characteristic of double radio relics (see Skillman et al. [213]), as well as many single relics [e.g. 234, 28].

The second key feature to this simulated double relic is the apparent aspect ratio of the radio emission. The length of the left relic (if we connect the two pieces that are separated by a short distance) is more than 2 Mpc/h, while the right-moving relic is  $1.5 - 2.0$  Mpc/h. While these relics are quite elongated, they are very thin. In many regions it is at most  $100 - 200$  kpc/h wide, even in projection. We note here, however, that this width is most likely underestimated since we are not tracking the aged populations of electrons that would exist for some amount of time behind the shock front.

Comparing to A3376 [11], we see many striking resemblances, including the complex morphology of the Eastern portion of the relic as well as the ring-like structure to the outline of the radio emission. This, at the very least, suggests that the radio-emitting electrons are indeed related to the shock structures formed in merging galaxy clusters. We see a similar structure in CIZA J2242.8+5301 [232], where the elongation of the X-ray emission points in the direction of the merger, aligning with the double radio relic. We also note the resemblance here with our simulation in terms of the very thin region of radio emission along the relic. This suggests that the cooling times of the relativistic electrons must be short.

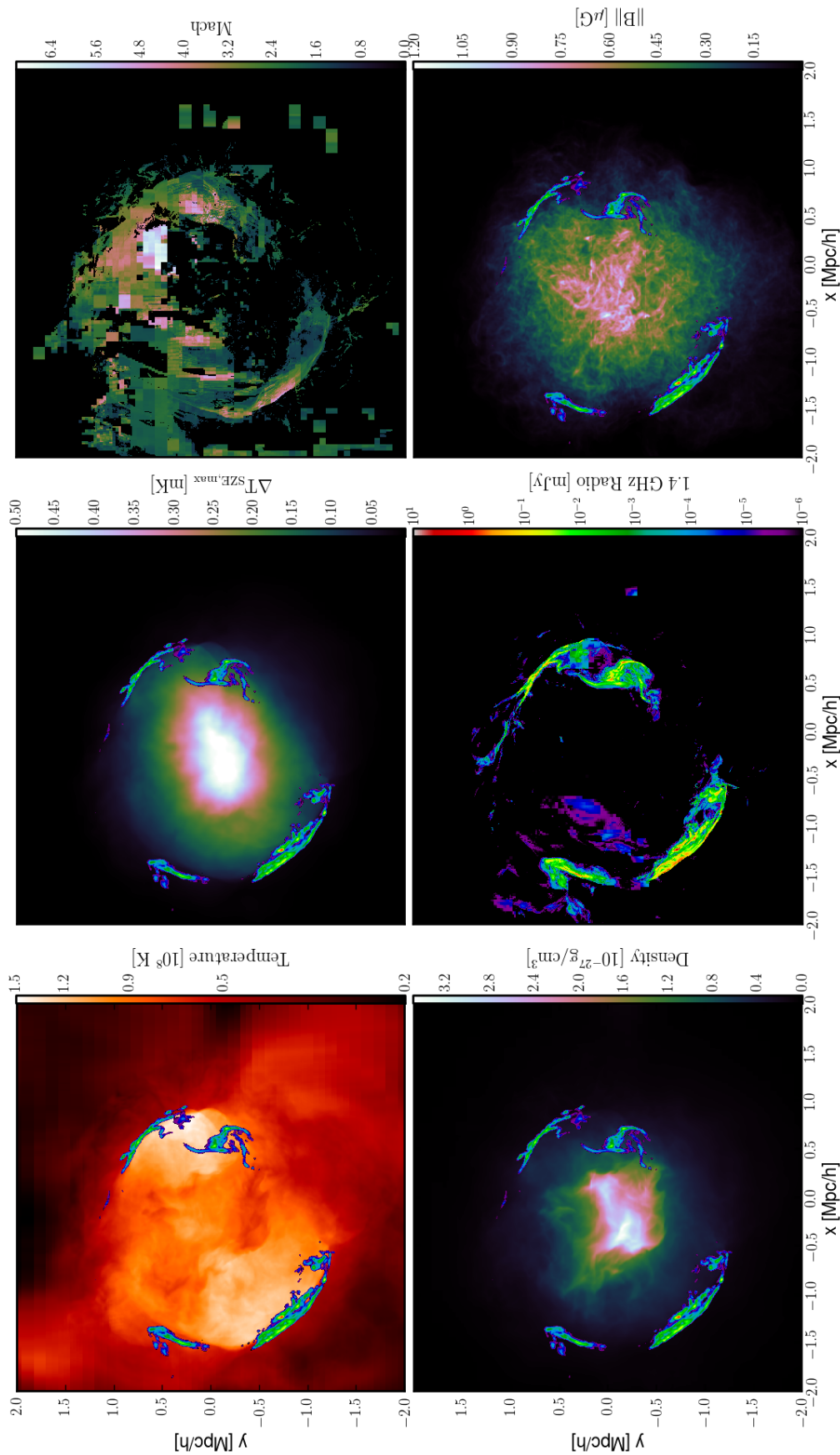


Figure 5.2 Projections of gas quantities. Upper left: Temperature, weighted by density. Upper middle: Sunyaev-Zel'dovich Compton-y value converted to the maximum temperature decrement. Upper right: Mach number, weighted by density. Lower left: Density, weighted by density. Lower middle: Integrated radio emissivity. Lower right: Magnetic field strength, weighted by density. Radio emission is overlaid on all panels except the Mach number, and is masked to show between  $10^{-3} - 10$  mJy. Radio emission assumes cluster is at a distance of 100 Mpc/h.

Figure 5.2 shows the fundamental quantities such as density, temperature, Mach number, and magnetic field strength, along with observable quantities such as the 1.4 GHz radio and temperature fluctuations in the CMB due to the thermal Sunyaev-Zel'dovich effect. The radio flux assumes a distance to the simulated cluster of 100 Mpc/h. Each panel shows the same field-of-view and depth of 4.0 Mpc/h at  $z=0$ . In all panels except for the radio and Mach number maps, we have overplotted the radio emission to help guide the reader's eye in determining the location of the emission relative to the underlying plasma. The top left panel shows the density-weighted temperature. Here the correlation between the radio emission and the temperature structure is very strong, as the outward moving shocks are heating the gas to several  $\times 10^8$ K. Note that the sharp edges in the temperature structure, as well as the maximum in the temperature distribution, occurs 1.5 – 2Mpc/h away from the center of the cluster. This highlights the unrelaxed nature of this merging cluster.

The bottom-left panel shows the density-weighted density, and has a similar structure to the X-ray image shown in Figure 5.1, as is expected since the X-ray emission is a strong function of gas density. We note that unlike the temperature, the density is strongly peaked towards the center of the cluster, though the unrelaxed nature is evident by the elongation along the merger axis. The top-right panel shows the kinetic energy flux-weighted Mach number. In addition, we masked out all pixels that contributed  $< 10^{-10}$  of the peak radio emission. This was done to eliminate some of the shocks along the line of sight that are external to the cluster. The bottom-right panel shows a projection of the absolute magnitude of the magnetic field, weighted by density. Here we weight by density since in many regions there is no relic emission, which would lead to difficult-to-interpret values in those regions. Notice that the magnetic field also peaks in the center of the cluster around  $1 \mu\text{G}$ . There appears to be a drop in field strength outside the radio relics. This makes sense because the merger shock is just reaching those regions, and then compresses the field behind the shock.

We now use these four quantities to produce the images in the middle bottom column. First, the middle-bottom image shows the radio emission calculated as outlined in Section 4.2.4. Notice that as expected, the radio emission traces the regions that combine all four of the quantities in



the left and right columns. This snapshot of the cluster properties suggests that **radio emission requires a combination of dense, hot, magnetically threaded gas in the presence of moderately strong shocks**. There are regions in the Mach panel of shocks in the  $\mathcal{M} = 5 - 7$  range that only contribute a small amount of radio emission. This region, which can be seen by rotating the viewpoint (not shown in this presentation), happens to lie outside the cluster a bit further where the magnetic field, temperature, and density have dropped considerably. We also notice that the strongest regions of radio emission correspond to Mach numbers in the  $3 - 5$  range with temperatures above  $10^8 K$ , similar to findings in Skillman et al. [213].

Finally, in the top-middle panel, we have overlaid the radio emission on top of the thermal Sunyaev Zel'dovich effect (tSZE). We have taken out the frequency dependence in the  $f(x)$  function, and multiplied the tSZE Compton  $y$ -parameter by the temperature of the CMB in order to get units of mK. Finally we multiply by 2.0, the maximum of  $f(x)$ , to get the maximum decrement value. Notice the very strong correlation with the jump in tSZE and the presence of radio emission. Also note that this image is shown in linear-scale, and the dynamic range in this image is  $< 20$ . This has interesting implications for ongoing and future high-resolution tSZE measurements with MUSTANG [159], CARMA [182], and CCAT [188]. Since the tSZE is sensitive to the integral of the pressure along the line of sight, it may be preferable to X-ray studies of galaxy cluster shocks because of its linear dependence on density and temperature instead of a roughly quadratic dependence on density and sub-linear dependence on temperature. This also minimizes the effects of gas clumping and increases sensitivity to low density gas. This advantage is amplified in the outer regions of galaxy clusters where many of these radio relic shocks are located.

### 5.3.2 Density & Magnetic Field Strength Relationship

In the next two sections we will describe the physical properties of the radio emitting plasma in order to compare to what has been found observationally. In the following analysis, we use the inner-most nested refined region of the simulation  $(32 \text{ Mpc}/h)^3$  and ignore the lower-resolution regions in the remainder of the simulation. We choose to study this entire sub-volume instead of

regions defined by the virial radius because the cluster is undergoing a major merger. Within this region, we bin various quantities such as radio emission, density, temperature, and magnetic field.

Before we discuss the radio emission, we first describe the structure of the magnetic field. In Figure 5.3, we show the average magnetic field strength as a function of density, along with the  $1 - \sigma$  standard deviation where the average is weighted by density. This is similar to plots found in Dubois and Teyssier [63], though in their study they also followed gas cooling. Similar results were also found using a smooth particle magneto-hydrodynamics code in [57] and [58], though there is less evidence for a flattening at high densities. Contrary to what has been assumed in prior studies such as Hoeft et al. [110], Skillman et al. [213], we find that the magnetic field does not scale with  $\rho^{2/3}$ , but instead with  $\rho$  at low density and has an inner core with roughly flat magnetic field at high density. This was discussed previously in Xu et al. [256], casting doubt on assumptions of any tight relationship between density and magnetic field strength. This suggests that the manner in which we inject the magnetic fields may ultimately determine quantities such as the total radio luminosity. Similar to what has been done in [60], future work should explore the effects of varying the magnetic field injection mechanism. For example, we may expect a shallower slope and more evenly distributed field strength if we inject magnetic fields from multiple sources instead of seeding each cluster with a single source. Observationally, this relationship is best probed by measuring the Faraday rotation for several lines of sight within a single galaxy cluster, as has been done for A2382 [98], A119 [76, 161], A2255 [96], Coma [129, 75, 27], and Hydra A [135]. In most of these cases there have been attempts to fit a relationship of  $B \propto \rho^\eta$ , where  $\eta$  is usually found in the range of  $0 - 1$ , with most values close to 0.5. In the case of Hydra A the authors found a range of  $\eta = 1 \pm 0.5$  was possible. Since our model predicts a flattening of magnetic field strengths at high densities ( $\eta = 0$ ), moving to a slope of  $\eta = 1$  at low densities, the observations are generally consistent with what we have found. An in-depth comparison between the radial dropoff of the magnetic field, analyzed using synthetic observation techniques, should be performed in the future.

Because of the steep drop in magnetic field strength at low densities, we expect that the radio emission will similarly decrease towards the outskirts of the cluster. Additionally, because the field

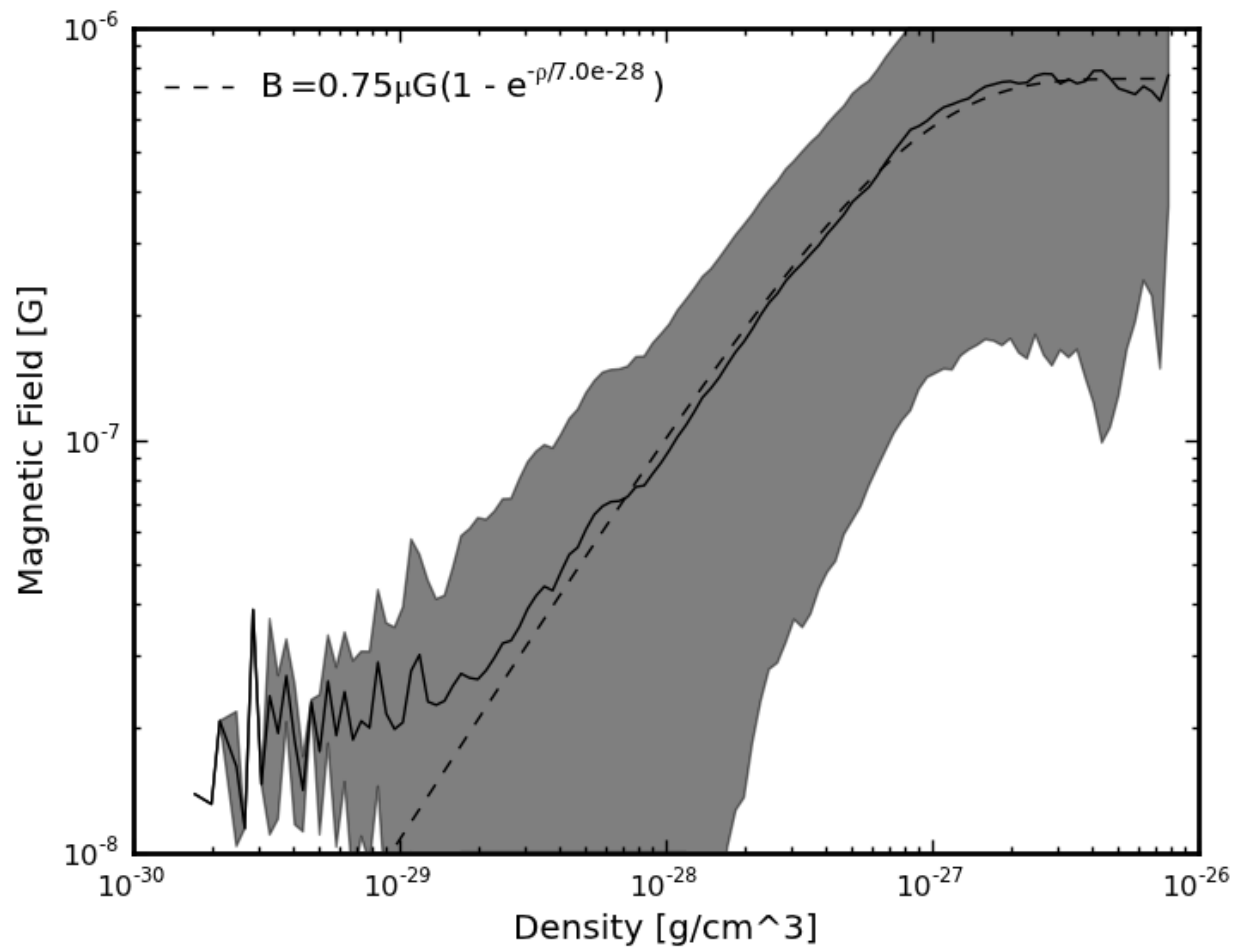


Figure 5.3 Average magnetic field strength as a function of density, where each cell is weighted by the density, with the shaded area denoting the standard deviation. For reference, we show an analytic function that is linear with  $\rho$  at low density and flattens at high density.

strength flattens out at high density, we expect to see radio emission that is not necessarily biased to the highest density regions near the center of the cluster.

### 5.3.3 Kinetic Energy & Radio Emission Distributions

The next quantity we will use to describe the gas properties of the cluster are the kinetic energy flux through shocks and the radio emission based on the Hoeft and Brüggen [109] model. We find it useful to show both of these quantities with respect to density, Mach number, magnetic field strength, and temperature in order to characterize the gas that is most responsible for the conversion of kinetic energy to cosmic-ray electrons. For this particular study, we choose to show both kinetic energy flux as well as the radio emission. As seen in Section 4.2.4, the radio emission is a complex function of many quantities, and it is difficult to disentangle each variable. The kinetic energy flux, however, is a much simpler quantity, relying only on the density, velocity, and temperature of the incoming gas:  $F_{KE} = 0.5\rho v^2 \mathcal{M}c_s$ .

The top left panel of 5.4 shows the kinetic energy flux through shocks as a function of Mach number on the x-axis, and the magnetic field strength on the y-axis. Note that all un-shocked cells in the volume are ignored. For each bin, we calculate the kinetic energy, and normalize by the maximum value from all the bins. This distribution is shown in logarithmic space, as only a small number regions dominate the kinetic energy flux. In this figure there appears to be 3 primary populations of gas that contribute to the kinetic energy flux. The first is a very low Mach number ( $\mathcal{M} < 1.5$ ), high-magnetic field, region of the simulation, which corresponds to the turbulent flow in the center of the galaxy cluster. This slightly supersonic flow processes a large amount of kinetic energy because of the high density and high temperature (and therefore sound speed), even though the Mach numbers are low. On the upper end of the shock Mach number scale, there are shocks around a Mach number of 6-8 with a magnetic field strength below  $0.01 \mu\text{G}$ . These, as we will discuss later, are associated with shocks onto filaments.

The third population in the kinetic energy flux is at Mach numbers between 3 – 5 with a magnetic field strength of between  $0.1 - 1.0 \mu\text{G}$ . These are the two primary merger shocks,

which we will see are the main source of the radio emission. Note that this is not a single or even pair of distinct Mach numbers, meaning that **observationally, a given merger shock should not be characterized by a single Mach number**. If the properties of shock-accelerated electrons are strongly dependent on the Mach number, ascribing a single Mach number may lead to inconsistencies in the fitting to the observed radio emission.

The lower-left panel shows the same quantity in color, but now decomposed into density and temperature bins. Here we get a different view of the same result. In this panel there are several knot-like regions in phase space, which likely correspond to each of the primary shocks in our cluster. However, in this case we see that there are 3-4 regions. There is a very low-density,  $10^6 - 10^7$  K region that likely corresponds to outer accretion shocks onto the filaments. The other regions of high kinetic energy at more intermediate densities correspond to each of the primary merger shocks in the cluster. The large clump at very high temperatures and a density of roughly  $10^{-28}$  g/cm<sup>3</sup> corresponds to the left-moving shock at  $\mathcal{M} \sim 4$ . This will become even more apparent when we examine the right panels of this figure. The primary results of this study of the kinetic energy flux agrees well with prior studies of the distribution of kinetic energy flux in shocks [204, 179, 212, 239, 240]. However, this is the first time they have also been correlated with the magnetic field distribution.

Now we contrast the distributions in kinetic energy flux with the radio emission. In the right panels of Figure 5.4, we use the color scale to signify the total radio emission. In the top right panel, we again show radio emission as a function of Mach number and magnetic field strength. Here we see that of the three features present in the kinetic energy flux, only one remains in the radio emission. This corresponds to the regions where the three ingredients needed to create radio emission are all present. The Mach number is above the threshold for accelerating high energy electrons, the gas is dense enough, and the magnetic field strength is high enough. We note that the falloff at low Mach numbers is due to the functional form of  $\Psi(\mathcal{M})$  from Equation 5.1. For this simulation, we find that **the majority of the radio emission in this cluster comes from shocks with Mach numbers of 3.0 – 6.0 and magnetic field strengths of 0.1 – 1.0  $\mu$ G**.

The same general conclusions are found from the lower right panel. We see that, instead of a fairly broad distribution in kinetic energy flux across densities and temperatures, the radio emission is confined to regions of relatively high densities and temperatures near  $10^8$  K. By combining this with the upper-right panel, we have determined the exact makeup of the gas responsible for the synchrotron radiating electrons in radio relics.

It is important to note that the magnetic field in our simulation does not reach the levels calculated from observations of several radio relics [48, 46, 232]. This suggests that the magnetic field injection mechanism used in this study may not correspond to how it occurs in observed galaxy clusters. Alternatively, amplification of pre-existing fields prior to AGN injection, primordial magnetic fields, and several other processes such as turbulent dynamo [111] in the post-shock region and the streaming instability [e.g. 2] may lead to higher magnetic field values, all of which could be investigated in future work. Finally, observations should be re-examined to determine if a lower value of magnetic field is possible, such as what has recently been found in Carretti et al. [42].

#### 5.3.4 Merger Evolution

Observationally, we are limited to a single snapshot in time, from which we must deduce the prior and future evolution of a given galaxy cluster. Fortunately this is not the case for simulations. In this section we describe in detail the evolution of the gas properties throughout the history of the clusters we are modeling. Figure 5.5 shows the evolution of bulk properties in the nested region of the simulation from redshift  $z = 2.95$  to  $z = 0.0$ . There are five quantities shown here.

- (1) Density: Average density, weighted by density.
- (2) Temperature: Average temperature, weighted by density.
- (3) Magnetic Field: Average magnetic field strength, weighted by density.
- (4) Radio: Total 1.4 GHz Radio Emission
- (5) Xray: Total 0.5-12 keV X-ray luminosity

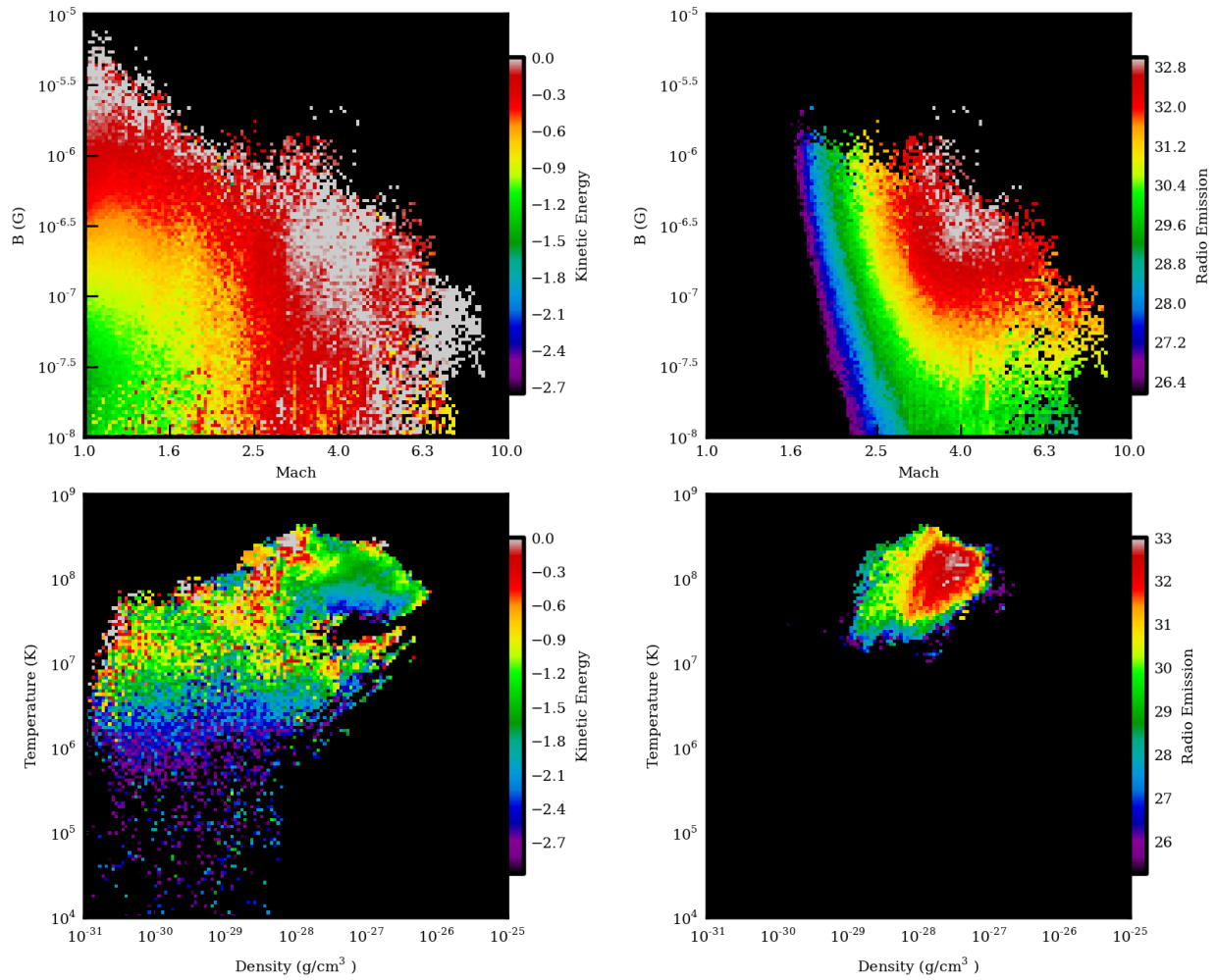


Figure 5.4 Phase plots of gas properties indicating the location of the kinetic energy flux and radio emission at shock fronts. The left plots show the kinetic energy distribution, while the right plots follow the radio emissivity. The top panels show the distributions as a function of magnetic field strength on the y-axis, and Mach number on the x-axis. The lower panels show them as a function of temperature on the y-axis, and density on the x-axis.

In each case we select the inner-nested region of the simulation, and use `WeightedAverageQuantity` or `TotalQuantity` “derived quantities”. Each of these averages and totals are then saved for future analysis. In the case of Figure 5.5, we normalize each of the quantities by their maximum value in order to fit them all on the same scale. In the case of the X-ray and radio luminosity, the emission is calculated using the blueshifted frequencies as these would be redshifted into the observer’s frame to be at the correct values (0.5 – 12keV and 1.4GHz for X-ray and radio, respectively).

We find a very interesting correlation with all of the fundamental and derived quantities. First, it is clear that there was not only the late-time merger near  $z = 0$ , but also earlier merger evolution near  $z = 1$ . First, we see that the density and temperature both start to rise 0.2 – 0.5Gyr before the radio emission spikes. Analogously, the magnetic field and X-ray luminosity also follow this slow rise to a peak. Near the peak, the radio emission jumps up several orders of magnitude. This corresponds to the formation of the shock front that then moves outwards from the cluster center towards the outskirts of the cluster. After the core passage, the density and temperature returns to a lower but elevated level with respect to the pre-merger values.

This suggests that the radio emission lags the merger event by a few  $\times 10^8$  years while the shock is setting up and expanding into the intracluster medium. It again highlights the dependence on not only the local characteristics of the emitting plasma, but also the shock surface area. Another key point is that the short timescales over which the radio luminosity varies implies that for a given mass or X-ray luminosity, there may be very large scatter in the radio luminosity. Overall, the radio emission is only above 10% of its peak value for  $\sim 0.5$  Gyr. This could help explain the observed lack of radio emission from clusters with obvious mergers such as Abell 2146 [200]. One caveat to this result is that we do not follow the electrons as they cool. However, because the cooling timescale,

$$\tau \approx 2 \times 10^{12} \gamma^{-1} ((1+z)^4 + (B/3.3\mu G)^2)^{-1} \text{ years} \quad (5.3)$$

for these electrons with  $\gamma \sim 1000 - 5000$  is short [80], this additional time has little effect. Therefore the characteristics of this time evolution should not change substantially with a proper treatment



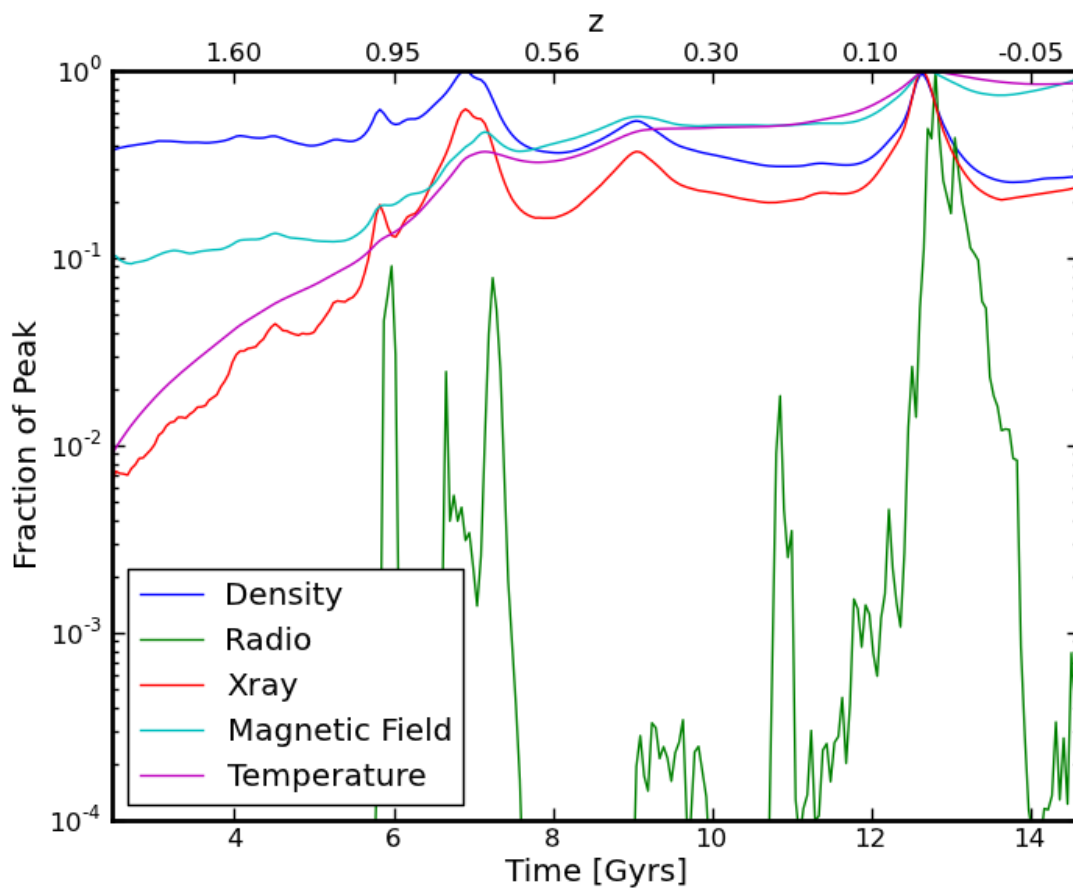


Figure 5.5 Time evolution of integrated gas properties in the volume surrounding the structures of interest. For density, temperature, and magnetic field, we calculate a weighted average, using density as the weight. For radio and X-ray values, we calculate the total emission within the innermost nested region of the simulation. Note the simulation was run beyond  $z = 0$  to allow the merger to finish.

of the aging electron population.

## 5.4 Observational Implications

In this section we set out to provide a theoretical perspective on the analysis of observed radio relics. In particular, we comment on some of the assumptions that are often employed, and in several cases point out how these may be dubious. We begin by examining how the viewing angle of a radio relic can impact its interpretation. We expand on this point in the context of spectral index analysis, where not only does viewpoint play a role, but small-scale fluctuations in the shock properties can lead to observational signatures that mimic an aging population of cosmic ray electrons. Finally, we point out the limitations of our models; specifically, we must include aging populations of electrons in future calculations in order to capture accurate polarization fraction and direction.

### 5.4.1 Viewpoint

Observationally, we are limited to a single viewing angle for each object. Unfortunately, because radio relic emission is not spherically symmetric, there will be a viewing angle-dependent emission strength and morphology. In this section we set out to demonstrate this fact and how it can affect our interpretation of radio emitting regions in galaxy clusters. We begin by taking our original viewpoint and rotate the viewing angle by 180 degrees over 18 frames. The result is shown in Figure 5.6, where radio emission is projected along each viewing angle.

What can be seen from Figure 5.6 is that, while for some orientations the radio emission forms an obvious “double relic” configuration, other orientations yield what seems to be a single, more diffuse, object. However, given a single frame, it would be difficult to determine the true structure of the emission. In fact, this may lead to a misinterpretation of the radio emission to be that of radio halo origin. We will expand upon this line of reasoning in Section 5.4.2. There are several other things to note here in the rotation of the radio emission. We see that in some orientations (see top row, 5th & 6th columns), we reproduce morphologies that include two outer

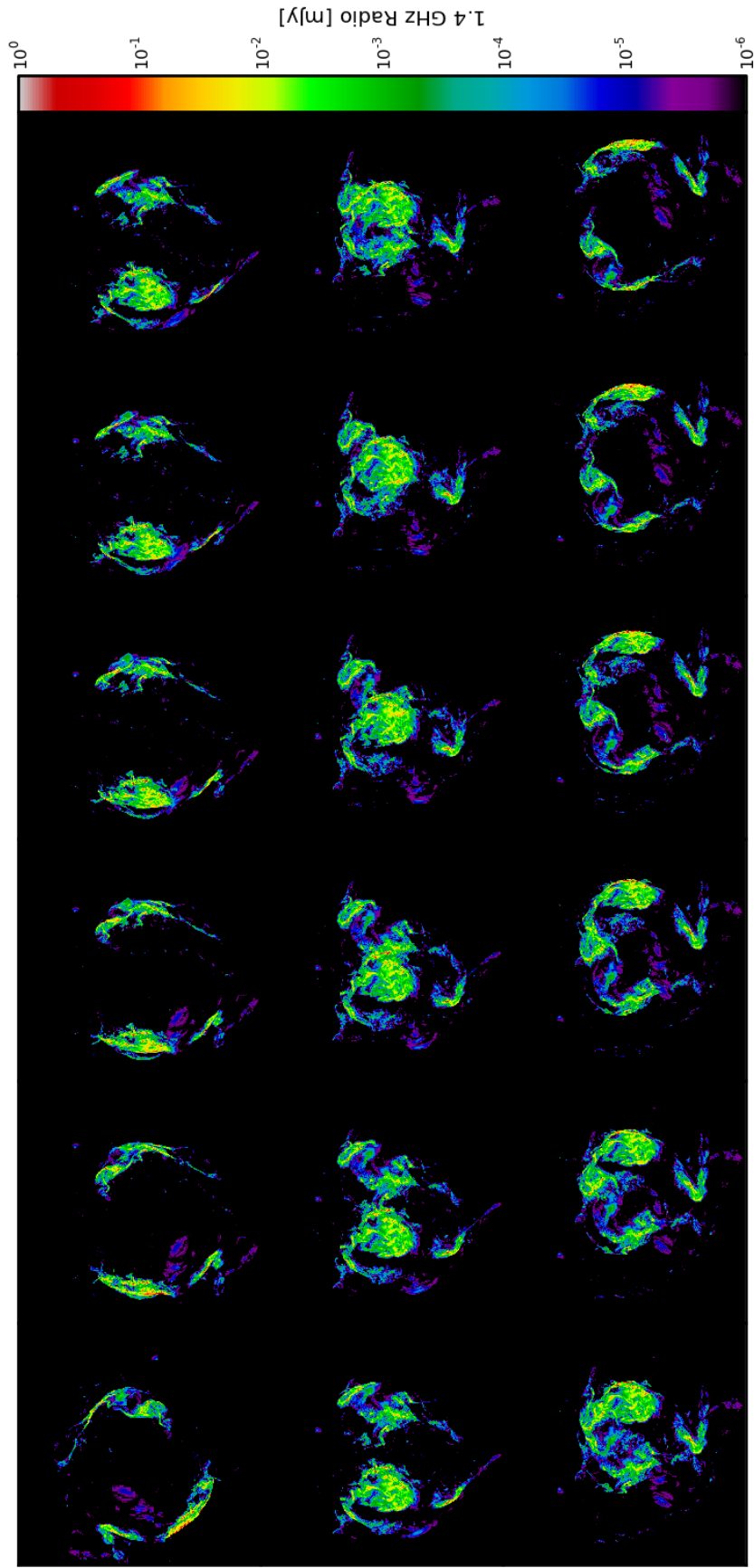


Figure 5.6 180 degree rotation of radio emission. Flux computed by assuming a distance of 100 Mpc. Each panel is rotated by 10 degrees from the previous, moving left to right, top to bottom. Note that this panel of images acts as a autostereogram, and can be used to see the 3D structure of the radio emission. See video in the electronic journal.

relics, with one of the relics ending up between the two, close to the center of the cluster. This is very similar to observed clusters such as MACS J1752.0 + 4440 [237], CIZAJ2242.8 + 5301 [236], and MACS J0717.5 + 3745 [25, 231]. It may be possible that the emission in these clusters be not of radio halo origin, but simply radio relic emission viewed coincident with the cluster center. Similar work has been done with hydrodynamic simulations of galaxy clusters and viewing them along the coordinate axes in Vazza et al. [241], where they found that the low emissivity due to the small size along the line of sight may explain the lack of central radio relics.

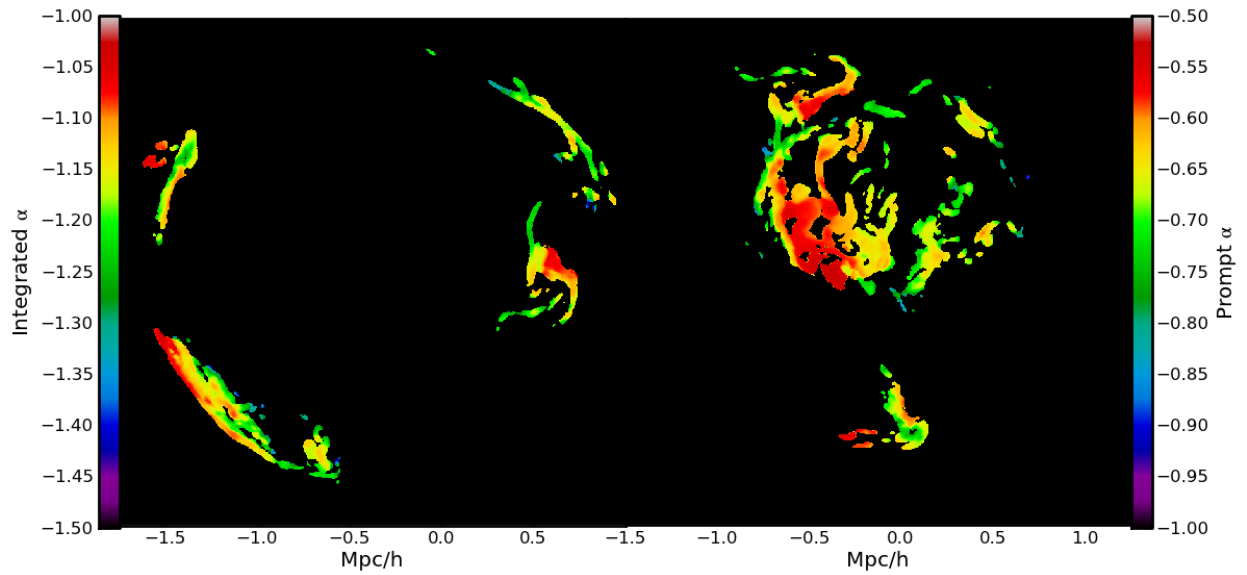


Figure 5.7 Spectral index of simulated radio relic emission. The left portion of the image shows the “edge-on” view, whereas the right shows the “face-on” view. Both views are on the same scale. The left colorbar shows the mapping of color to the integrated spectral index including particle aging. The right colorbar shows the mapping of color to the prompt spectral index. Both colorbars apply to both views, providing a rough estimate of the uncertainty in our models of the spectral index.

#### 5.4.2 Spectral Index

Observationally, the spectral index of cluster radio relics is measured by comparing the emission at several different observed frequencies. In our work, we calculate the spectral index by first calculating the radio emission at two frequencies (here we use 1.4 GHz and 330 MHz). After smoothing by a Gaussian with a full-width half maximum size of 4 pixels, we then use these two

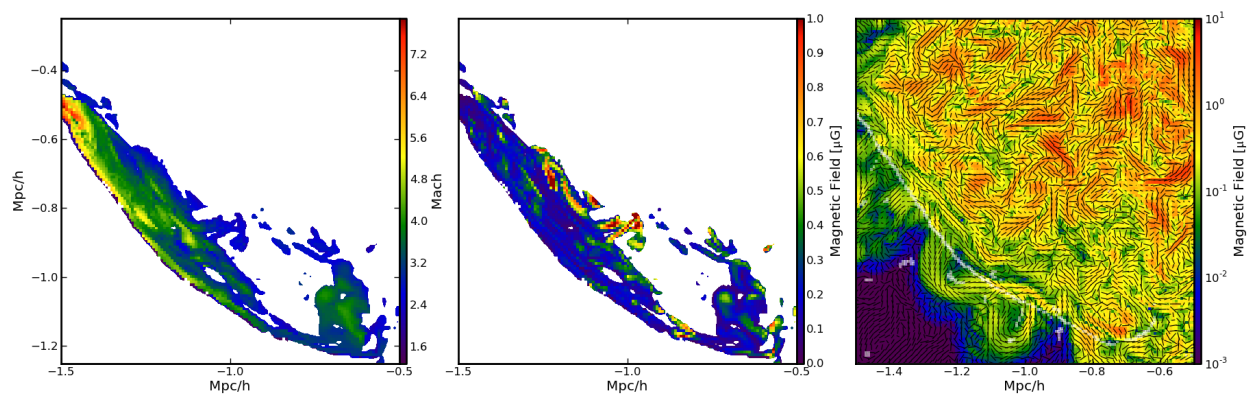


Figure 5.8 A zoom in of the lower left radio relic. The left two panels show radio emission-weighted projections of the Mach number (left), and magnetic field strength (middle). The right panel shows a slice of the magnetic field strength, with black lines indicating the local magnetic field direction in the plane of the slice and the white overlay show the location of cells identified to be shocks.

maps to calculate the spectral index, similar to what would be done observationally. Because we use the Hoeft and Brüggén [109] model, we will recover a spectral index from comparing these two maps that is equal to the cumulative spectral index due to the emission from electrons over their entire lifetime. This is steeper than the spectral index that would be predicted from the prompt emission from a shock front, which is related by  $\alpha_{prompt} = (1 + 2\alpha_{integrated})/2$ .

In reality, what is thought to happen is the leading edge of the shock front should accelerate electrons to  $\alpha_{prompt}$ . As the radio emitting electrons move downstream from the shock they cool and the spectrum steepens. Qualitatively, we would expect that “edge-on” observations should produce values near  $\alpha_{prompt}$ , whereas a “face-on” view would be sensitive to the entire lifetime of the electrons, and therefore be closer to  $\alpha_{integrated}$ .

Spectral steepening is found to happen in several observed clusters [233] and measuring the steepening of the electrons as they progress away from the shock can help constrain the local magnetic field, as was done in van Weeren et al. [233]. However, the assumption in these calculations is that the spectral steepening is due entirely to the aging of the electrons. However, we see similar steepening even though we do not include the spectral aging of the electrons as they advect downstream! These variations are entirely due to a varying magnetic field and shock strength in a non-uniform medium. The spectral indices of the prompt and integrated spectra are shown in Figure 5.7, and the fluctuations in the underlying fields for the lower-left “edge-on” relic are shown in the right panel of Figure 5.8.

In Figure 5.7, we see that the “edge-on” view shows a spectral steepening whereas the “face-on” view shows the spatially variant spectral shape due to the shock properties. For completeness we have mapped the colormap of both viewing angles to both the prompt and integrated spectral indices. The same qualitative behavior is seen with both calculations. These fluctuations are explained in Figure 5.8, where we see that the radio emission-weighted Mach number can vary between 2 – 8, and the magnetic field can vary from 0.1 – 1 $\mu$ G. **Therefore we warn that extrapolating from the measured spectral steepening to calculate gas properties should be done with care, as projection effects and spatial variation of the gas properties are**

**important. It may be insufficient to prescribe a single Mach number or magnetic field to a given radio relic.**

### 5.4.3 Polarization Fraction & Direction

Using our newly developed method, we have created radio polarization fraction and direction maps for our galaxy cluster from two viewing positions. The first gives an “edge-on“ view of the radio relic, whereas the second is aligned such that the relics are viewed “face-on.” We will examine, in detail, the polarization signatures of the “edge-on,” and then describe the differences in the “face-on” view. Much of this work is related to the very early predictions from Ensslin et al. [70].

In Figure 5.9, we show the linear polarization fraction and direction of 1.4GHz radio emission. Lines denote the local linear polarization direction, the length of which corresponds to the polarization fraction. For clarity, the polarization fraction is also shown in color. The polarization fraction is calculated using

$$f_p = \frac{\sqrt{I_x^2 + I_y^2}}{I} \quad (5.4)$$

In this case we use a  $512 \times 512$  pixel image plane to project through a cube of length 4 Mpc/h on a side. At full resolution (7.8kpc/h), we see that the polarization fraction reaches a maximum of  $\sim 75\%$ , and that the polarization direction is correlated along the relic, primarily perpendicular to the shock. This is very similar to what is found observationally in CIZA J2242.8+5301 [233]. The authors find strong (50-75%) polarization at what is presumed to be the leading edge of the shock. Additionally, they find that the polarization direction is fairly constant over the length of the relic. We do, however, see greater variation in the polarization fraction and direction both across and along the relic. These fluctuations in our simulation may suggest that there are additional physical processes which lead to a more ordered field. In order to investigate the small scale fluctuations in the polarization direction, we examined a slice of the magnetic field strength and direction through this relic. This is shown in Figure 5.8. What we found is that while the shock (overlaid in white)

cuts through regions which have fairly strong variations in the magnetic field direction, the region “behind” the shock has a magnetic field that is compressed along the shock propagation direction. Therefore, it may be possible that if we were to follow the evolution of the cooling electrons as they moved downstream across the shock, the magnetic field that they reside in may become more ordered parallel to the shock, leading to a longer coherence length as more constant polarization direction. **Therefore we would expect that in future work when we examine the emission from an evolving population of cosmic rays, we should see even better agreement with observations of polarization direction.**

In the top-right panel of Figure 5.9, we show the same polarization map, but this time for when the relic is viewed “face-on”. We again see a very high polarization fraction. However, this time the polarization direction is significantly less coherent. This is due to the magnetic field not being modified as strongly in the plane of the shock as it is perpendicular to the shock. Therefore the turbulent structure is preserved in the image plane and the polarization vectors are not preferentially modified.

However, the behavior of the polarization fraction and direction drastically changes if we then apply a gaussian kernel with a size of 4 pixels. In the “edge-on” view, the polarization fraction and direction is fairly well preserved. The fraction only drops to between 30 – 65% and the direction is still fairly correlated across the relic. In contrast, for the “face-on” view the polarization has dropped to between 0 – 15% in most regions. This is a classic example of beam depolarization. Because the polarization direction is highly disordered, smoothing the image drastically reduces the overall polarization.

Currently our simulations do not exhibit as much of a constant polarization as that found in observations of clusters such as CIZA J2242.8+5301, where the polarization direction is constant over Mpc-scale distances. There are several possible explanations. Because we are not tracking the electron distribution as it cools behind the shock, we may be missing the emission from the more ordered field line regions behind the shock. Simulations capable of tracking these electrons are therefore needed to explore that possibility, and will be addressed in future work. If doing so is



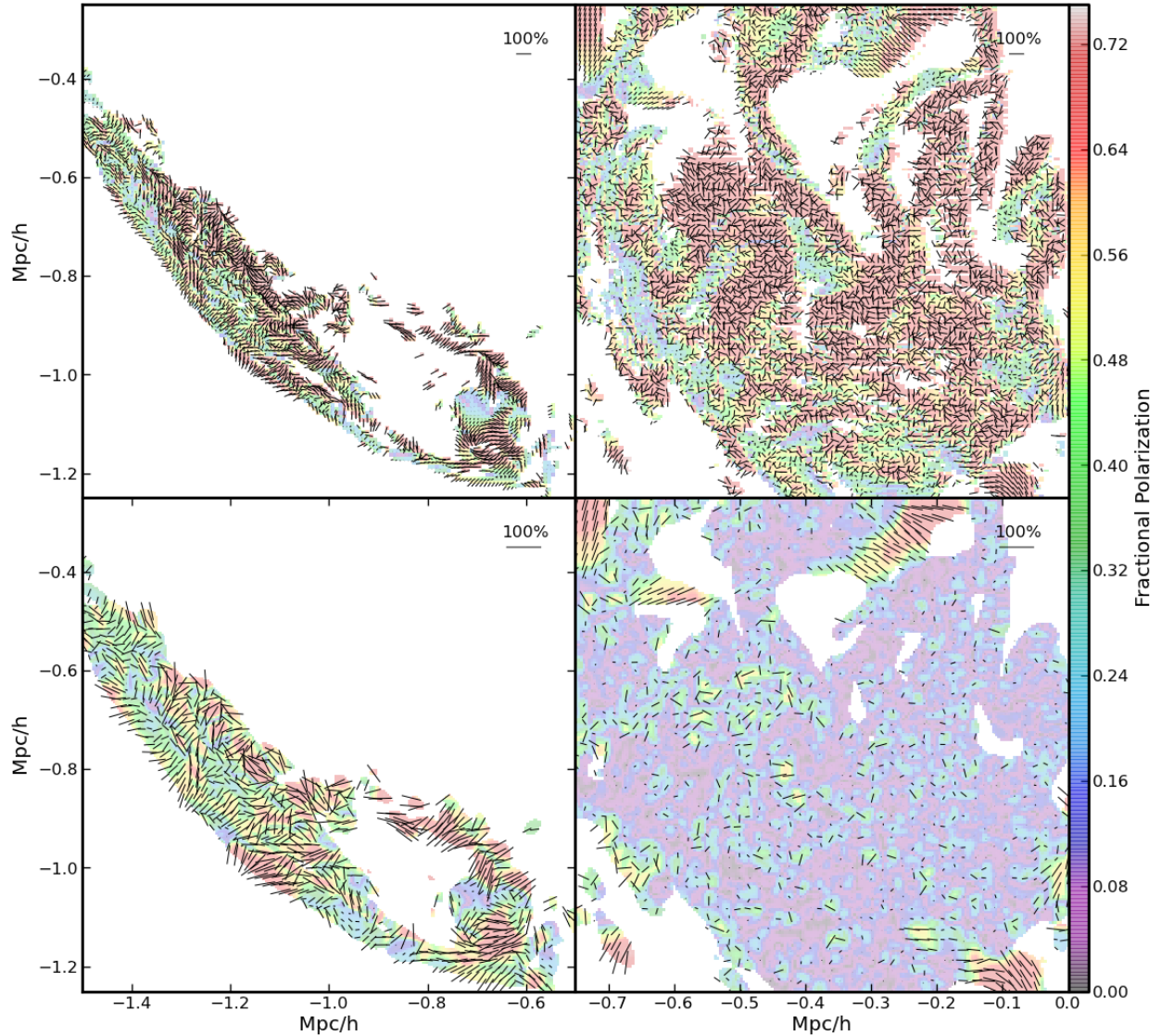


Figure 5.9 Polarization fraction and direction. In each panel, the polarization direction is denoted by the black quivers, while the polarization fraction is represented by both the color scale as well as quiver length. The top panel shows the relic at full resolution (7.8kpc/h), while the lower panels show the same view at 4 times worse resolution. At  $z = 0.2$ , the redshift of CIZA J2242.8+5301, this corresponds to angular resolutions of  $3.36''$  and  $13.44''$ , respectively. The left panels show the polarization for the “edge-on” (top) while the right shows the “face-on” view.

still incapable of producing Mpc-scale ordered polarization maps, it may suggest that the injection mechanism or magnetic field evolution is different than what we have simulated.

## 5.5 Discussion & Future Directions

We have carried out high resolution MHD AMR cosmological simulations using an accurate shock finding algorithm with a radio emission model for shock-accelerated electrons to examine the properties of radio relics in galaxy clusters. We summarize the physical conditions of the cluster, and several of the warnings for the interpretations of observed radio features:

- Cosmological initial conditions lead naturally to the formation of giant radio relics whose properties are very similar to observed relics. This is a natural result of the process of mergers that create galaxy clusters, where the magnetized intracluster medium is subject to a series of strong, large-area shocks.
- We find that the radio emission in our simulated clusters is strongest in plasma that has  $0.1 - 1.0 \mu\text{G}$  magnetic fields with a shock Mach number between  $3 - 6$ , with densities near  $10^{-28} \text{ g/cm}^3$  and temperatures of  $10^8 \text{ K}$ .
- If the shock acceleration efficiency for electrons is higher than assumed at low Mach numbers, a large reservoir of kinetic energy becomes available in hot ( $10^7 \text{ K}$ ) gas at both lower and higher densities than what is currently producing emission in our simulations.
- We find a magnetic field distribution that does not follow the often assumed  $B \propto \rho^{2/3}$  relation. Instead, it follows  $B \propto \rho$  at low densities, and flattens out to sub- $\mu\text{G}$  levels above densities of  $10^{-27} \text{ g/cm}^3$ .
- **Warning:** Without a model of spectral aging of electrons, we still recover a spectral index gradient, indicating that observed gradients should not necessarily be interpreted as the spectral aging of electrons. It may simply be due to the projection of a curved shock front with varying Mach number.

- **Warning:** From the time evolution of our simulated galaxy cluster, it is clear that only a small portion of its lifetime may be spent in a regime where it is bright in the radio wavelengths. This may explain the apparent lack of observed radio emission in some massive galaxy clusters with early or late phase merger.
- **Warning:** The viewing angle of a given galaxy cluster may have significant impact on the classification of its radio emission. Double radio relics viewed at some orientations are difficult to differentiate from radio halo emission.
- **Warning:** Future simulations of galaxy cluster radio relics must follow the temporal evolution of the electron population in order to reproduce valid polarization results, as the downstream conditions from the shock may include more ordered magnetic fields, leading to different polarization maps than when the emission is assumed to come only from the shock center.

Many of these warnings apply both to observational and theoretical studies, and the classification and analysis of radio relics in all contexts must be done with care to avoid confusion with radio halo emission. There are several advancements that can be made theoretically. We are in the process of developing and testing the numerical framework necessary to follow the cosmic ray electron and proton populations, using a method similar to Miniati [152] and Jones and Kang [117]. Doing so will allow us to probe the spectral distribution of these non-thermal populations in the context of high-resolution cosmological simulations. Once this is merged with our ability to produce synthetic emission and polarization maps, we will be able to more directly compare to current observations. Additionally, we do not explicitly include any magnetic field source terms at the shock fronts. Exploring local field generation mechanisms such as the Weibel instability [248, 83] may allow for alternate magnetic field strength and structure behind the shock front from what we present here. Finally, we may need to push to higher resolution studies at the shock fronts to be able to follow the shock-amplification of magnetic fields. Doing so in a cosmological simulation is currently intractable; however, improvements in computational speed and parallelization may allow

for future studies.

Observationally we are entering a golden age of radio telescopes with the upgraded Jansky VLA, GMRT, and LOFAR, and are looking forward to the SKA, and possibly a lunar farside radio telescope[37, 138]. These improvements will lead to greater sensitivity and bandwidth, allowing for multifrequency studies of galaxy cluster environments in unprecedented detail. However, only through a coordinated effort between simulations and observations will we be able to fully understand the plasma physics in these cosmic environments.

## Chapter 6

### CRT: A Library for Cosmic Ray Transport

In this chapter, I will describe the analytical and numerical framework for a solver capable of following the momentum-space evolution of a distribution of cosmic rays. This work is distinct from all other prior methods in that there is a separation between the driving hydrodynamic code and the cosmic ray solver. This, in principle, allows multiple hydrodynamic codes to use the framework outlined here through a lightweight interface. Much of this chapter will describe methods and techniques outlined in a series of papers by Jones, Miniati, Kang, Ryu, and Engel[118, 152, 116], and also heavily relies on processes described in [226].

The development of this capability has been motivated by our previous studies. In Chapter 3, we estimated the amount of proton acceleration through cosmic time, but a robust study requires following the distribution of CR protons as they are accelerated and cool. Additionally, better estimates of CR acceleration efficiency can be made if we understand the pre-shock population of protons and whether there exists a non-thermal tail. In Chapter 4, we began to describe the instantaneous radio emission that is present in cosmological structure formation. A key limitation to this study was that the aging of the electron population was not included, and therefore the time-evolution was only accurate for high frequency emission where the electrons cool rapidly. In Chapter 5, we found that by including MHD in our simulations, we are able to make polarization fraction and direction maps that compare well to observations of radio relics. However, this was again assuming that all of the emission was originating from the location of shocks. In reality the electrons cool over some length scale, therefore perhaps sampling different magnetic field configurations. By

following the distribution of CR protons and electrons, we will be able to address these concerns. Additionally, we will be able to study aged populations and acceleration mechanisms that are gradual, such as turbulent acceleration.

Finally, previous studies had very little information on the spectral shape of the electrons and protons. This can be very important when comparing simulations to observations, where a deviation from an assumed spectrum of CRs could lead to unexpected features in the observed quantity.

We will begin by describing the analytical theory behind evolving the momentum-space distribution function. We then introduce the computational framework that we have written to solve these equations. After presenting single-zone tests of our solver, we then present tests that are incorporated within the hydrodynamic code Enzo. Finally, we use this to simulate a galaxy cluster from cosmological initial conditions as it grows, merges, and evolves. From it we are able to create synchrotron emission maps, and compare them to the density, temperature, X-ray and SZ morphology.

## 6.1 Solving the Diffusion-Convection Equation for Cosmic Rays

In principle the system we would like to follow is a distribution of ions and electrons that are described by particle-particle interactions. However, given the number of particles in any of the astrophysical situations that we are interested in for this dissertation, it is computationally impossible to follow the orbits of each individual particle. We therefore choose to describe the simulation by a distribution function  $f(\vec{x}, \vec{p}, t)$ , which assumes that the entire state of the system can be described by a function that only depends number density of particles at a particular position, momentum, and time, ignoring the explicit particle paths. We then choose to make the next simplifying assumption - namely, that the momentum distribution of all the particles are isotropic, meaning that their evolution can be described by a single total momentum rather than its vector components. This reduces the dimensionality of the simulation from 7 (3 spatial, 3 momentum, 1 time) to 5 (3 spatial, 1 momentum, 1 time). Therefore our task at hand is to

solve for the isotropic distribution function  $f(\vec{x}, p, t)$ , where the number density of particles in at a position  $\vec{x}$  at time  $t$  is

$$n(\vec{x}, t) = \int_0^\infty 4\pi p^2 f(\vec{x}, p, t) dp. \quad (6.1)$$

To start our derivation, one should really begin with the diffusion-convection equation from Skilling, 1975 [211]. This can be written in terms of the isotropic distribution function as

$$\frac{\partial f}{\partial t} + \vec{u} \cdot \nabla f - \nabla(D_{xx} \nabla f) = \frac{1}{3} \nabla \cdot \vec{u} p \frac{\partial f}{\partial p} \quad (6.2)$$

which describes the full evolution including hydrodynamic advection and diffusion. This equation can also be re-written in a conservative form, by adding  $f(\nabla \cdot \vec{u})$  to each side and combining terms. By including now a term for explicit momentum loss and momentum diffusion, we are left with the propagation equation for an isotropic distribution function, as in [225].

$$4\pi p^2 \frac{\partial f}{\partial t} = 4\pi p^2 \nabla \cdot (D_{xx} \nabla f - \vec{u} f) + 4\pi \frac{\partial}{\partial p} p^2 D_{pp} \frac{\partial f}{\partial p} - 4\pi \frac{\partial}{\partial p} \left[ \dot{p} p^2 f - \frac{p}{3} (\nabla \cdot \vec{u}) p^2 \right] + q(\vec{x}, p, t) \quad (6.3)$$

where  $D_{xx}$  is the spatial diffusion coefficient,  $\vec{u}$  is the gas velocity,  $D_{pp}$  is the momentum diffusion coefficient,  $\dot{p}$  is the radiative momentum loss, and  $q(\vec{x}, p, t)$  is a source term. For this dissertation, we explicitly ignore the spatial and momentum diffusion. Spatial diffusion should occur on significantly longer timescales than the lifetimes of the ions and electrons. The momentum diffusion is primarily responsible for the re-acceleration of particles, which we ignore for now even though its implementation is straightforward. We then choose to solve this equation in an operator split fashion, where we leave the changes due to the underlying hydrodynamics such as advection and divergence to the driving hydrodynamic code. We then only care about the update due to the terms that are momentum-dependent. We are left with the reduced equation,

$$4\pi p^2 \frac{\partial f}{\partial t} = -4\pi \frac{\partial}{\partial p} \left[ \dot{p} p^2 f - \frac{p}{3} (\nabla \cdot \vec{u}) p^2 \right] + 4\pi q(\vec{x}, p, t) \quad (6.4)$$

In principle this equation can be solved using standard finite difference techniques in the momentum dimension, as was done in [225, 121]. This approach usually requires fine momentum bins in order to follow the evolution, of order  $\Delta \ln(p) < 0.1$ . For the application of, for example,

a distribution of cosmic ray electrons with  $\gamma$  factors of  $100 - 10^6$ , this would require 92 bins. However, since our goal is to run cosmological simulations that themselves are of order  $10^9$  zones, this would be computationally infeasible, requiring nearly 750GB of total memory just to store 1 copy of the fields.

To counteract this need, Jones & Kang (2005) [116] outline a method that subdivides the momentum space into logarithmically spaced bins, but also assume that the distribution function can be approximated as a piece-wise power-law. They call this the Coarse Grained Momentum finite Volume (CGMV) method, and we adopt the same assumptions in our work. Fundamentally, the method takes the full distribution function  $f(\vec{x}, p, t)$  and replaces it by

$$f(\vec{x}, p, t) \approx f_i(\vec{x}, t) \left( \frac{p}{p_i} \right)^{-q_i(\vec{x}, t)} : p_i \leq p < p_{i+1} \quad (6.5)$$

for  $i = [0..NBins]$  where  $f_i$  is the normalization and  $q_i$  is the power-law index of the distribution at  $p = p_i$ . Here we explicitly include the dependence on space and time in  $f_i, q_i$ .

In principle, one could carry the NBins values for  $f_i, q_i$ , at each point in space. However, unlike normal fluid properties such as energy or density, these variables can not be simply advected with the flow. In other words, one can not estimate a flux of  $f_i, q_i$  in a conservative fashion. Instead, we follow [116] and construct a pair of moments  $n_i$  and  $g_i$  that are proportional to the total number and energy densities of the CR population in momentum bin  $i$ ,

$$n_i = \int_{p_i}^{p_{i+1}} p^2 f(p) dp \quad (6.6)$$

and

$$g_i = \int_{p_i}^{p_{i+1}} p^3 f(p) dp. \quad (6.7)$$

These integrals can be analytically calculated in terms of the piece-wise power-law,

$$n_i = \frac{f_i p_i^3}{q_i - 3} \left[ 1 - d_i^{3-q_i} \right], \quad (6.8)$$

$$g_i = \frac{f_i p_i^4}{q_i - 4} \left[ 1 - d_i^{4-q_i} \right], \quad (6.9)$$



where  $d_i = \frac{p_{i+1}}{p_i}$ . Unfortunately, when  $q_i = 3, 4$ , these equations are not well-defined. However, the integrals for  $n_i$  and  $g_i$  can be redone using these values explicitly to find for when  $q_i$  is equal to 3 and 4 respectively,

$$n_i(q = 3) = f_i p_i^3 \ln \left( \frac{p_{i+1}}{p_i} \right) \quad (6.10)$$

and

$$g_i(q = 4) = f_i p_i^4 \ln \left( \frac{p_{i+1}}{p_i} \right). \quad (6.11)$$

These values can then easily be advected with the fluid flow like any other passive scalar field. Once the distribution function is needed, we use a Newton's method iteration to find  $q_i$  based on the ratio of  $n_i p_i / g_i$  for each bin, and then either  $n_i$  or  $g_i$  to determine the normalization. The function that needs to be minimized is

$$Err(q_i) = \frac{q_i - 4}{q_i - 3} \frac{1 - d_i^{3-q_i}}{1 - d_i^{4-q_i}} - \frac{n_i p_i}{g_i}. \quad (6.12)$$

Once the distribution function is known, we are equipped to evolve the system as described with Eq 6.4. For the update of  $n_i$ , we can simply integrate over  $[p_i, p_{i+1}]$ ,

$$\frac{dn_i}{dt} = 4\pi \int_{p_i}^{p_{i+1}} p^2 f(p) q(\vec{x}, t) dp + F_{n_i} - F_{n_{i+1}}, \quad (6.13)$$

where we define the flux of particles through each momentum bin boundary,

$$F_{n_i} = 4\pi p_i^2 \left( \dot{p} - \frac{p}{3} (\nabla \cdot \vec{u}) \right) f_i. \quad (6.14)$$

Similarly, we can multiply Equation 6.4 by  $p$  and then integrate to recover the evolution of  $g_i$ ,

$$\frac{dg_i}{dt} = 4\pi \int_{p_i}^{p_{i+1}} p^3 f(p) q(\vec{x}, t) dp + F_{g_i} - F_{g_{i+1}} - \frac{1}{3} (\nabla \cdot \vec{u}) g_i + 4\pi \int_{p_i}^{p_{i+1}} p^2 f(p) \dot{p}, \quad (6.15)$$

where here the flux of energy through each bin boundary is  $F_{g_i} = p_i F_{n_i}$ . Note here that there are additional terms due to the integration by parts of the adiabatic losses/gains and momentum loss terms. This can be understood knowing that while the number density is conserved other than fluxes of particles in and out of the bin, there is explicit energy loss within the bin and energy is therefore not conserved.

We note here that the update of these equations will rely somewhat on the accuracy of the flux calculations and integral of the losses for the  $g_i$ . In order to obtain a higher-order estimate of the fluxes, we can time-center the estimate of  $f_i$  based on the slope of the distribution and the timestep chosen,

$$\begin{aligned}
 \bar{f}_i &= (f_i(t=0) + f_i(t=\Delta t))/2 \\
 &= f_i + 0.5\Delta t \frac{\partial f_i}{\partial t} \\
 &= f_i + 0.5\Delta t \frac{\partial f_i}{\partial p} \frac{\partial p}{\partial t} \\
 &= f_i + 0.5\Delta t \dot{p} \frac{f_i}{p} \\
 &= f_i(1 + 0.5\Delta t \frac{\dot{p}}{p} q)
 \end{aligned} \tag{6.16}$$

## 6.2 Introducing Cosmic Ray Transport (CRT)

I have taken the evolution equations from the previous section and implemented them in a C++ library that can be used to link with a hydrodynamical code such as Enzo. In this section we will describe the structure of CRT as well as the numerical tools used to follow the cosmic ray distribution.

CRT is composed of 4 fundamental pieces: Solvers, Structures, Support, and Tests. Solvers are any piece of the code that is used to modify the CR population. This includes acceleration, cooling, time-stepping, as well as all supporting calculations such as a Newton’s method iteration scheme to solve for the inter-bin power-law slope. In a sense, Solvers encompass all of the physics of the CRs. Structures are composed of the data structures that simplify the management of the CR distribution both in physical and momentum-space. Support functions are used for problem initialization, data input/output (I/O), debugging statements, error/output logging, and physical constants. Finally, we have built in a number of unit tests and answer tests that can be used to verify the results of the solver. These tests can be run at compile time to allow for robust code modification. The entire CRT library is encapsulated in a C++ namespace called “crt.”

### 6.2.1 Structures

There are a three primary structures that we utilize in CRT to help manage the data which carries spatial and momentum dependence. The `Data` struct contains information about a single zone of a simulation. As such, it stores information about the thermodynamic and CR distribution. In particular, it stores the momentum space distribution of  $n_i$ ,  $g_i$ ,  $f_i$ , and  $q_i$ , as well as the number of momentum bins. It also has uninitialized pointers to other arrays that are not always needed/present. As for thermodynamic quantities, it keeps track of the density, temperature, divergence, magnetic field energy density, CMB energy density (for inverse Compton), cosmological expansion factor,  $a$ , and it's derivative,  $\dot{a}$ , and finally the shock properties (Mach number, pre-shock density/temperature).

The next most important data object is the `MomentumGrid`, which keeps track of the momentum-space used in the current discretization. This C++ class tracks the number of bins,  $NBins$ , and bin edge locations ( $NBins + 1$ ) in size. During initialization, it also constructs a number of arrays that are useful to not be recalculated each time, such as  $p^2$ ,  $p^3$ ,  $p^4$ ,  $d$ ,  $d^3$ ,  $d^4$ . A final very important value is the conversion factor to convert from cgs units to hydrodynamic (driver) code units. These units are multiplied by when initializing the `Data` values for  $n_i$ ,  $g_i$  from what is handed to CRT by the driver code, and divided out before handing back.

The final data object used in CRT is a C++ class object for storing a uniform spatial grid of data, `Grid`. This `Grid` object is used as the translation layer between the driver code and CRT, and is used to provide an Application Programming Interface (API) for construction the data needed by CRT to evolve the system. It contains helper functions for initialization and memory management, as well as tools to write out a grid of data to disk. It uses the C++ Standard Template Library `map` to organize all the fields, units, and layout in a simple access pattern. For example, using it to access the density field works as:

```
crt::Grid *grid = new crt::Grid(16, 16, 16);
grid->new_zero_field("Density", 1.0e-28); // Sets conversion factor
```

```

grid->set_field_to_value("Density", 1.0e-30);

crt::CRfloat *dens;

dens = grid["Density"];

delete grid;

```

### 6.2.2 Solvers

The primary purpose of the solver is to take a distribution of CRs and evolve them in momentum-space by a timestep  $dt$ . Because of the differences in timescales associated with hydrodynamic flow and cooling of cosmic rays, it may be necessary to subcycle this solver so as not to require limiting the hydrodynamical timestep. For protons, this is usually not a stringent constraint given the long lifetimes. However, for high energy electrons under the influence of inverse Compton and synchrotron cooling, lifetimes will sometimes be much shorter than a single hydrodynamical timestep. The code flow for a single update of the CR distribution is shown in Figure 6.1.

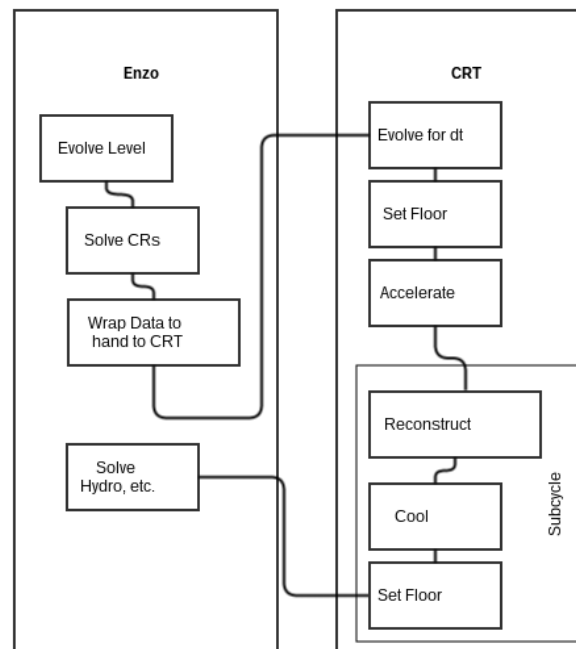


Figure 6.1 Code flow for one evolution of the cosmic rays. On the left is the evolution handled by Enzo, and on the right is the evolution handled by CRT. The reconstruction and cooling is subcycled based on a fraction of a cooling time until the final  $dt$  is reached.

During each evolution, we first set a floor for the  $n_i$ ,  $g_i$  by some `tiny_number` usually on the order of  $10^{-30}$  in code units. At this step, we also ensure that the ratio of  $\frac{n_i * p_i}{g_i}$  is in the valid range,

$$\frac{g_i}{d_i} < n_i p_i < g_i. \quad (6.17)$$

We do this in a conservative fashion where if  $g_i$  is less than the valid range, we lower the number density,  $n_i$ . If  $g_i$  is too large, then we lower it. Specifically, we set

$$n_i = \left( \frac{g_i}{p_{i+1}} + \frac{g_i}{p_i} \right) / 2 : g_i < 1.03 n_i p_i \quad (6.18)$$

$$g_i = (n_i p_{i+1} + n_i p_i) / 2 : g_i > 0.97 n_i p_{i+1}. \quad (6.19)$$

In this way we are always lowering the total number or energy density of the flow. This limiter is rarely activated, and primarily in very low density regions or when there is a very large gradient in the vicinity of shocks where the hydrodynamical solver may have errors due to interpolation of the fields (especially in an AMR context).

Once the floor is set, we inject CRs due to shocks. We inject shocks by assuming that the particle distribution smoothly joins between the Maxwellian distribution,

$$f_m = n \pi^{-3/2} p_{th}^{-3} e^{-(p/p_{th})^2} \quad (6.20)$$

where  $p_{th} = \sqrt{2mk_B T}$ , and the non-thermal tail. We therefore calculate the value of the thermal distribution at a momentum equal to

$$p_{inj} = C * 2 * p_{th}, \quad (6.21)$$

as is done in [122]. We then calculate  $n_i, g_i$  for each bin assuming that above  $p_{inj}$ , the distribution is a power-law with slope  $q_s = 3.0 * r / (r - 1)$ , where  $r$  is the compression ratio of the shock,  $r = \frac{(\gamma_{ad} + 1) * \mathcal{M}^2}{((\gamma_{ad} - 1) * \mathcal{M}^2 + 2)}$ . Other models of shock acceleration as well as any other injection mechanism could be easily implemented. If shock acceleration is active for a cell, we then explicitly skip the cooling of the cosmic rays.

After acceleration, we then reconstruct the distribution function explicitly for  $f_i$  and  $q_i$ . This involves using a Newton's method iteration for determining  $q_i$  for each ratio of  $n_i p_i / g_i$ . The stopping

criteria for this iteration is based on both the absolute error and the convergence of the calculated  $q_i$ . Newton's method depends on both the value and the derivative of the function, creating the next guess using:

$$q_{new} = q_{old} - \frac{\partial Err(q)}{\partial q} * Err(q_{old}) \quad (6.22)$$

where  $E(q_{old})$  is the evaluated error at the current guess  $q_{old}$ . In our approach, we can use both the analytical derivative of the function or determine the derivative numerically, with very similar results.

After the reconstruction phase, we now have  $f_i$  and  $q_i$  at each momentum bin. Using these, it is finally possible to calculate the updates to  $n_i$  and  $g_i$ , based on Equations 6.13 and 6.15. The only remaining numerical detail to discuss is the integral of the radiative losses term in the update of  $g_i$ ,

$$\frac{dg_{rad}}{dt} = \int_{p_i}^{p_{i+1}} p^2 \dot{p} f(p) dp. \quad (6.23)$$

As an initial improvement over assuming a constant  $\dot{p}$  over the momentum bin, we use a Runge-Kutta 4th-order integration method over the momentum range, with a static number of substeps. We have found that a value of  $N_{steps} = 4$  is adequate for the momentum bin sizes and  $\dot{p}$  functions in this work, but an obvious extension to this is an adaptive integration scheme.

As a last step, we again set the floor of the data using the same method mentioned above in order to avoid sending very small numbers back to the driving hydrodynamical code, which can sometimes be sensitive to small numbers. At the conclusion of the evolution phase, we then return the updated values of  $n_i$ ,  $g_i$  to the hydrodynamical code.

### 6.2.2.1 Radiative Losses

Here we list the radiative loss terms that have been incorporated into the CRT framework. These are directly adopted from Miniati [152]. For electrons, we have incorporated Coulomb losses

and synchrotron/inverse Compton cooling. Coulomb losses are described by

$$\begin{aligned} \left(\frac{dp}{dt}\right)_{Coulomb} &= \frac{2\pi Z^2 e^4}{m_e c^2} n \left\{ \ln \left( \frac{m_e^3 c^4}{4\pi e^2 \hbar^2 Z} \right) + \ln \left[ \frac{(1 + \hat{p}^2)^{1/2}}{n} \right] - \frac{3}{4} \right\} \\ &= 3.01 \times 10^{-29} \left\{ 1 + \left[ \ln(1 + \hat{p}^2)^{1/2} - \ln n \right] \frac{1}{73.56} \right\} n \text{ erg cm}^{-1}. \end{aligned} \quad (6.24)$$

$Z$  is the electron charge of the interacting ion,  $n$  is the number density of the thermal background gas, and  $\hat{p} = p/m_e c$ .

Synchrotron and inverse Compton losses are described by

$$\begin{aligned} \left(\frac{dp}{dt}\right)_{sync+IC} &= \frac{4}{3} \frac{\sigma_T p^2}{m_e^2 c^2} (u_B + u_{CMB}) \\ &= 8.94 \times 10^{-25} (u_B + u_{CMB}) \hat{p}^2 \text{ erg cm}^{-1}. \end{aligned} \quad (6.25)$$

The magnetic field energy density and equivalent energy density of the CMB are given by  $u_B$  and  $u_{CMB}$ .

For protons, we have incorporated coulomb losses and losses from proton-proton collisions.

For these next equations,  $\hat{p} = p/m_p c$ . Coulomb losses are given by,

$$\begin{aligned} \left(\frac{dp}{dt}\right)_{Coulomb} &= \frac{2\pi Z^2 e^4}{m_e c^2} n \ln \left( \frac{\gamma^2 m_e^3 c^4}{\pi e^2 \hbar^2 n} \frac{m_p \beta^4}{m_p + 2\gamma m_e} \right) \frac{\beta^3}{x_m^3 + \beta^3} \\ &= 3.01 \times 10^{-29} \left\{ 1 + \left[ \ln \left( \frac{\hat{p}^4 / (1 + \hat{p}^2)}{1 + 2(m_e/m_p)(1 + \hat{p})^{1/2}} \right) - \ln n \right] \frac{1}{75.7} \right\} \frac{\beta^3}{x_m^3 + \beta^3} n \text{ erg cm}^{-1}. \end{aligned} \quad (6.26)$$

Here  $\beta = v/c$ , and  $x_m = \left(\frac{3\pi}{4}\right)^{1/3} \left(\frac{2kT_e}{m_e c^2}\right)^{1/2} = 6.4 \times 10^2 \left(\frac{T_e}{10^7 K}\right)^{1/2}$ . Collisions between CR protons and thermal protons are efficient, particularly at high energies. Here we include their cooling as inelastic collisions,

$$\begin{aligned} \left(\frac{dp}{dt}\right)_{p-p} &= \sigma_{\pi,inel}(E_p - m_p c^2) n \\ &= 2.91 \times 10^{-29} (\hat{p} - \beta) n \text{ erg cm}^{-1} : e_p \geq 1.22 \text{ GeV}. \end{aligned} \quad (6.27)$$

Here only protons with energies above 1.22 GeV are cooled.

### 6.2.3 Support

The Support section of CRT is used for file I/O, initialization, logging, and storing physical constants. In particular, file I/O is implemented in a simple fashion where we use the hierarchical

data format HDF5 to store the contents of a `crt::Grid` in an HDF5 file. Initialization functions are also implemented to help create a simple power-law distribution for a single zone or an entire test grid of cosmic rays.

#### 6.2.4 Tests

The final module of CRT is that of unit and answer testing. These are two distinct types of tests, used in large scale software projects. Unit tests are typically small, light-weight tests that serve as sanity checks and to ensure API stability. For example, one of the unit tests we use is that if we run the shock acceleration module on a cell that has a Mach number less than 1, we should get identically zero acceleration. Other slightly less obvious tests include testing that the synchrotron cooling is equal to a pre-determined value for a particular set of plasma conditions. These tests can be run at compile time using `make test`, and allow developers and modifications to be made with some amount of confidence that the change has not inadvertently broken a piece of the code. In an ideal situation, unit tests would cover nearly the entire code from array creation/destruction to solver evolution and stability. At this point, a fair fraction of the code is covered, but future work is necessary to obtain complete coverage. We implement our unit testing with the googletest C++ unit testing framework<sup>1</sup>.

The remainder of this section will detail the answer tests that we also use to verify the functionality and correctness of CRT. Answer tests are physically meaningful tests that will be used to show both the internal CRT tests for single-zone calculations such as synchrotron cooling or converging flow, as well as tests involving our driver code, Enzo. We begin with single-zone tests that are used to demonstrate the evolution of a single zone of gas when it is subjected to various cooling mechanisms as well as divergence terms. These both test the accuracy as well as the robustness of CRT.

---

<sup>1</sup> <https://code.google.com/p/googletest/>



### 6.2.4.1 Adiabatic Expansion/Contraction

Our first test problem is that of a single zone undergoing adiabatic expansion and contraction. One can show that under such evolution assuming that the boundary conditions at the edges of the momentum distribution are such that the slope is constant, that the overall slope of the power-law should not change. Additionally, the evolution of  $n_i(t)$  with a  $\nabla \cdot \vec{u}/3 = C$  is

$$\begin{aligned}
 \frac{\partial n}{\partial t} &= C [f_{i+1}p_{i+1}^3 - f_i p_i^3] \\
 &= C \left[ f_i \left( \frac{p_{i+1}}{p_i} \right)^{-q_i} p_{i+1}^3 - f_i p_i^3 \right] \\
 &= C f_i p_i^3 [d_i^{3-q_i} - 1] \\
 &= (3 - q_i) C \frac{f_i p_i^3 [1 - d_i^{3-q_i}]}{q_i - 3} \\
 &= (3 - q_i) C n_i.
 \end{aligned} \tag{6.28}$$

The results of this test are shown in Figure 6.2. While there are some errors in the evolution, this

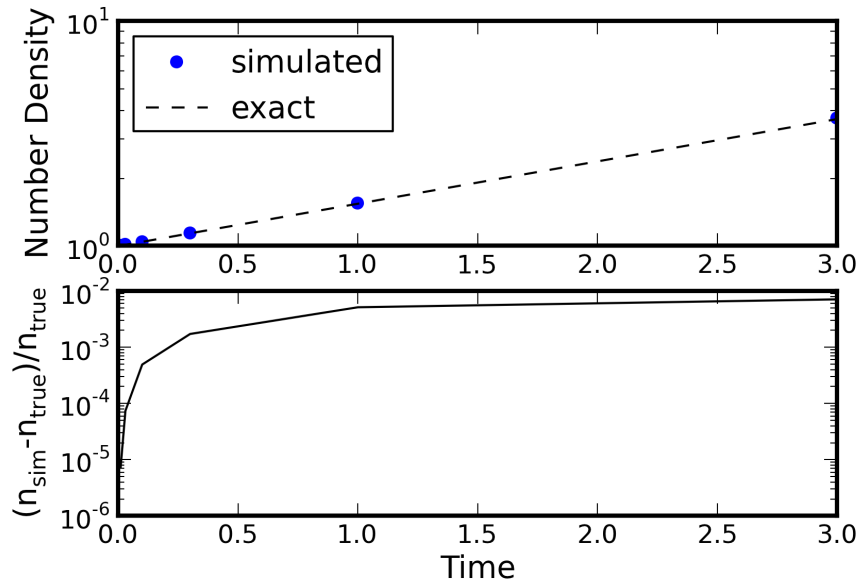


Figure 6.2 Evolution of a converging flow of a single zone, due only to the momentum-space evolution.

is expected to be the case for an explicit integration scheme that is trying to capture exponential growth.

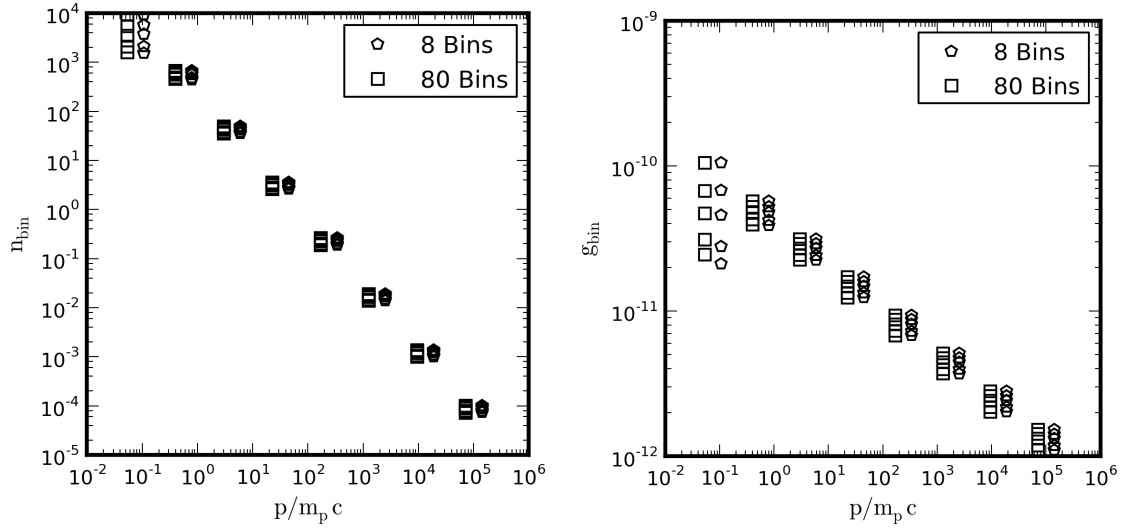


Figure 6.3 Evolution of distribution of CR protons undergoing ion-coulomb and proton-proton interactions after  $t/15\text{Gyr} = 0.1, 0.3, 0.5, 0.8, 1.0$ ). In each panel, the pentagons correspond to using 8 logarithmic bins and the squares correspond to using 80 logarithmic bins. The left panel shows the total number of protons in momentum bins defined by the low-resolution (8 bin) simulation. The right shows  $g_i$ , which is proportional to the energy density.

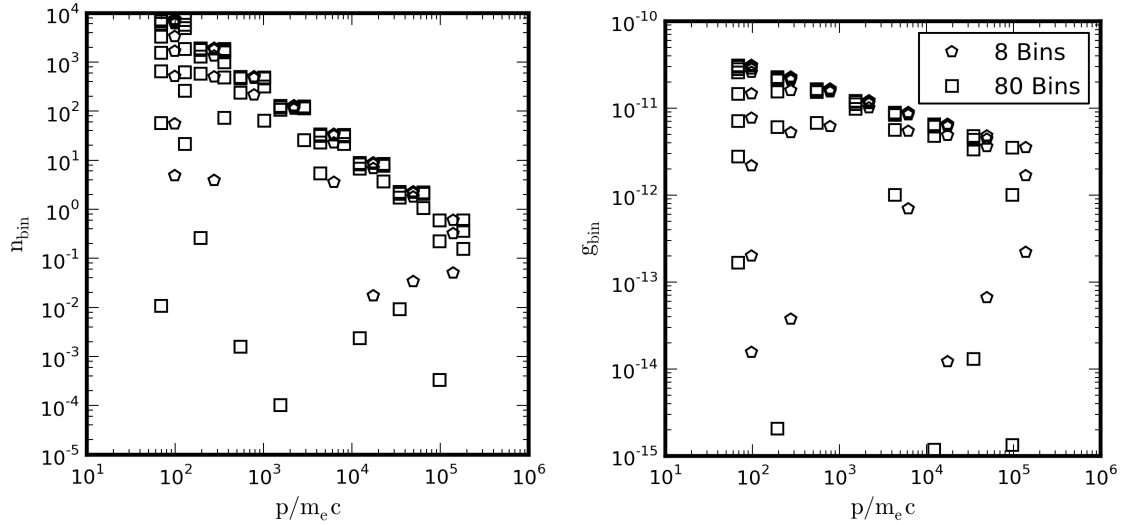


Figure 6.4 Evolution of distribution of CR electrons undergoing inverse Compton and electron-coulomb interactions after  $t/15\text{Gyr} = (5.0 \times 10^{-4}, 1.0 \times 10^{-3}, 3.0 \times 10^{-3}, 1.0 \times 10^{-2}, 2.0 \times 10^{-2}, 0.1, 0.25, 0.45, 0.6, 0.7)$ . In each panel, the pentagons correspond to using 8 logarithmic bins and the squares correspond to using 80 logarithmic bins. The left panel shows the total number of electrons in momentum bins defined by the low-resolution (8 bin) simulation. The right shows  $g_i$ , proportional to the energy density.

### 6.2.4.2 Proton Cooling

The next test we present is that of a population of protons cooling due to Coulomb and proton-proton interactions. We set up a single zone that has a temperature of  $10^7 K$ , thermal gas number density of  $10^{-3} \text{cm}^{-3}$ , and a range of proton energies from  $0.1 - 10^6 \text{GeV}$ , corresponding to relativistic  $\gamma$  factors of  $100 - 10^6$ . This can be directly compared to Miniati [152]. We allow the simulation to evolve for 15 Gyr, and present the results using both  $\text{NBins} = 8$  and  $\text{NBins} = 80$  momentum bins in Figure 6.3. These compare well to the semi-analytical results presented in Miniati [152]. Here we focus less on comparing to the semi-analytical result and rather on the robustness in the resolution needed to follow the evolution of this proton population.

### 6.2.4.3 Electron Cooling

To test the electron cooling evolution, we first test the effects of momentum space resolution, and then compare a high resolution test to an analytical result. First we use the same gas conditions as the proton test, but instead follow a distribution of electrons with energies ranging from  $50 - 2 \times 10^5 \text{MeV}$ . Here the primary cooling mechanisms are due to inverse Compton, synchrotron, and coulomb interactions. Because the synchrotron emission depends on the sum of the CMB energy density and the local magnetic field in the same fashion, we choose to set  $U_B = 0$ , and  $U_{\text{CMB}} = 4.2 \times 10^{-13} \text{erg cm}^{-3}$ , which corresponds to the current CMB energy density at  $z = 0$ . This is shown in Figure 6.4. What we see is that the comparison between 8 and 80 bins is less clear than the proton case, due to the much faster cooling times. The highest energy bins drop off within the first few timesteps. The 80 bin simulation cools slightly faster than the 8 bin because it captures the high energy evolution more accurately where the cooling is strongest. In the 8-bin, the power-law has to extend over the entire momentum range. There are other differences between the 80 and 8 bin simulations, but each of them are at a time when the population has already dropped by over a factor of 10, and the rest of the population is soon to disappear. These have little effect on any observable quantity.

To test the accuracy of a high-resolution electron simulation, we now turn off all cooling mechanisms other than synchrotron cooling. In this case, there is an analytical solution for the power-law index of the distribution as it cools. The first presentation of the analytical result appeared in Kardashev [126] and we use the form presented in Jones et al. [118], where the evolution of the power-law index,  $q(p, t)$ , is found in the presence of a uniform magnetic field. The result is

$$q(p, t) = q_0 + (q_0 - 4.0) \frac{tp/(\tau_{so}\hat{p})}{1 - tp/(\tau_{so}\hat{p})}, \quad (6.29)$$

where  $q_0$  is the initial power-law slope, and  $\tau_{so}$  is the cooling time

$$\tau_{so} = \frac{3}{4} [(m_e c^2)/(\sigma_T U_B)] (1/\hat{p}). \quad (6.30)$$

The comparison between the numerical and analytical solutions are shown in Figure 6.5 for the original distribution in purple followed by 9 logarithmically spaced times from  $10^{-5}$  to 1.0 in units of 15Gyr. The numerical solution fits very well except the first few timesteps at the highest momenta. This is due to the choice of a constant slope upper boundary condition. This impacts the flux estimate and causes the small ripple in the slope. This has a very small impact on the number density, which is more important for any synthetic observation.

### 6.3 Hydrodynamic Tests with Enzo

In this section, we focus on tests run when integrating CRT with Enzo, an adaptive mesh refinement magneto-hydrodynamic plus N-body cosmological code. We begin with following the cosmological expansion of a uniform field of gas and cosmic rays. We then use a shock-tube simulation to demonstrate the shock-acceleration mechanism, allowing the cosmic rays to cool behind it.

#### 6.3.1 Cosmological Expansion

The first test we present is that of cosmological expansion of a uniform density volume. The hydrodynamical timestep is limited by the usual Enzo mechanisms, while the cosmic rays

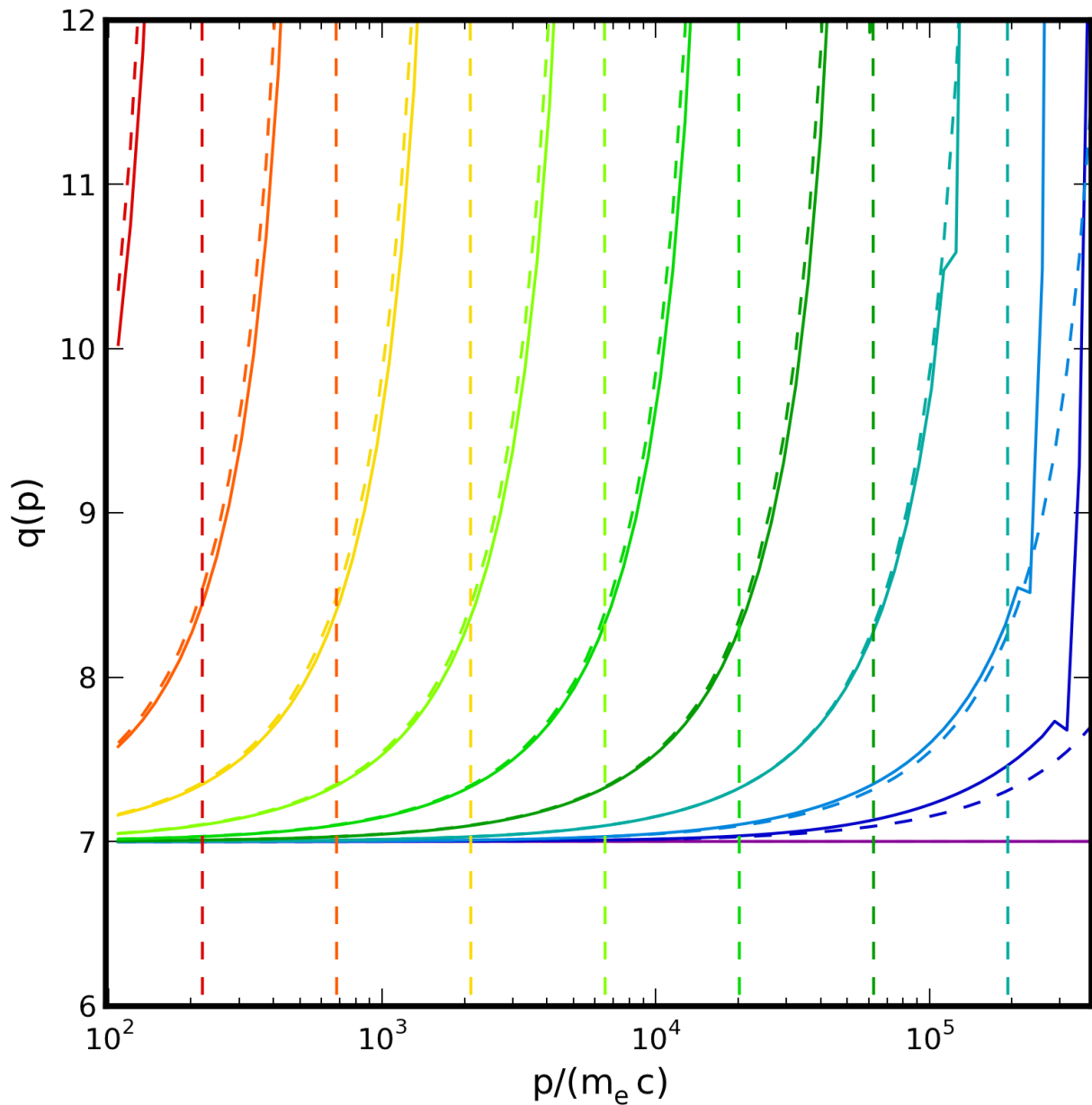


Figure 6.5 Evolution of distribution of CR electrons undergoing synchrotron cooling. Each line corresponds to a snapshot in time corresponding to fractions of 15Gyr,  $t/15\text{Gyr} = (0, 10^{-5}, 10^{-4.5} \dots 10^{-0.5}, 1.0)$ , starting from purple and moving to red. The vertical dashed shows the critical momenta for each time in the same color where all the electrons will have cooled at that point. The results from an 80 bin simulation are shown in solid lines, and the analytical results for each time is shown in dashed.

are subcycled at 10% of  $p/\dot{p}$ . As with the adiabatic expansion/contraction test above, this has a simple analytic solution. The constant in Equation 6.28 can be replaced by  $\frac{\dot{a}}{a}$ , and with a bit of manipulation,

$$\begin{aligned}
\frac{\partial n}{\partial t} &= (3 - q_i) C n_i \\
\frac{\partial \log(n)}{\partial t} &= (3 - q_i) \frac{\partial a / \partial t}{a} \\
\frac{\partial \log(n)}{\partial \log(1+z)} \frac{\partial \log(1+z)}{\partial t} &= (3 - q_i) \frac{\partial \log(1/(1+z))}{\partial t} \\
\frac{\partial \log(n)}{\partial \log(1+z)} \frac{\partial \log(1+z)}{\partial t} &= -(3 - q_i) \frac{\partial \log(1+z)}{\partial t} \\
\frac{\partial \log(n)}{\partial \log(1+z)} &= q_i - 3.
\end{aligned} \tag{6.31}$$

Since this is only the term relating the momentum-space evolution, we have to add in the effects of cosmological expansion, which like baryonic density is proportional to  $(1+z)^3$ . This results in a total evolution of the CR number density as

$$\frac{\partial \log(n)}{\partial \log(1+z)} = q_i, \tag{6.32}$$

which is plotted against the results of our test simulation in Figure 6.6 for an initial power-law slope of  $q_i = 4.3$ . We note here that the hydrodynamical term due to the expansion is implemented by modification to the length units in Enzo rather than an explicit term, which is why the baryons are exactly aligned with the analytical solution. That same hydrodynamical term is also accounted for exactly with the cosmic rays, but the explicit nature of the momentum-space term leads to small deviations for long integration times. However, these deviations will be unimportant in most situations where the cooling and acceleration terms dominate the evolution.

### 6.3.2 Shock Tube

These tests are meant to demonstrate the behavior of the cosmic ray spectrum as it is accelerated at a shock front, and either advects downstream or is subject to cooling terms. These shocks are simulated in galaxy cluster environments in order to extract meaningful cooling times for relevant magnetic field, temperature, and density values. In this test, we initialize a shock with

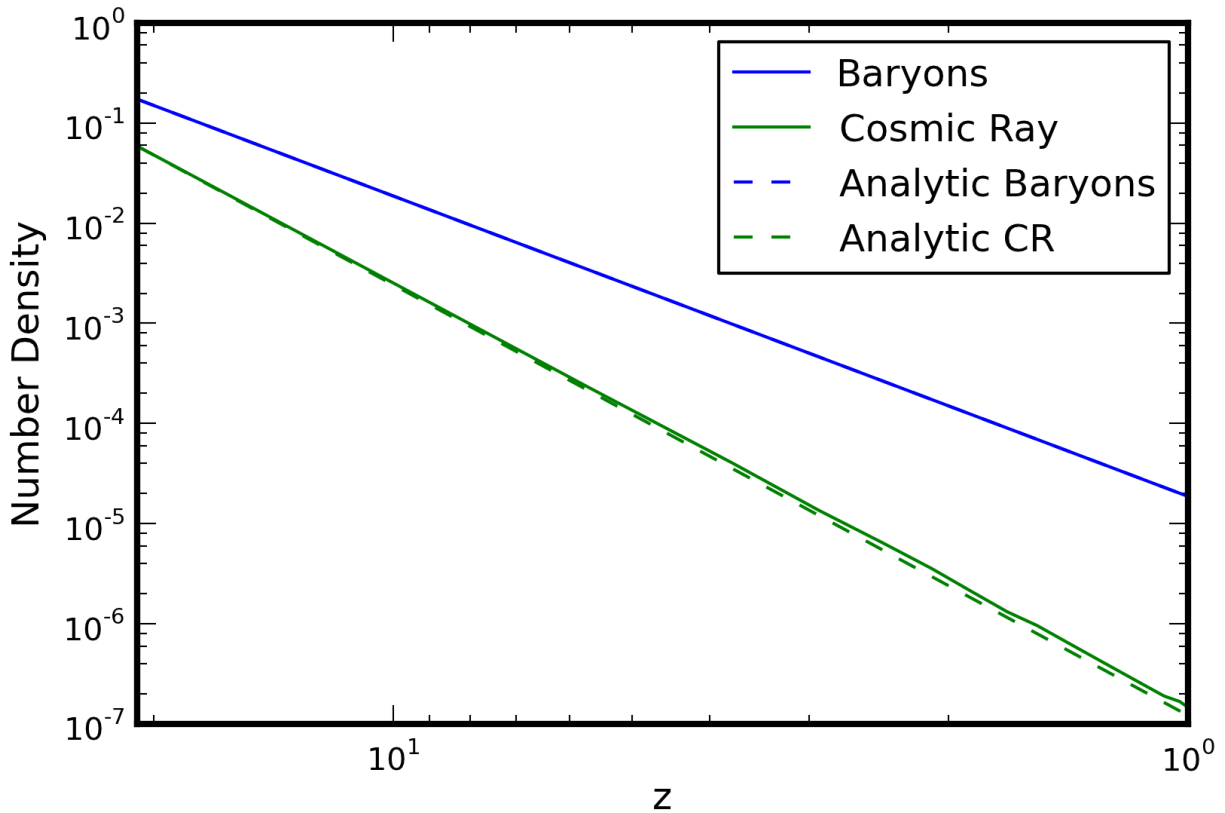


Figure 6.6 Evolution of the total number density of electrons in an adiabatically expanding, uniform density Enzo simulation (AdiabaticExpansion in the Enzo test problems). Shown are the baryon and cosmic ray number densities as a function of cosmological redshift, with the analytical solutions in dashed lines according to Equation 6.32 with an initial power-law slope to the CR distribution of  $q_i = 4.3$ .

$\mathcal{M} = 5$ , with a post-shock temperature of  $10^8$  K and pre-shock density of  $10^{-3} \text{cm}^{-3}$ . The resulting structure if viewed in the rest-frame of the shock front will become stable, with the advection of the flow highlighting the cooling of the electrons. Note that we do not take energy out of the shock as we inject energy into the cosmic rays. In this test we assume that the magnetic field is defined by the plasma  $\beta = \frac{U_{th}}{U_B} = 100.0$ . This leads to micro-Gauss field levels in the  $10^8 \text{K}$  gas, as can be seen in Figure 6.7. The resulting structure is seen in Figure 6.8.

As expected, the cosmic rays are accelerated at the shock to a power-law distribution that quickly cools for the highest energy bins. The low energy bins take longer to fully decay to zero. On the far right side, we see that the CRs have not made it completely downstream yet, and we see the remnants of the initial low level population of CRs. The exact efficiency of the shock acceleration is tested in our unit testing framework to ensure that our model numerically matches our theoretical model.

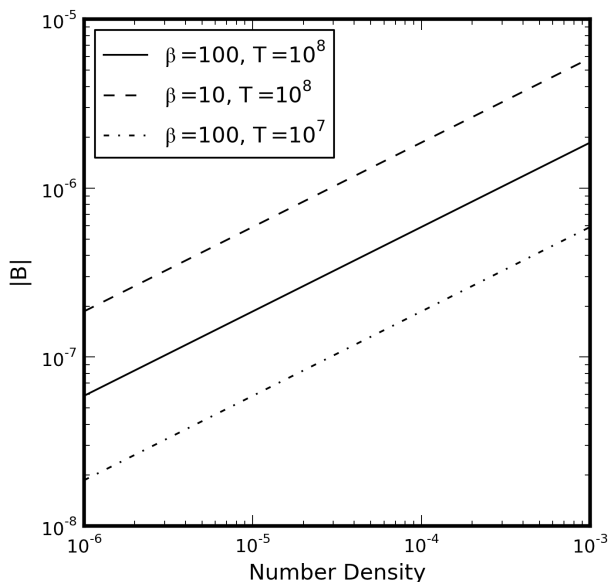


Figure 6.7 The magnetic field strength as a function of number density for a constant  $\beta$  plasma.



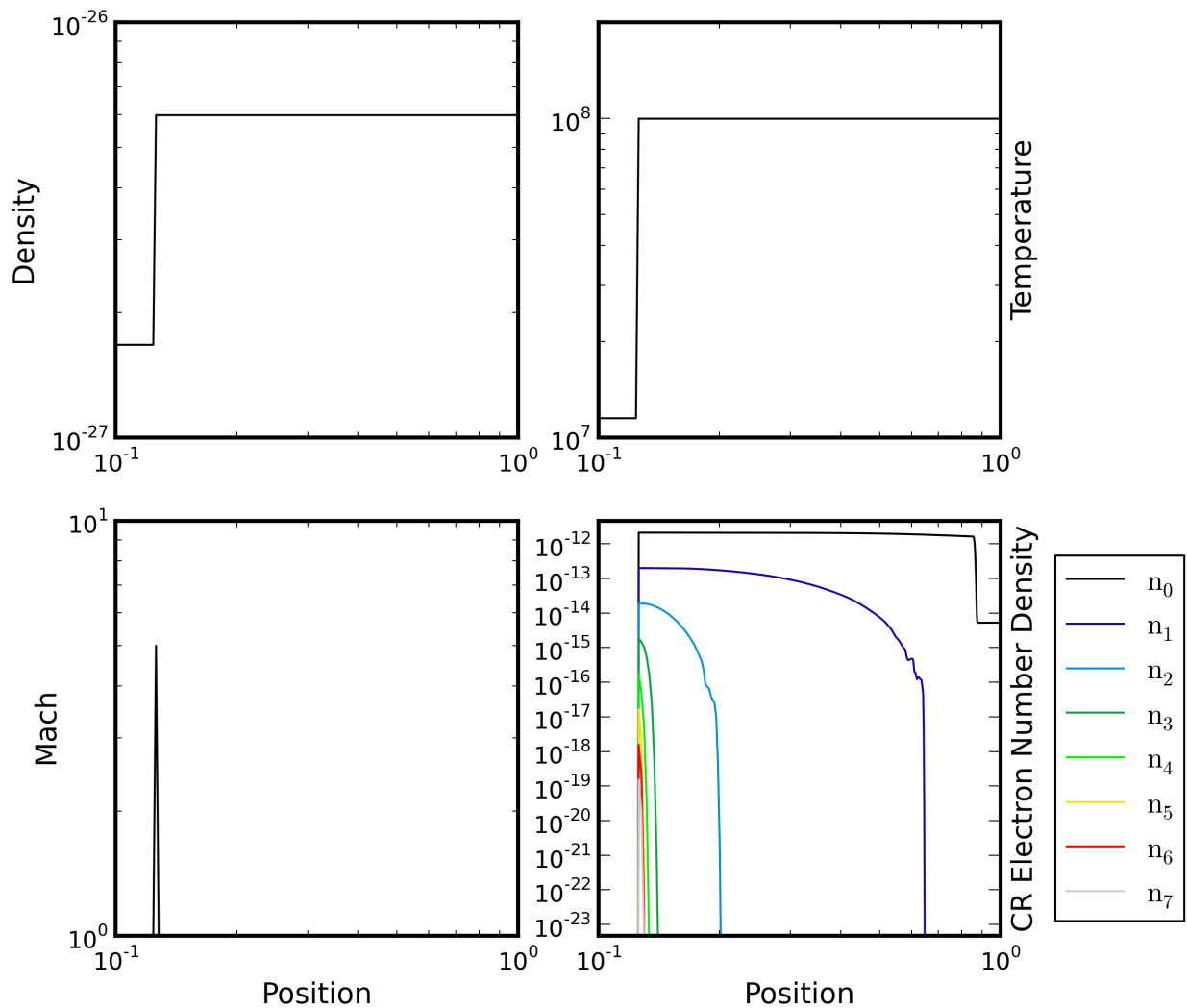


Figure 6.8 Evolution of distribution of CR electrons behind a stationary  $\mathcal{M} = 5$  shock, with gas entering from the left characterized by a post-shock temperature of  $10^8\text{K}$  and pre-shock number density of  $10^{-3}\text{cm}^{-3}$ . Shown are gas density (upper left) and temperature upper right), shock Mach number (lower left), and the number density of electrons in each of the 8 momentum bins, spanning from  $\gamma = 100 - 2 \times 10^6$ . An equipartition magnetic field with  $\beta = 100$  is chosen to determine the synchrotron cooling behind the shock.

## 6.4 Cosmic Ray Electrons in a Massive Galaxy Cluster

Here we introduce and describe the evolution of a galaxy cluster including a population of cosmic ray electrons. This is the highest resolution simulation of a galaxy cluster that includes the evolution of multiple-momentum bin populations of electrons ever done. Even from this single simulation, we will see how naturally and self-consistently diffuse radio emission is formed, solidifying our theories of shock-(re)accelerated electrons. We'll begin by describing the simulation, then move on to describing the first analysis and time evolution of the cluster.

### 6.4.1 Simulation Setup

We begin by selecting a galaxy cluster from a low-resolution unigrid simulation of a comoving  $(360Mpc/h)^3$  volume using cosmological parameters prescribed by WMAP9 [106]. We then construct a merger tree using *yt* to find the most massive halo, which happens to have a major merger (less than 3:1 mass ratio) near redshift  $z = 0.5$  and is beginning to have a near equal-mass merger at  $z = 0.0$ . We then construct high-resolution “zoom-in” initial conditions using MUSIC [101] which results in a highest-resolution region using a root grid and 3 nested regions with the following characteristics:

- volume:  $56.25 \times 56.25 \times 61.875h^{-3}Mpc^3$
- particle mass:  $2.7313 \times 10^9h^{-1}M_\odot$
- baryon mass/cell:  $5.48672 \times 10^8h^{-1}M_\odot$
- dims:  $160 \times 160 \times 176$  cells
- dx:  $0.351562h^{-1}Mpc$

We then allow the AMR based on overdensity of gas and dark matter to refine up to level 7, corresponding to  $\Delta x = 21.97h^{-1}(1+z)^{-1}kpc$  maximum resolution. We note that this is not particularly high spatial resolution for this size galaxy cluster, but that it does have very high

mass resolution. As described in Chapter 3, this is more than adequate mass resolution, and sufficient spatial resolution, to capture the shock characteristics and kinetic energy dissipation through shocks. We initialize the simulation at  $z = 100$ , and follow its evolution to  $z = 0$ . We utilize the PPM hydrodynamic solver in Enzo.

Along with the gas-dynamical quantities, we follow a distribution of cosmic ray electrons with energies between  $50\text{MeV} - 2 \times 10^6\text{MeV}$ , corresponding to relativistic factors of  $\gamma \sim 100 - 4 \times 10^6$ . We use 8 logarithmically spaced momentum bins. Instead of following the magnetic field evolution explicitly, we instead parameterize the magnetic field such that the ratio of the gas pressure to the magnetic pressure is a constant  $\beta = \frac{P_{th}}{P_B} = 10.0$ . For  $n = 10^{-4}$  and  $T = 10^7 - 10^8\text{K}$  gas, this leads to  $\approx 2 - 6\mu\text{G}$  field strengths, consistent with many rotation-measure estimates of magnetic fields [96, 77] in cluster environments. We include electron Coulomb, inverse Compton, and synchrotron cooling self-consistently in the CRT solver. Note that for the majority of the low-density/temperature gas, the inverse Compton cooling term dominates over the synchrotron cooling since the equivalent magnetic field strength corresponding to the CMB energy density is  $B_{CMB} = 3.24(1+z)^4\mu\text{G}$ , which is higher than most of the assumed magnetic field strength. For injection, we only include shock acceleration, and assume that the momentum where the power-law distribution connects to the thermal distribution is described by equation 6.21 with a value of  $C_{inj} = 2.1$ .

#### 6.4.2 Time Evolution

We start by presenting the time evolution of the cluster from  $z = 1.14$  to  $z = 0.0$  in Figures 6.9 - 6.15. In each of the 6-panel figures, we show the time evolution of a single quantity from  $z \approx 1.14 - 0.0$ . We begin by presenting the mass-weighted density in Figure 6.9, where we see an initial pair of two comparably-sized clusters separated by several comoving Mpc. At  $z \approx 0.5$ , they merge along the plane of the “sky” and the cluster then relaxes until  $z = 0$  when a second merger is beginning from the right side. Along with the main clusters, we see a flurry of sub-halos surrounding the galaxy cluster, each representing cluster galaxies. We note here that resolving these

sub-halos are only possible due to our very high dark matter mass resolution of a few  $\times 10^9 M_\odot$ .

The corresponding evolution in temperature is shown in Figure 6.10. Whereas the density is very high only near the centers of the halos, the gas temperature is high far out into the ICM,  $2 - 3 Mpc/h$  out from the center of the cluster. In particular, we see that at  $z = 0.5$  the major merger produces two outward-moving shocks that heat the gas up to  $\sim 10^8 K$  along the direction the merger. These shocks eventually move out through the entire ICM, heating the gas to  $10^7 K$  beyond the virial radius towards the accretion shock. Cooler sub-clusters can be seen, particularly in the final frame in the lower-left region of the cluster where the over-dense halo has fallen through the ICM. At the final timestep, we see that the majority of the field of view has been heated to above a few  $\times 10^6 K$ , and we also see the effects of the merger from the right begin to heat the gas and create a weak shock at the intersection of the two clusters.

Next, we integrate the total synchrotron emission at a given frequency that is contributed by each of the cosmic ray electron bins. We do this in an initial pass by simply approximating the entire populations of each electron bin as being located at the bottom of the momentum bin. Future work will incorporate a full integral over the distribution within each cell. Our approximation here will shift some amount of radiation from higher frequencies to lower frequencies, but should not change the overall interpretation. Therefore for each momentum bin, we take the value of  $n_i$  and multiply it by the power emitted by a single electron from Equation 1.21. Doing so, we are able to calculate the total synchrotron power at any frequency, and integrate it along the line of sight to obtain a surface brightness. In our presentation here, we show the emission at the front of the simulation domain, meaning that in order to estimate the flux for a realistic observation, the simulation would need to be placed at a realistic distance, and the frequency of the radiation would need to be modified to take cosmological redshift into account.

In Figure 6.11, we show the main visual result of this simulation – the synchrotron radiation at  $1.4 GHz$ . Strikingly, this simulation has what looks very similar to a classic double radio-relic at  $z = 0.5$ , where two large  $> Mpc$  arcs are moving outward from the center of the cluster. Examining the time evolution (not shown), one can see that it the radio emission moves out from the center,

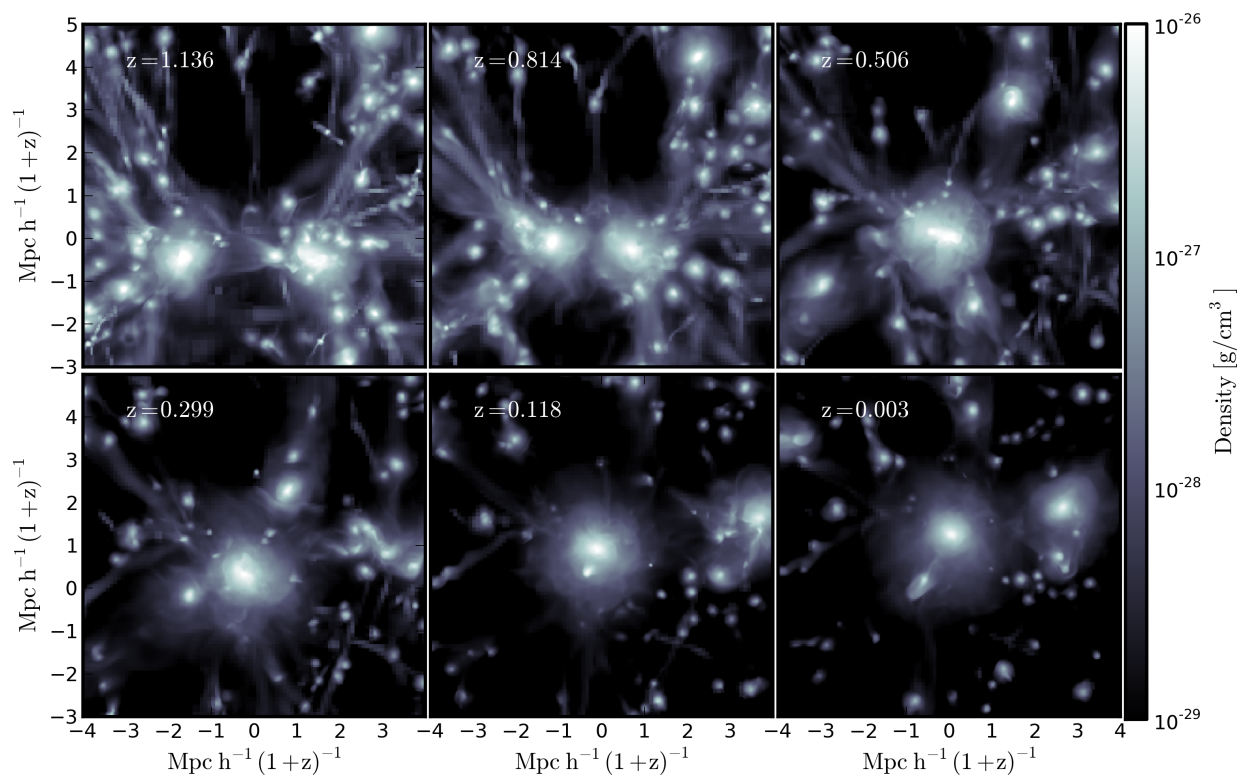


Figure 6.9 A projection of baryonic gas density, weighted by cell mass in a  $(10Mpc/h)^3$  comoving volume, shown at 6 different redshifts. A major merger occurs at  $z = 0.5$  in the top right panel, and a second major merger is just beginning at  $z = 0.0$  in the bottom right panel.

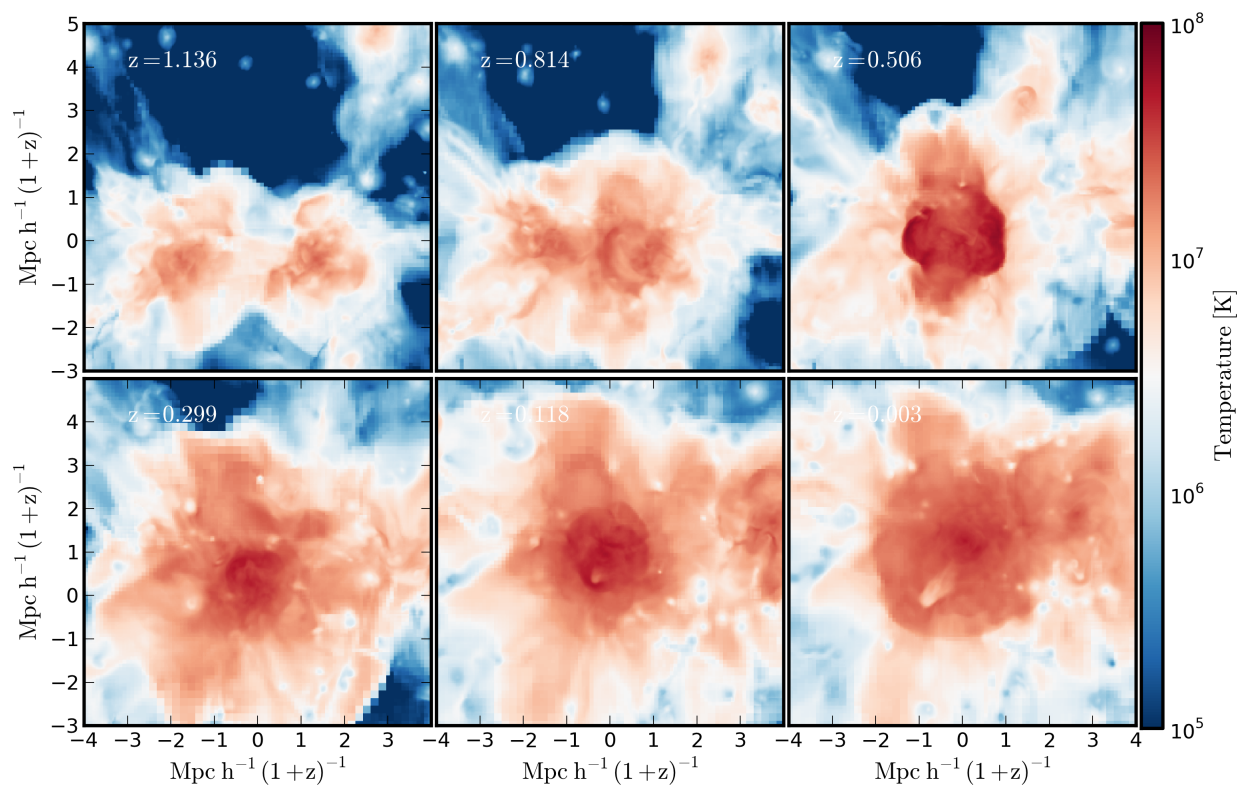


Figure 6.10 The same as Figure 6.9, except now gas temperature weighted by cell mass.

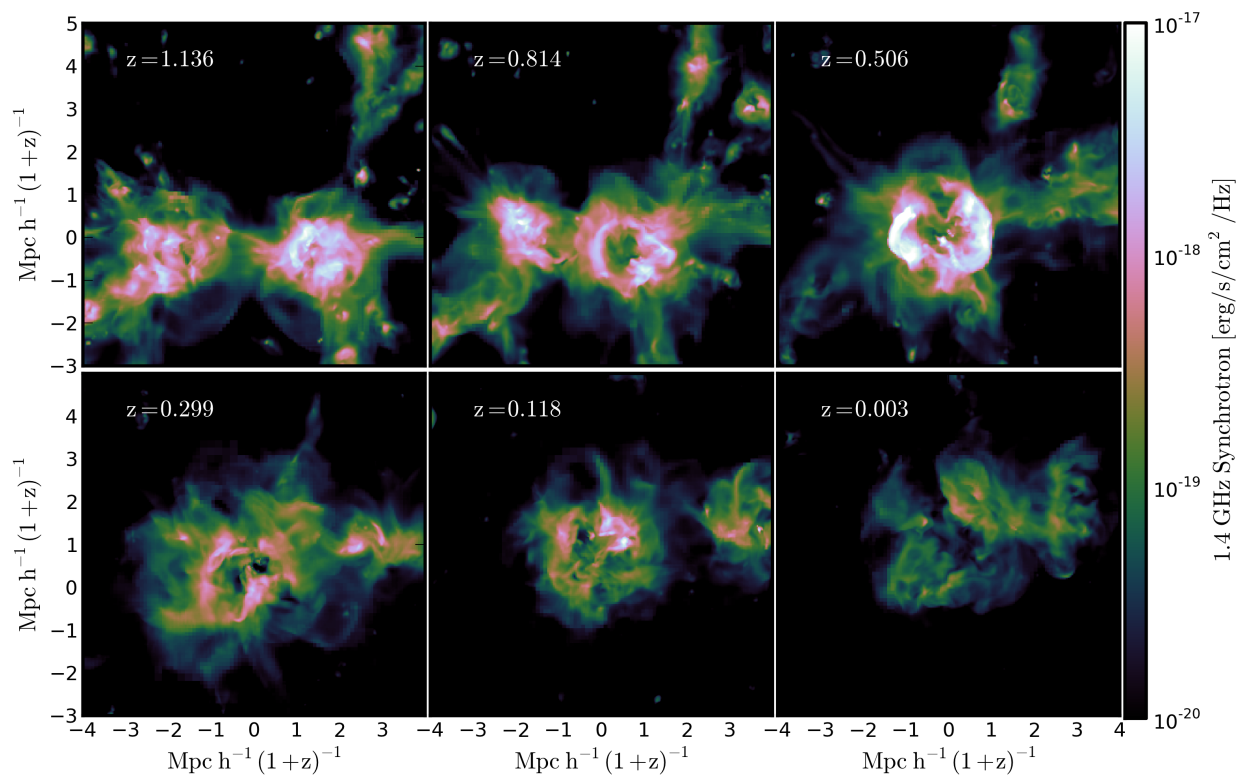


Figure 6.11 The same as Figure 6.9, except now 1.4 GHz Synchrotron emission projected along the line of sight.

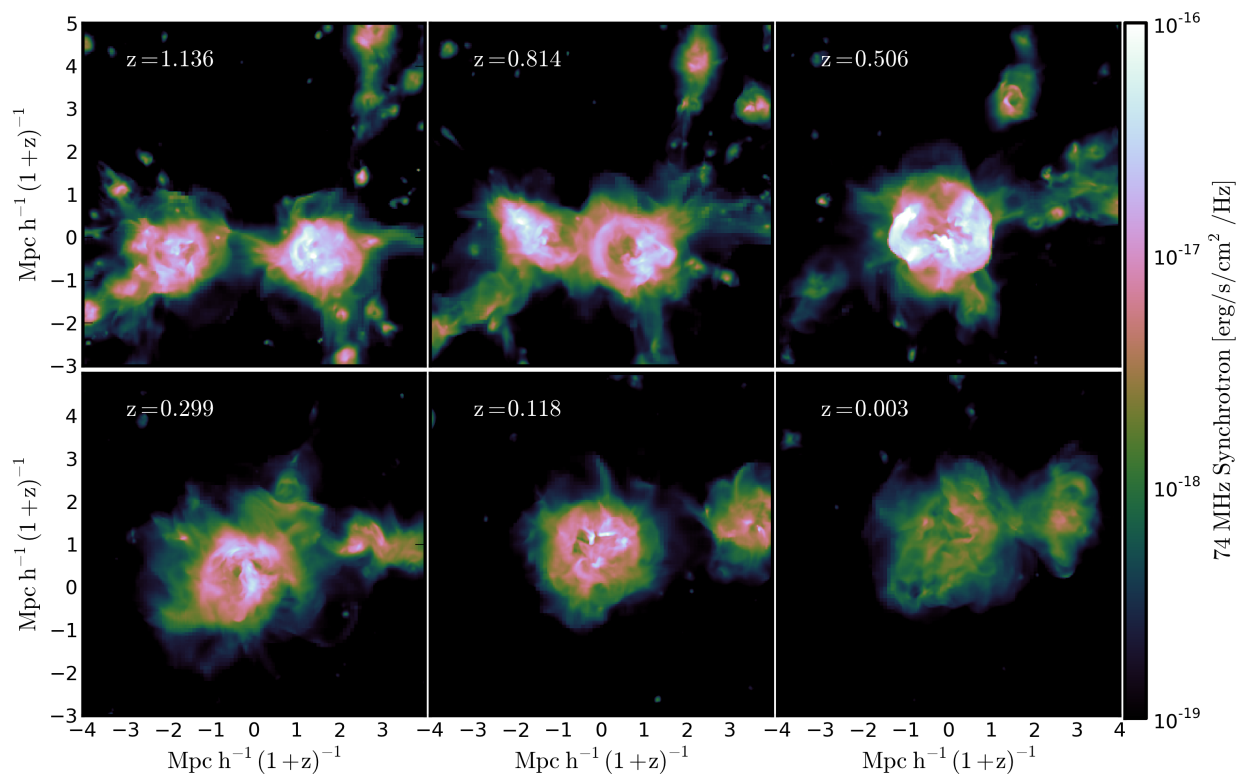


Figure 6.12 The same as Figure 6.9, except now 74 MHz Synchrotron emission projected along the line of sight. Note the scale has shifted by an order of magnitude.



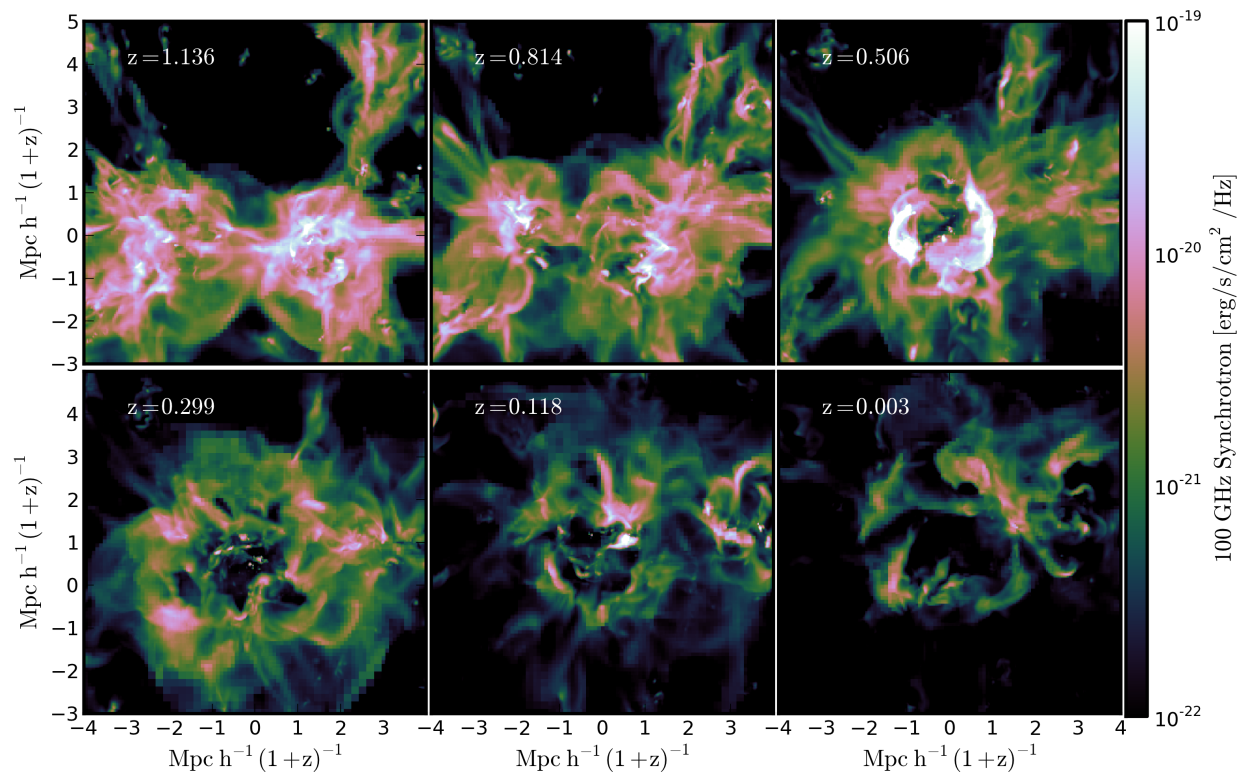


Figure 6.13 The same as Figure 6.9, except now 100 GHz Synchrotron emission projected along the line of sight. Though unlikely to be observed, this shows the rapid cooling of the high energy electrons, where now the emission is constrained around sites of acceleration (shocks). Note that the color scale has changed from the previous two figures.

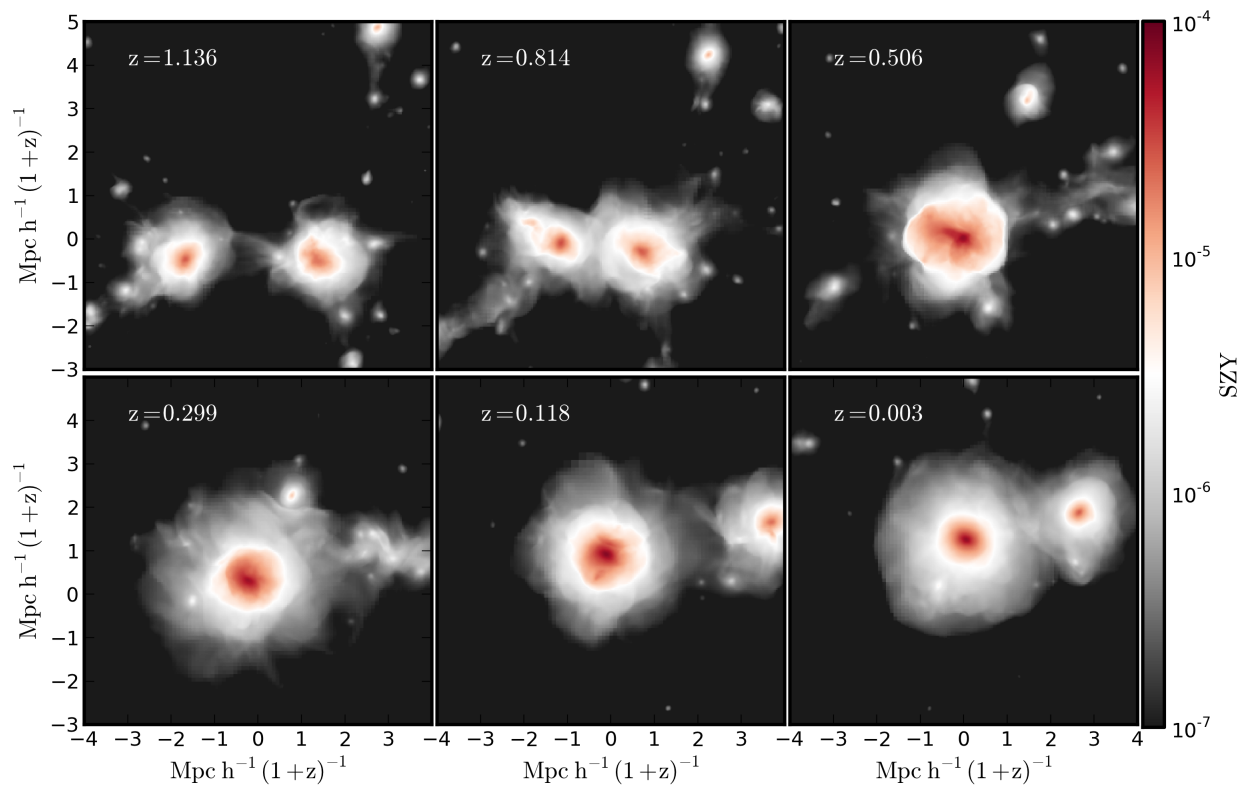


Figure 6.14 The same as Figure 6.9, except now shows the integrated thermal Sunyaev-Zel'dovich effect  $y$ -parameter.

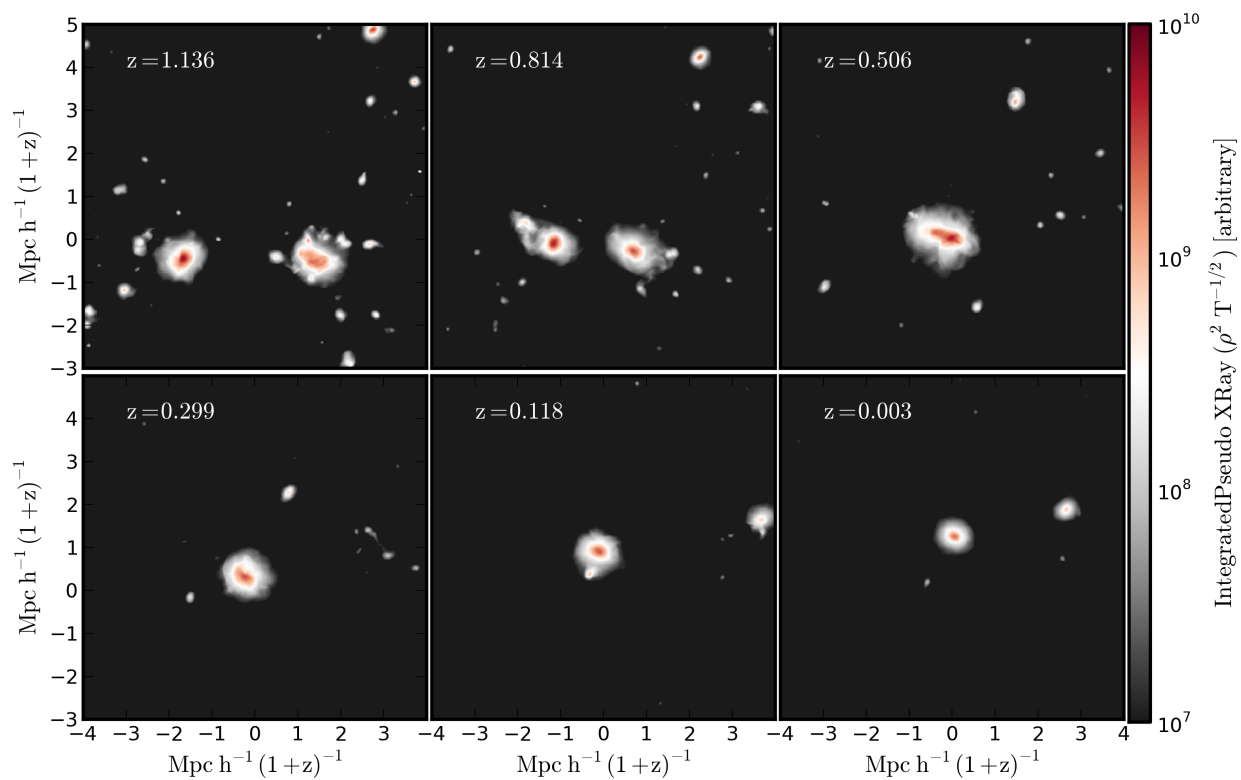


Figure 6.15 The same as Figure 6.9, except now shows the integrated Pseudo-Xray emission, which captures the  $\rho^2 T^{-1/2}$  dependence.

accelerating electrons behind the shock front. Like in many observations, we see the emission fall off behind the shock towards the center due to the cooling of the high energy electrons. As the electrons cool, the peak frequency of the radio emission falls out of the  $1.4GHz$  band. Prior to this major merger, we see that there is still a substantial amount of radio emission, likely due to the enhanced merger activity at high redshift. At  $z = 0.8$ , we see the remnants of a previous merger in the right cluster where a ring-like structure has formed.

After  $z = 0.5$ , the emission rapidly falls off, though the emission extends further out into the cluster for a short period of time. There are additional minor mergers as small halos fall in, creating small pockets of radio emission. Finally, by  $z = 0$ , the emission has dropped by over an order of magnitude from the peak, much like what we have seen in earlier studies of the time evolution of radio relic emission [213, 214]. Throughout the evolution, we see a strong gradient from the outskirts of the cluster towards the center, where the increased density and temperature (which corresponds to a higher magnetic field strength using our constant- $\beta$  model) decreases the synchrotron cooling time, and the electrons rapidly cool out of this band.

We contrast this now with Figure 6.12, where we instead show the 74MHz emission for the same set of six snapshots. Here we see that the emission fills a larger fraction of the interiors of the clusters, particularly after the major merger. Instead of rapidly cooling in the centers, the emission remains in the cluster core even at late times. At these low energies, the dominant cooling is due to Coulomb collisions, which is a fairly weak function of momentum and number density. Because of this, the electrons do not preferentially cool faster in the cores of the cluster, and the entire region remains bright at this frequency. This is similar to the shock tube test problem in Figure 6.8. These cooling low energy electrons are also being replenished by those from high energy bins. In the outskirts, there is a slower supply of new low-energy electrons. This momentum-space balance will be investigated in detail in future work.

At the other end of the spectrum, we now show the very high frequency emission at 100GHz. At this high of frequency, the relative synchrotron emission is quite low and likely undetectable with current telescopes. However, it serves the purpose of describing what happens to the very high

energy electrons. What we see is a very complex network of shock structures that are accelerating electrons. However, because the lifetimes are so short, the emission appears in very thin shells and filaments. Here we see the emission in the center of the cluster drop out very rapidly after the major merger, leaving behind only the emission due to minor mergers passing through the cluster atmosphere.

Finally, we include the same six panel evolution of both the thermal Sunyaev-Zel'dovich effect integrated along the line of sight and a pseudo-X-ray field that integrates  $\rho^2 T^{-1/2}$  that is proportional to the Bremsstrahlung emission. For the tSZE, we present the Compton  $y$  parameter in Figure 6.14, leaving the frequency dependence out for the current presentation. The X-ray is shown in Figure 6.15. As expected, both quantities trace the paths of the clusters as they merge. Both are shown with an arbitrary dynamic range of  $10^3$ . We see that unlike the X-ray, which closely follows the density distribution, the tSZE seems to correlate very well with the radio emission. This is particularly true at low frequencies where the low energy electrons remain near the cluster core. During the major merger, the sharp spatial drop in the tSZE signal is precisely where the radio emission is the strongest. This is as expected since the same shock that is accelerating the electrons also causes a jump in the gas pressure, which is what the tSZE is sensitive to. Future work will investigate the correlation between the tSZE and radio synchrotron emission in significant detail.

### 6.4.3 Radial Profiles

Here we show the radial profile of the cluster at  $z = 0.5$  and  $z = 0.0$ , during a merger and at the end of our simulation just before a major merger occurs. These profiles primarily serve the point of giving a complete picture of the structure of this cluster. In each of the Figures 6.16- 6.22, we show the structure at  $z = 0.5$  on the left, and  $z = 0$  on the right. All the solid lines are the average profiles, with the dashed lines showing the standard deviation of the profiles. Any time the dashed lines are above the solid line, it signifies that there is significant variation in a given field. For example, we can see the effects of the merger in Figure 6.16 where the density profile and its standard deviation overlap beginning around 0.5Mpc from the core, meaning the cluster is very

un-relaxed at that time compared to  $z = 0$  in the right panel where we see the density smoothly drop out to  $\sim 2\text{Mpc}$  near the virial radius of the cluster. Therefore, the standard deviation dashed lines should be thought of as measures of scatter, and not measurement or systematic error.

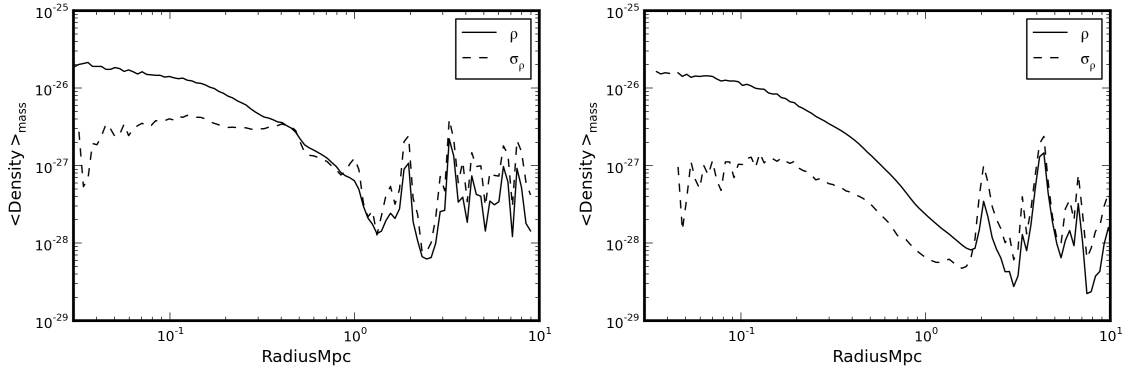


Figure 6.16 Gas density radial profile for  $z = 0.5$  (left) and  $z = 0.0$  (right). The solid line indicates the average density, while the dashed line shows the standard deviation of the gas density.

The same general structure is seen in the temperature (Figure 6.17), pressure (Figure 6.18), and X-ray (Figure 6.19) profiles. The X-ray profiles are particularly sensitive to the un-relaxed state of the cluster since it has such a strong dependence on gas density. The pressure profile, however, is still relatively smooth.

In Figure 6.20, we present the radial profile of three different populations of electrons, with relativistic  $\gamma$  factors of  $\sim 100, 3000$ , and  $10^5$ . At  $z = 0.5$ , we see that the cosmic rays extend quite far into the central regions of the cluster, and the high energy electrons show a peak at  $\sim 200\text{kpc}$  and  $\sim 1\text{Mpc}$ , near the locations of the strong radio emission. Also note that the standard deviation of these profiles is well above the average, meaning that the distribution is spatially asymmetric in nature. We compare this distribution to that at  $z = 0$ , and see instead a relatively smooth profile, but one that is significantly reduced particularly for the higher energy electrons. Only in the outskirts where there is still considerable shock activity is there any significant population of electrons.

The behavior of the CR electron number density is very similar to the corresponding profiles of synchrotron radiation, shown in Figure 6.21. Four different frequencies are shown, highlighting

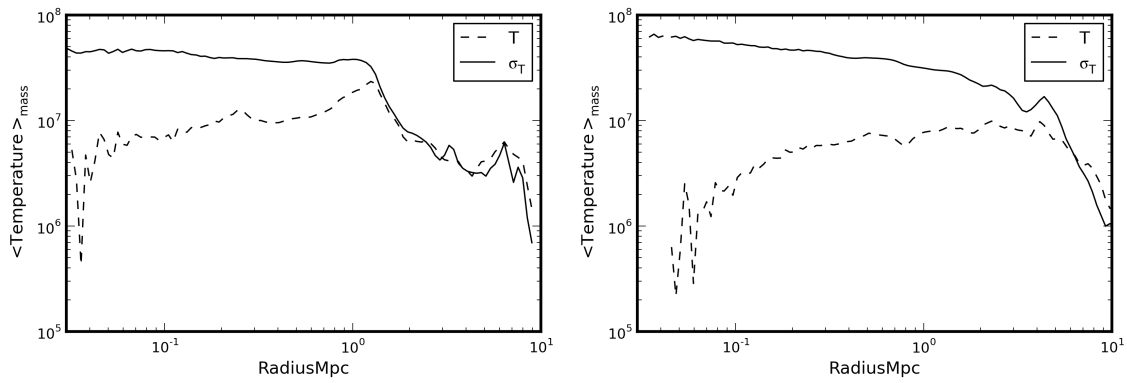


Figure 6.17 Same as Figure 6.16, but for gas temperature.

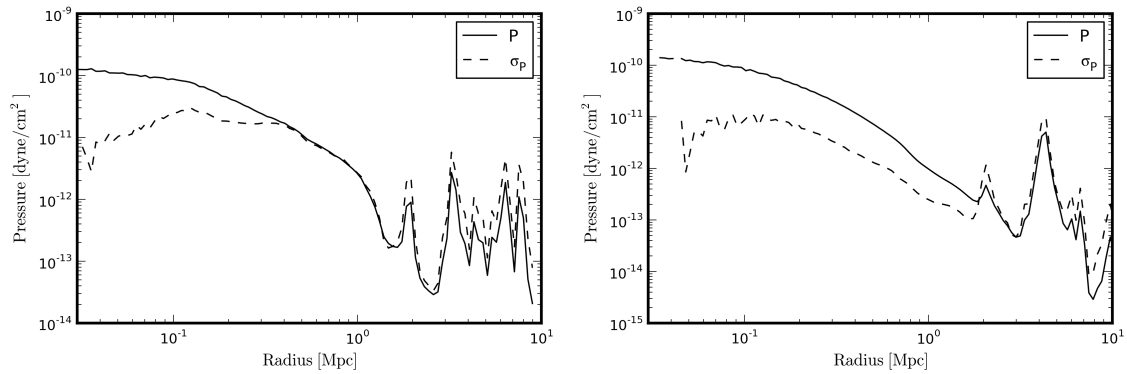


Figure 6.18 Same as Figure 6.16, but for gas pressure.

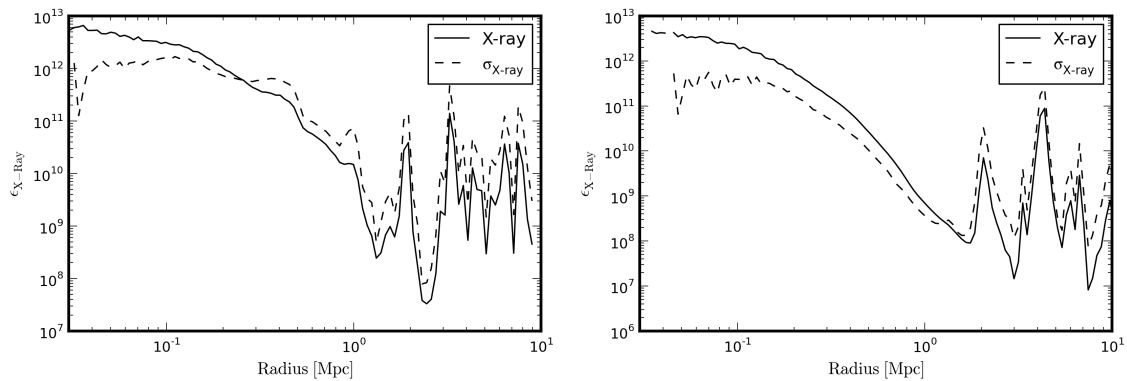


Figure 6.19 Same as Figure 6.16, but for pseudo X-ray emissivity.

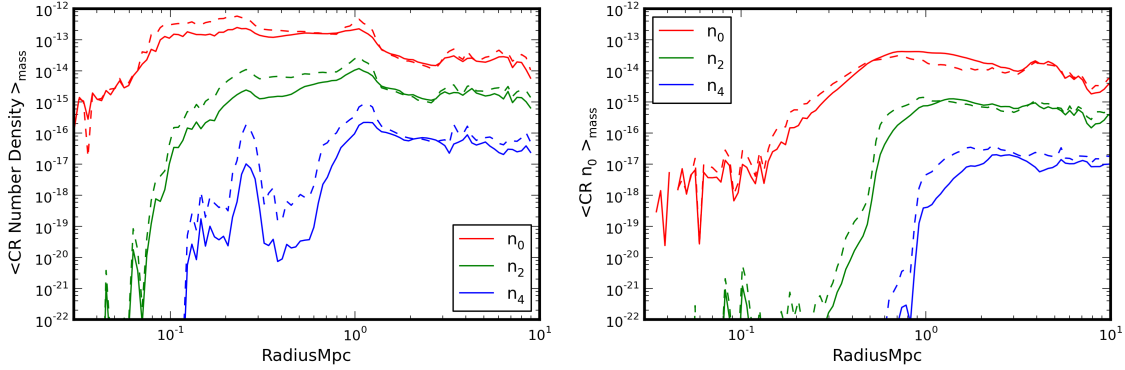


Figure 6.20 Cosmic ray electron number density radial profile for  $z = 0.5$  (left) and  $z = 0.0$  (right). Shown are three of the eight momentum bins, corresponding to  $\gamma$  factors of  $\sim 100$ , 3000, and  $10^5$ .

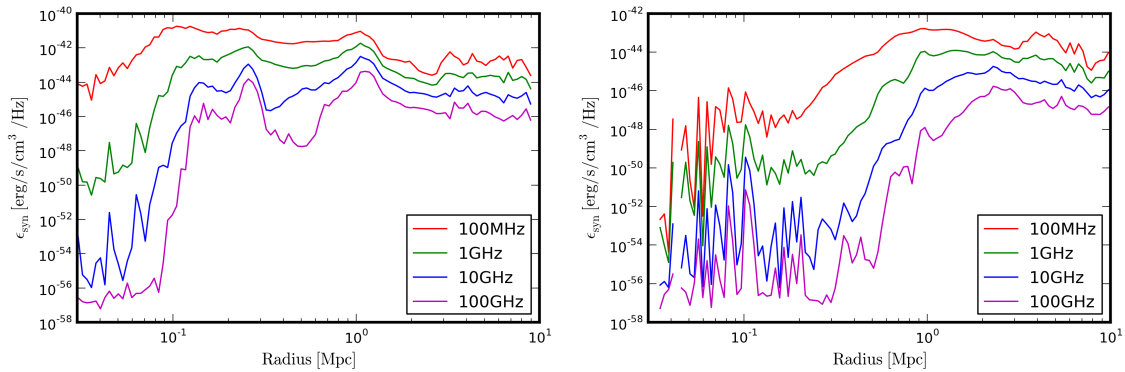


Figure 6.21 Synchrotron emission radial profile for  $z = 0.5$  (left) and  $z = 0.0$  (right). Shown are four different frequencies ranging from 100MHz to 100GHz.

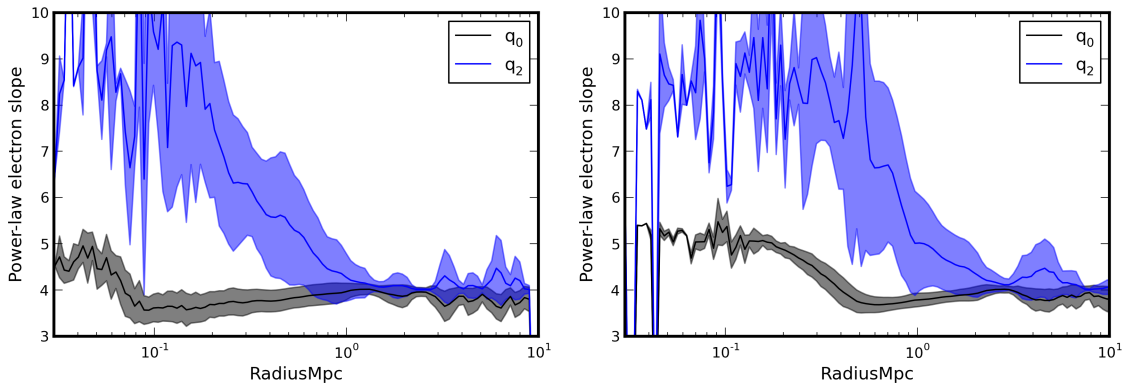


Figure 6.22 Cosmic ray electron distribution power-law index radial profile for  $z = 0.5$  (left) and  $z = 0.0$  (right). Shown are two of the eight momentum bins, corresponding to  $\gamma$  factors of  $\sim 100$  and 3000. The shaded regions indicate the range of 1 standard deviation.



again how quickly the radiation drops off at  $z = 0$  in the center of the cluster compared to the highly disturbed state at  $z = 0.5$ . Like we saw in the electron number density, we see a peak in the higher frequency radio emission at the location of the shocks as they move outward through the cluster. These are the locations of the strong emission seen in Figure 6.11.

Finally, we can also see the effects of the aging electrons by showing the profile of the CR distribution power-law slope, as done in Figure 6.22. Here we only show the lowest energy bin at  $\gamma \sim 100$  and the second bin  $\gamma \sim 3000$ . On the left, we see a very flat distribution for the  $q_0$  slope very far in to the center of the cluster, indicating that the population has been recently accelerated. The  $q_2$  distribution is also relatively flat in the outskirts where there is continuous acceleration due to shocks. However, by  $z = 0$ , both profiles have significantly steepened on the interior of the cluster, and we can see a wave of cooling in the  $q_0$  profile moving out as the electrons age behind the shock. There is a wealth of information still to be uncovered in these profiles and projections, which will be investigated in future work.

#### 6.4.4 Initial Conclusions & Future Work

In this chapter we have introduced a new framework for following a distribution of cosmic ray electrons and protons as well as integrate it with the hydrodynamic code, Enzo. We have provided a suite of test problems that demonstrate both the accuracy of the CRT library as well as its integration with some of the standard test problems in Enzo. Finally, we have demonstrated this capability by simulating a massive galaxy cluster as it evolves and undergoes several mergers. This is the first galaxy cluster simulation that follows the electron population that also utilizes adaptive mesh refinement, and as such is the highest resolution simulation of its type. From it, we have seen how cosmological structure formation naturally leads to the creation of single and double radio-relic structures by incorporating only shock acceleration with Coulomb and synchrotron/inverse Compton cooling.

There are obvious directions for future analysis of this simulation. First, it would be extremely interesting to determine the time evolution of the  $P_{1.4GHz} - L_X$  relationship for this cluster and

compare it to the population of observed radio relics and radio halos. It is possible that all radio halos are simply the result of recently shock re-accelerated electrons that are cooling more quickly in the centers of galaxy clusters due to higher magnetic field strengths in the hotter, more dense plasma? What spectral characteristics are needed for such an argument? Given the profile of synchrotron emission trailing a shock, is it possible to recover the underlying shock characteristics such as Mach number, magnetic field strength, and acceleration efficiency? Do the fluctuations in spectral index along the length of a shock match those observed in known giant radio relics? I will investigate these questions in the near future, and leave a further in-depth study of populations of galaxy clusters to longer-term projects.

## Chapter 7

### Future Directions & Conclusions

There are many immediate projects that are now possible with the combination of the CRT solver, Enzo, and a suite of high resolution simulations. In addition, there are also technological and theoretical improvements that can be made to the existing framework. In this chapter I will motivate some of the future work and conclude with the overarching lessons learned from this dissertation.

#### 7.1 Immediate Projects with CR Electrons

The first project enabled by the new CRT framework is to finish the preliminary work presented in the previous chapter and complete and in-depth analysis of the evolution of CR electrons in a galaxy cluster simulation. The outstanding questions to be explored are:

- What fraction of the time is the cluster bright/observable in the radio and at what radio frequency?
- How does the spectral index vary along/behind the radio relic as the electrons cool?
- Can the shock-accelerated electrons ever lead to situations in which the radio emission could be confused for a radio halo? If so, for how long?
- How do the X-ray and radio luminosities correlate in space and time throughout the merger history of the cluster?

- What is the spatial and temporal correlation between the radio and thermal Sunyaev-Zel'dovich effect, and how can they be used together to constrain the thermal and non-thermal processes in galaxy cluster mergers?

These questions can now all be addressed with our new capabilities. However, to fully enable comparisons with observations, we also need to develop new synthetic observation tools. First, while we are able to make basic synchrotron emissivity maps it would be significantly more accurate to create a full spectral and spatial data cube that can then be processed through existing NRAO synthetic observing pipelines such as AIPS<sup>1</sup> and CASA<sup>2</sup>.

Using the same simulations of CR electrons, it is possible to calculate the expected inverse Compton emission from the electrons that up-scatter the Cosmic Microwave Background photons to X-ray energies. This should make it possible to construct synthetic X-ray observations at high energies where the IC emission is most obvious for current satellite missions such as NuStar, and help explain the current lack of evidence for a high energy tail in observations of most galaxy clusters [4]. Current observations from the Nustar team [249] have thus far hinted at, but not confirmed, a hard non-thermal tail in observations of the Bullet cluster. However, it may be that sources such as the Bullet cluster are still too early in their merger history to have established large shocks capable of accelerating the requisite electrons. A detailed view of the time evolution of our simulation with respect to both the radio emission and non-thermal X-ray emission could help us to understand the current lack of observed emission in the Bullet cluster.

## 7.2 CRT Micro-physics

There are a number of additional sources of CR acceleration that we could include in our CRT framework and hydrodynamical simulations. In the context of the ICM, we can prescribe a “second-order Fermi” acceleration mechanism that provides a slow but steady process from the turbulent flow of the gas. Because of the difficulty in capturing the full turbulent cascade present

---

<sup>1</sup> <http://www.aips.nrao.edu>

<sup>2</sup> <http://casa.nrao.edu/>

in the gas, it would also be possible to fold this source term in with a subgrid turbulence model such as that from Scannapieco and Brüggén [207] or Iapichino et al. [112]. To clarify, this would return the term from equation 6.3

$$\frac{\partial}{\partial p} p^2 D_{pp} \frac{\partial}{\partial p} f, \quad (7.1)$$

where  $D_{pp}$  is the momentum space diffusion coefficient. Including this term in the CRT framework is straightforward after this coefficient is chosen.

So far we have used a fairly simple prescription to include shock-acceleration by connecting the power-law CR population to the thermal Maxwellian. For example, the power-law index that is set is only a function of the Mach number, and the normalization  $C_{inj}$  is constant. However, the acceleration mechanism and resulting momentum-space distribution could be quite complicated and depend on complex functions of the shock orientation, pre- and post-shock thermodynamic properties, and pre-existing population of non-thermal particles. Acceleration from an existing non-thermal power-law distribution is much more efficient than from a completely thermal distribution.

Supernova remnant shocks also accelerate cosmic rays [194]. In addition to attempting to model this process directly, we can use the aggregate effect of many supernova within a single galaxy as sources into the intracluster medium of galaxy clusters. To do so, we would utilize galaxy particles within our simulations to model the CR feedback. Similarly, we could account for active galactic nuclei (AGN) feedback or CRs, which is likely more important than supernovae. By combining all of these sources it will then be possible to inject initial CR populations from supernovae and AGNs and follow their re-acceleration at shock fronts. From these types of simulations, it will be possible to determine quantities such as the volume fraction that AGN/supernovae injected CRs fill in the absence of shock acceleration and compare the emission properties from these sources against those from shocks. By following all such mechanisms for acceleration, we can construct a more complete view of CRs in cluster environments.

We have also ignored several microphysical plasma processes. While electrons can be directly injected from shocks, supernova, and AGN, they can also be produced hadronically through CR

proton-thermal proton collisions (p-p process). Modelling both this process as well as turbulent acceleration of electrons will be important in studying radio halos. It may be possible to predict observational signatures of each injection mechanism and settle the debate over the origin of these CR electrons.

We have ignored spatial diffusion because of the time and length scales involved in the ICM by setting the spatial diffusion coefficient,  $D_{xx} = 0$ . For Bohm diffusion in ICM environments, this is an acceptable approximation. However, this capability may be necessary in the context of either a dramatically different diffusion coefficient or in smaller scale systems such as galaxies or supernovae. Including spatial diffusion is somewhat difficult since the equation is parabolic in nature, and explicit methods are often hampered by restrictive timestep constraints. However, the machinery to follow heat conduction has been recently implemented in Enzo, and authors Britton Smith and Brian O’Shea have found several methods for sub-cycling the conduction step that work reasonably well. Therefore it should be relatively straightforward to include both isotropic and anisotropic (w.r.t. magnetic field orientation) diffusion for the CR fields. If the computational cost proves too high, new implicit methods may be needed to follow this evolution.

Finally, we have also ignored the feedback from the CRs on the thermal gas. The simplest route to including their effects requires incorporating an additional pressure term that can be constructed by integrating the distribution function over momentum space,

$$P_{CR} = \frac{4\pi}{3mc} \int_{p_0}^{\infty} f(p) \frac{p^4}{\sqrt{1 + (p/(mc))^2}} dp. \quad (7.2)$$

A full treatment of the CRs would require a “two-fluid” solver that allows for an interaction term between the thermal and non-thermal fluids. This would necessitate a completely new hydrodynamical solver within Enzo or other similar code.

### 7.3 Other Applications of CRT

The CRT solver can also be applied to a variety of contexts including galaxy and supernovae models, though for both of these cases one should incorporate the effects of the CR pressure and

spatial diffusion. In fact, one of our test problems for the stability of the CRT solver within Enzo is to set up a radiating shock from a supernovae blast wave, setting the boundary conditions of the simulation to reflecting. This creates a very complex flow that tests many of the hydrodynamic regimes that we are likely to encounter, providing a robust stability test of our framework. However, this “test problem” is also very interesting from the perspective of studying CR acceleration in supernovae remnants, and could be used in both 2D and 3D to make preliminary estimates of the synchrotron and X-ray emission of the outgoing shock. To demonstrate this, we set up a 2D radiating shock in Enzo that injects thermal energy at the center of the domain to simulate the supernova explosion. This creates a shock that moves out through the interstellar medium. Gas is allowed to radiatively cool, which happens quickly in the region from the center out to the reverse shock. As a preview, in Figure 7.1, we calculate the synchrotron emission at 1.4 GHz and 74 MHz. We immediately notice the differences in the thickness of the emitting regions due to the relative cooling times of the high and low energy electrons. We also see that using our simplistic model for shock acceleration that there seems to be comparable acceleration efficiencies in both the forward and reverse shocks.

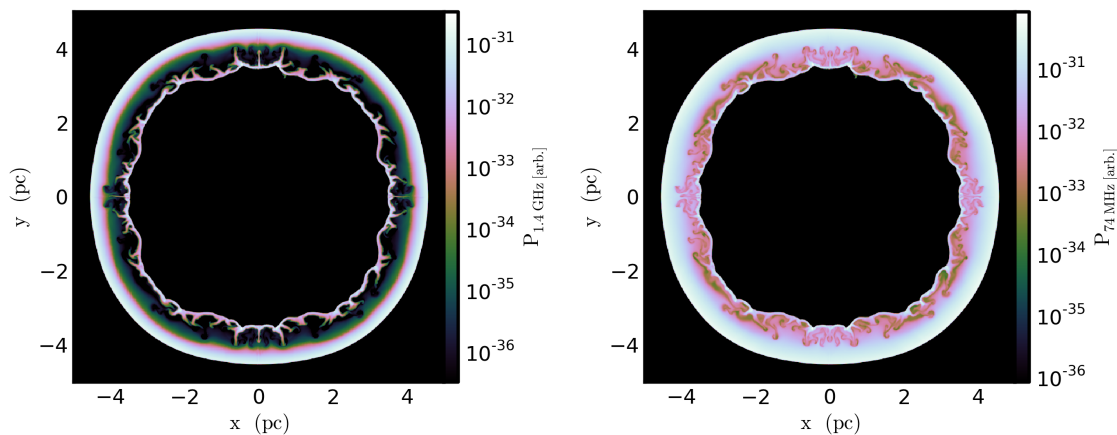


Figure 7.1 1.4 GHz (left) and 74 MHz (right) synchrotron emission from a 2D supernovae remnant simulation.

CRT can also be used in a more fundamental and simplistic form outside of Enzo, allowing one to solve the diffusion convection equation quickly and easily. There are several possible applications

of this mode, including use as a post-processing tool to evolve an initial population of CRs for given amount of time. This could be useful as a “first-look” process of calculating the expected CR distribution in a simulation that was not run with CRs included in the evolution. It can also be used to calculate the balance between acceleration and cooling to provide the expected spectra in single-zone experiments.

## 7.4 Next Generation Galaxy Cluster Simulations

There are several projects that would be enabled by a new set of galaxy cluster simulations that have the following characteristics:

- 10 kpc resolution out to the cluster accretion shock ( $\sim 5$  Mpc)
- High-cadence analysis on 50 Myr timescales
- Ability to follow the injection of energy/momentum/CRs from galaxies

High spatial resolution throughout the cluster will enable accurate assessments of ICM turbulence to be used for acceleration models. This resolution will also match or exceed the majority of observations at all wavelengths/energies. High cadence analysis will allow us to follow the breakup of shock fronts as they move through the ICM as they encounter cluster substructure. This is useful in finding analogs to known radio relics. Following all of the injection mechanisms will enable us to model the entire cluster ecosystem for the first time.

We will achieve this unprecedented resolution by the combination of three recent developments. The first is focused on the generation of high resolution initial conditions that are enabled by the Multi-Scale Initial Conditions (MUSIC) code written by Oliver Hahn and collaborators [101]. MUSIC enables the creation of deeply nested initial conditions by using an adaptive multi-grid Poisson solver, where one can choose to focus the majority of the resolution and computational resources on a small sub-volume. This enables, for example, the re-simulation of a galaxy cluster originally chosen from a large cosmological volume ( $\sim$ Gpc) at high mass and spatial resolution



utilizing many nested high resolution grids. It has also been shown to achieve significantly lower rms error in the particle displacements and velocities as compared to previous methods. A key feature to the MUSIC code is its ability to output the data in a variety of widely-used simulation formats (Enzo, Gadget, Graphic2), as well as using generic HDF5<sup>3</sup> output.

Second, while many of the simulations we have presented in this dissertation have utilized refinement on the gas and dark matter densities, our simulation in Chapter 5 also refined on the magnetic field strength. This had the effect of refining quite far out into the ICM, allowing for the study of MHD turbulence throughout the cluster. Simulations that only refine on the density tend to under-resolve the turbulence present in the ICM, lowering its contribution to the total energy of the cluster. In order to counter this behavior, I have recently implemented a method of refinement in Enzo suggested by Loehner et al. [141] that is based on a threshold value of the second derivative normalized by an averaged first derivative. This has the effect of refining many discontinuities and fluctuations in a fluid code. This same method has been used in many engineering applications, as well as in the Paramesh library [145].

Both of these improvements come with a significant computational cost given the number of resolution elements that each add to a given simulation. Therefore, the improvements in performance and hybrid MPI+OpenMP parallelism mentioned in Chapter 2 will be crucial to our studies. By combining all of these efforts, we will be in a position to provide a gold standard of galaxy clusters.

#### 7.4.1 Comparison to High-Resolution Sunyaev-Zel'dovich Imaging

In particular, these simulations will be useful in the era of very high resolution Sunyaev-Zel'dovich observations of clusters. Here we highlight some recent preliminary work done to model what will be possible with the combination of next generation simulations and telescopes.

CCAT is a proposed 25 meter telescope located in the Atacama desert in Chile that will study the cosmos at sub-millimeter wavelengths. While many people will use CCAT to study the

---

<sup>3</sup> <http://www.hdfgroup.org/HDF5/>

formation and evolution of stars, planets, and galaxies, it will be revolutionary in the field of high resolution SZE observations[188]. One of the proposed instruments for CCAT is a long wavelength camera (LW-Cam) that will utilize a set of observing bands that bracket the thermal SZE signal from 90 – 350 GHz[95].

In recent months I have become involved in the CCAT cosmology working group, and have focused on creating a synthetic observation pipeline that is applied to the simulation introduced in Chapter 5. In doing so, I’ve developed a framework that is capable of incorporating simulation results with realistic noise estimates that is simple to extend to alternate simulation data and telescope specifications. I’ve collaborated primarily with Jack Sayers at Caltech, who has provided synthetic noise maps that include the primary CMB and signal from high redshift “sub-mm” galaxies.

During this first exploration, I have focused on the time-evolution and frequency space morphology of the tSZE emission. By including the accurate noise estimates, we’ve been able to explore where and when we should expect to see emission from these major cluster mergers that are also responsible for the radio relic emission. Figure 7.2 shows the evolution of our merger simulation from  $z = 2$  to  $z = 0$ , highlighting critical stages in its merger evolution.

What we can learn from such synthetic observations is that unlike the X-ray emission, the tSZE should have the capability of mapping the outskirts of clusters and the interaction between shocks, gas pressure, and the CR electrons that are illuminating the radio wavelengths. While this interplay can be very useful for determining the systematic biases present in using galaxy clusters as cosmological probes, I will focus on the thermodynamics and plasma physics of the ICM. By combining the estimates of pressure jumps in the tSZE with synchrotron emission and spectral index maps, it should be possible to estimate the shock Mach number and acceleration efficiency.

Figure 7.3 shows the relative performance in detecting the tSZE signal using both the South Pole Telescope 3G receivers and CCAT for three different cluster survey depths and noise subtraction, and finally the raw tSZE signal. The bottom row shows a first pass at using a technique called “unsharp-masking” that is widely used in the X-ray community to locate sharp gradients in the

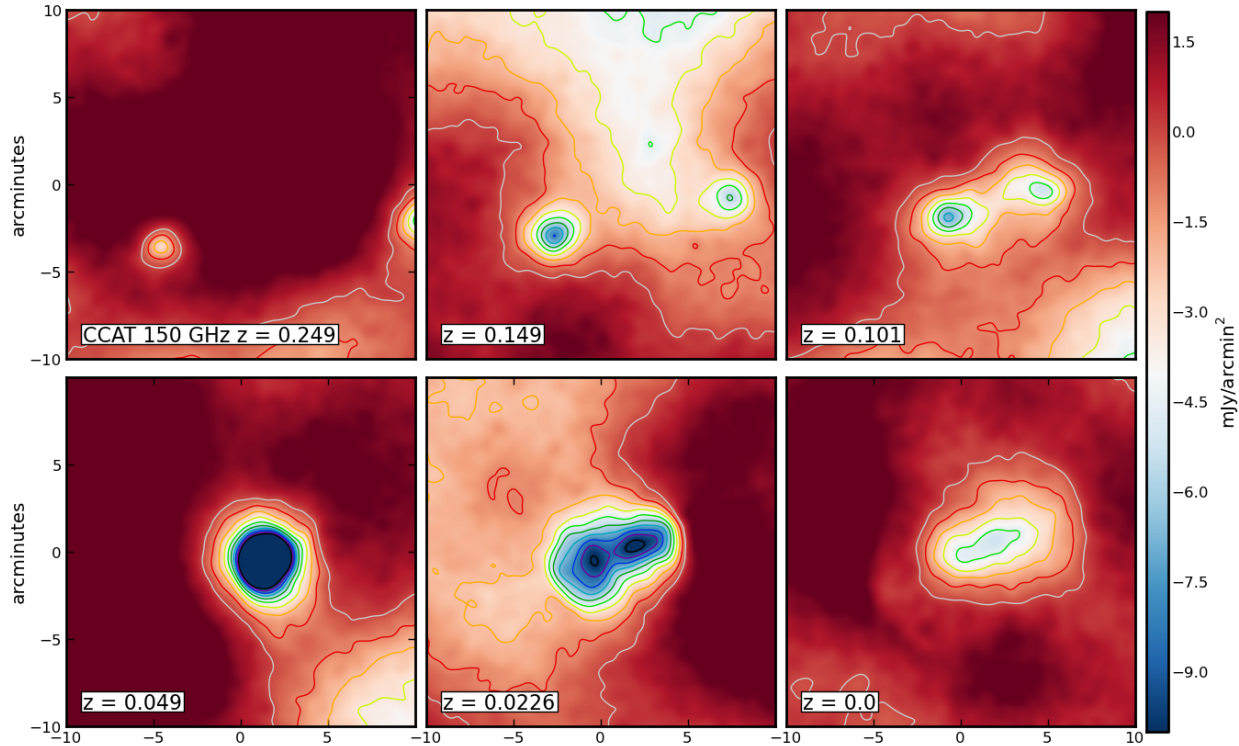


Figure 7.2 Evolution of the tSZE signal in a galaxy cluster merger simulation, showing the 150GHz for 6 different redshifts. Contours indicate integer multiplications of the signal-to-noise ratio.

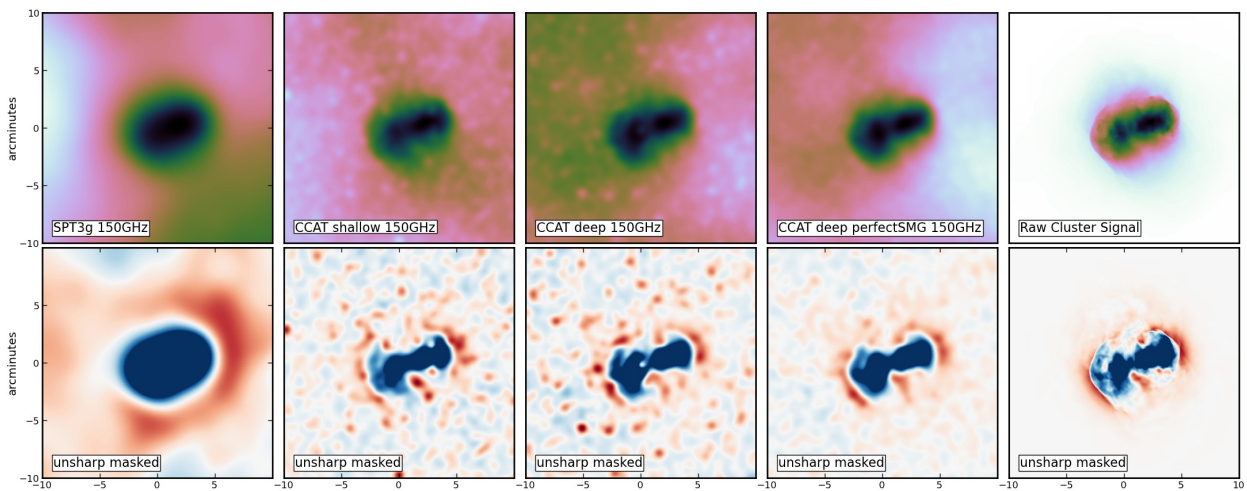


Figure 7.3 The thermal Sunyaev-Zel'dovich emission seen at 150 GHz for various instrument configurations. In the top panels are the tSZE signals, while the bottom panels show an unsharp-masked processing of the signal to highlight gradients and shocks. The far right image shows the tSZE y-parameter at the resolution of the simulation. In each of the other four panels, this signal is convolved with a beam and added to background noise. The far left panel uses the expected South Pole Telescope 3G receiver specifications. The middle three show CCAT LW-Cam specifications for a “shallow” survey, “deep” survey and a “deep” survey with idealized sub-mm galaxy subtraction.

signal, indicative of shock fronts. What is abundantly obvious from this result is that the relative resolution of the 25 meter CCAT to that of SPT allows us to probe the un-relaxed state of the cluster, highlighting the shocks and asymmetric pressure profile. These simulation tools are being used to help guide decisions by the CCAT design team.

#### 7.4.2 Turbulence and Cluster Cooling/Heating

A second application of these high-resolution galaxy clusters is to study the turbulent acceleration of cosmic rays in the cluster cores once the turbulent acceleration mechanism is developed. By combining injection sources from galaxy particles and AGN, turbulent (re-)acceleration, and shock acceleration, we will be capable of producing the most detailed account of galaxy cluster non-thermal populations ever studied.

Finally, all of the simulations presented in this thesis have ignored the cooling and heating sources that are present in the ICM. We have done so knowing that while we would not be accurately modelling the cores of clusters where there are certainly effects of metal cooling, star formation, and feedback, the cluster outskirts where a large fraction of shocks exist should not change dramatically with the inclusion of these processes. However, a complete view of galaxy clusters should certainly include these processes. Our group, in collaboration with several of Enzo developers, are building the capability to prescribe a subgrid model for galaxy formation and feedback. This method, generally referred to as “Active Particles,” describes a framework that is capable of first calculating the non-local (as in using several-many neighboring cells) to constrain the dynamical evolution of a tracer particle. This allows, for example, the insertion of a “galaxy” at the center of a dark matter potential that extends over several computational zones that tracks the gas and metal content of the galaxy. One can include gas stripping from the galaxy-ICM interaction, and feed back on the ICM through supernovae feedback of mass, energy, and momentum. This abstracts away the evolution of the galaxy itself, allowing us to attain resolution-convergent results without having to span the entire resolution range from large scale structure to giant molecular clouds and star formation.

In order to accommodate all of these additional physical processes in a regime of enhanced

resolution, it is imperative to continue to enhance and extend the parallelism and performance of Enzo. In addition, the sheer size of the datasets will require a new paradigm of data analysis, and one that moves away from long term storage of simulation data at high frequency cadence and towards an inline or co-processing of the data while still in supercomputer main memory. Therefore it is imperative to fully integrate analysis tools with Enzo, something that has been started but still requires much work and tuning.

## 7.5 Conclusions

In this dissertation, I have explored the thermal and non-thermal nature of how clusters of galaxies form and evolve. I've done so using the (magneto)hydrodynamical code Enzo and analysis toolkit, yt. These investigations are driven by the truly extraordinary supply of observational data in the X-ray and radio wavelengths that is beginning to unveil the true nature of the Universe's largest objects.

In my first project, I investigated how the hierarchical structure formation leads to cosmological shocks, laying the groundwork for discussing their behavior in and around galaxy clusters. I defined shocks in terms of their pre-shock plasma conditions, finding that the majority of the kinetic energy dissipation in shocks occur for relatively low Mach numbers of 3 – 5, and not from the giant and strong accretion shocks on the outer edge of the clusters.

In Chapter 4, I described how such shocks are capable of accelerating electrons and how they may appear in radio wavelengths due to their synchrotron emission. Using this framework, I then related the radio luminosity to other measures such as mass and X-ray luminosity. We found that unlike the long-lasting enhancement in the X-ray emission, the radio emission is relatively short-lived. This may help explain why objects such as radio relics are so rare.

In Chapter 5, through a collaboration with the developers of the constrained transport MHD solver in Enzo, I applied the radio synchrotron models to a cosmological MHD simulation of a galaxy cluster. This was the first AMR simulation of this type, and led to a magnificent recreation of classic double radio relic clusters, showing radio emission on Mpc scales. Some of the conclusions of this

study led to the motivation behind our final development of cosmic ray evolution in momentum space as the cosmic ray electrons cool behind the shock. What we see from the instantaneous emission is that even along a single cluster radio relic, the Mach number and therefore spectral index of the radio emission may vary along the length and behind the shock front due only to variations in the plasma conditions. Projection effects may also alter our interpretation, as observed spectral aging may be due partly to different Mach numbers along the line of sight.

In Chapter 6, we introduced a new framework for calculating the momentum space distribution function of electrons and protons. After presenting the analytical framework, we provided a series of test problems demonstrating its accuracy and capabilities. Once paired with Enzo, we introduce the first cosmological AMR simulation of a galaxy cluster following the momentum space distribution of CR electrons. During its formation, the cluster undergoes a major merger that leads to the formation of two shocks moving outwards from the cluster core. These shocks accelerate electrons and naturally produce a double radio relic. As expected, the emission falls off quickly at high frequencies as the high energy electrons cool. However, the low-frequency ( $\sim 74\text{MHz}$ ) emission remains throughout the cluster even after the merger has finished.

Throughout this dissertation I have utilized high performance computing resources at both the University of Colorado and at national supercomputing facilities to investigate the effects that shocks have on the largest scales in the Universe. During each project we have added a new physical model (shock acceleration, radio emission, magnetohydrodynamics, aging populations of cosmic rays) to our simulation capabilities that has allowed us to study the interaction between large scale structure formation and cosmic ray acceleration. Each of these developments have been motivated by the findings in a previous study. For example, the decision to follow the momentum-space distribution of cosmic rays and their cooling was motivated by the need to constrain the effects of radio emission spectral aging in observations of radio relics. A recurrent theme throughout this dissertation is that as we introduce new simulation capabilities it has revealed warnings that were previously ignored or unknown, such as projection effects on the polarization and spectral distribution of the radio emission. It has taught us that only through a coordinated effort between

theory, computation, and observation that we will be able to understand the complex phenomena in the ICM and galaxy cluster environment. Fortunately, the future is very bright with the constant construction of new observatories and next-generation supercomputer centers.

## Bibliography

- [1] M. Abramowitz and I. A. Stegun. Handbook of mathematical functions : with formulas, graphs, and mathematical tables. 1970.
- [2] A. Achterberg and J. Wiersma. The Weibel instability in relativistic plasmas. I. Linear theory. A&A, 475:1–18, November 2007. doi: 10.1051/0004-6361:20065365.
- [3] M. Ackermann, M. Ajello, A. Allafort, L. Baldini, J. Ballet, G. Barbiellini, D. Bastieri, K. Bechtol, R. Bellazzini, R. D. Blandford, P. Blasi, E. D. Bloom, E. Bonamente, A. W. Borgland, A. Bouvier, T. J. Brandt, J. Bregeon, M. Brigida, P. Bruel, R. Buehler, S. Buson, G. A. Caliandro, R. A. Cameron, P. A. Caraveo, S. Carrigan, J. M. Casandjian, E. Cavazzuti, C. Cecchi, Ö. Çelik, E. Charles, A. Chekhtman, C. C. Cheung, J. Chiang, S. Ciprini, R. Claus, J. Cohen-Tanugi, S. Colafrancesco, L. R. Cominsky, J. Conrad, C. D. Dermer, F. de Palma, E. d. C. e. Silva, P. S. Drell, R. Dubois, D. Dumora, Y. Edmonds, C. Farnier, C. Favuzzi, M. Frailis, Y. Fukazawa, S. Funk, P. Fusco, F. Gargano, D. Gasparrini, N. Gehrels, S. Germani, N. Giglietto, F. Giordano, M. Giroletti, T. Glanzman, G. Godfrey, I. A. Grenier, M.-H. Grondin, S. Guiriec, D. Hadasch, A. K. Harding, M. Hayashida, E. Hays, D. Horan, R. E. Hughes, T. E. Jeltema, G. Jóhannesson, A. S. Johnson, T. J. Johnson, W. N. Johnson, T. Kamae, H. Katagiri, J. Kataoka, M. Kerr, J. Knödseder, M. Kuss, J. Lande, L. Latronico, S.-H. Lee, M. Lemoine-Goumard, F. Longo, F. Loparco, B. Lott, M. N. Lovellette, P. Lubrano, G. M. Madejski, A. Makeev, M. N. Mazziotta, P. F. Michelson, W. Mitthumsiri, T. Mizuno, A. A. Moiseev, C. Monte, M. E. Monzani, A. Morselli, I. V. Moskalenko, S. Murgia, M. Naumann-Godo, P. L. Nolan, J. P. Norris, E. Nuss, T. Ohsugi, N. Omodei, E. Orlando, J. F. Ormes, M. Ozaki, D. Paneque, J. H. Panetta, M. Pepe, M. Pesce-Rollins, V. Petrosian, C. Pfrommer, F. Piron, T. A. Porter, S. Profumo, S. Rainò, R. Rando, M. Razzano, A. Reimer, O. Reimer, T. Reposeur, J. Ripken, S. Ritz, A. Y. Rodriguez, R. W. Romani, M. Roth, H. F.-W. Sadrozinski, A. Sander, P. M. Saz Parkinson, J. D. Scargle, C. Sgrò, E. J. Siskind, P. D. Smith, G. Spandre, P. Spinelli, J.-L. Starck, L. Stawarz, M. S. Strickman, A. W. Strong, D. J. Suson, H. Tajima, H. Takahashi, T. Takahashi, T. Tanaka, J. B. Thayer, J. G. Thayer, L. Tibaldo, O. Tibolla, D. F. Torres, G. Tosti, A. Tramacere, Y. Uchiyama, T. L. Usher, J. Vandenbroucke, V. Vasileiou, N. Vilchez, V. Vitale, A. P. Waite, P. Wang, B. L. Winer, K. S. Wood, Z. Yang, T. Ylinen, and M. Ziegler. GeV Gamma-ray Flux Upper Limits from Clusters of Galaxies. ApJ, 717:L71–L78, July 2010. doi: 10.1088/2041-8205/717/1/L71.
- [4] M. Ajello, P. Rebusco, N. Cappelluti, O. Reimer, H. Böhringer, J. Greiner, N. Gehrels, J. Tueller, and A. Moretti. Galaxy Clusters in the Swift/Burst Alert Telescope Era: Hard X-rays in the Intracluster Medium. ApJ, 690:367–388, January 2009. doi: 10.1088/0004-637X/690/1/367.



- [5] H. Akamatsu, M. Takizawa, K. Nakazawa, Y. Fukazawa, Y. Ishisaki, and T. Ohashi. X-Ray View of the Shock Front in the Merging Cluster Abell 3376 with Suzaku. *PASJ*, 64:67, August 2012.
- [6] J. Aleksić, L. A. Antonelli, P. Antoranz, M. Backes, C. Baixeras, S. Balestra, J. A. Barrio, D. Bastieri, J. Becerra González, W. Bednarek, A. Berdyugin, K. Berger, E. Bernardini, A. Biland, R. K. Bock, G. Bonnoli, P. Bordas, D. Borla Tridon, V. Bosch-Ramon, D. Bose, I. Braun, T. Bretz, D. Britzger, M. Camara, E. Carmona, A. Carosi, P. Colin, S. Commichau, J. L. Contreras, J. Cortina, M. T. Costado, S. Covino, F. Dazzi, A. De Angelis, E. De Cea del Pozo, R. De los Reyes, B. De Lotto, M. De Maria, F. De Sabata, C. Delgado Mendez, M. Doert, A. Domínguez, D. Dominis Prester, D. Dorner, M. Doro, D. Elsaesser, M. Errando, D. Ferenc, M. V. Fonseca, L. Font, N. Galante, R. J. García López, M. Garczarczyk, M. Gaug, N. Godinovic, D. Hadasch, A. Herrero, D. Hildebrand, D. Höhne-Mönch, J. Hose, D. Hrupec, C. C. Hsu, T. Jogler, S. Klepser, T. Krähenbühl, D. Kranich, A. La Barbera, A. Laille, E. Leonardo, E. Lindfors, S. Lombardi, F. Longo, M. López, E. Lorenz, P. Majumdar, G. Maneva, N. Mankuzhiyil, K. Mannheim, L. Maraschi, M. Mariotti, M. Martínez, D. Mazin, M. Meucci, J. M. Miranda, R. Mirzoyan, H. Miyamoto, J. Moldón, M. Moles, A. Moralejo, D. Nieto, K. Nilsson, J. Ninkovic, R. Orito, I. Oya, S. Paiano, R. Paoletti, J. M. Paredes, S. Partini, M. Pasanen, D. Pascoli, F. Pauss, R. G. Pegna, M. A. Perez-Torres, M. Persic, L. Peruzzo, F. Prada, E. Prandini, N. Puchades, I. Puljak, I. Reichardt, W. Rhode, M. Ribó, J. Rico, M. Rissi, S. Rügamer, A. Saggion, T. Y. Saito, M. Salvati, M. A. Sánchez-Conde, K. Satalecka, V. Scalzotto, V. Scapin, C. Schultz, T. Schweizer, M. Shayduk, S. N. Shore, A. Sierpowska-Bartosik, A. Sillanpää, J. Sitarek, D. Sobczynska, F. Spanier, S. Spiro, A. Stamerra, B. Steinke, J. C. Struebig, T. Suric, L. Takalo, F. Tavecchio, P. Temnikov, T. Terzic, D. Tescaro, M. Teshima, D. F. Torres, H. Vankov, R. M. Wagner, V. Zabalza, F. Zandanel, R. Zanin, J. Zapatero, C. Pfrommer, A. Pinzke, T. A. Enßlin, S. Inoue, G. Ghisellini, and MAGIC Collaboration. MAGIC Gamma-ray Telescope Observation of the Perseus Cluster of Galaxies: Implications for Cosmic Rays, Dark Matter, and NGC 1275. *ApJ*, 710: 634–647, February 2010. doi: 10.1088/0004-637X/710/1/634.
- [7] J. Aleksić, E. A. Alvarez, L. A. Antonelli, P. Antoranz, M. Asensio, M. Backes, U. Barres de Almeida, J. A. Barrio, D. Bastieri, J. Becerra González, W. Bednarek, A. Berdyugin, K. Berger, E. Bernardini, A. Biland, O. Blanch, R. K. Bock, A. Boller, G. Bonnoli, D. Borla Tridon, I. Braun, T. Bretz, A. Cañellas, E. Carmona, A. Carosi, P. Colin, E. Colombo, J. L. Contreras, J. Cortina, L. Cossio, S. Covino, F. Dazzi, A. de Angelis, G. de Caneva, E. de Cea Del Pozo, B. de Lotto, C. Delgado Mendez, A. Diago Ortega, M. Doert, A. Domínguez, D. Dominis Prester, D. Dorner, M. Doro, D. Eisenacher, D. Elsaesser, D. Ferenc, M. V. Fonseca, L. Font, C. Fruck, R. J. García López, M. Garczarczyk, D. Garrido, G. Giavitto, N. Godinović, S. R. Gozzini, D. Hadasch, D. Häfner, A. Herrero, D. Hildebrand, D. Höhne-Mönch, J. Hose, D. Hrupec, T. Jogler, H. Kellermann, S. Klepser, T. Krähenbühl, J. Krause, J. Kushida, A. La Barbera, D. Lelas, E. Leonardo, N. Lewandowska, E. Lindfors, S. Lombardi, M. López, R. López, A. López-Oramas, E. Lorenz, M. Makariev, G. Maneva, N. Mankuzhiyil, K. Mannheim, L. Maraschi, M. Mariotti, M. Martínez, D. Mazin, M. Meucci, J. M. Miranda, R. Mirzoyan, J. Moldón, A. Moralejo, P. Munar-Adrover, A. Niedzwiecki, D. Nieto, K. Nilsson, N. Nowak, R. Orito, S. Paiano, D. Paneque, R. Paoletti, S. Pardo, J. M. Paredes, S. Partini, M. A. Perez-Torres, M. Persic, L. Peruzzo, M. Pilia, J. Pochon, F. Prada, P. G. Prada Moroni, E. Prandini, I. Puerto Gimenez, I. Puljak, I. Reichardt, R. Reintal, W. Rhode, M. Ribó, J. Rico, S. Rügamer, A. Saggion, K. Saito, T. Y. Saito, M. Salvati, K. Satalecka,

- V. Scalzotto, V. Scapin, C. Schultz, T. Schweizer, M. Shayduk, S. N. Shore, A. Sillanpää, J. Sitarek, I. Snidaric, D. Sobczynska, F. Spanier, S. Spiro, V. Stamatescu, A. Stamerra, B. Steinke, J. Storz, N. Strah, S. Sun, T. Surić, L. Takalo, H. Takami, F. Tavecchio, P. Temnikov, T. Terzić, D. Tescaro, M. Teshima, O. Tibolla, D. F. Torres, A. Treves, M. Uellenbeck, H. Vankov, P. Vogler, R. M. Wagner, Q. Weitzel, V. Zabalza, F. Zandanel, R. Zanin, MAGIC Collaboration, C. Pfrommer, and A. Pinzke. Constraining cosmic rays and magnetic fields in the Perseus galaxy cluster with TeV observations by the MAGIC telescopes. *A&A*, 541:A99, May 2012. doi: 10.1051/0004-6361/201118502.
- [8] S. W. Allen, D. A. Rapetti, R. W. Schmidt, H. Ebeling, R. G. Morris, and A. C. Fabian. Improved constraints on dark energy from Chandra X-ray observations of the largest relaxed galaxy clusters. *MNRAS*, 383:879–896, January 2008. doi: 10.1111/j.1365-2966.2007.12610.x.
- [9] E. Amato and P. Blasi. Non-linear particle acceleration at non-relativistic shock waves in the presence of self-generated turbulence. *MNRAS*, 371:1251–1258, September 2006. doi: 10.1111/j.1365-2966.2006.10739.x.
- [10] W. I. Axford, E. Leer, and G. Skadron. The acceleration of cosmic rays by shock waves. In *International Cosmic Ray Conference*, volume 11 of *International Cosmic Ray Conference*, pages 132–137, 1977.
- [11] J. Bagchi, F. Durret, G. B. L. Neto, and S. Paul. Giant Ringlike Radio Structures Around Galaxy Cluster Abell 3376. *Science*, 314:791–794, November 2006. doi: 10.1126/science.1131189.
- [12] M. Bartelmann, M. Limousin, M. Meneghetti, and R. Schmidt. Internal Cluster Structure. *Space Sci. Rev.*, April 2013. doi: 10.1007/s11214-013-9977-6.
- [13] N. Battaglia, C. Pfrommer, J. L. Sievers, J. R. Bond, and T. A. Enßlin. Exploring the magnetized cosmic web through low-frequency radio emission. *MNRAS*, 393:1073–1089, March 2009. doi: 10.1111/j.1365-2966.2008.14136.x.
- [14] A. R. Bell. The acceleration of cosmic rays in shock fronts. I. *MNRAS*, 182:147–156, January 1978.
- [15] A. R. Bell. The acceleration of cosmic rays in shock fronts. II. *MNRAS*, 182:443–455, February 1978.
- [16] B. A. Benson, T. de Haan, J. P. Dudley, C. L. Reichardt, K. A. Aird, K. Andersson, R. Armstrong, M. Bautz, M. Bayliss, G. Bazin, L. E. Bleem, M. Brodwin, J. E. Carlstrom, C. L. Chang, H. M. Cho, A. Clocchiatti, T. M. Crawford, A. T. Crites, S. Desai, M. A. Dobbs, R. J. Foley, W. R. Forman, E. M. George, M. D. Gladders, N. W. Halverson, F. W. High, G. P. Holder, W. L. Holzzapfel, S. Hoover, J. D. Hrubes, C. Jones, M. Joy, R. Keisler, L. Knox, A. T. Lee, E. M. Leitch, J. Liu, M. Lueker, D. Luong-Van, A. Mantz, D. P. Marrone, M. McDonald, J. J. McMahon, J. Mehl, S. S. Meyer, L. Mocanu, J. J. Mohr, T. E. Montroy, S. S. Murray, T. Natoli, S. Padin, T. Plagge, C. Pryke, A. Rest, J. Ruel, J. E. Ruhl, B. R. Salivanchik, A. Saro, K. K. Schaffer, L. Shaw, E. Shirokoff, J. Song, H. G. Spieler, B. Stalder, Z. Staniszewski, A. A. Stark, K. Story, C. W. Stubbs, R. Suhada, A. van Engelen, K. Vanderlinde, J. D. Vieira, A. Vikhlinin, R. Williamson, O. Zahn, and A. Zenteno. Cosmological Constraints from Sunyaev-Zel’dovich-Selected Clusters with X-ray Observations in the First 178 Square Degrees of the South Pole Telescope Survey. *ArXiv e-prints*, December 2011.

- [17] M. J. Berger and P. Colella. Local adaptive mesh refinement for shock hydrodynamics. *Journal of Computational Physics*, 82:64–84, May 1989. doi: 10.1016/0021-9991(89)90035-1.
- [18] J. Beringer, J.-F. Arguin, R. M. Barnett, K. Copic, O. Dahl, D. E. Groom, C.-J. Lin, J. Lys, H. Murayama, C. G. Wohl, W.-M. Yao, P. A. Zyla, C. Amsler, M. Antonelli, D. M. Asner, H. Baer, H. R. Band, T. Basaglia, C. W. Bauer, J. J. Beatty, V. I. Belousov, E. Bergren, G. Bernardi, W. Bertl, S. Bethke, H. Bichsel, O. Biebel, E. Blucher, S. Blusk, G. Brooijmans, O. Buchmueller, R. N. Cahn, M. Carena, A. Ceccucci, D. Chakraborty, M.-C. Chen, R. S. Chivukula, G. Cowan, G. D’Ambrosio, T. Damour, D. de Florian, A. de Gouvêa, T. DeGrand, P. de Jong, G. Dissertori, B. Dobrescu, M. Doser, M. Drees, D. A. Edwards, S. Eidelman, J. Erler, V. V. Ezhela, W. Fetscher, B. D. Fields, B. Foster, T. K. Gaisser, L. Garren, H.-J. Gerber, G. Gerbier, T. Gherghetta, S. Golwala, M. Goodman, C. Grab, A. V. Gritsan, J.-F. Grivaz, M. Grünewald, A. Gurtu, T. Gutsche, H. E. Haber, K. Hagiwara, C. Hagmann, C. Hanhart, S. Hashimoto, K. G. Hayes, M. Heffner, B. Heltsley, J. J. Hernández-Rey, K. Hikasa, A. Höcker, J. Holder, A. Holtkamp, J. Huston, J. D. Jackson, K. F. Johnson, T. Junk, D. Karlen, D. Kirkby, S. R. Klein, E. Klempt, R. V. Kowalewski, F. Krauss, M. Kreps, B. Krusche, Y. V. Kuyanov, Y. Kwon, O. Lahav, J. Laiho, P. Langacker, A. Liddle, Z. Ligeti, T. M. Liss, L. Littenberg, K. S. Lugovsky, S. B. Lugovsky, T. Mannel, A. V. Manohar, W. J. Marciano, A. D. Martin, A. Masoni, J. Matthews, D. Milstead, R. Miquel, K. Mönig, F. Moortgat, K. Nakamura, M. Narain, P. Nason, S. Navas, M. Neubert, P. Nevski, Y. Nir, K. A. Olive, L. Pape, J. Parsons, C. Patrignani, J. A. Peacock, S. T. Petcov, A. Piepke, A. Pomarol, G. Punzi, A. Quadt, S. Raby, G. Raffelt, B. N. Ratcliff, P. Richardson, S. Roesler, S. Rolli, A. Romaniouk, L. J. Rosenberg, J. L. Rosner, C. T. Sachrajda, Y. Sakai, G. P. Salam, S. Sarkar, F. Sauli, O. Schneider, K. Scholberg, D. Scott, W. G. Seligman, M. H. Shaevitz, S. R. Sharpe, M. Silari, T. Sjöstrand, P. Skands, J. G. Smith, G. F. Smoot, S. Spanier, H. Spieler, A. Stahl, T. Stanev, S. L. Stone, T. Sumiyoshi, M. J. Syphers, F. Takahashi, M. Tanabashi, J. Terning, M. Titov, N. P. Tkachenko, N. A. Törnqvist, D. Tovey, G. Valencia, K. van Bibber, G. Venanzoni, M. G. Vincter, P. Vogel, A. Vogt, W. Walkowiak, C. W. Walter, D. R. Ward, T. Watari, G. Weiglein, E. J. Weinberg, L. R. Wiencke, L. Wolfenstein, J. Womersley, C. L. Woody, R. L. Workman, A. Yamamoto, G. P. Zeller, O. V. Zenin, J. Zhang, R.-Y. Zhu, G. Harper, V. S. Lugovsky, and P. Schaffner. Review of Particle Physics. *Phys. Rev. D*, 86(1):010001, July 2012. doi: 10.1103/PhysRevD.86.010001.
- [19] J. Binney and G. Tabor. Evolving Cooling Flows. *MNRAS*, 276:663, September 1995.
- [20] M. Birkinshaw and K. Lancaster. The Sunyaev-Zel’dovich Effect in Cosmology and Cluster Physics. In M. Plionis, O. López-Cruz, and D. Hughes, editors, *A Pan-Chromatic View of Clusters of Galaxies and the Large-Scale Structure*, volume 740 of *Lecture Notes in Physics*, Berlin Springer Verlag, page 255, 2008. doi: 10.1007/978-1-4020-6941-3.8.
- [21] A. Biviano. From Messier to Abell: 200 Years of Science with Galaxy Clusters. In *Constructing the Universe with Clusters of Galaxies*, 2000.
- [22] R. Blandford and D. Eichler. Particle acceleration at astrophysical shocks: A theory of cosmic ray origin. *Phys. Rep.*, 154:1–75, October 1987. doi: 10.1016/0370-1573(87)90134-7.
- [23] R. D. Blandford and J. P. Ostriker. Particle acceleration by astrophysical shocks. *ApJ*, 221:L29–L32, April 1978. doi: 10.1086/182658.

- [24] T. Bogdanović, C. S. Reynolds, S. A. Balbus, and I. J. Parrish. Simulations of Magnetohydrodynamics Instabilities in Intracluster Medium Including Anisotropic Thermal Conduction. *ApJ*, 704:211–225, October 2009. doi: 10.1088/0004-637X/704/1/211.
- [25] A. Bonafede, L. Feretti, G. Giovannini, F. Govoni, M. Murgia, G. B. Taylor, H. Ebeling, S. Allen, G. Gentile, and Y. Pihlström. Revealing the magnetic field in a distant galaxy cluster: discovery of the complex radio emission from MACS J0717.5 +3745. *A&A*, 503:707–720, September 2009. doi: 10.1051/0004-6361/200912520.
- [26] A. Bonafede, G. Giovannini, L. Feretti, F. Govoni, and M. Murgia. Double relics in Abell 2345 and Abell 1240. Spectral index and polarization analysis. *A&A*, 494:429–442, February 2009. doi: 10.1051/0004-6361:200810588.
- [27] A. Bonafede, L. Feretti, M. Murgia, F. Govoni, G. Giovannini, D. Dallacasa, K. Dolag, and G. B. Taylor. The Coma cluster magnetic field from Faraday rotation measures. *A&A*, 513:A30, April 2010. doi: 10.1051/0004-6361/200913696.
- [28] A. Bonafede, M. Brüggen, R. van Weeren, F. Vazza, G. Giovannini, H. Ebeling, A. C. Edge, M. Hoeft, and U. Klein. Discovery of radio haloes and double relics in distant MACS galaxy clusters: clues to the efficiency of particle acceleration. *MNRAS*, 426:40–56, October 2012. doi: 10.1111/j.1365-2966.2012.21570.x.
- [29] H. Bondi and F. Hoyle. On the mechanism of accretion by stars. *MNRAS*, 104:273, 1944.
- [30] G. Brunetti and A. Lazarian. Acceleration of primary and secondary particles in galaxy clusters by compressible MHD turbulence: from radio haloes to gamma-rays. *MNRAS*, 410:127–142, January 2011. doi: 10.1111/j.1365-2966.2010.17457.x.
- [31] G. Brunetti, G. Setti, L. Feretti, and G. Giovannini. Particle reacceleration in the Coma cluster: radio properties and hard X-ray emission. *MNRAS*, 320:365–378, January 2001. doi: 10.1046/j.1365-8711.2001.03978.x.
- [32] G. Brunetti, P. Blasi, O. Reimer, L. Rudnick, A. Bonafede, and S. Brown. Probing the origin of giant radio haloes through radio and  $\gamma$ -ray data: the case of the Coma cluster. *MNRAS*, 426:956–968, October 2012. doi: 10.1111/j.1365-2966.2012.21785.x.
- [33] G. L. Bryan and M. L. Norman. Simulating X-Ray Clusters with Adaptive Mesh Refinement. In D. A. Clarke and M. J. West, editors, *Computational Astrophysics; 12th Kingston Meeting on Theoretical Astrophysics*, volume 123 of *Astronomical Society of the Pacific Conference Series*, page 363, 1997.
- [34] G. L. Bryan and M. L. Norman. A Hybrid AMR Application for Cosmology and Astrophysics. *ArXiv Astrophysics e-prints*, October 1997.
- [35] G. L. Bryan, M. L. Norman, J. M. Stone, R. Cen, and J. P. Ostriker. A piecewise parabolic method for cosmological hydrodynamics. *Computer Physics Communications*, 89:149–168, August 1995. doi: 10.1016/0010-4655(94)00191-4.
- [36] B. J. Burn. On the depolarization of discrete radio sources by Faraday dispersion. *MNRAS*, 133:67, 1966.

- [37] J. Burns and J. Lazio. Year 3 LUNAR Annual Report to the NASA Lunar Science Institute. [ArXiv e-prints](#), March 2012.
- [38] J. O. Burns. The radio properties of cD galaxies in Abell clusters. I - an X-ray selected sample. *AJ*, 99:14–30, January 1990. doi: 10.1086/115307.
- [39] J. O. Burns and t. LUNAR Consortium. Science from the Moon: The NASA/NLSI Lunar University Network for Astrophysics Research (LUNAR). [ArXiv e-prints](#), September 2009.
- [40] J. O. Burns, S. W. Skillman, and B. W. O’Shea. Galaxy Clusters at the Edge: Temperature, Entropy, and Gas Dynamics Near the Virial Radius. *ApJ*, 721:1105–1112, October 2010. doi: 10.1088/0004-637X/721/2/1105.
- [41] E. T. Byram, T. A. Chubb, and H. Friedman. Cosmic X-ray Sources, Galactic and Extragalactic. *Science*, 152:66–71, April 1966. doi: 10.1126/science.152.3718.66.
- [42] E. Carretti, S. Brown, L. Staveley-Smith, J. M. Malarecki, G. Bernardi, B. M. Gaensler, M. Haverkorn, M. J. Kesteven, and S. Poppi. Detection of a radio bridge in Abell 3667. [ArXiv e-prints](#), May 2012.
- [43] R. Cassano, G. Brunetti, and G. Setti. Statistics of giant radio haloes from electron reacceleration models. *MNRAS*, 369:1577–1595, July 2006. doi: 10.1111/j.1365-2966.2006.10423.x.
- [44] R. Cassano, G. Brunetti, R. P. Norris, H. J. A. Röttgering, M. Johnston-Hollitt, and M. Trasatti. Radio halos in future surveys in the radio continuum. *A&A*, 548:A100, December 2012. doi: 10.1051/0004-6361/201220018.
- [45] R. Cen and J. P. Ostriker. Where Are the Baryons? *ApJ*, 514:1–6, March 1999. doi: 10.1086/306949.
- [46] T. E. Clarke. Faraday Rotation Observations of Magnetic Fields in Galaxy Clusters. *Journal of Korean Astronomical Society*, 37:337–342, December 2004.
- [47] T. E. Clarke and T. A. Ensslin. Deep 1.4 GHz Very Large Array Observations of the Radio Halo and Relic in Abell 2256. *AJ*, 131:2900–2912, June 2006. doi: 10.1086/504076.
- [48] T. E. Clarke, P. P. Kronberg, and H. Böhringer. A New Radio-X-Ray Probe of Galaxy Cluster Magnetic Fields. *ApJ*, 547:L111–L114, February 2001. doi: 10.1086/318896.
- [49] P. Colella and P. R. Woodward. The Piecewise Parabolic Method (PPM) for Gas-Dynamical Simulations. *Journal of Computational Physics*, 54:174–201, September 1984. doi: 10.1016/0021-9991(84)90143-8.
- [50] D. C. Collins, H. Xu, M. L. Norman, H. Li, and S. Li. Cosmological Adaptive Mesh Refinement Magnetohydrodynamics with Enzo. *ApJS*, 186:308–333, February 2010. doi: 10.1088/0067-0049/186/2/308.
- [51] J. J. Condon, W. D. Cotton, E. W. Greisen, Q. F. Yin, R. A. Perley, G. B. Taylor, and J. J. Broderick. The NRAO VLA Sky Survey. *AJ*, 115:1693–1716, May 1998. doi: 10.1086/300337.
- [52] H. D. Curtis. Descriptions of 762 Nebulae and Clusters Photographed with the Crossley Reflector. *Publications of Lick Observatory*, 13:9–42, 1918.

- [53] R. Davé, L. Hernquist, N. Katz, and D. H. Weinberg. The Low-Redshift LYalpha Forest in Cold Dark Matter Cosmologies. *ApJ*, 511:521–545, February 1999. doi: 10.1086/306722.
- [54] T. J. Dennis and B. D. G. Chandran. Turbulent Heating of Galaxy-Cluster Plasmas. *ApJ*, 622:205–216, March 2005. doi: 10.1086/427424.
- [55] B. Dennison. Formation of radio halos in clusters of galaxies from cosmic-ray protons. *ApJ*, 239:L93–L96, August 1980. doi: 10.1086/183300.
- [56] K. Dolag and T. A. Enßlin. Radio halos of galaxy clusters from hadronic secondary electron injection in realistic magnetic field configurations. *A&A*, 362:151–157, October 2000.
- [57] K. Dolag, M. Bartelmann, and H. Lesch. SPH simulations of magnetic fields in galaxy clusters. *A&A*, 348:351–363, August 1999.
- [58] K. Dolag, D. Grasso, V. Springel, and I. Tkachev. Constrained simulations of the magnetic field in the local Universe and the propagation of ultrahigh energy cosmic rays. *J. Cosmology Astropart. Phys.*, 1:009, January 2005. doi: 10.1088/1475-7516/2005/01/009.
- [59] K. Dolag, A. M. Bykov, and A. Diaferio. Non-Thermal Processes in Cosmological Simulations. *Space Sci. Rev.*, 134:311–335, February 2008. doi: 10.1007/s11214-008-9319-2.
- [60] J. Donnert, K. Dolag, H. Lesch, and E. Müller. Cluster magnetic fields from galactic outflows. *MNRAS*, 392:1008–1021, January 2009. doi: 10.1111/j.1365-2966.2008.14132.x.
- [61] L. O. Drury. An introduction to the theory of diffusive shock acceleration of energetic particles in tenuous plasmas. *Reports on Progress in Physics*, 46:973–1027, August 1983. doi: 10.1088/0034-4885/46/8/002.
- [62] L. O. Drury and S. A. E. G. Falle. On the Stability of Shocks Modified by Particle Acceleration. *MNRAS*, 223:353, November 1986.
- [63] Y. Dubois and R. Teyssier. Cosmological MHD simulation of a cooling flow cluster. *A&A*, 482:L13–L16, May 2008. doi: 10.1051/0004-6361:200809513.
- [64] A. C. Edge. X-ray Surveys of Low-redshift Clusters. *Clusters of Galaxies: Probes of Cosmological Structure and Galaxy Evolution*, page 58, 2004.
- [65] G. Efstathiou, M. Davis, S. D. M. White, and C. S. Frenk. Numerical techniques for large cosmological N-body simulations. *ApJS*, 57:241–260, February 1985. doi: 10.1086/191003.
- [66] D. J. Eisenstein and W. Hu. Power Spectra for Cold Dark Matter and Its Variants. *ApJ*, 511:5–15, January 1999. doi: 10.1086/306640.
- [67] D. J. Eisenstein and P. Hut. HOP: A New Group-Finding Algorithm for N-Body Simulations. *ApJ*, 498:137, May 1998. doi: 10.1086/305535.
- [68] T. A. Enßlin and M. Brüggen. On the formation of cluster radio relics. *MNRAS*, 331: 1011–1019, April 2002. doi: 10.1046/j.1365-8711.2002.05261.x.
- [69] T. A. Enßlin and Gopal-Krishna. Reviving fossil radio plasma in clusters of galaxies by adiabatic compression in environmental shock waves. *A&A*, 366:26–34, January 2001. doi: 10.1051/0004-6361:20000198.

- [70] T. A. Ensslin, P. L. Biermann, U. Klein, and S. Kohle. Cluster radio relics as a tracer of shock waves of the large-scale structure formation. *A&A*, 332:395–409, April 1998.
- [71] A. C. Fabian, R. M. Johnstone, J. S. Sanders, C. J. Conselice, C. S. Crawford, J. S. Gallagher, III, and E. Zweibel. Magnetic support of the optical emission line filaments in NGC 1275. *Nature*, 454:968–970, August 2008. doi: 10.1038/nature07169.
- [72] A. C. Fabian, J. S. Sanders, S. W. Allen, R. E. A. Canning, E. Churazov, C. S. Crawford, W. Forman, J. Gabany, J. Hlavacek-Larrondo, R. M. Johnstone, H. R. Russell, C. S. Reynolds, P. Salomé, G. B. Taylor, and A. J. Young. A wide Chandra view of the core of the Perseus cluster. *MNRAS*, 418:2154–2164, December 2011. doi: 10.1111/j.1365-2966.2011.19402.x.
- [73] L. Feretti. Observational Properties of Diffuse Halos in Clusters. In A. Pramesh Rao, G. Swarup, and Gopal-Krishna, editors, *The Universe at Low Radio Frequencies*, volume 199 of *IAU Symposium*, page 133, 2002.
- [74] L. Feretti and G. Giovannini. Clusters of Galaxies in the Radio: Relativistic Plasma and ICM/Radio Galaxy Interaction Processes. In M. Plionis, O. López-Cruz, and D. Hughes, editors, *A Pan-Chromatic View of Clusters of Galaxies and the Large-Scale Structure*, volume 740 of *Lecture Notes in Physics*, Berlin Springer Verlag, page 143, 2008. doi: 10.1007/978-1-4020-6941-3\_5.
- [75] L. Feretti, D. Dallacasa, G. Giovannini, and A. Tagliani. The magnetic field in the Coma cluster. *A&A*, 302:680, October 1995.
- [76] L. Feretti, D. Dallacasa, F. Govoni, G. Giovannini, G. B. Taylor, and U. Klein. The radio galaxies and the magnetic field in Abell 119. *A&A*, 344:472–482, April 1999.
- [77] L. Feretti, G. Giovannini, F. Govoni, and M. Murgia. Clusters of galaxies: observational properties of the diffuse radio emission. *A&A Rev.*, 20:54, May 2012. doi: 10.1007/s00159-012-0054-z.
- [78] G. J. Ferland, K. T. Korista, D. A. Verner, J. W. Ferguson, J. B. Kingdon, and E. M. Verner. CLOUDY 90: Numerical Simulation of Plasmas and Their Spectra. *PASP*, 110:761–778, July 1998. doi: 10.1086/316190.
- [79] E. Fermi. On the Origin of the Cosmic Radiation. *Physical Review*, 75:1169–1174, April 1949. doi: 10.1103/PhysRev.75.1169.
- [80] C. Ferrari, F. Govoni, S. Schindler, A. M. Bykov, and Y. Rephaeli. Observations of Extended Radio Emission in Clusters. *Space Sci. Rev.*, 134:93–118, February 2008. doi: 10.1007/s11214-008-9311-x.
- [81] A. Finoguenov, C. L. Sarazin, K. Nakazawa, D. R. Wik, and T. E. Clarke. XMM-Newton Observation of the Northwest Radio Relic Region in A3667. *ApJ*, 715:1143–1151, June 2010. doi: 10.1088/0004-637X/715/2/1143.
- [82] C. S. Frenk, S. D. M. White, P. Bode, J. R. Bond, G. L. Bryan, R. Cen, H. M. P. Couchman, A. E. Evrard, N. Gnedin, A. Jenkins, A. M. Khokhlov, A. Klypin, J. F. Navarro, M. L. Norman, J. P. Ostriker, J. M. Owen, F. R. Pearce, U.-L. Pen, M. Steinmetz, P. A. Thomas, J. V. Villumsen, J. W. Wadsley, M. S. Warren, G. Xu, and G. Yepes. The Santa Barbara

- Cluster Comparison Project: A Comparison of Cosmological Hydrodynamics Solutions. *ApJ*, 525:554–582, November 1999. doi: 10.1086/307908.
- [83] B. D. Fried. Mechanism for Instability of Transverse Plasma Waves. *Physics of Fluids*, 2:337, May 1959. doi: 10.1063/1.1705933.
- [84] Y. Fujita and C. L. Sarazin. Nonthermal Emission from Accreting and Merging Clusters of Galaxies. *ApJ*, 563:660–672, December 2001. doi: 10.1086/324030.
- [85] R. Fusco-Femiano, D. Dal Fiume, M. Orlandini, G. Brunetti, L. Feretti, and G. Giovannini. Hard X-Ray Emission from the Galaxy Cluster A3667. *ApJ*, 552:L97–L100, May 2001. doi: 10.1086/320340.
- [86] S. Gabici and P. Blasi. The gamma ray background from large scale structure formation. *Astroparticle Physics*, 19:679–689, September 2003. doi: 10.1016/S0927-6505(03)00106-3.
- [87] S. Gabici and P. Blasi. Nonthermal Radiation from Clusters of Galaxies: The Role of Merger Shocks in Particle Acceleration. *ApJ*, 583:695–705, February 2003. doi: 10.1086/345429.
- [88] L. Gargat  and A. Spitkovsky. Ion Acceleration in Non-relativistic Astrophysical Shocks. *ApJ*, 744:67, January 2012. doi: 10.1088/0004-637X/744/1/67.
- [89] R. Giacconi, H. Gursky, F. R. Paolini, and B. B. Rossi. Evidence for x Rays From Sources Outside the Solar System. *Physical Review Letters*, 9:439–443, December 1962. doi: 10.1103/PhysRevLett.9.439.
- [90] S. Giacintucci, T. Venturi, G. Macario, D. Dallacasa, G. Brunetti, M. Markevitch, R. Cassano, S. Bardelli, and R. Athreya. Shock acceleration as origin of the radio relic in A 521? *A&A*, 486:347–358, August 2008. doi: 10.1051/0004-6361/200809459.
- [91] G. Giovannini, L. Feretti, T. Venturi, K.-T. Kim, and P. P. Kronberg. The halo radio source Coma C and the origin of halo sources. *ApJ*, 406:399–406, April 1993. doi: 10.1086/172451.
- [92] G. Giovannini, M. Tordi, and L. Feretti. Radio halo and relic candidates from the NRAO VLA Sky Survey. *New A*, 4:141–155, March 1999. doi: 10.1016/S1384-1076(99)00018-4.
- [93] G. Giovannini, A. Bonafede, L. Feretti, F. Govoni, M. Murgia, F. Ferrari, and G. Monti. Radio halos in nearby ( $z < 0.4$ ) clusters of galaxies. *A&A*, 507:1257–1270, December 2009. doi: 10.1051/0004-6361/200912667.
- [94] M. Gitti, F. Brighenti, and B. R. McNamara. Evidence for AGN Feedback in Galaxy Clusters and Groups. *Advances in Astronomy*, 2012, 2012. doi: 10.1155/2012/950641.
- [95] S. R. Golwala, CCAT Cosmology/SZ Science Working Group, and CCAT Instrumentation Working Group. The Design and Science Goals of LWCam, the CCAT Long-Wavelength Imager. In *American Astronomical Society Meeting Abstracts*, volume 221 of *American Astronomical Society Meeting Abstracts*, page 150.08, January 2013.
- [96] F. Govoni, M. Murgia, L. Feretti, G. Giovannini, K. Dolag, and G. B. Taylor. The intracluster magnetic field power spectrum in Abell 2255. *A&A*, 460:425–438, December 2006. doi: 10.1051/0004-6361:20065964.



- [97] L. Greengard and V. Rokhlin. A fast algorithm for particle simulations. Journal of Computational Physics, 73:325–348, December 1987. doi: 10.1016/0021-9991(87)90140-9.
- [98] D. Guidetti, M. Murgia, F. Govoni, P. Parma, L. Gregorini, H. R. de Ruiter, R. A. Cameron, and R. Fanti. The intracluster magnetic field power spectrum in Abell 2382. A&A, 483: 699–713, June 2008. doi: 10.1051/0004-6361:20078576.
- [99] J. E. Gunn and J. R. Gott, III. On the Infall of Matter Into Clusters of Galaxies and Some Effects on Their Evolution. ApJ, 176:1, August 1972. doi: 10.1086/151605.
- [100] F. Guo, S. P. Oh, and M. Ruszkowski. A Global Stability Analysis of Clusters of Galaxies with Conduction and AGN Feedback Heating. ApJ, 688:859–874, December 2008. doi: 10.1086/592320.
- [101] O. Hahn and T. Abel. Multi-scale initial conditions for cosmological simulations. MNRAS, 415:2101–2121, August 2011. doi: 10.1111/j.1365-2966.2011.18820.x.
- [102] Z. Haiman, J. J. Mohr, and G. P. Holder. Constraints on Cosmological Parameters from Future Galaxy Cluster Surveys. ApJ, 553:545–561, June 2001. doi: 10.1086/320939.
- [103] E. J. Hallman and T. E. Jeltema. Structure and turbulence in simulated galaxy clusters and the implications for the formation of radio haloes. MNRAS, 418:2467–2480, December 2011. doi: 10.1111/j.1365-2966.2011.19637.x.
- [104] E. J. Hallman, B. W. O’Shea, J. O. Burns, M. L. Norman, R. Harkness, and R. Wagner. The Santa Fe Light Cone Simulation Project. I. Confusion and the Warm-Hot Intergalactic Medium in Upcoming Sunyaev-Zel’dovich Effect Surveys. ApJ, 671:27–39, December 2007. doi: 10.1086/522912.
- [105] C. Heiles. A Heuristic Introduction to Radioastronomical Polarization. In S. Stanimirovic, D. Altschuler, P. Goldsmith, and C. Salter, editors, Single-Dish Radio Astronomy: Techniques and Applications, volume 278 of Astronomical Society of the Pacific Conference Series, pages 131–152, December 2002.
- [106] G. Hinshaw, D. Larson, E. Komatsu, D. N. Spergel, C. L. Bennett, J. Dunkley, M. R. Nolte, M. Halpern, R. S. Hill, N. Odegard, L. Page, K. M. Smith, J. L. Weiland, B. Gold, N. Jarosik, A. Kogut, M. Limon, S. S. Meyer, G. S. Tucker, E. Wollack, and E. L. Wright. Nine-Year Wilkinson Microwave Anisotropy Probe (WMAP) Observations: Cosmological Parameter Results. ArXiv e-prints, December 2012.
- [107] R. W. Hockney and J. W. Eastwood. Computer simulation using particles. 1988.
- [108] R.W. Hockney, S.P. Goel, and J.W. Eastwood. A 10000 particle molecular dynamics model with long range forces. Chemical Physics Letters, 21(3):589 – 591, 1973. ISSN 0009-2614. doi: 10.1016/0009-2614(73)80315-X. URL <http://www.sciencedirect.com/science/article/pii/000926147380315X>.
- [109] M. Hoeft and M. Brüggen. Radio signature of cosmological structure formation shocks. MNRAS, 375:77–91, February 2007. doi: 10.1111/j.1365-2966.2006.11111.x.

- [110] M. Hoeft, M. Brüggen, G. Yepes, S. Gottlöber, and A. Schwobe. Diffuse radio emission from clusters in the MareNostrum Universe simulation. *MNRAS*, 391:1511–1526, December 2008. doi: 10.1111/j.1365-2966.2008.13955.x.
- [111] L. Iapichino and M. Brüggen. Magnetic field amplification by shocks in galaxy clusters: application to radio relics. *MNRAS*, 423:2781–2788, July 2012. doi: 10.1111/j.1365-2966.2012.21084.x.
- [112] L. Iapichino, W. Schmidt, J. C. Niemeyer, and J. Merklein. Turbulence production and turbulent pressure support in the intergalactic medium. *MNRAS*, 414:2297–2308, July 2011. doi: 10.1111/j.1365-2966.2011.18550.x.
- [113] N. Itoh, Y. Kohyama, and S. Nozawa. High-temperature plasmas in clusters of galaxies. *Journal of Physics Condensed Matter*, 10:11273–11283, December 1998. doi: 10.1088/0953-8984/10/49/016.
- [114] T. E. Jeltema and S. Profumo. Implications of Fermi Observations For Hadronic Models of Radio Halos in Clusters of Galaxies. *ApJ*, 728:53, February 2011. doi: 10.1088/0004-637X/728/1/53.
- [115] F. C. Jones and D. C. Ellison. The plasma physics of shock acceleration. *Space Sci. Rev.*, 58:259–346, December 1991. doi: 10.1007/BF01206003.
- [116] T. W. Jones and H. Kang. An efficient numerical scheme for simulating particle acceleration in evolving cosmic-ray modified shocks. *Astroparticle Physics*, 24:75–91, September 2005. doi: 10.1016/j.astropartphys.2005.05.006.
- [117] T. W. Jones and H. Kang. Time Evolution of Cosmic-Ray Modified MHD Shocks. In *International Cosmic Ray Conference*, volume 3 of *International Cosmic Ray Conference*, page 269, 2005.
- [118] T. W. Jones, D. Ryu, and A. Engel. Simulating Electron Transport and Synchrotron Emission in Radio Galaxies: Shock Acceleration and Synchrotron Aging in Axisymmetric Flows. *ApJ*, 512:105–124, February 1999. doi: 10.1086/306772.
- [119] J. S. Kaastra, A. M. Bykov, S. Schindler, J. A. M. Bleeker, S. Borgani, A. Diaferio, K. Dolag, F. Durret, J. Nevalainen, T. Ohashi, F. B. S. Paerels, V. Petrosian, Y. Rephaeli, P. Richter, J. Schaye, and N. Werner. Clusters of Galaxies: Beyond the Thermal View. *Space Sci. Rev.*, 134:1–6, February 2008. doi: 10.1007/s11214-008-9326-3.
- [120] H. Kang and T. W. Jones. Efficiency of Nonlinear Particle Acceleration at Cosmic Structure Shocks. *ApJ*, 620:44–58, February 2005. doi: 10.1086/426855.
- [121] H. Kang and T. W. Jones. Self-similar evolution of cosmic-ray-modified quasi-parallel plane shocks. *Astroparticle Physics*, 28:232–246, October 2007. doi: 10.1016/j.astropartphys.2007.05.007.
- [122] H. Kang and D. Ryu. Re-acceleration of Non-thermal Particles at Weak Cosmological Shock Waves. *ApJ*, 734:18, June 2011. doi: 10.1088/0004-637X/734/1/18.
- [123] H. Kang and D. Ryu. Cosmic ray acceleration at weak cosmological shocks in test-particle regime. *Mem. Soc. Astron. Italiana*, 82:648, 2011.

- [124] H. Kang, T. W. Jones, and U. D. J. Gieseler. Numerical Studies of Cosmic-Ray Injection and Acceleration. *ApJ*, 579:337–358, November 2002. doi: 10.1086/342724.
- [125] H. Kang, D. Ryu, R. Cen, and J. P. Ostriker. Cosmological Shock Waves in the Large-Scale Structure of the Universe: Nongravitational Effects. *ApJ*, 669:729–740, November 2007. doi: 10.1086/521717.
- [126] N. S. Kardashev. Nonstationarity of Spectra of Young Sources of Nonthermal Radio Emission. *Soviet Ast.*, 6:317, December 1962.
- [127] J. C. Kempner, C. L. Sarazin, and P. M. Ricker. Chandra Observations of A85: Merger of the South Subcluster. *ApJ*, 579:236–246, November 2002. doi: 10.1086/342748.
- [128] K.-T. Kim, P. P. Kronberg, G. Giovannini, and T. Venturi. Discovery of intergalactic radio emission in the Coma-A1367 supercluster. *Nature*, 341:720–723, October 1989. doi: 10.1038/341720a0.
- [129] K.-T. Kim, P. P. Kronberg, P. E. Dewdney, and T. L. Landecker. The halo and magnetic field of the Coma cluster of galaxies. *ApJ*, 355:29–37, May 1990. doi: 10.1086/168737.
- [130] E. Komatsu, J. Dunkley, M. R. Nolta, C. L. Bennett, B. Gold, G. Hinshaw, N. Jarosik, D. Larson, M. Limon, L. Page, D. N. Spergel, M. Halpern, R. S. Hill, A. Kogut, S. S. Meyer, G. S. Tucker, J. L. Weiland, E. Wollack, and E. L. Wright. Five-Year Wilkinson Microwave Anisotropy Probe Observations: Cosmological Interpretation. *ApJS*, 180:330–376, February 2009. doi: 10.1088/0067-0049/180/2/330.
- [131] E. Komatsu, K. M. Smith, J. Dunkley, C. L. Bennett, B. Gold, G. Hinshaw, N. Jarosik, D. Larson, M. R. Nolta, L. Page, D. N. Spergel, M. Halpern, R. S. Hill, A. Kogut, M. Limon, S. S. Meyer, N. Odegard, G. S. Tucker, J. L. Weiland, E. Wollack, and E. L. Wright. Seven-year Wilkinson Microwave Anisotropy Probe (WMAP) Observations: Cosmological Interpretation. *ApJS*, 192:18, February 2011. doi: 10.1088/0067-0049/192/2/18.
- [132] A. V. Kravtsov and S. Borgani. Formation of Galaxy Clusters. *ARA&A*, 50:353–409, September 2012. doi: 10.1146/annurev-astro-081811-125502.
- [133] Oliver Kreylos, Gunther H. Weber, E. Wes Bethel, E. Wes, Bethel John, John M. Shalf, Bernd Hamann, and Kenneth I. Joy. Remote interactive direct volume rendering of amr data, 2002.
- [134] G. F. Krymskii. A regular mechanism for the acceleration of charged particles on the front of a shock wave. *Akademiia Nauk SSSR Doklady*, 234:1306–1308, June 1977.
- [135] P. Kuchar and T. A. Enßlin. Magnetic power spectra from Faraday rotation maps. REALMAF and its use on Hydra A. *A&A*, 529:A13, May 2011. doi: 10.1051/0004-6361/200913918.
- [136] M. Kuhlen, M. Vogelsberger, and R. Angulo. Numerical simulations of the dark universe: State of the art and the next decade. *Physics of the Dark Universe*, 1:50–93, November 2012. doi: 10.1016/j.dark.2012.10.002.
- [137] M. I. Large, D. S. Mathewson, and C. G. T. Haslam. A High-Resolution Survey of the Coma Cluster of Galaxies at 408 Mc./s. *Nature*, 183:1663–1664, June 1959. doi: 10.1038/1831663a0.

- [138] J. Lazio, S. Neff, J. Hewitt, J. Burns, R. Bradley, C. L. Carilli, S. Ellingson, S. Furlanetto, P. Ford, R. Goeke, D. Jones, C. Lawrence, G. Lee, A. Loeb, R. MacDowall, G. Maki, G. B. Taylor, H. Thronson, J. Villasenor, and K. Weiler. Technology Development for the Lunar Radio Array. In *astro2010: The Astronomy and Astrophysics Decadal Survey*, volume 2010 of *ArXiv Astrophysics e-prints*, page 50, 2009.
- [139] Randall J LeVeque. *Finite volume methods for hyperbolic problems*, volume 31. Cambridge university press, 2002.
- [140] H. Li, G. Lapenta, J. M. Finn, S. Li, and S. A. Colgate. Modeling the Large-Scale Structures of Astrophysical Jets in the Magnetically Dominated Limit. *ApJ*, 643:92–100, May 2006. doi: 10.1086/501499.
- [141] R. Loehner, K. Morgan, J. Peraire, and M. Vahdati. Finite Element Flux-Corrected Transport (FEM-FCT) for the Euler and Navier-Stokes equations. Technical report, January 1987.
- [142] M. Loewenstein, E. G. Zweibel, and M. C. Begelman. Cosmic-ray heating of cooling flows - A critical analysis. *ApJ*, 377:392–402, August 1991. doi: 10.1086/170369.
- [143] Rainald Löhner, Ken Morgan, Jaime Peraire, and Mehdi Vahdati. Finite element flux-corrected transport (fem-fct) for the euler and navier-stokes equations. *International Journal for Numerical Methods in Fluids*, 7(10):1093–1109, 1987.
- [144] M. S. Longair. *High energy astrophysics. Vol.2: Stars, the galaxy and the interstellar medium*. 1994.
- [145] P. MacNeice, K. M. Olson, C. Mobarry, R. de Fainchtein, and C. Packer. PARAMESH: A parallel adaptive mesh refinement community toolkit. *Computer Physics Communications*, 126:330–354, April 2000. doi: 10.1016/S0010-4655(99)00501-9.
- [146] M. A. Malkov and L. O’C Drury. Nonlinear theory of diffusive acceleration of particles by shock waves. *Reports on Progress in Physics*, 64:429–481, April 2001. doi: 10.1088/0034-4885/64/4/201.
- [147] A. Mantz, S. W. Allen, H. Ebeling, and D. Rapetti. New constraints on dark energy from the observed growth of the most X-ray luminous galaxy clusters. *MNRAS*, 387:1179–1192, July 2008. doi: 10.1111/j.1365-2966.2008.13311.x.
- [148] M. McCourt, I. J. Parrish, P. Sharma, and E. Quataert. Can conduction induce convection? On the non-linear saturation of buoyancy instabilities in dilute plasmas. *MNRAS*, 413:1295–1310, May 2011. doi: 10.1111/j.1365-2966.2011.18216.x.
- [149] B. R. McNamara and P. E. J. Nulsen. Heating Hot Atmospheres with Active Galactic Nuclei. *ARA&A*, 45:117–175, September 2007. doi: 10.1146/annurev.astro.45.051806.110625.
- [150] J. F. Meekins, G. Fritz, T. A. Chubb, and H. Friedman. Physical Sciences: X-rays from the Coma Cluster of Galaxies. *Nature*, 231:107–108, May 1971. doi: 10.1038/231107a0.
- [151] D. Mihalas and B. Weibel Mihalas. *Foundations of radiation hydrodynamics*. 1984.
- [152] F. Miniati. COSMOCR: A numerical code for cosmic ray studies in computational cosmology. *Computer Physics Communications*, 141:17–38, November 2001. doi: 10.1016/S0010-4655(01)00293-4.

- [153] F. Miniati. Intergalactic shock acceleration and the cosmic gamma-ray background. *MNRAS*, 337:199–208, November 2002. doi: 10.1046/j.1365-8711.2002.05903.x.
- [154] F. Miniati. Numerical modelling of gamma radiation from galaxy clusters. *MNRAS*, 342:1009–1020, July 2003. doi: 10.1046/j.1365-8711.2003.06647.x.
- [155] F. Miniati. Glimm Godunov’s method for cosmic-ray hydrodynamics. *Journal of Computational Physics*, 227:776–796, November 2007. doi: 10.1016/j.jcp.2007.08.013.
- [156] F. Miniati, D. Ryu, H. Kang, T. W. Jones, R. Cen, and J. P. Ostriker. Properties of Cosmic Shock Waves in Large-Scale Structure Formation. *ApJ*, 542:608–621, October 2000. doi: 10.1086/317027.
- [157] F. Miniati, T. W. Jones, H. Kang, and D. Ryu. Cosmic-Ray Electrons in Groups and Clusters of Galaxies: Primary and Secondary Populations from a Numerical Cosmological Simulation. *ApJ*, 562:233–253, November 2001. doi: 10.1086/323434.
- [158] F. Miniati, D. Ryu, H. Kang, and T. W. Jones. Cosmic-Ray Protons Accelerated at Cosmological Shocks and Their Impact on Groups and Clusters of Galaxies. *ApJ*, 559:59–69, September 2001. doi: 10.1086/322375.
- [159] T. Mroczkowski, M. J. Devlin, S. R. Dicker, P. M. Korngut, B. S. Mason, E. D. Reese, C. Sarazin, J. Sievers, M. Sun, and A. Young. New high-resolution Sunyaev-Zel’dovich observations with GBT+MUSTANG. *Mem. Soc. Astron. Italiana*, 82:485, 2011.
- [160] T. Mroczkowski, S. Dicker, J. Sayers, E. D. Reese, B. Mason, N. Czakon, C. Romero, A. Young, M. Devlin, S. Golwala, P. Korngut, C. Sarazin, J. Bock, P. M. Koch, K.-Y. Lin, S. M. Molnar, E. Pierpaoli, K. Umetsu, and M. Zemcov. A Multi-wavelength Study of the Sunyaev-Zel’dovich Effect in the Triple-Merger Cluster MACS J0717.5+3745 with MUSTANG and Bolocam. *ArXiv e-prints*, April 2012.
- [161] M. Murgia, F. Govoni, L. Feretti, G. Giovannini, D. Dallacasa, R. Fanti, G. B. Taylor, and K. Dolag. Magnetic fields and Faraday rotation in clusters of galaxies. *A&A*, 424:429–446, September 2004. doi: 10.1051/0004-6361:20040191.
- [162] P. J. Napier. The EVLA Project: Ten Times More Capability for the VLA. In D. C. Backer, J. M. Moran, and J. L. Turner, editors, *Revealing the Molecular Universe: One Antenna is Never Enough*, volume 356 of *Astronomical Society of the Pacific Conference Series*, page 65, December 2006.
- [163] M. L. Norman and G. L. Bryan. Cosmological Adaptive Mesh Refinement<sup>CD</sup>. In S. M. Miyama, K. Tomisaka, and T. Hanawa, editors, *Numerical Astrophysics*, volume 240 of *Astrophysics and Space Science Library*, page 19, 1999.
- [164] S. E. Nuza, M. Hoeft, R. J. van Weeren, S. Gottlöber, and G. Yepes. How many radio relics await discovery? *MNRAS*, 420:2006–2019, March 2012. doi: 10.1111/j.1365-2966.2011.20118.x.
- [165] L. O’C. Drury. Origin of Cosmic Rays. *ArXiv e-prints*, March 2012.

- [166] E. Orrú, M. Murgia, L. Feretti, F. Govoni, G. Brunetti, G. Giovannini, M. Girardi, and G. Setti. Low-frequency study of two clusters of galaxies: A2744 and A2219. *A&A*, 467: 943–954, June 2007. doi: 10.1051/0004-6361:20066118.
- [167] B. W. O’Shea, G. Bryan, J. Bordner, M. L. Norman, T. Abel, R. Harkness, and A. Kritsuk. Introducing Enzo, an AMR Cosmology Application. *ArXiv Astrophysics e-prints*, March 2004.
- [168] B. W. O’Shea, K. Nagamine, V. Springel, L. Hernquist, and M. L. Norman. Comparing AMR and SPH Cosmological Simulations. I. Dark Matter and Adiabatic Simulations. *ApJS*, 160: 1–27, September 2005. doi: 10.1086/432645.
- [169] K. Otmianowska-Mazur, M. Soida, B. Kulesza-Żydzik, M. Hanasz, and G. Kowal. Can the Cosmic Ray Driven Dynamo Model Explain the Observations of the Polarized Emission of Edge-On Galaxies? *ApJ*, 693:1–7, March 2009. doi: 10.1088/0004-637X/693/1/1.
- [170] I. J. Parrish and E. Quataert. Nonlinear Simulations of the Heat-Flux-driven Buoyancy Instability and Its Implications for Galaxy Clusters. *ApJ*, 677:L9–L12, April 2008. doi: 10.1086/587937.
- [171] I. J. Parrish, E. Quataert, and P. Sharma. Anisotropic Thermal Conduction and the Cooling Flow Problem in Galaxy Clusters. *ApJ*, 703:96–108, September 2009. doi: 10.1088/0004-637X/703/1/96.
- [172] I. J. Parrish, E. Quataert, and P. Sharma. Turbulence in Galaxy Cluster Cores: A Key To Cluster Bimodality? *ApJ*, 712:L194–L198, April 2010. doi: 10.1088/2041-8205/712/2/L194.
- [173] S. Paul, L. Iapichino, F. Miniati, J. Bagchi, and K. Mannheim. Evolution of Shocks and Turbulence in Major Cluster Mergers. *ApJ*, 726:17, January 2011. doi: 10.1088/0004-637X/726/1/17.
- [174] V. Pavlidou and B. D. Fields. Analytical Models for the Energetics of Cosmic Accretion Shocks, Their Cosmological Evolution, and the Effect of Environment. *ApJ*, 642:734–745, May 2006. doi: 10.1086/501428.
- [175] A. Pedlar, H. S. Ghataure, R. D. Davies, B. A. Harrison, R. Perley, P. C. Crane, and S. W. Unger. The Radio Structure of NGC1275. *MNRAS*, 246:477, October 1990.
- [176] A. A. Penzias and R. W. Wilson. A Measurement of Excess Antenna Temperature at 4080 Mc/s. *ApJ*, 142:419–421, July 1965. doi: 10.1086/148307.
- [177] R. A. Perley, J. W. Dreher, and J. J. Cowan. The jet and filaments in Cygnus A. *ApJ*, 285: L35–L38, October 1984. doi: 10.1086/184360.
- [178] C. Pfrommer. Simulating cosmic rays in clusters of galaxies - III. Non-thermal scaling relations and comparison to observations. *MNRAS*, 385:1242–1256, April 2008. doi: 10.1111/j.1365-2966.2008.12957.x.
- [179] C. Pfrommer, V. Springel, T. A. Enßlin, and M. Jubelgas. Detecting shock waves in cosmological smoothed particle hydrodynamics simulations. *MNRAS*, 367:113–131, March 2006. doi: 10.1111/j.1365-2966.2005.09953.x.

- [180] C. Pfrommer, T. A. Enßlin, V. Springel, M. Jubelgas, and K. Dolag. Simulating cosmic rays in clusters of galaxies - I. Effects on the Sunyaev-Zel'dovich effect and the X-ray emission. *MNRAS*, 378:385–408, June 2007. doi: 10.1111/j.1365-2966.2007.11732.x.
- [181] C. Pfrommer, T. A. Enßlin, and V. Springel. Simulating cosmic rays in clusters of galaxies - II. A unified scheme for radio haloes and relics with predictions of the  $\gamma$ -ray emission. *MNRAS*, 385:1211–1241, April 2008. doi: 10.1111/j.1365-2966.2008.12956.x.
- [182] T. J. Plagge, D. P. Marrone, Z. Abdulla, M. Bonamente, J. E. Carlstrom, M. Gralla, C. H. Greer, M. Joy, J. W. Lamb, E. M. Leitch, A. Mantz, S. Muchovej, and D. Woody. CARMA Measurements of the Sunyaev-Zel'dovich Effect in RXJ1347.5-1145. *ArXiv e-prints*, March 2012.
- [183] Planck Collaboration, P. A. R. Ade, N. Aghanim, C. Armitage-Caplan, M. Arnaud, M. Ashdown, F. Atrio-Barandela, J. Aumont, C. Baccigalupi, A. J. Banday, R. B. Barreiro, J. G. Bartlett, E. Battaner, K. Benabed, A. Benoît, A. Benoit-Lévy, J.-P. Bernard, M. Bersanelli, P. Bielewicz, J. Bobin, J. J. Bock, A. Bonaldi, J. R. Bond, J. Borrill, F. R. Bouchet, M. Bridges, M. Bucher, C. Burigana, R. C. Butler, E. Calabrese, B. Cappellini, J.-F. Cardoso, A. Catalano, A. Challinor, A. Chamballu, R.-R. Chary, X. Chen, L.-Y. Chiang, H. C. Chiang, P. R. Christensen, S. Church, D. L. Clements, S. Colombi, L. P. L. Colombo, F. Couchot, A. Coulais, B. P. Crill, A. Curto, F. Cuttaia, L. Danese, R. D. Davies, R. J. Davis, P. de Bernardis, A. de Rosa, G. de Zotti, J. Delabrouille, J.-M. Delouis, F.-X. Désert, C. Dickinson, J. M. Diego, K. Dolag, H. Dole, S. Donzelli, O. Doré, M. Douspis, J. Dunkley, X. Dupac, G. Efstathiou, F. Elsner, T. A. Enßlin, H. K. Eriksen, F. Finelli, O. Forni, M. Frailis, A. A. Fraisse, E. Franceschi, T. C. Gaier, S. Galeotta, S. Galli, K. Ganga, M. Giard, G. Giardino, Y. Giraud-Héraud, E. Gjerløw, J. González-Nuevo, K. M. Górski, S. Gratton, A. Gregorio, A. Gruppuso, J. E. Gudmundsson, J. Haissinski, J. Hamann, F. K. Hansen, D. Hanson, D. Harrison, S. Henrot-Versillé, C. Hernández-Monteagudo, D. Herranz, S. R. Hildebrandt, E. Hivon, M. Hobson, W. A. Holmes, A. Hornstrup, Z. Hou, W. Hovest, K. M. Huffenberger, T. R. Jaffe, A. H. Jaffe, J. Jewell, W. C. Jones, M. Juvela, E. Keihänen, R. Kesitalo, T. S. Kisner, R. Kneissl, J. Knoche, L. Knox, M. Kunz, H. Kurki-Suonio, G. Lagache, A. Lähteenmäki, J.-M. Lamarre, A. Lasenby, M. Lattanzi, R. J. Laureijs, C. R. Lawrence, S. Leach, J. P. Leahy, R. Leonardi, J. León-Tavares, J. Lesgourgues, A. Lewis, M. Liguori, P. B. Lilje, M. Linden-Vørnle, M. López-Caniiego, P. M. Lubin, J. F. Macías-Pérez, B. Maffei, D. Maino, N. Mandolesi, M. Maris, D. J. Marshall, P. G. Martin, E. Martínez-González, S. Masi, S. Matarrese, F. Matthai, P. Mazzotta, P. R. Meinhold, A. Melchiorri, J.-B. Melin, L. Mendes, E. Mene-goni, A. Mennella, M. Migliaccio, M. Millea, S. Mitra, M.-A. Miville-Deschênes, A. Moneti, L. Montier, G. Morgante, D. Mortlock, A. Moss, D. Munshi, P. Naselsky, F. Nati, P. Natoli, C. B. Netterfield, H. U. Nørgaard-Nielsen, F. Noviello, D. Novikov, I. Novikov, I. J. O'Dwyer, S. Osborne, C. A. Oxborrow, F. Paci, L. Pagano, F. Pajot, D. Paoletti, B. Partridge, F. Pasian, G. Patanchon, D. Pearson, T. J. Pearson, H. V. Peiris, O. Perdereau, L. Perotto, F. Perrotta, V. Pettorino, F. Piacentini, M. Piat, E. Pierpaoli, D. Pietrobon, S. Plaszczynski, P. Platania, E. Pointecouteau, G. Polenta, N. Ponthieu, L. Popa, T. Poutanen, G. W. Pratt, G. Prézeau, S. Prunet, J.-L. Puget, J. P. Rachen, W. T. Reach, R. Rebolo, M. Reinecke, M. Remazeilles, C. Renault, S. Ricciardi, T. Riller, I. Ristorcelli, G. Rocha, C. Rosset, G. Roudier, M. Rowan-Robinson, J. A. Rubiño-Martín, B. Rusholme, M. Sandri, D. Santos, M. Savelainen, G. Savini, D. Scott, M. D. Seiffert, E. P. S. Shellard, L. D. Spencer, J.-L. Starck, V. Stolyarov, R. Stompor, R. Sudiwala, R. Sunyaev, F. Sureau, D. Sutton, A.-S.

- Suur-Uski, J.-F. Sygnet, J. A. Tauber, D. Tavagnacco, L. Terenzi, L. Toffolatti, M. Tomasi, M. Tristram, M. Tucci, J. Tuovinen, M. Türler, G. Umama, L. Valenziano, J. Valiviita, B. Van Tent, P. Vielva, F. Villa, N. Vittorio, L. A. Wade, B. D. Wandelt, I. K. Wehus, M. White, S. D. M. White, A. Wilkinson, D. Yvon, A. Zacchei, and A. Zonca. Planck 2013 results. XVI. Cosmological parameters. ArXiv e-prints, March 2013.
- [184] W. H. Press and P. Schechter. Formation of Galaxies and Clusters of Galaxies by Self-Similar Gravitational Condensation. ApJ, 187:425–438, February 1974. doi: 10.1086/152650.
- [185] D. J. Price. Smoothed particle hydrodynamics and magnetohydrodynamics. Journal of Computational Physics, 231:759–794, February 2012. doi: 10.1016/j.jcp.2010.12.011.
- [186] R. A. Proctor. Nebular regions in Virgo and Coma Berenices. MNRAS, 33:14, November 1872.
- [187] E. Quataert. Buoyancy Instabilities in Weakly Magnetized Low-Collisionality Plasmas. ApJ, 673:758–762, February 2008. doi: 10.1086/525248.
- [188] S. J. E. Radford, R. Giovanelli, T. A. Sebring, and J. Zmuidzinas. Ccat. In D. C. Lis, J. E. Vaillancourt, P. F. Goldsmith, T. A. Bell, N. Z. Scoville, and J. Zmuidzinas, editors, Submillimeter Astrophysics and Technology: a Symposium Honoring Thomas G. Phillips, volume 417 of Astronomical Society of the Pacific Conference Series, page 113, December 2009.
- [189] J. C. Raymond and B. W. Smith. Soft X-ray spectrum of a hot plasma. ApJS, 35:419–439, December 1977. doi: 10.1086/190486.
- [190] T. H. Reiprich, K. Basu, S. Ettori, H. Israel, L. Lovisari, S. Molendi, E. Pointecouteau, and M. Roncarelli. Outskirts of Galaxy Clusters. ArXiv e-prints, March 2013.
- [191] Y. Rephaeli and D. Gruber. Rossi X-Ray Timing Explorer Observations of A2256. ApJ, 595: 137–141, September 2003. doi: 10.1086/377257.
- [192] Y. Rephaeli and J. Silk. Energetic proton heating of gas in the core of the Perseus cluster. ApJ, 442:91–95, March 1995. doi: 10.1086/175426.
- [193] Y. Rephaeli, D. Gruber, and Y. Arieli. Long RXTE Observations of A2163. ApJ, 649: 673–677, October 2006. doi: 10.1086/506310.
- [194] S. P. Reynolds. Particle acceleration in supernova-remnant shocks. Ap&SS, 336:257–262, November 2011. doi: 10.1007/s10509-010-0559-8.
- [195] K. Roettiger, J. O. Burns, and J. M. Stone. A Cluster Merger and the Origin of the Extended Radio Emission in Abell 3667. ApJ, 518:603–612, June 1999. doi: 10.1086/307327.
- [196] K. Roettiger, J. M. Stone, and J. O. Burns. Magnetic Field Evolution in Merging Clusters of Galaxies. ApJ, 518:594–602, June 1999. doi: 10.1086/307298.
- [197] R. Rosner and W. H. Tucker. On magnetic fields, heating and thermal conduction in halos, and the suppression of cooling flows. ApJ, 338:761–769, March 1989. doi: 10.1086/167234.
- [198] H. J. A. Rottgering, M. H. Wieringa, R. W. Hunstead, and R. D. Ekers. The extended radio emission in the luminous X-ray cluster A3667. MNRAS, 290:577–584, September 1997.



- [199] L. Rudnick, P. Alexander, H. Andernach, N. Battaglia, S. Brown, G. Brunetti, J. Burns, T. Clarke, K. Dolag, D. Farnsworth, G. Giovannini, E. Hallman, M. Johnston-Hollitt, T. Jones, H. Kang, N. Kassim, A. Kravtsov, J. Lazio, C. Lonsdale, B. McNamara, S. Myers, F. Owen, C. Pfrommer, D. Ryu, C. Sarazin, R. Subrahmanyan, G. Taylor, and R. Taylor. Clusters and Large-Scale Structure: the Synchrotron Keys. In astro2010: The Astronomy and Astrophysics Decadal Survey, volume 2010 of ArXiv Astrophysics e-prints, page 253, 2009.
- [200] H. R. Russell, R. J. van Weeren, A. C. Edge, B. R. McNamara, J. S. Sanders, A. C. Fabian, S. A. Baum, R. E. A. Canning, M. Donahue, and C. P. O’Dea. A merger mystery: no extended radio emission in the merging cluster Abell 2146. MNRAS, 417:L1–L5, October 2011. doi: 10.1111/j.1745-3933.2011.01098.x.
- [201] M. Ruszkowski and S. P. Oh. Shaken and Stirred: Conduction and Turbulence in Clusters of Galaxies. ApJ, 713:1332–1342, April 2010. doi: 10.1088/0004-637X/713/2/1332.
- [202] M. Ruszkowski, M. Brüggén, and M. C. Begelman. Cluster Heating by Viscous Dissipation of Sound Waves. ApJ, 611:158–163, August 2004. doi: 10.1086/422158.
- [203] G. B. Rybicki and A. P. Lightman. Radiative processes in astrophysics. 1985.
- [204] D. Ryu, H. Kang, E. Hallman, and T. W. Jones. Cosmological Shock Waves and Their Role in the Large-Scale Structure of the Universe. ApJ, 593:599–610, August 2003. doi: 10.1086/376723.
- [205] D. Ryu, H. Kang, J. Cho, and S. Das. Turbulence and Magnetic Fields in the Large-Scale Structure of the Universe. Science, 320:909–, May 2008. doi: 10.1126/science.1154923.
- [206] C. L. Sarazin. X-ray emission from clusters of galaxies. Reviews of Modern Physics, 58:1–115, January 1986. doi: 10.1103/RevModPhys.58.1.
- [207] E. Scannapieco and M. Brüggén. Subgrid Modeling of AGN-driven Turbulence in Galaxy Clusters. ApJ, 686:927–947, October 2008. doi: 10.1086/591228.
- [208] R. K. Sheth and G. Tormen. Large-scale bias and the peak background split. MNRAS, 308:119–126, September 1999. doi: 10.1046/j.1365-8711.1999.02692.x.
- [209] D. Sijacki, V. Springel, T. Di Matteo, and L. Hernquist. A unified model for AGN feedback in cosmological simulations of structure formation. MNRAS, 380:877–900, September 2007. doi: 10.1111/j.1365-2966.2007.12153.x.
- [210] A. Simionescu, S. W. Allen, A. Mantz, N. Werner, Y. Takei, R. G. Morris, A. C. Fabian, J. S. Sanders, P. E. J. Nulsen, M. R. George, and G. B. Taylor. Baryons at the Edge of the X-ray-Brightest Galaxy Cluster. Science, 331:1576–, March 2011. doi: 10.1126/science.1200331.
- [211] J. Skilling. Cosmic ray streaming. I - Effect of Alfvén waves on particles. MNRAS, 172:557–566, September 1975.
- [212] S. W. Skillman, B. W. O’Shea, E. J. Hallman, J. O. Burns, and M. L. Norman. Cosmological Shocks in Adaptive Mesh Refinement Simulations and the Acceleration of Cosmic Rays. ApJ, 689:1063–1077, December 2008. doi: 10.1086/592496.

- [213] S. W. Skillman, E. J. Hallman, B. W. O’Shea, J. O. Burns, B. D. Smith, and M. J. Turk. Galaxy Cluster Radio Relics in Adaptive Mesh Refinement Cosmological Simulations: Relic Properties and Scaling Relationships. ApJ, 735:96, July 2011. doi: 10.1088/0004-637X/735/2/96.
- [214] S. W. Skillman, H. Xu, E. J. Hallman, B. W. O’Shea, J. O. Burns, H. Li, D. C. Collins, and M. L. Norman. Cosmological Magnetohydrodynamic Simulations of Galaxy Cluster Radio Relics: Insights and Warnings for Observations. ApJ, 765:21, March 2013. doi: 10.1088/0004-637X/765/1/21.
- [215] S. Skory, E. Hallman, J. O. Burns, S. W. Skillman, B. W. O’Shea, and B. D. Smith. On the Road to More Realistic Galaxy Cluster Simulations: The Effects of Radiative Cooling and Thermal Feedback Prescriptions on the Observational Properties of Simulated Galaxy Clusters. ApJ, 763:38, January 2013. doi: 10.1088/0004-637X/763/1/38.
- [216] B. Smith, S. Sigurdsson, and T. Abel. Metal cooling in simulations of cosmic structure formation. MNRAS, 385:1443–1454, April 2008. doi: 10.1111/j.1365-2966.2008.12922.x.
- [217] D. N. Spergel, L. Verde, H. V. Peiris, E. Komatsu, M. R.olta, C. L. Bennett, M. Halpern, G. Hinshaw, N. Jarosik, A. Kogut, M. Limon, S. S. Meyer, L. Page, G. S. Tucker, J. L. Weiland, E. Wollack, and E. L. Wright. First-Year Wilkinson Microwave Anisotropy Probe (WMAP) Observations: Determination of Cosmological Parameters. ApJS, 148:175–194, September 2003. doi: 10.1086/377226.
- [218] A. Spitkovsky. Particle Acceleration in Relativistic Collisionless Shocks: Fermi Process at Last? ApJ, 682:L5–L8, July 2008. doi: 10.1086/590248.
- [219] V. Springel. The cosmological simulation code GADGET-2. MNRAS, 364:1105–1134, December 2005. doi: 10.1111/j.1365-2966.2005.09655.x.
- [220] V. Springel. E pur si muove: Galilean-invariant cosmological hydrodynamical simulations on a moving mesh. MNRAS, 401:791–851, January 2010. doi: 10.1111/j.1365-2966.2009.15715.x.
- [221] V. Springel. Larger, faster, better: Current trends in cosmological simulations. Astronomische Nachrichten, 333:515–522, June 2012. doi: 10.1002/asna.201211701.
- [222] M. Stephan. Nebulæ (new) discovered and observed at the observatory of Marseilles, 1876 and 1877, M. Stephan. MNRAS, 37:334, April 1877.
- [223] J. M. Stone and M. L. Norman. ZEUS-2D: A radiation magnetohydrodynamics code for astrophysical flows in two space dimensions. I - The hydrodynamic algorithms and tests. ApJS, 80:753–790, June 1992. doi: 10.1086/191680.
- [224] J. M. Stone and M. L. Norman. ZEUS-2D: A Radiation Magnetohydrodynamics Code for Astrophysical Flows in Two Space Dimensions. II. The Magnetohydrodynamic Algorithms and Tests. ApJS, 80:791, June 1992. doi: 10.1086/191681.
- [225] A. W. Strong and I. V. Moskalenko. Propagation of Cosmic-Ray Nucleons in the Galaxy. ApJ, 509:212–228, December 1998. doi: 10.1086/306470.

- [226] A. W. Strong, I. V. Moskalenko, and V. S. Ptuskin. Cosmic-Ray Propagation and Interactions in the Galaxy. Annual Review of Nuclear and Particle Science, 57:285–327, November 2007. doi: 10.1146/annurev.nucl.57.090506.123011.
- [227] R. A. Sunyaev and Y. B. Zeldovich. The Observations of Relic Radiation as a Test of the Nature of X-Ray Radiation from the Clusters of Galaxies. Comments on Astrophysics and Space Physics, 4:173, November 1972.
- [228] E. J. Tasker, R. Brunino, N. L. Mitchell, D. Michielsen, S. Hopton, F. R. Pearce, G. L. Bryan, and T. Theuns. A test suite for quantitative comparison of hydrodynamic codes in astrophysics. MNRAS, 390:1267–1281, November 2008. doi: 10.1111/j.1365-2966.2008.13836.x.
- [229] M. J. Turk, B. D. Smith, J. S. Oishi, S. Skory, S. W. Skillman, T. Abel, and M. L. Norman. yt: A Multi-code Analysis Toolkit for Astrophysical Simulation Data. ApJS, 192:9, January 2011. doi: 10.1088/0067-0049/192/1/9.
- [230] R. J. van Weeren, H. J. A. Röttgering, J. Bagchi, S. Raychaudhury, H. T. Intema, F. Miniati, T. A. Enßlin, M. Markevitch, and T. Erben. Radio observations of ZwCl 2341.1+0000: a double radio relic cluster. A&A, 506:1083–1094, November 2009. doi: 10.1051/0004-6361/200912287.
- [231] R. J. van Weeren, H. J. A. Röttgering, M. Brüggen, and A. Cohen. Diffuse radio emission in the merging cluster MACS J0717.5+3745: the discovery of the most powerful radio halo. A&A, 505:991–997, October 2009. doi: 10.1051/0004-6361/200912528.
- [232] R. J. van Weeren, H. J. A. Röttgering, M. Brüggen, and M. Hoeft. Particle Acceleration on Megaparsec Scales in a Merging Galaxy Cluster. Science, 330:347–, October 2010. doi: 10.1126/science.1194293.
- [233] R. J. van Weeren, M. Brüggen, H. J. A. Röttgering, and M. Hoeft. Using double radio relics to constrain galaxy cluster mergers: a model of double radio relics in CIZA J2242.8+5301. MNRAS, 418:230–243, November 2011. doi: 10.1111/j.1365-2966.2011.19478.x.
- [234] R. J. van Weeren, M. Brüggen, H. J. A. Röttgering, M. Hoeft, S. E. Nuza, and H. T. Intema. Radio continuum observations of new radio halos and relics from the NVSS and WENSS surveys. Relic orientations, cluster X-ray luminosity, and redshift distributions. A&A, 533:A35, September 2011. doi: 10.1051/0004-6361/201117149.
- [235] R. J. van Weeren, M. Hoeft, H. J. A. Röttgering, M. Brüggen, H. T. Intema, and S. van Velzen. A double radio relic in the merging galaxy cluster ZwCl 0008.8+5215. A&A, 528:A38, April 2011. doi: 10.1051/0004-6361/201016185.
- [236] R. J. van Weeren, H. T. Intema, H. J. A. Röttgering, M. Brüggen, and M. Hoeft. Low-frequency radio observations of the galaxy cluster CIZA J2242.8+5301. Mem. Soc. Astron. Italiana, 82:569, 2011.
- [237] R. J. van Weeren, A. Bonafede, H. Ebeling, A. C. Edge, M. Brüggen, G. Giovannini, M. Hoeft, and H. J. A. Röttgering. Diffuse radio emission in MACS J1752.0+4440. MNRAS, 425:L36–L40, September 2012. doi: 10.1111/j.1745-3933.2012.01301.x.

- [238] R. J. van Weeren, H. J. A. Röttgering, D. A. Rafferty, R. Pizzo, A. Bonafede, M. Brüggen, G. Brunetti, C. Ferrari, E. Orrù, G. Heald, J. P. McKean, C. Tasse, F. de Gasperin, L. Birzan, J. E. van Zwieten, S. van der Tol, A. Shulevski, N. Jackson, A. R. Offringa, J. Conway, H. T. Intema, T. E. Clarke, I. van Bemmelen, G. K. Miley, G. J. White, M. Hoeft, R. Cassano, G. Macario, R. Morganti, M. W. Wise, C. Horellou, E. A. Valentijn, O. Wucknitz, K. Kuijken, T. A. Enßlin, J. Anderson, A. Asgekar, I. M. Avruch, R. Beck, M. E. Bell, M. R. Bell, M. J. Bentum, G. Bernardi, P. Best, A.-J. Boonstra, M. Brentjens, R. H. van de Brink, J. Broderick, W. N. Brouw, H. R. Butcher, W. van Cappellen, B. Ciardi, J. Eislöffel, H. Falcke, R. Fender, M. A. Garrett, M. Gerbers, A. Gunst, M. P. van Haarlem, J. P. Hamaker, T. Hassall, J. W. T. Hessels, L. V. E. Koopmans, G. Kuper, J. van Leeuwen, P. Maat, R. Millenaar, H. Munk, R. Nijboer, J. E. Noordam, V. N. Pandey, M. Pandey-Pommier, A. Polatidis, W. Reich, A. M. M. Scaife, A. Schoenmakers, J. Sluman, B. W. Stappers, M. Steinmetz, J. Swinbank, M. Tagger, Y. Tang, R. Vermeulen, M. de Vos, and M. P. van Haarlem. First LOFAR observations at very low frequencies of cluster-scale non-thermal emission: the case of Abell 2256. *A&A*, 543:A43, July 2012. doi: 10.1051/0004-6361/201219154.
- [239] F. Vazza, G. Brunetti, and C. Gheller. Shock waves in Eulerian cosmological simulations: main properties and acceleration of cosmic rays. *MNRAS*, 395:1333–1354, May 2009. doi: 10.1111/j.1365-2966.2009.14691.x.
- [240] F. Vazza, K. Dolag, D. Ryu, G. Brunetti, C. Gheller, H. Kang, and C. Pfrommer. A comparison of cosmological codes: properties of thermal gas and shock waves in large-scale structures. *MNRAS*, 418:960–985, December 2011. doi: 10.1111/j.1365-2966.2011.19546.x.
- [241] F. Vazza, M. Brüggen, R. van Weeren, A. Bonafede, K. Dolag, and G. Brunetti. Why are central radio relics so rare? *MNRAS*, 421:1868–1873, April 2012. doi: 10.1111/j.1365-2966.2011.20160.x.
- [242] T. Venturi, R. Morganti, S. Bardelli, D. Dallacasa, and R. W. Hunstead. A radio survey of merging clusters in the Shapley Concentration. In G. Giuricin, M. Mezzetti, and P. Salucci, editors, *Observational Cosmology: The Development of Galaxy Systems*, volume 176 of *Astronomical Society of the Pacific Conference Series*, page 256, June 1999.
- [243] A. Vikhlinin, A. V. Kravtsov, R. A. Burenin, H. Ebeling, W. R. Forman, A. Hornstrup, C. Jones, S. S. Murray, D. Nagai, H. Quintana, and A. Voevodkin. Chandra Cluster Cosmology Project III: Cosmological Parameter Constraints. *ApJ*, 692:1060–1074, February 2009. doi: 10.1088/0004-637X/692/2/1060.
- [244] A. Vladimirov, D. C. Ellison, and A. Bykov. Nonlinear Diffusive Shock Acceleration with Magnetic Field Amplification. *ApJ*, 652:1246–1258, December 2006. doi: 10.1086/508154.
- [245] W. Voges, B. Aschenbach, T. Boller, H. Bräuninger, U. Briel, W. Burkert, K. Dennerl, J. Englhauser, R. Gruber, F. Haberl, G. Hartner, G. Hasinger, M. Kürster, E. Pfeffermann, W. Pietsch, P. Predehl, C. Rosso, J. H. M. M. Schmitt, J. Trümper, and H. U. Zimmermann. The ROSAT all-sky survey bright source catalogue. *A&A*, 349:389–405, September 1999.
- [246] G. M. Voit. Quasi-steady Configurations of Conductive Intracluster Media. *ApJ*, 740:28, October 2011. doi: 10.1088/0004-637X/740/1/28.
- [247] M. S. Warren, K. Abazajian, D. E. Holz, and L. Teodoro. Precision Determination of the Mass Function of Dark Matter Halos. *ApJ*, 646:881–885, August 2006. doi: 10.1086/504962.

- [248] E. S. Weibel. Spontaneously Growing Transverse Waves in a Plasma Due to an Anisotropic Velocity Distribution. Physical Review Letters, 2:83–84, February 1959. doi: 10.1103/PhysRevLett.2.83.
- [249] D. R. Wik, S. E. Boggs, F. Christensen, W. Craig, D. Ferreira, C. J. Hailey, F. Harrison, A. Hornstrup, T. Kitaguchi, G. M. Madejski, S. Molendi, K. Pedersen, D. Stern, W. Zhang, A. Zoglauer, and NuSTAR Team. NuSTAR’s Hard Look at Clusters and Relics: Bullet Cluster First Results. In American Astronomical Society Meeting Abstracts, volume 221 of American Astronomical Society Meeting Abstracts, page 244.20, January 2013.
- [250] M. A. G. Willson. Radio observations of the cluster of galaxies in Coma Berenices - the 5C4 survey. MNRAS, 151:1–44, 1970.
- [251] M. Wolf. Notiz. Astronomische Nachrichten, 155:127, April 1901. doi: 10.1002/asna.19011550608.
- [252] P. Woodward and P. Colella. The numerical simulation of two-dimensional fluid flow with strong shocks. Journal of Computational Physics, 54:115–173, April 1984. doi: 10.1016/0021-9991(84)90142-6.
- [253] H. Xu, H. Li, D. Collins, S. Li, and M. L. Norman. Formation of X-Ray Cavities by the Magnetically Dominated Jet-Lobe System in a Galaxy Cluster. ApJ, 681:L61–L64, July 2008. doi: 10.1086/590407.
- [254] H. Xu, H. Li, D. C. Collins, S. Li, and M. L. Norman. Turbulence and Dynamo in Galaxy Cluster Medium: Implications on the Origin of Cluster Magnetic Fields. ApJ, 698:L14–L17, June 2009. doi: 10.1088/0004-637X/698/1/L14.
- [255] H. Xu, H. Li, D. C. Collins, S. Li, and M. L. Norman. Evolution and Distribution of Magnetic Fields from Active Galactic Nuclei in Galaxy Clusters. I. The Effect of Injection Energy and Redshift. ApJ, 725:2152–2165, December 2010. doi: 10.1088/0004-637X/725/2/2152.
- [256] H. Xu, H. Li, D. C. Collins, S. Li, and M. L. Norman. Evolution and Distribution of Magnetic Fields from Active Galactic Nuclei in Galaxy Clusters. II. The Effects of Cluster Size and Dynamical State. ApJ, 739:77, October 2011. doi: 10.1088/0004-637X/739/2/77.
- [257] K. Yoshikawa, N. Yoshida, and M. Umemura. Direct Integration of the Collisionless Boltzmann Equation in Six-dimensional Phase Space: Self-gravitating Systems. ApJ, 762:116, January 2013. doi: 10.1088/0004-637X/762/2/116.

## Appendix A

### Varying Magnetic Field Models

Here we briefly examine the impact of an alternate magnetic field model. We will concentrate on two of our results, and leave further in-depth analysis to future work. In both cases, we present 6 alternate models. The first four concentrate on changing the reference magnetic field value,  $B_0 = \{0.01, 0.03, 0.3, 1.0\} \mu\text{G}$ . The second two models test the dependence of the magnetic field with respect to the electron number density. For these two cases, we chose simple parameterizations that simply give a feel for how this relationship affects our results. In one case, we keep the magnetic field constant throughout the domain at  $B = B_0 = 0.1 \mu\text{G}$ . In the second case, we scale the magnetic field proportionally with the number density  $B = B_0(n_e/n_{e,0})$ , with  $B_0 = 0.1 \mu\text{G}$  and  $n_{e,0} = 10^{-4} \text{cm}^{-3}$ .

First we examined the fundamental impact on the phase of the gas responsible for the radio emission. In Figure A.1 where we show the relative emission to our fiducial parameters, the primary effect of lowering  $B_0$  is to decrease the total emission as roughly  $B^{5/2}$ , as expected. If we instead increase  $B_0$ , because it starts to become comparable to  $B_{CMB}$ , the emission enhancement is preferably increased in the high temperature, low-Mach number regime corresponding to merger shocks. In the case where we have a flat magnetic field, the emission in the high temperature, high density, low Mach number regions is greatly diminished. However, the accretion shock emission is increased by a factor of 100-1000. If we let the magnetic field scale proportionally to number density, the opposite is true. Accretion shocks have weaker radio emission, whereas the merger shocks are more luminous.

If we instead examine the effect of a changing magnetic field model on the radio luminosity-mass relationship, we again find a coherent picture, as shown in Figure A.2. The key concept is that as the magnetic field approaches  $B_{CMB}$ , the added emission per unit increase is diminished by the second  $B^2$  term in the denominator of Eq. (4.3). Therefore, for low values of  $B_0$  when the magnetic field is much lower than  $B_{CMB}$ , the higher magnetic field strengths in larger clusters has more of an effect, steepening the radio luminosity-mass relationship. On the other hand, when  $B_0$  is increased, the relative gains in magnetic field in large clusters does not impact the emission as strongly, flattening the relationship. In changing the  $B \propto n_e$  relationship, a flat magnetic field removes the density bias between large and small clusters, thereby flattening the scaling relationship. A linear scaling with number density increases this bias, steepening the relationship.

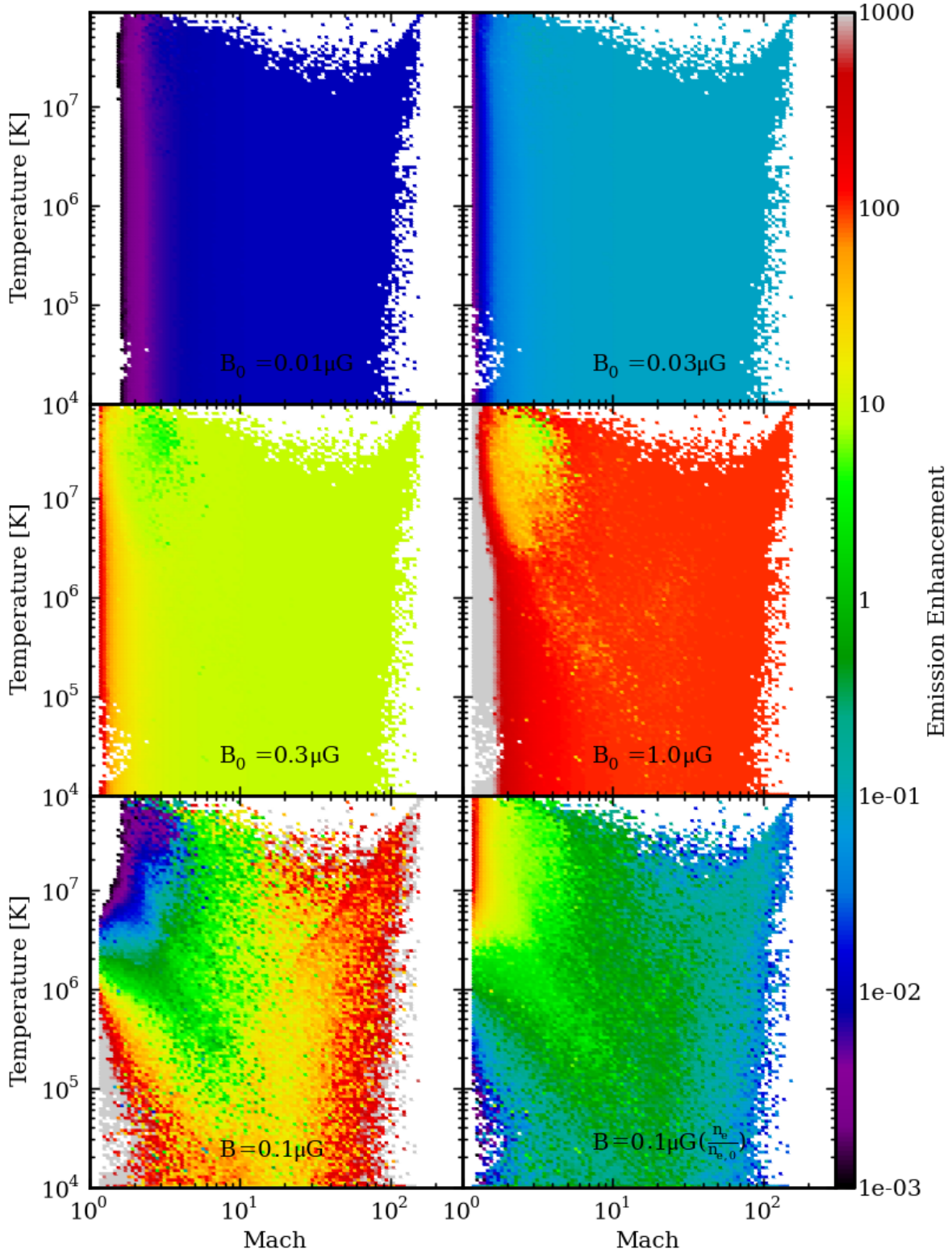


Figure A.1 Relative radio emission with respect to our fiducial magnetic field model for the *relic200* simulation at  $z = 0$ , shown in Figure 4.4. In the upper four panels, the reference magnetic field parameter,  $B_0$  is varied. In the bottom left panel, the magnetic field strength is flat at  $B = 0.1 \mu\text{G}$ . In the bottom right panel, the magnetic field strength scales linearly with electron number density.



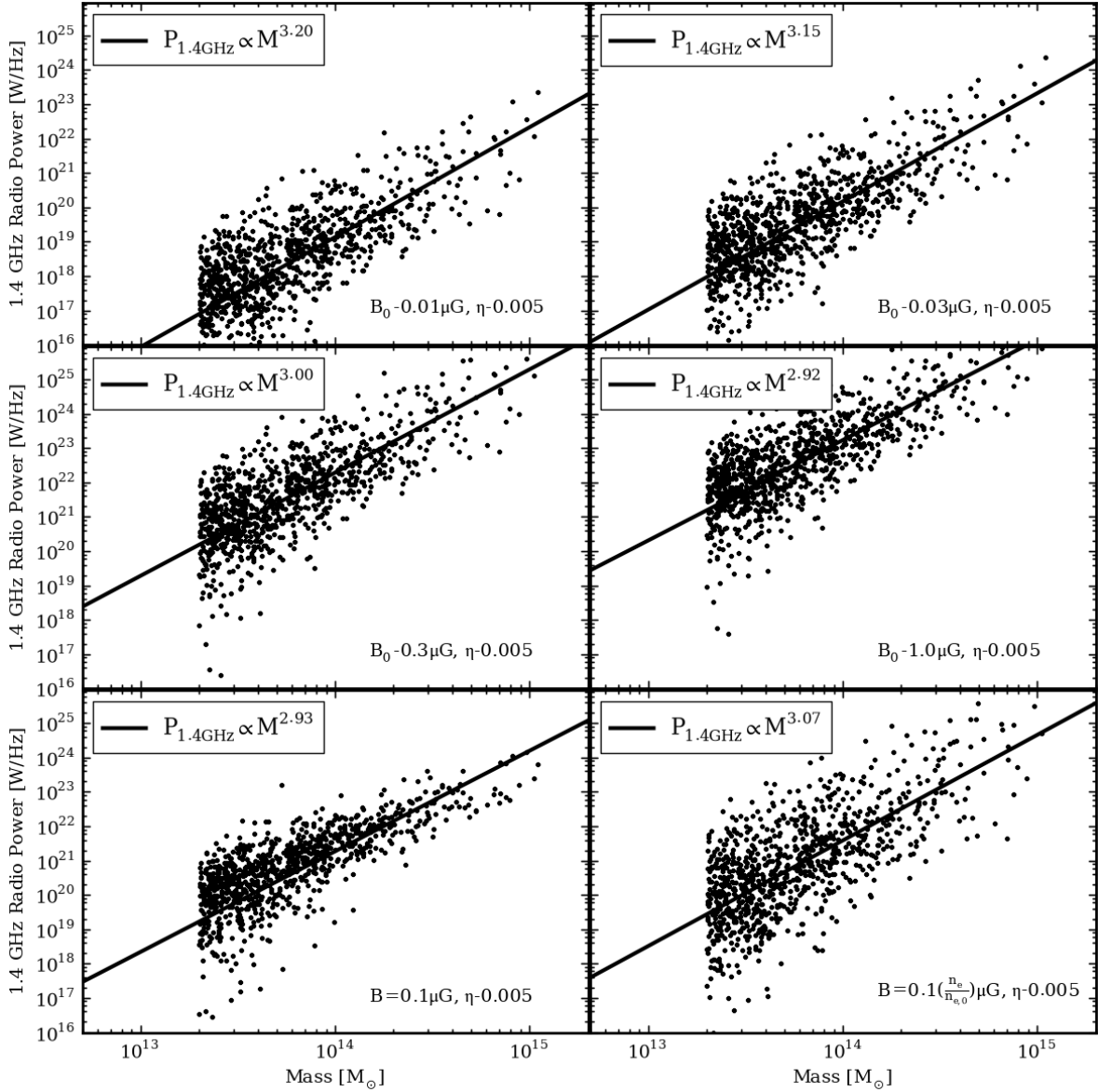


Figure A.2 As in Figure 4.8, but for varying magnetic field model parameters. In the upper four panels, the reference magnetic field parameter,  $B_0$  is varied. In the bottom left panel, the magnetic field strength is flat at  $B = 0.1 \mu\text{G}$ . In the bottom right panel, the magnetic field strength scales linearly with electron number density.

## Appendix B

### Polarized Emission Integration

In this section we detail the integration methods used to calculate the total and polarized radio emission Faraday rotation. Where possible, we follow the conventions listed in Longair [144] and Otmianowska-Mazur et al. [169]. As input to the system, we will assume that there is an emissivity,  $\epsilon$  [ $erg/s/cm^3/Hz$ ]; magnetic field,  $\vec{B}$  [ $G$ ]; electron number density  $n_e$  [ $cm^{-3}$ ]; and viewing angle,  $\vec{L}$ .

From the viewing angle and magnetic field, we first decompose the magnetic field into components along the line of sight  $B_{||}$  and perpendicular to it  $B_{\perp}$ . We use  $\theta$  to represent the angle between the  $\vec{L}$  and  $\vec{B}$ , where  $\theta$  has a range of  $0 - \pi$ .

$$B_{||} = \vec{B} \cdot \vec{L} = |B| \cos(\theta) \quad (\text{B.1})$$

$$B_{\perp} = |B| \sin(\theta) \quad (\text{B.2})$$

We then further decompose  $B_{\perp}$  into components aligned with the east and north vectors in the image plane, here referred to as  $B_x$  and  $B_y$ . Using  $B_x$  and  $B_y$ , we then define an angle field,  $\chi$ ,

$$\chi = (\tan^{-1}(B_y/B_x) + \pi/4) \% \pi \quad (\text{B.3})$$

where we explicitly cast the  $\tan^{-1}$  into  $[0..\pi]$ .  $\chi$  represents the local direction of the electric field in the image plane. We then use this value to calculate the fractional polarized emission along the

east and north vectors,

$$f_p = (s + 1)/(s + 7/3) \quad (\text{B.4})$$

$$\epsilon_{px} = \epsilon f_p \left| \frac{B_\perp}{B} \right| \cos(\chi) \quad (\text{B.5})$$

$$\epsilon_{py} = \epsilon f_p \left| \frac{B_\perp}{B} \right| \sin(\chi) \quad (\text{B.6})$$

where  $f_p$  is the polarization fraction, defined using the spectral index of the relativistic electrons,  $s$ .

Once these emission terms have been defined, we then integrate through a simulation, accounting for the Faraday rotation,

$$\Delta\psi = 2.62 \times 10^{-17} n_e \lambda^2 B_{||} dl \quad (\text{B.7})$$

where  $dl$  is in units of cm. All of this is then integrated to calculate the total intensity  $I$ , and the polarized components  $I_x$  and  $I_y$ , which is written using the discrete approximation:

$$\begin{bmatrix} I_{i+1} \\ I_{x,i+1} \\ I_{y,i+1} \end{bmatrix} = \begin{bmatrix} dl & 0 & 0 \\ dl f_p (\vec{v}_x \cdot \vec{E}) & \cos(\Delta\phi) & -\sin(\Delta\phi) \\ dl f_p (\vec{v}_y \cdot \vec{E}) & \sin(\Delta\phi) & \cos(\Delta\phi) \end{bmatrix} \begin{bmatrix} \epsilon_i \\ I_{x,i} \\ I_{y,i} \end{bmatrix} \quad (\text{B.8})$$

where the index  $i$  represents the  $i$ 'th cell along the line of sight.

As a test of this method, as implemented using `yt`, we initialize a completely polarized background at the simulation domain boundary, with the polarization angle pointing horizontal in the image plane. To do so, we override the emission, polarization fraction, density, and magnetic field strengths in the simulation presented in this paper. In this case, we set the magnetic field equal to 0 (though for numerical reasons we use a very small number), except for a sphere of with a radius equal to one-quarter of the simulation domain size. Inside this sphere, we allow the magnetic field parallel to the line of sight to be exactly that which will, for rays passing through the center of the sphere towards the ‘‘observer’’, be enough to rotate the polarization vector by  $\pi$ . We show the results of this test using  $128^2$  pixels in Figure B.1 for both on-axis ( $\vec{L} = (1, 0, 0)$ ) and off-axis ( $\vec{L} = (1.0, 0.3, 0.7)$ ), where we find excellent agreement with the expected behavior. For

both viewing angles, the maximum of  $f_p - 1.0 \approx 10^{-14}$ , and the polarization angle has a fractional error in the center of the image of  $1.7 \times 10^{-5}$  for on-axis, and  $1.3 \times 10^{-2}$  for off-axis. Given the coarse nature of the sampling of this image and the likelihood that the center pixel doesn't exactly traverse the center of the sphere, these should be viewed as upper limits.

As a second test, we initialize two  $y-z$  planes of radiation each with electric field vectors that are perpendicular to each other along. For the first plane, we set  $B_x = B_z = 0.0$ , and  $B_y = 1.0$ . The second plane has  $B_x = B_y = 0.0$  and  $B_z = 1.0$ . Each plane has a width equal to  $\frac{1}{32}$  of the simulation width, centered at  $x = \frac{1}{64}$  and  $\frac{63}{64}$  in units of the simulation width. We set the image width equal to 2.0 and use  $256^2$  pixels. Finally, we begin by looking from  $(-1, 0, 0)$  towards  $(1, 0, 0)$ , centered on  $(0.5, 0.5, 0.5)$ , and rotate in the  $x-y$  plane. Therefore in all cases plane 2 has a magnetic field that is vertical and plane 1 begins with a horizontal magnetic field but then proceeds to have a component along the line of sight. For this test we disable the Faraday rotation, and examine only the effects of combining two planes of radiation on off-axis lines of sight. We vary the rotation from the original viewpoint to have angles of  $\theta = (0, 5, 15, 30, 60)$ . In Figure B.2, we show the fractional polarization as a function of image pixel. In all cases for the portions of the planes that overlap along the line of sight, the calculated polarization fraction is within double precision fractional error of the expected polarization fraction.

All of these capabilities are demonstrated in a public repository, found using the change-set with hash fc3acb747162 here: <https://bitbucket.org/samskillman/yt-stokes>. Future improvements to this code as well as tighter integration in the primary yt repository is expected, both in performance and usability.

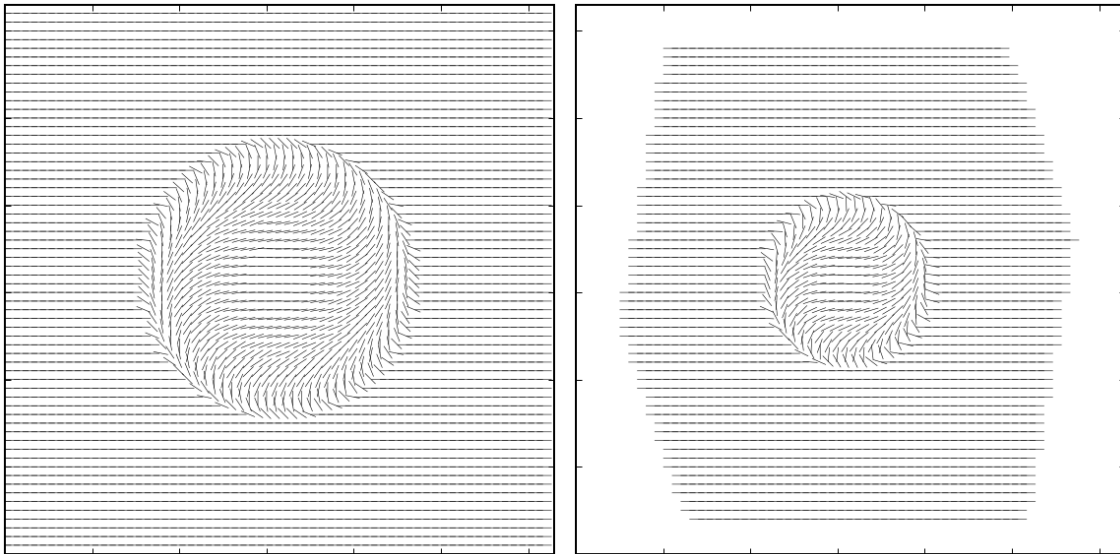


Figure B.1 On and off-axis Faraday rotation test. The left panel shows the on-axis Faraday rotation through a magnetized sphere, with an image width equal to the domain size. The right panel shows the same rotation, but off-axis and with a width of 1.6 larger than the left, to show the off-axis nature of the domain. The electron number density and magnetic field strength of the sphere are chosen to rotate the polarization angle  $\pi$  radians for the rays passing through the center of the sphere.

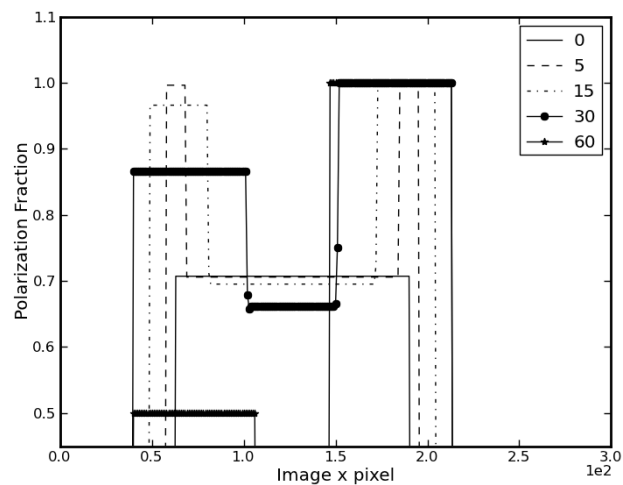


Figure B.2 Dual plane polarization test. The polarization fraction as a function of image pixel across the mid-plane of the image, shown for varying viewing angles that are measured as an offset in the  $x - y$  plane from a viewing direction of  $\vec{L} = (1, 0, 0)$ .